INTEGRATED RF MODULES AND PASSIVES ON LOW-COST FLEXIBLE MATERIALS FOR APPLICATIONS UP TO THE MM-WAVE FREQUENCY RANGE

A Dissertation
Presented to
The Academic Faculty

by

Amin Rida

In Partial Fulfillment
of the Requirements for the Degree
Doctor of Philosophy
in
Electrical and Computer Engineering

School of Electrical and Computer Engineering
Georgia Institute of Technology
May 2011

Integrated RF Modules and Passives on Low-Cost Flexible Materials

for applications up to the mm-Wave Frequency Range

Approved by:

Dr. Manos Tentzeris, Advisor
School of ECE
Georgia Institute of Technology

Dr. Mary Ann Ingram
School of ECE
Georgia Institute of Technology

Dr. Andrew Peterson
School of ECE
Georgia Institute of Technology

Dr. Wang Yang
School of CEE
Georgia Institute of Technology

Dr. Gregory Durgin
School of ECE
Georgia Institute of Technology

Date Approved: March 8, 2011

The direction in which education starts a man will determine his future life

– Plato

To my friends and family,

whose blessings and support made this work possible.

ACKNOWLEDGEMENTS

First and foremost, I want to thank my advisor, Manos Tentzeris, for showing me what it takes to be successful. I would like to extend my most sincere thanks to my colleagues whom I worked with at Georgia Tech: Li Yang, Javier Alvarado, Terence Wu, Serkan Basat, Daniela Staiculescu, Bo Pan, Dane Thompson, Jong-Hoon Lee, Trang Thai, Rushi Vyas, Vasileios Lakafosis, Vidyasagar Mukala, Amil Haque, Catherine Kruesi, Gerald DeJean, Napol Chaisilwattana, Toni Ferrer Vidal, Giulia Orecchini, Cecilia Occhiuzzi, George Shaker, Dimitris Anagnostou, Ronglin Li, and Symeon Nikolaou. You have been and invaluable source of knowledge and support.

I'd like to thank: my committee members for taking the time to study, understand, and appreciate my research. I also want to thank all GEDC staff for providing world-class research facility. Many thanks to Jill Auerbach and Julie Ridings, my mentoring programs coordinators; your advice has been invaluable. Special thanks to Professor Gregory Durgin for being very inspiring and allowing my passion to grow not just in the material but also in teaching.

Thanks to all of the undergraduate students who allowed me to mentor them: Sebastian Palacios, Andre Farzad Nasri, Sam Elia, Vernell Woods, Edward Tan, Trevale Reynolds, Lara Vogelaar, Rishab Gubta; many of which already made it to graduate school or are working professionals. I thank them for the knowledge we shared working together.

I would like to tip my hat to all of our administrators: Joi Adams, Lisa Gardner, Deborah Milliner, Chris Malbrue and Angelika Braig for making things run extra smooth on the administrative side.

To my friends and family, thank you, thank you, thank you! You rarely knew what the heck I was talking about (radio frequency what?) but that never stopped you from supporting me. I always knew that I could overcome any obstacle because of your faith in me.

To my best friends Shenee Reid and Lara Zeineddine, thank you for everything. Toyosi, thank you for keeping the kid inside of me alive. Li Yang, thank you! We now have an ISBN and I couldn't have done it without you. Ronglin Li, you will always be my antenna hero.

Lastly, I'd like to thank those who sponsored this research: Toyota, Raytheon, National Science Foundation (NSF), the Georgia Electronic Design Center (GEDC), Research Promotion Foundation, Frederick Research Center, and ATHENA research group.

Alex Margomenos (supervisor) and myself at Toyota's Labs in Ann Arbor

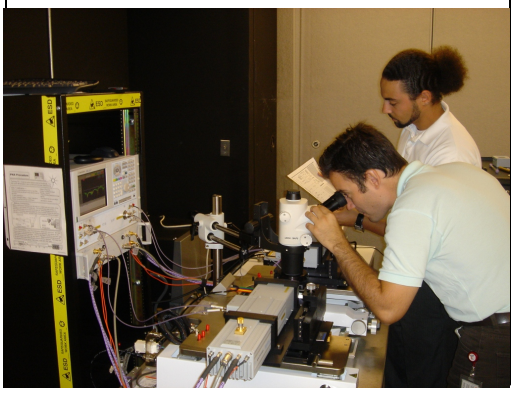

RFID Group, from right to left: Li Yang, Serkan Basat, prof. Manos Tentzeris and myself in TSRB, Gatech

TABLE OF CONTENTS

ACKNOWLEDGEMENTS.....v

LIST OF TABLES.....ix

LIST OF FIGURES.....x

LIST OF SYMBOLS AND ABBREVIATIONS.....xxi

SUMMARY.....xxiii

CHAPTER 1: INTRODUCTION 1
1.1.Wireless Platforms for Identification, Sensing, and Communication..... 3
1.2.Challenges for RF Passives and Front Ends in Mm-Wave Frequencies 11

CHAPTER 2: MATERIAL CONSIDERATIONS 16
2.1.Paper as an Ultra Low Cost Solution for Direct Write Fabrication Methods for Frequencies up to 10GHz 19
2.2.LCP as a Low Cost Solution for Frequencies up to 100GHz 21

PART I: LOW COST SOLUTIONS FOR RF MODULES UP TO 60GHz 26

CHAPTER 3: HIGH PERFORMANCE RF SOLUTIONS FOR RFID AND COMMUNICATIONS APPLICATIONS ON LCP SUBSTRATE 27
3.1.Design and Development of Novel Antennas for Miniaturized UHF RFID Tags..... 27
3.1.1. UHF RFID S-shaped Antenna Modeling..... 30
3.1.2. UHF RFID S-shaped Antenna Measurements..... 33
3.1.3. Effect on Antenna Performance when placed on Common Packaging Materials: Papers and Plastics..... 35
3.2.Design and Development of X-Band Passive Filters on LCP with Ultra High Selectivity 39
3.2.1. The Need for High Selectivity Filters and Previous Work 39
3.2.2. Filter Design and Characterization 40

CHAPTER 4: CONDUCTIVE INKJET PRINTING ON LOW COST PAPER AND LCP SUBSTRATES..... 48
4.1. Inkjet-Printed Bowtie T-match RFID Antenna at UHF Frequencies 51
4.2. Inkjet-Printed Dual Band Conformal Antenna for Use in Wifi Frequency Bands..... 54
4.3. Inkjet-Printed UWB Conformal Antenna 55
4.4. Inkjet-Printed UHF Antenna on Flexible and Organic LCP Substrate..... 60
4.5. Inkjet-Printed mm-Wave Antennas on Flexible and Organic LCP Substrate 62

PART II: 3D INTEGRATED MM-WAVE RADAR FRONT-END 64

CHAPTER 5: INTEGRATED RF ARCHITECTURE FOR MM-WAVE SYSTEMS 65

CHAPTER 6.WIDEBAND RF INTERCONNECTIONS UP TO 100GHZ 74
6.1.Wideband 3D Transitions 75
6.1.1.Wideband 3D Transitions: CPW-CPW-MSTRIP 76
6.1.1.1.CPW-CPW-MSTRIP: Design 76
6.1.1.2.CPW-CPW-MSTRIP: Sensitivity Analysis 81
6.1.1.3.CPW-CPW-MSTRIP: Measurement Considerations 82
6.1.1.4.CPW-CPW-MSTRIP: Discussion of Results 86
6.1.2.Wideband 3D Transitions: CPW-CPW 87
6.1.2.1.CPW-CPW: Design & Discussion of Results 87
6.2.Wideband 2D Transitions up to 110GHz 89
6.2.1.Wideband 2D Transitions: MICROSTRIP LINE Transitions 90
6.2.2.Wideband 2D Transitions: CPW-G Transitions 93

CHAPTER 7: INTEGRATION OF 3D TRANSITIONS WITH ANTENNA ARRAY 98
7.1.4x1 Array for S-parameter measurements 98
7.2.8x2 Antenna Array for S-parameter and Radiation Measurements 100

CHAPTER 8: ISOLATION/CROSSTALK REDUCTION MECHANISMS FOR MM-WAVE INTERCONNECTIONS AND TRANSMISSION LINES 109
8.1. Microstrip TL Crosstalk analysis and Reduction 109
8.2. CPW TL Crosstalk analysis and Reduction 118

CHAPTER 9: NOVEL ANTENNA ARRAY DESIGNS FOR MM-WAVE PHASED ARRAY APPLICATIONS 123
9.1. Antenna Considerations at Millimeter Waves 123
9.2. Edge Fed Microstrip Antennas 128
9.3. Proximity Coupled Microstrip Antenna 146

CHAPTER 10: CONTRIBUTIONS, PATENTS, AND PUBLICATIONS TO DATE 161

REFERENCES 173

LIST OF TABLES

Table 1. Survey of High Frequency Laminates from Rogers Corp. [12] 17

Table 2. Microstrip Design Parameters of the Five-Pole, Parallel-Coupled Half-Wavelength Resonator Filter, dimensions in mm. S is the separation between parallel lines, i,i+1 refer to the overlapping elements and W refers to the width of the lines (resonators). 43

Table 3. Measured Radiation Patterns at select in-band frequencies (— for xz-plane and - - for yz-plane) 59

Table 4. Survey of existing (state of the art) automotive radars and the main parameters related to the field of study. 68

Table 5. S-parameters Comparison between Microstrip TL (Sharp Corners and the Chamfered Design) 92

Table 6. Gain (dB) for ideal array configuration at 80GHz. 139

Table 7. Gain and Aperture Efficiency Comparison Among ideal, corporate feed, and shielded feed at 77GHZ for the 16x16 antenna array. 153

LIST OF FIGURES

Figure 1. Identification – various scenarios. 4

Figure 2. Comparison of Auto-ID systems. 5

Figure 3. Conceptual Diagram of an RFID System. 6

Figure 4. Suggested outline of integrated RFID antenna with IC, sensor, and power supply. 8

Figure 5. Flexible RFID Tag. 10

Figure 6. Conceptual diagram of Passive Millimeter-Wave Imaging System for concealed objects detection. 11

Figure 7. Detection Technologies to be used in future vehicles. 13

Figure 8. Commercial Automotive Radar. 13

Figure 9. 60 GHz Wireless Operational Scenario for Gbits/s communication. 14

Figure 10. EM Spectrum from DC up to UV wavelengths. Various classes of material characterization techniques are shown [20]. 19

Figure 11. Characterization of paper material through the split ring resonator method. .. 21

Figure 12. Free Space EM Characterization System. 24

Figure 13. Dielectric Constant vs. Frequency for LCP using Free Space Characterization Technique. 24

Figure 14. Loss/mm vs. Frequency for a through microstrip line at different temperatures: 25°C, 80°C, 105°C, and 125°C. The temperature is cycled back to 25°C in order to test

possible hysteresis. With 1 cycle no hysteresis was observed. It is within calibration error. 25

Figure 15. Step by step antenna design showing (a) Radiating body (b) Radiating body plus double inductive stub and (c) final antenna structure with the resistive stub. 28

Figure 16. Photo of fabricated RFID Antenna Structure showing stubs. 28

Figure 17. Simulated Input Impedance of the S-shaped Antenna. 29

Figure 18. 2D far-field radiation plot for the Φ=0° and Φ=90° as defined in Figure 16.. 30

Figure 19. S_{11} for the exact structure and for the equivalent circuit model. 31

Figure 20. Cross-sectional detail (left) showing equivalent lumped model of RFID antenna shown in Figure 15 a and in Figure 15 b and its simplified version (right). 32

Figure 21. Equivalent circuit for antenna structure shown in Figure 15 c. 32

Figure 22. Photograph of the probe plus S-Shaped antenna. 34

Figure 23. Measured and simulated data of input impedance: Resistance (left) and Reactance (right). 34

Figure 24. S_{11} of measured and simulated data. 35

Figure 25. S_{11} for 4mm thick paper and PET substrates. 36

Figure 26. S_{11} for 4mm thick paper and PET substrates with modified antenna dimensions. 37

Figure 27. Radiation Pattern of the Gain of the S-shaped antenna on paper and LCP substrates. 38

Figure 28. General Structure of parallel (edge)-coupled microstrip BPF. 42

Figure 29. Illustration of hybrid microstrip filter concept. 43

Figure 30. Filter Responses and schematics for BPF and the Hybrid Filter. 44

Figure 31. Photos of fabricated board on LCP (left) and ribbon-bonded JMT CPW-to-microstrip transition (right). 44
Figure 32. S-parameters (simulations and measurements) for the 10% BW Filter Design. 45
Figure 33. Measured S-parameters for the 25% BW Filter. 46
Figure 34. Measured S-parameters for the 35% BW Filter Design. 47
Figure 35. Details of Dimatix Material Printer DMP 2800 50
Figure 36. Realized feature size of 50 μm. 50
Figure 37. DC characterization for inkjet printed traces with epoxy and SMD 1Ω Resistor. 51
Figure 38. T-match folded bowtie RFID tag module configuration (left) and current distribution at 900MHz (right). 52
Figure 39. Measured and simulated Return Loss of the inkjet-printed RFID tag. Also showing a photograph of measurement setup using GS pitch probe. 53
Figure 40. Normalized 2D far-field radiation plots of simulation, chamber measurement and tag reading distance measurement. Also showing a photo of radiation pattern measurement setup. 53
Figure 41. Dual Band Antenna Structure. 54
Figure 42. S_{11} results for the proposed antenna on paper. 55
Figure 43. EM Model for the printed UWB antenna. 56
Figure 44. Simulated and Measured S_{11} performance of the UWB Antenna. 57
Figure 45. Measured and Simulated Directivity of the UWB Antenna. 58

Figure 46. Planar rectangular UHF monopole antenna configuration (left) and a photograph of the fabricated antenna (right) 61

Figure 47. Measurement and Simulation Results for the S_{11} of the CPW-Monopole Antenna 61

Figure 48. Simulated gain at 24GHz (left) and 70GHz (right). 63

Figure 49. Simulated and measured S_{11} of an inkjet printed antenna on LCP up to 100GHz. Also in this figure are photographs of the inkjet printed antennas on LCP and the model in HFSS. 63

Figure 50. Average atmospheric gaseous attenuation of mm-Wave propagation at sea level [49]. 66

Figure 51. Photograph of an existing automotive radar showing all the metallization and WG transitions [56]..... 69

Figure 52. Key Aspects of mm-Wave Design. 70

Figure 53. Current Radars and evolution towards proposed Radar Architecture. 71

Figure 54. Front and Back side views for the proposed architecture for the 3D integrated mm-Wave Radar Front-End showing the necessity for Microstrip TL bends, CPW TL bends, 3D RF Transitions as well as Cross-talk reduction. 71

Figure 55. Schematic of multilayer low cost mm-Wave RF substrate based radar including vertical transitions and microstrip planar arrays. 72

Figure 56. Proposed Radar Front-End Assembly, showing front and back views of Printed Circuit Board and LCP Antenna Substrate with a detailed view of part of the Front-End assembly focusing on the 3D RF transition. 73

Figure 57. Cross Sectional View of the 3D CPW-CPW-MSTRIP Transition. 77

Figure 58. Schematic for Wideband Vertical CPW-CPW-MSTRIP Transition (a) Bottom view (b) Top view. 79

Figure 59. S_{11} and E-field distribution at 76.5 GHz for the design stages in the CPW-CPW-MSTRIP Transition. 80

Figure 60. E-field distribution at 76.5 GHz for the final design back-to-back structure. . 80

Figure 61. Return Loss of 3D Transition for off-center vias. 81

Figure 62. Insertion Loss of 3D Transition for off-center vias. 82

Figure 63. Photograph of the fabricated 3D transitions on LCP (Top View). 83

Figure 64. Photograph of the fabricated 3D transitions on LCP (bottom view) with FR4 support on the boundaries for mechanical support during measurements. 84

Figure 65. Photograph of an individual fabricated back-to-back CPW-CPW-MSTRIP 3D Transition showing transition to narrower CPW input for probe measurements. 84

Figure 66. Photograph of the fabricated CPW-CPW-MSTRIP transition with dimensions. 85

Figure 67. Photograph of the probe measurement setup. 85

Figure 68. S-parameters and photos of the fabricated structure for CPW-CPW-MSTRIP Transition. 86

Figure 69. Cross Sectional View of the 3D CPW-CPW-MSTRIP Transition. 88

Figure 70. Photograph of the fabricated structures with different via spacings. 88

Figure 71. S-parameters and photos of the fabricated structure for CPW-CPW Transition. 89

Figure 72. Schematic of optimum 90° microstrip bend. 90

Figure 73. Simulated S_{11} vs. Frequency Response of several cases of bending microstrip line..... 91

Figure 74. S-parameters measurements for Microstrip transmission line bends. 92

Figure 75. Schematic of CPWG TL Bend and E-field at 76.5 GHz. 95

Figure 76. S_{11} vs. Frequency of the CPWG TL Bend at the different design stages. 96

Figure 77. S-parameters measurements for Microstrip transmission line bends. 96

Figure 78. S_{11} for the step-by-step design process for the CPW-Bends. 97

Figure 79. Schematic of the integration of 3D CPW-MSTRIP Transition with 4-Element Patch Antenna Array. 99

Figure 80. S_{11} results for the integrated 3D CPW-MSTRIP Transition with the 4-Element Patch Antenna Array. 99

Figure 81. Schematic of the 8x2 prototype array with 3D Transition (Top View). 101

Figure 82. Schematic of the 8x2 prototype array with 3D Transition (Bottom View). .. 101

Figure 83. E-field distribution at 79 GHz for the integrated 8x2 antenna array with the 3D transition (a) top view and (b) bottom view..... 102

Figure 84. Artwork of the integrated 8x2 antenna array with 3D transitions or antenna under test (AUT). 103

Figure 85. Microstrip-Waveguide Transition for radiation measurements in the mm-Wave Antenna Chamber. 104

Figure 86. Photograph of the AUT with the Waveguide connected in the mm-Wave Antenna Chamber. 105

Figure 87. Photographs of the fabricated AUT (a) Top View and (b) bottom view..... 105

Figure 88. S_{11} results for the 8x2 AUT. 106

Figure 89. Antenna Gain results for the 8x2 AUT..... 106

Figure 90. Top view of the schematic of an eight-channeled phased array concept. 107

Figure 91. Bottom view of the schematic of an eight-channeled phased array concept. 108

Figure 92. Demonstration of Microstrip TLs and E-Field distribution for different separations at 76.5 GHz. 110

Figure 93. Illustration of Forward and Backward Coupling. 110

Figure 94. Crosstalk reduction by adding a wall of vias in between the Microstrip TLs. 112

Figure 95. Forward and Backward coupling improvement through the placement of a via wall. 112

Figure 96. Backward coupling or S_{13} vs. frequency with different VIA separations for C=600 μm. 113

Figure 97. Forward coupling or S_{14} vs. frequency with different VIA separations (S) for C=600 μm. 114

Figure 98. Schematic of the double VIA Columns for crosstalk reduction, xr was kept 50 μm. 115

Figure 99. Backward coupling or S_{13} vs. frequency with different VIA separations for single and double via columns. 116

Figure 100. Forward coupling or S_{14} vs. frequency for no via fence, single and double row of vias, with s=750 μm and xr=50μm. 117

Figure 101. Forward (S_{14}) and Backward (S_{13}) Coupling analysis vs. C (center-to-center distance of the Microstrip TLs) for single via wall with S=0.75 mm. 117

Figure 102. Schematic (back-side) of the 3D Integrated mm-Wave Radar showing the CPW interconnections. 118

Figure 103. Schematic of CPW lines used for modeling crosstalk reduction. 119

Figure 104. Backward coupling S_{13} crosstalk analysis: Ground Separation. 120

Figure 105. Backward coupling S_{13} crosstalk analysis: Ground Width..... 120

Figure 106. S-parameter summary for: no vias, single and double via rows..... 121

Figure 107. Schematic of interface of RF interconnections w/3D transitions at the T/R Module or RFIC showing crosstalk reduction implementation. 122

Figure 108. Atmospheric attenuation of electromagnetic energy by water vapor and oxygen as function of frequency at sea level and at an altitude of 9150 meters from 10GHz till 400GHz. 124

Figure 109. An 8' x 12' artwork layout for several Antenna Arrays and other RF structures on LCP. This provides a good example of how LCP can benefit from fabricating large areas which is a characteristic of a low cost fabrication technology... 125

Figure 110. Multifunctional Automotive Radar showing Long Range Radar (LRR) for collision avoidance and automatic cruise control (ACC) as well as Short Range Radar (SRR) for road condition monitoring..... 127

Figure 111. Comparison between the existing Radar (switched beam) and the Proposed Automotive Radar using phase array antenna. 128

Figure 112. Physical and effective lengths of rectangular microstrip patch [68]. 129

Figure 113. Illustration of recessed Feeding..... 130

Figure 114. S_{11} vs. Frequency of the rectangular recessed feed microstrip patch (L=1.05 W=1.96 W_o=0.24 xa=0.35 ya=0.2 h=0.1016, all in mm with center frequency at 77GHz). 130

Figure 115. Simulated E- and H- plane gain patterns of the rectangular recessed feed microstrip patch (L=1.05 W=1.96 W_o=0.24 xa=0.35 ya=0.2 h=0.1016, all in mm). Maximum gain is 6.6dBi..... 131

Figure 116. S_{11} Measurements for two edge fed microstrip antennas with recessed feeding on 4mils LCP substrate designed for 77GHz and 96GHz. The antennas were measured using GSG probes and the structures had a microstrip to CPW transition for probing purposes. 131

Figure 117. Layout of the 16x1 Subarray. 133

Figure 118. S_{11} for the 16x1 Sub-array shown in Figure 117. 133

Figure 119. Gain (E-cut, Phi=90) for the 16x1 Sub-array at 79GHz. 134

Figure 120. Gain (E-cut, Phi=90) for the 16x1 Sub-array at 80GHz. 134

Figure 121. Gain (H-cut, Phi=0) for the 16x1 Sub-array at 80GHz. 135

Figure 122. Illustration for the phase shift concept, Array Factor. 137

Figure 123. Surface Currents for 16x16 array showing uniformity in distribution among all elements. 137

Figure 124. Gain (ideal) for the 16x16 array at 79GHz showing E-cut and H-cut. 138

Figure 125. Illustration for T-match section for the array antenna. 140

Figure 126. S-parameters (in dB units) for the T-match section shown in Figure 125 with S_{12}=S_{13}=-3.4dB which is close to ideal case (half energy or -3dB). 141

Figure 127. Layout for the 16x32 Array with Feeding Network. 141

Figure 128. S_{11} for the 16x32 Sub-array shown in Figure 127. 142
Figure 129. Gain (E-cut, Phi=90) for the 16x32 Antenna Array at 80GHz. 143
Figure 130. Gain (H-cut, Phi=0) for the 16x32 Antenna Array at 80GHz. 143
Figure 131. Gain in 3D at 80GHz also showing the definition of theta (elevation) and phi (azimuth) angles. 144
Figure 132. Layout for the shielded feeding 16x32 Antenna Array. 145
Figure 133. Zoomed in version of the layout for the shielded feed. 145
Figure 134. Gain (E-cut, Phi=90) for the 16x32 Antenna Array with shielded feeding 146
Figure 135. Cross section of the proximity coupled Microstrip Antenna with dual layer LCP (4mils thick each). 147
Figure 136. Schematic of the dual layer proximity coupled (Sub-Array) Antenna. 148
Figure 137. S_{11} for the sub-array antenna shown in Figure 136. 148
Figure 138. Normalized gain for the sub-array antenna at 76GHz. 149
Figure 139. Normalized gain for the sub-array antenna at 77 GHz. 149
Figure 140. Schematic of the 16x16 antenna array, showing Port1 and Port2 for coupling analysis. 150
Figure 141. S_{11} and S_{12} (coupling of Port1 and Port2). 151
Figure 142. Normalized gain for the 16x16 array antenna at 76 GHz. 151
Figure 143. Normalized gain for the 16x16 array antenna at 77 GHz. 152
Figure 144. Schematic of the 16x16 antenna array with corporate feeding. 153
Figure 145. S_{11} vs. frequency for the corporate fed antenna array. 154
Figure 146. Normalized gain for the corporate fed antenna array at 77GHz. 154
Figure 147. Normalized gain for the shielded feeding 16x16 antenna array at 77GHz. 155

Figure 148. S_{11} results for the 16x1 sub-array antenna. 157

Figure 149. Measured S_{11} for the 16x1 sub-array (73GHz → 80GHz) 157

Figure 150. Cross-sectional illustration of the AUT and a microscopic photo of the feeding (CPW) to the Antenna. 158

Figure 151. Measured and simulated S_{11} for the corporate feed 16x16 AUT. 158

Figure 152. Photo of this antenna with a transition to Waveguide input to oscillator for radiation pattern measurement. 159

Figure 153. W-band Antenna chamber setup. 159

Figure 154. Antenna Total Gain for the structure shown in Figure 152. 160

LIST OF SYMBOLS AND ABBREVIATIONS

°	degrees
ADS	Advanced Design System
AUT	Antenna Under Test
BW	Bandwidth
CPW	Coplanar Waveguide
CPWG	Grounded Coplanar Waveguide
CTE	Coefficient of Thermal Expansion
dB	decibels
dBi	dB isotropic
EM	Electromagnetics
ε_r	Dielectric constant
ε_e	Effective dielectric
f_o	Resonant frequency
Gbps	Giga bits per second
GHz	Giga Hertz
GS	Ground Signal
GSG	Ground Signal Ground
LCP	Liquid Crystal Polymer
λ	wavelength (Greek lambda)
LTCC	Low-Temperature cofired Ceramic
LNA	Low Noise Amplifier
LRR	Long Range Radar

MSTRIP	Microstrip
mm	millimeter
mm-Wave	millimeter wave
μm	micrometer
NF	Noise Figure
Ω	Ohms
PNA	Power Network Analyzer
PCB	Printed Circuit Board
RF	Radio Frequency
RFID	Radio Frequency Identification
SiGe	Silicon Germanium
SMD	Surface Mount Device
SRR	Short Range Radar
TL	Transmission Line
T/R	Transmit/Receive
TRL	Thru-Reflect-Line
tanδ	loss tangent
UWB	Ultra Wide band
VNA	Vector Network Analyzer
VCO	Voltage Controlled Oscillator
WSN	Wireless Sensor Network
WLAN	Wireless Local Area Network
WG	Waveguide

SUMMARY

The objective of the proposed research is to develop solutions for High-Performance Low-Cost Passives for Radar, Identification, and Communication Applications up to mm-Wave Frequencies. This research will bring to the table potential solutions that will meet three main requirements: small size (or low weight), high performance, and low cost. This research embarks on antenna design and development for passive RFID tags on LCP substrates, and then a transition towards lower cost modules investigates and explores the possibilities of using paper as RF substrates with inkjet printing as a low cost fabrication technology. Modules such as dual band antenna for Wifi frequencies (2.4 GHz and 5 GHz) and UWB (up to 10GHz) on paper substrate using inkjet printing are presented. This work then bridges into developing higher frequency modules. These include: highly selective filter design on LCP for X-band Radar application to be used as a benchmark for an easy adjustment for higher frequencies, and antenna modules LCP using inkjet printing for communication such as mm-Wave WLAN or WPAN.

A transition into mm-Wave Modules then takes place for the general realization of low-cost high-performance mm-Wave modules and more specifically the low cost automotive radar. After proposing an architecture for integrated mm-Wave module, this work then investigates 2D/3D interconnections (and their integration with antennas) on LCP using conventional etching design guidelines up to 100GHz. Antenna arrays that are implemented with phase shifters for beam steering are then designed using edge fed and multilayer technology. Furthermore, crosstalk reductions for highly dense transmission lines are analyzed via simulations for the optimum performance and space saving of such mm-Wave modules such as the IC interface where space restrictions are strictly enforced.

Chapter 1.

Introduction

There has been a growing demand in the Radio Frequency (RF) applications in the past couple decades primarily concerning sensing/detection, identification and communication applications. On a general scale the demand for increasingly higher rates of data, voice, and video coupled with the advancements in the SiGe and CMOS integrated circuit technologies up to mm-Wave frequencies has driven the need for high-performance applications such as wireless sensor networks, high resolution sensing such as mm-Wave automotive radar, imaging in the mm-Wave and THz frequencies, Gb/s wireless personal area network WPAN, and other communication systems such as multi access systems. In addition to the aforementioned, Radio Frequency identification (RFID) is an emerging compact wireless technology for the identification of objects, and is considered an eminent candidate for the realization of completely ubiquitous ad hoc wireless networks. A listing of applications that utilizes RFID and which is still increasing to date is: automation, transportation, logistics, tracking, access control, real time location systems (RTLS), warehousing, and inventory systems. Other specific causes to this burst of RF demand are mirrored by recent observations such as:

1) World Health Organization predicting the cause of deaths due to road traffic accidents to change from 9th in 2005 to 5th in 2030 [1]. This pushes for technological advancements in sensing and detection which has already been influencing automotive companies to invest in R&D for not just improving the performance of existing automotive radars but also to replace them with a low

cost implementation. This allows for mass production in most if not all cars in the future.

2) Radio Frequency Identification has been gaining in popularity, especially as we find ourselves in a communication age that is heading towards a ubiquitous computing (cognitive intelligence) world. Automatic identification and sensing systems become an important aspect not just in today's technology but also as part of our daily life where we need RFID in cars, transportation systems, access points, and even simple transactions not to mention the extensive usage of RFID (i.e. logistics systems, healthcare, and tracking and localization applications). In 2010 the RFID market, according to ABIResearch [2] appears set to reach a size of $4.47 billion excluding automobile immobilization; a large segment that uses RFID technology. This represents 15% more that the adjusted 2009 figure. Furthermore, statistics depict a market that exceeds $8.25 billion in 2014, a number that represents a 14% compound annual growth rate over the next five years.

3) The phenomenal global growth in consumer electronics industry with forecasted growth of 15% in the market size from 2008 to 2013 [3].

These RF and wireless applications demanding higher data rates and in most cases have defined new directions in the passive RF world. Aspects such as: performance, integration, size requirements, flexibility (in certain scenarios), not to mention cost become extremely important for the realization of such applications and RF ambitions. This work tries to answer the need for the growing list of RF applications in a mass-quantity (ubiquitous) fashion for applications that require low-cost integration platforms

and fabrication techniques such as RFID/Sensing, security/safety high-performance telecom, and radar.

Since this work starts primarily with improvements in the design and fabrication methods of RF structures at UHF and progresses up to mm-Wave frequencies, this chapter will also be structured in a similar fashion. It starts by talking about the challenges in RFID tag design expanding into microwave structures for communications, sensing, and identification up till 40GHz range. After which the chapter will discuss the many challenges and technological shortfalls for mm-Wave technology with specific examples to automotive radars. The automotive radar example covers a substantial part on the electronics for the safety and well being of drivers, passengers, as well as pedestrians.

1.1. Wireless Platforms for Identification, Sensing, and Communication

This section illustrates the justification of the researched topic through a literature survey of existing technologies, their shortfalls, and the capability gaps in terms of performance and cost for the passive RF aspect of wireless technologies like RFID, Wifi, and Sensing.

Identification plays a major function in our lives, the operations that we run, and even businesses. Identification and/or authentication are essential in most, if not all, of the objects, people, or procedures that we deal with on a daily basis. Examples include: barcode technology for identifying groceries, vehicle identification numbers (VIN) for recognizing vehicles, magnetic stripe cards used for payment methods (like credit cards), biometrics procedures for identifying humans, and holography techniques used for the authentication of stamps and/or money. There are several other techniques that are used

for identification/authentication such as: access cards, proximity cards, contactless smart cards, and radio frequency identification (RFID), which takes on several forms and may be used in any other identification or authentication wireless methods mentioned [4].

Moreover, automatic identification known as Auto-ID has seen tremendous demand, especially in our current communication age as we have witnessed a large transition in technological fields towards wireless. Immediate identification of people, animals, goods, and products becomes essential. Several huge industries are requiring an increased utilization of Auto-ID systems. A listing of such industries includes: logistics, supply chain, transportation, manufacturing, warehousing systems, health care, security, space, and navigation [5]. Figure 1 shows various scenarios that incorporate the use of automatic identification.

Figure 1. Identification – various scenarios.

Figure 2 compares the most employed Auto-ID methods in terms of technological gaps and capabilities. Certain methods such as biometrics were omitted since they only

apply to identifying personnel and do not fit under the general low cost identification techniques.

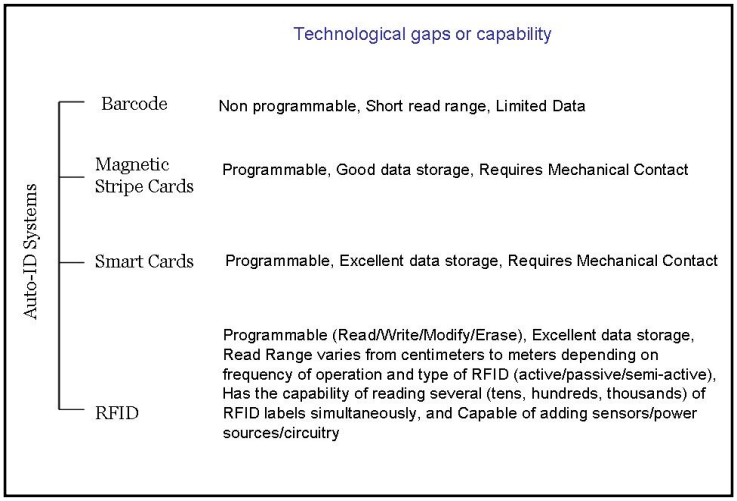

Figure 2. Comparison of Auto-ID systems.

Radio frequency identification (RFID) is an emerging compact wireless technology for the identification of objects, and is considered an eminent candidate for the realization of completely ubiquitous ad hoc wireless networks. RFID utilizes electromagnetic waves for transmitting and receiving information stored in a tag or transponder to/from a reader. This technology has several benefits over the conventional ways of identification. Some advantages are higher read range, faster data transfer, the ability of RFID tags to be embedded within objects, no requirement of line of sight, and the ability to read a massive amount of tags simultaneously. A listing of applications that currently use RFID are: transportation and logistics, product tracking and inventory systems, access control, library book tracking and management, passports, parcel and document tracking, automatic payment solutions, real time location systems (RTLS), automatic vehicle identification, and livestock or pet tracking.

An RFID system consists of readers and tags. A typical system has a few readers, either stationary or mobile, and tags that are attached to objects to be identified, as illustrated in Figure 3. A reader communicates with the tags in its wireless range and collects information about the objects to which tags are attached.

Figure 3. Conceptual Diagram of an RFID System.

As the demand for low cost, flexible, and power efficient broadband wireless electronics increases, materials and integration techniques become critical and face more challenges. This is witnessed as a result of the growing demand for "cognitive intelligence" married with RFID technologies. In order to create a completely ubiquitous network, the cost of the RFID tags would need to be extremely inexpensive. This is also a crucial factor for the mass production of RFID tags and/or sensor-enabled RFID tags. While current fabrication processes use the conventional metal etching techniques, the theme of this work will be about environmentally friendly fabrication techniques and materials, namely inkjet printing and paper-based substrates. This will also allow for the easy disposal of a massive number (in the billions) of RFID tags.

In addition to the cost of the RFID tag, another main parameter considered in RFID

systems is the tag performance. RFID tags need to have good matching between their antenna and RFID IC. This is crucial since unlike most of the common RF front-ends in which antennas have been designed primarily to match either 50Ω or 75Ω loads, an RFID tag antenna has to be directly interfaced with an IC which exhibits complex impedance. Therefore, the impedance matching technique plays an important role in a successful RFID tag design. Parameters such as the power reflection coefficient as described by Kurokawa [6] need to be minimized, in addition to the optimization of other antenna parameters such as directivity and bandwidth. However, adding an external matching network with lumped elements proves costly and impractical for implementing low cost RFID tags for mass production, not to mention size issues. In this instance, effective matching networks need to be implemented.

A wireless sensor is a device that combines the capabilities of a sensor and an RF or wireless device and therefore is capable of sensing, processing data, transmitting, and/or communicating to other wireless device(s). In addition to the basic RFID automatic identification capabilities, wireless sensors can bridge identification and sensing technology through their integration. The aim is to create a system that is capable of not only tracking, but also monitoring (condition). With real-time cognition, a secured intelligent network of RFID-enabled sensors may be formed.

A suggested module of an already existing RFID tag operating at UHF frequencies and that is planned to include sensing capabilities is shown in Figure 4 [7]. High efficiency antennas at UHF frequencies are characterized in general by their dimensions, which can have half a wavelength at the operating frequency (such as 15 cm around 900 MHz in one dimension) or some squared/rectangular configuration. In this case, the

squared or rectangular configuration would be a better candidate to fit the host electronics, power supply, and sensing devices. With the status, location, and movement of objects and/or personnel on hand, a plethora of information can be mined and utilized in several application such as warehousing and healthcare to significantly improve business processes and reduce capital expenses. A simple real-time location system (RTLS) may also be embedded for tracking expensive equipment and assets and hence improve security. However, considering the dense deployment of RFID-enabled sensors, the cost of installing access points such as RFID readers creates a bottleneck in the application costs and becomes less efficient from application point of view. Networks such as the well established pervasive TCP/IP has served as a backbone for all computing infrastructure and is the basis for other networks such as Wi-Fi or wireless local area network (LAN).

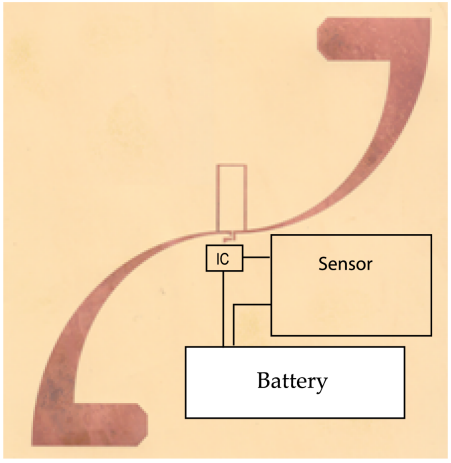

Figure 4. Suggested outline of integrated RFID antenna with IC, sensor, and power supply.

A technology that has the potential of short-range high-bandwidth communications utilizing very low power levels spreading the transmitted signal over a significantly large

portion of the radio spectrum is Ultra-wideband (UWB) RF technologies, commonly between 3.1-10.5 GHz [8]. UWB applications have great variety [8]. Some of the current and potential applications are listed below.

- Altimeter/Obstacle avoidance radars
- Collision voidance sensors
- Intrusion detection radars (through wall imaging)
- Industrial RF monitoring systems
- Wearable electronics for wireless body area network (WBAN)
- High speed WLANs and wireless personal area network (WPANs)

Interestingly, numerous recent applications of UWB radios target sensor data collection, precision localization, and tracking applications. Such applications necessitate the deployment of a large number of UWB antennas to meet system requirements. To this end, it is important to keep the cost per antenna as low as possible to maintain an adequate operational cost for such UWB systems. A quick look at the most common techniques for the fabrication of printed UWB antennas reveals that photolithography has been the most dominant technology. However, this method involves multiple steps including etching, masking, and electroplating, thus being a time consuming, labor intensive and expensive. In addition, since the solvent used in the etching process is corrosive, the choice of substrates is limited. Moreover, the photolithography process generates high volumes of hazardous waste, which are environmentally detrimental. An alternative technique would be favored.

In addition to the technologies mentioned above, flexible electronics (also known as flex circuits) is a technology that not only witnessed an increase in attention and

investments in research and development, but also is becoming more essential in today's growing market in every day's mobile devices as well as in applications that demand flexibility, light weight, and space savings. Figure 5 shows a photograph of a flexible RFID tag using nano-technology. Flex electronics also allow the screen printing and more recently the inkjet printing on substrates such as paper and Liquid Crystal Polymer (LCP). These are especially important in communication systems' design where a planar antenna that meets the specifications of a certain application is physically non-realizable, enforcing the utilization of a conformal antenna as a necessity.

In a similar scheme, the substrate material and integration techniques are becoming more of a critical materials research topic due to the ever growing demand for low cost, flexible and power-efficient broadband wireless electronics. This demand may also be further enhanced by the need for inexpensive, reliable, and durable wireless automatic identification (i.e. RFIDs) and communication devices (i.e. mobile Wifi enabled systems).

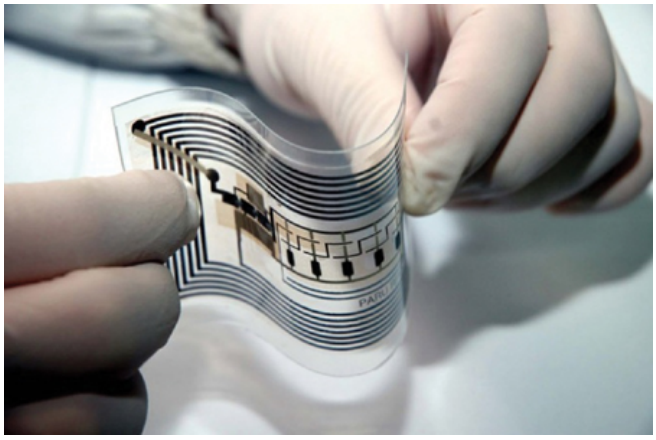

Figure 5. Flexible RFID Tag.

1.2. Challenges for RF Passives and Front Ends in Mm-Wave Frequencies

Mm-Wave radars were once considered unsuitable due to the absence of practical means of generation, reception, channelization, and transmission of EM waves in the mm-Wave range. This was also due to the fact that the physics of mm-Waves was not studied; however theory and practice discover new advantages of mm-Waves, which open up new opportunities in communications and radar applications in various fields. Some of the main applications that utilize mm-Wave are: vehicle radars, high-speed wireless access, radiometry for concealed weapon detection, and ultra-high-speed wireless local area network (WLAN). Figure 6 shows a conceptual diagram for passive millimeter-wave Imaging System for detection of concealed objects. Compared to low-GHz frequency bands, mm-Wave exhibits more bandwidth, less interference, and smaller antenna dimensions which makes possible the creation of large antenna arrays. High gain antennas at rather small aperture coupled with the possibility of using wideband facilitate high resolution, improve accuracy of radar measurements, and delivers huge amount of data and information in communication systems due to the increased RF bandwidth [9].

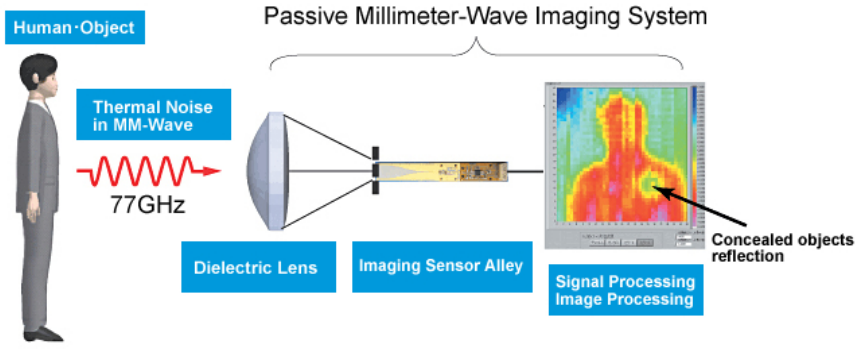

Figure 6. Conceptual diagram of Passive Millimeter-Wave Imaging System for concealed objects detection.

In addition to the fact that lower frequency bands are filling up, a great deal of credit for the realization of sensing and communication systems operating at mm-Wave frequencies goes towards the recent advancements in the Si-based monolithic microwave integrated circuits (MMIC) technology (i.e. SiGe HBT). This is due to its low cost production [10]. Of particular interest is the mm-Wave automotive radar. Figure 7 illustrates the several functionalities that could be introduced to vehicles in the effort to produce safer driving environments. As shown in the figure an "intelligent vehicle" would be able to perform: adaptive cruise control (ACC), collision notification and avoidance, blind spot detection, park mate, back up aid, lane departure warning, lane keeping, traffic sign recognition, and night vision. It is to be noted that Figure 7 also illustrates detection technologies such as video, ultrasonic, and lidar to aid the main radar functions. Figure 8 shows a detailed picture of a commercial automotive radar by Bosch (www.bosch.com) and reveals a complicated design with a lensed radome used to focus the beam of the antenna and achieve high gain. This work will focus on the mm-Wave radar as it forms the main principal detection safety mechanism in vehicle radars/sensors. It is also important to note that the passive RF components designed in this work that targets mm-Wave radar could be utilized for other mm-Wave RF structures, and not limited to the use of automotive radars.

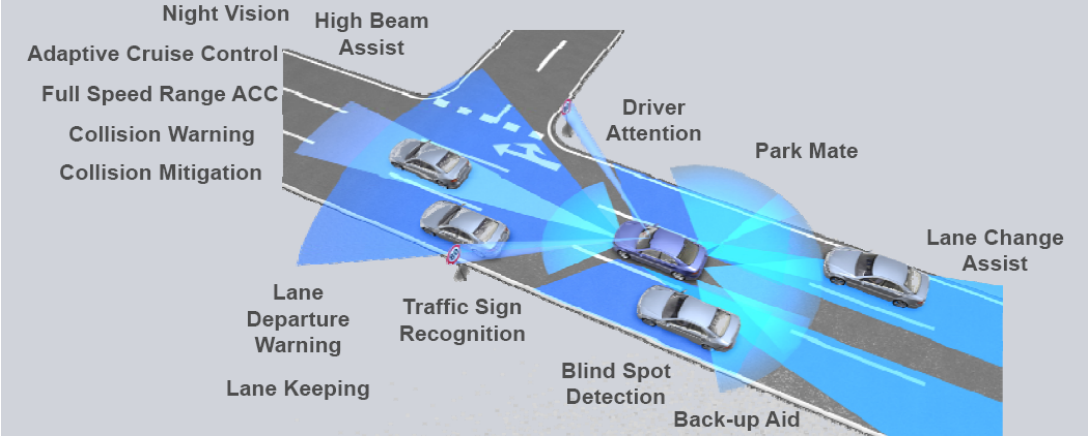

Figure 7. Detection Technologies to be used in future vehicles.

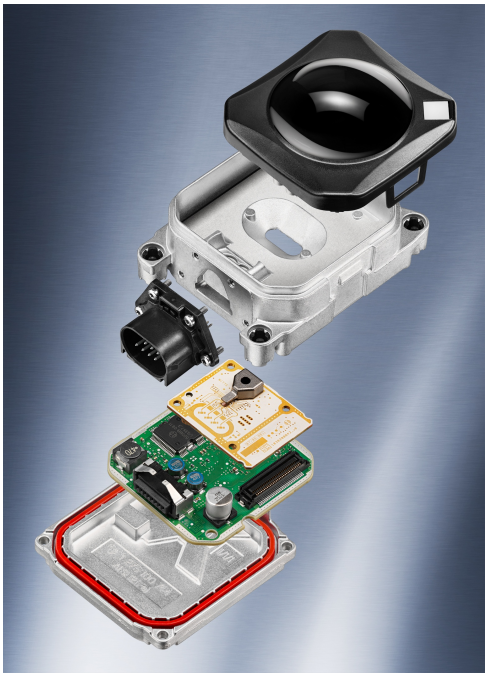

Figure 8. Commercial Automotive Radar.

Driven by the demand for high-data-rate, mm-wave technologies with broad bandwidth are being explored in high speed-data wireless communications. This has also pushed towards issuing standards such as IEEE 802.15.3c. Figure 9 shows a conceptual image of the 60GHz Wireless Operational Scenario for: PC connectivity wireless docking, HDMI cable replacement, kiosk downloading, and high-speed ad-hoc networking. The

benefits that mm-Wave technology presents are vast, especially for communication. These are:

- Unlicensed operation
- Secure operation resulting from short transmission distances due to oxygen absorption, narrow antenna beamwidth and no wall penetration
- High speed data transition in Gbps range
- Advantage of antenna diversity
- Good co-existence between mm-Wave systems and 802.11a/b/g and Bluetooth due to large frequency difference

Figure 9. 60 GHz Wireless Operational Scenario for Gbits/s communication.

Mm-Wave electronics whether for radar, short range broadband or other applications require low cost and high performance. After researching the area of mm-Wave, it was found that novelty and advancements are up for grabs [11]. Realization of planar ink jet printed mm-Wave structures are worth an attempt. Other ideas such as the migration from successful implementation of RF structures (from lower frequency bands - ranging from high bandwidth antennas to integrated passives) to mm-Waves become crucial.

The research being presented in this work has a direct application in the areas of detection, identification, and communication. All of these areas share three main

requirements: small size (or low weight) high performance, and low cost. This research will bring to the table potential solutions that will meet these three main requirements. Starting with RFID passive antenna design and characterization on LCP substrates into using paper as an RF substrates with inkjet printing as a low cost fabrication technology for RFID and wireless platforms, this work then bridges into the development of higher frequency modules. Examples include a highly selective filter design for X-band radar application on LCP and antenna modules for WLAN and WPAN communication up to mm-Wave frequencies on LCP and paper substrates. A transition into mm-Wave Modules then takes place for the general realization of low-cost high-performance mm-Wave modules and more specifically the low cost automotive radar. This work investigates 2D/3D transitions on high frequency laminates by using conventional etching design guidelines up to 100GHz. Crosstalk reduction for highly dense transmission lines will be analyzed via simulations for the optimum performance and space saving of such mm-Wave modules especially at the IC interface where space restrictions are strictly enforced. Furthermore, antenna arrays to be implemented with phase shifters for beam steering are then designed using edge fed and multilayer antenna technology.

Chapter 2.

Material Considerations

The scope of this work also calls for a general evaluation of high frequency materials. This chapter analyzes the electromagnetic properties of substrates such as dielectric properties, which are vitally important in the design, and application of any particular device at any frequency range. In addition, a discussion of other properties relevant to their application in identification, communication, and sensing will be provided. A general comparison of available materials is provided, followed by the choice of the materials used for this work. EM Characterization methods such as ring resonators and free space have been utilized for this research and within the frequencies of interest for the applications given. As a result, dielectric properties such as dielectric constant ϵ_r and loss tangent tanδ were available for inputting in the EM simulators for circuit/antenna designs. Table 1 shows a survey of the current custom high frequency material available at Rogers Corp. (www.rogerscorp.com), which is a major supplier of materials for circuit board markets.

Table 1. Survey of High Frequency Laminates from Rogers Corp. [12]

Name or Series	Material or Composition	Dielectric Constant Range (Values typical at 10GHz)
RT/Duroid	PTFE Glass Fiber, Filled PTFE Composite, PTFE Ceramic or PTFE Ceramic Woven Glass reinforced	1.96 – 10.2
ULTRALAM	PTFE Woven Glass (ULTRALAM 2000), Liquid Crystal Polymer (ULTRALAM 3000)	2.4 – 3.05
RO 3000 Series	PTFE Ceramic	3.0 – 10.2
RO 3200 Series	PTFE Ceramic Woven Glass reinforced	3.0 – 10.2
RO 3730	PTFE Ceramic	3.0
RO 4000, RO 4500 Series, RO 4730	Hydrocarbon Ceramic	3.38 – 6.15
XT/Duroid	High Temperature Thermoplastic Ceramic (HTTC)	3.34
Syron 7000	High Temperature Thermoplastic Ceramic (HTTC)	3.4
TMM	Hydrocarbon Ceramic	3.4

Current materials used to overcome water absorption difficulties are advanced microwave composites and ceramics. Both of these material categories have generally excellent electrical performance and very low moisture absorption and transmission, but they can also be relatively expensive. Other types of ceramics not shown in Table 1 are Low-temperature co-fired ceramics (LTCC), which has very low electrical loss and can be used in multilayer laminated modules that have densely integrated passive and active devices stacked and connected vertically to save space and cost [13]. Overall, LTCC is a very attractive material technology, especially for applications that require the greatest functionality in the smallest footprint, however; LTCC also has many limitations. These are namely:

- High lamination temperature 850°C which is far above that which destroys active devices.
- High dielectric constant (ε_r = 5.9 – 9.1). The high dielectric constant is detrimental to antenna radiation efficiency [14].

Of specific interest from the list of materials from Table 1 is Liquid crystal polymer, which has drawn much attention for its outstanding packaging characteristics for high frequencies [14] especially as a low cost material. LCP as discussed later is a superior substrate for high frequency packaging (up to mm-Wave frequencies). In other cases (for lower frequencies), one has to look in own backyard for innovative ways using already existing materials, especially if the aim is cost. In this case, this work has considered using paper as an RF substrate and did the analyses and tests to prove its applicability and to see how high in frequency it can operate.

This chapter is divided into two sections. The first section will discuss the characterization of paper as a ultra low cost substrate for frequencies up to 10GHz. Following is a section on LCP's outstanding characteristics as a high frequency substrate and packaging material using several articles found in the literature [14,15,16, 17, 18,19]; in addition, a free space EM characterization has been performed at Toyota Technical Center labs, the sponsor for the most part of this mm-Wave research.

The dielectric behavior of a material is defined by its complex permittivity:

$$\boldsymbol{\epsilon = \epsilon' - j\epsilon''} \qquad \textbf{Equation 1}$$

However we deal separately with the relative permittivity ϵ_r which is referred to as the dielectric constant and the loss tangent $tan\delta$:

$$\epsilon_r = \frac{\epsilon'}{\epsilon_o} \qquad \textbf{Equation 2}$$

$$tan\delta = \frac{\epsilon''}{\epsilon'} \qquad \textbf{Equation 3}$$

A variety of characterization techniques exist that would allow acquiring the dielectric properties. Figure 10 shows the EM spectrum from DC up to Ultra-Violet (UV) wavelengths as well as the appropriate material characterization techniques covering different frequency ranges. These characterization techniques are extremely necessary as we go higher in frequencies to the mm-Wave regions and beyond in the Terahertz (THz) bands especially with the promise of applications in biomedical imaging, detection of chemicals or explosives, communications and a plethora of other fields.

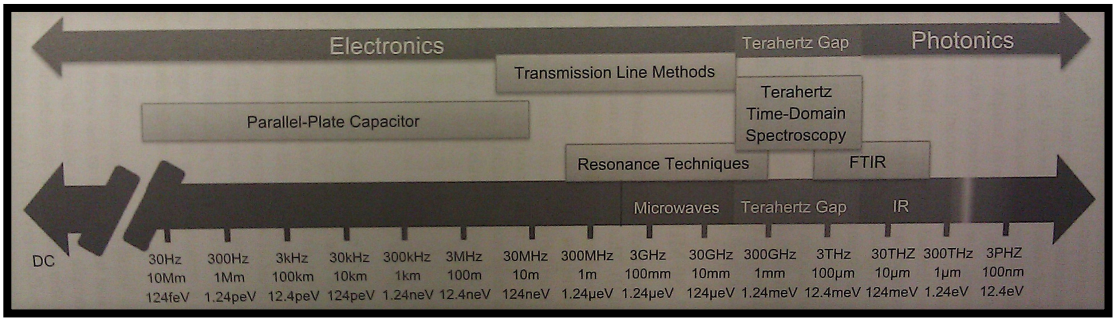

Figure 10. EM Spectrum from DC up to UV wavelengths. Various classes of material characterization techniques are shown [20].

2.1. Paper as an Ultra Low Cost Solution for Direct Write Fabrication Methods for Frequencies up to 10GHz

There are many aspects of paper (as a material) that make it an excellent candidate for an extremely low-cost substrate for RF applications and other applications where mass deployment is required such as RFID and wireless sensor networks (WSN). Paper, an organic-based substrate, is widely available. The high demand and the mass production of paper make it the cheapest material ever made. From a manufacturing point of view, paper is well suited for reel-to-reel processing, thus mass fabricating RFID inlays on

paper (to name an example) becomes more feasible. Paper also has low surface profile and, with appropriate coating, it is suitable for fast printing processes such as direct write methodologies instead of the traditional metal etching techniques. A fast process, like inkjet printing, which is discussed in more detail in Chapter 4, can be used efficiently to print electronics on/in paper substrates. Lastly, paper is one of the most environmentally friendly materials and the proposed approach could potentially set the foundation for the first generation of truly "green" RF electronics and modules.

RF characterization of paper becomes a critical step for the qualification of the paper material for a wide range of frequency domain applications. The knowledge of the dielectric properties such as dielectric constant (ε_r) and loss tangent ($\tan\delta$) become necessary for the design of any high frequency structure such as RFID antennas on the paper substrate, and more importantly, if it is to be embedded inside the substrate. Precise methods for high-frequency dielectric characterization for this frequency range are Transmission Line and Resonant Techniques. In an extensive literature review, dielectric properties of paper beyond few hundred megahertz were not available. A parallel plate capacitor characterization technique has been utilized in [21] in order to characterize paper up to 400MHz. Besides the inaccuracy of such a technique, a different characterization method needed to be considered in order to step up the frequency to 10GHz.

The dielectric properties of paper have been studied at Georgia Tech and has been included in the author's Masters' thesis and other IEEE publications [22, 23] for frequencies up to 2 GHz using ring resonators [24]. In this work the properties of the benchmarking paper substrates were studied in the UWB frequency range through the use

of the split-post dielectric resonator technique [25] and were performed by the Electromagnetics Division at the National Institute of Standards and Technology (NIST), Boulder, CO, USA. Several cavities covering the band from 1GHz to 10GHz were utilized. Each blank paper sample was cured first in a thermal oven for 2 hours at 120 degrees to mimic the curing process of the printed ink as explained in Chapter 4. The results for the extracted relative permittivity of the 10mil thick cured paper are shown in Figure 11. The measured dielectric loss tangent or $tan\delta$ values were bounded between 0.06 and 0.07 for the whole frequency range.

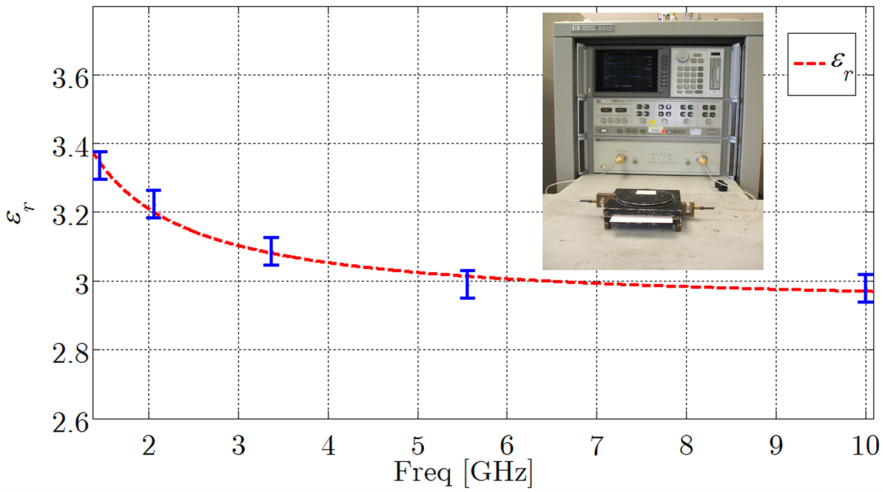

Figure 11. Characterization of paper material through the split ring resonator method.

2.2. LCP as a Low Cost Solution for Frequencies up to 100GHz

The purpose of this work is to describe methods for the development of easy-to-fabricate low-cost practical designs on flexible substrates for use in mm-wave (up to 100GHz) front-end applications such as broadband high-speed wireless LAN [11], and automotive radar and imaging systems. The choice of the substrate is Liquid Crystal Polymer (LCP), which has gained much consideration in the past decade as a potential high-performance microwave medium with excellent "dual" (substrate and packaging) functionality due to

its very good electrical, mechanical, and hermeticity properties. Previous literature has described the numerous benefits of LCP [14-17]:

- Excellent high-frequency electrical properties with dielectric constant low and stable near 3.16 from 30–110 GHz [14],
- a frequency dependent loss tangent from 2–110 GHz that follows the equation [26]:

$$\boldsymbol{tan\delta(f[GHz]) \simeq 2.8076e-5 * f[GHz] + 0.00184} \qquad \textbf{Equation 4}$$

- Quasi-hermetic (water absorption < 0.038%) [14],
- Low cost (`$5/ft^2 for 2-mil single-clad low-melt LCP) [14],
- Low xy coefficient of thermal expansion (CTE), which may be engineered to match metals or semiconductors,
- Naturally non-flammable (no need to add halogens, environmentally friendly),
- Recyclable,
- Flexible for conformal and/or flex circuit applications,
- Multilayer all-LCP lamination capabilities to create multilayer LCP RF modules,
- Relatively low lamination processing temperature (~285 ◦C),

A major previous work [14, 26] has established the choice of LCP as a mm-Wave substrate to be used in the designs of this work. In more detail, LCP has shown to be an excellent material for high temperature dielectric stability up to mm-wave frequencies. This was demonstrated in [13], where the average of the absolute values of τ_{ϵ_r}(the temperature coefficient of dielectric constant, which describes how much a material's dielectric constant changes with a given temperature change) showed to be ~-42 [ppm/

°C] from 11–105 and which is claimed to be comparatively better than a majority of other standard microwave substrate materials in this parameter.

Since it is not the objective of this work to re-evaluate LCP's main characteristics; simple measures have been taken to verify the value of the dielectric constant ε_r especially since the process tolerances in manufacturer's dielectric properties may differ slightly from one manufacturer to another. A free space characterization technique, offered as a package by Agilent Technologies (www.agilent.com) was utilized for verifying the value of ε_r and took place at Toyota Technical Center labs. The free space characterization technique belongs under the umbrella of transmission line methods, is a non-contact method where the substrate is assumed to have large area and perfect plane wave illumination by horn/lens antennas is assumed. Figure 12 shows the setup for the free space characterization system including the Power Network Analyzer (PNA), two horn antennas facing each other and a sample holder in between. The results for ε_r are shown in Figure 13 and are within 3-5% of the findings of [13], which could have a significant influence on antenna resonance behavior. This difference also proves that such steps are essential prior to the design stage of any mm-Wave (or higher frequencies) system or subsystem.

Figure 12. Free Space EM Characterization System.

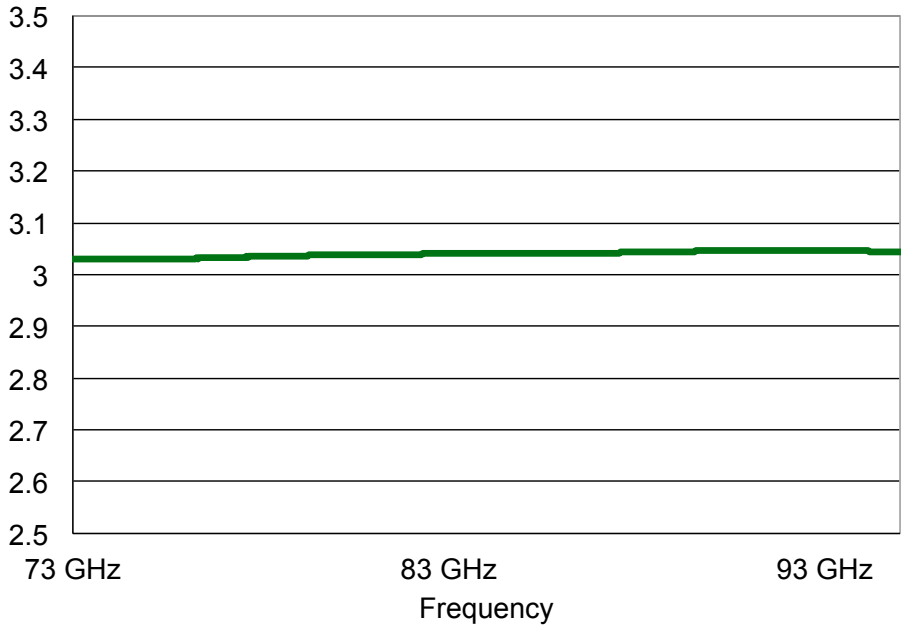

Figure 13. Dielectric Constant vs. Frequency for LCP using Free Space Characterization Technique.

In addition to that, a simple temperature test was performed to make sure that no hysteresis behavior is present with respect to amplitude (or loss) performance of a through microstrip line. Figure 14 summarizes the Insertion Loss (Loss/mm) results of a through microstrip line on 4mils thick LCP exhibiting a linear behavior of loss and

temperature at different temperatures: 25°C, 80°C, 105°C, and 125°C. The temperature is cycled back to 25°C in order to test possible hysteresis. It was observed that with 1 cycle no hysteresis took place and the measurements were within calibration error.

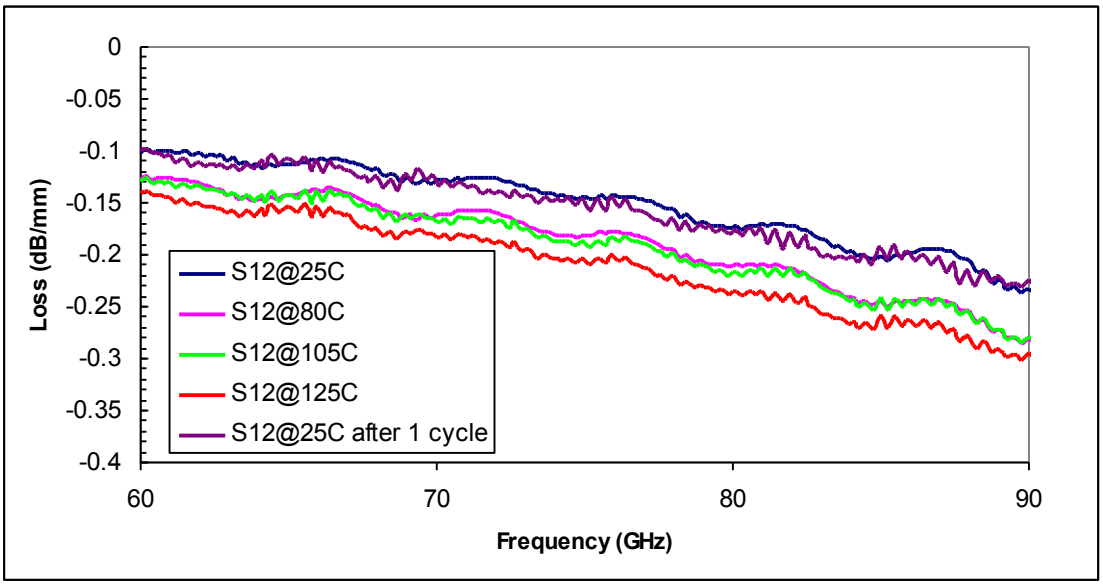

Figure 14. Loss/mm vs. Frequency for a through microstrip line at different temperatures: 25°C, 80°C, 105°C, and 125°C. The temperature is cycled back to 25°C in order to test possible hysteresis. With 1 cycle no hysteresis was observed. It is within calibration error.

PART I. LOW COST SOLUTIONS FOR RF MODULES UP TO 60GHz

Chapter 3.

High Performance RF Solutions for RFID and Communications Applications on LCP Substrate

This chapter demonstrates the applicability of LCP by providing two designs for identification and communication applications. An RFID tag operating at UHF Frequencies is presented first, with detailed information on the design, modeling, and measurements. Following is a section on an ultra high selectivity filter design operating at X-Band (10-12 GHz) frequencies.

3.1. Design and Development of Novel Antennas for Miniaturized UHF RFID Tags

In this design approach, a compact configuration (in an area less than 3"x 3") of a λ /2 dipole antenna was developed. The step by step design is illustrated in the Figure 15 showing the main radiating element which if stretched from one end to the other corresponds to a length of ~16cm (which is λ /2 around the center frequency 935 MHz in air). The tapering of the antenna was chosen for maximum current flow and to achieve a high bandwidth. The antenna was folded at a distance (~0.16 λ) not to cause any significant current perturbation (keeping maximum radiation efficiency), while making the design more compact. Without loss of generality, the overall matching network is designed to conjugately match an RFID chip with a high capacitive impedance of Z_{IC}=73-j113Ω. To satisfy the conformality RFID requirements, the proposed antenna was fabricated on flexible 4-mil LCP.

The resistive shorting stub and the double inductive stub as illustrated in Figure 16 constitute the overall matching network. The resistive stub is used to tune the resistance of the antenna to match that of the IC. The size and shape (thin long loop shaped line) of the resistive stub were designed to have an optimum match to Z_{IC}=73-j113 Ω. The double inductive stub is composed of two inductive stubs to provide symmetry on both sides of the antenna. The double inductive stub also serves as the reactive tuning element of the antenna. The stubs were designed to have a center frequency f_0 at 895 MHz with a BW of 70MHz operating from 860→930 MHz, covering European and U.S. RFID frequency bands [27]. Those variables can be fine tuned to optimize the antenna characteristics on the RFID tag at any frequency and matched to any IC impedance.

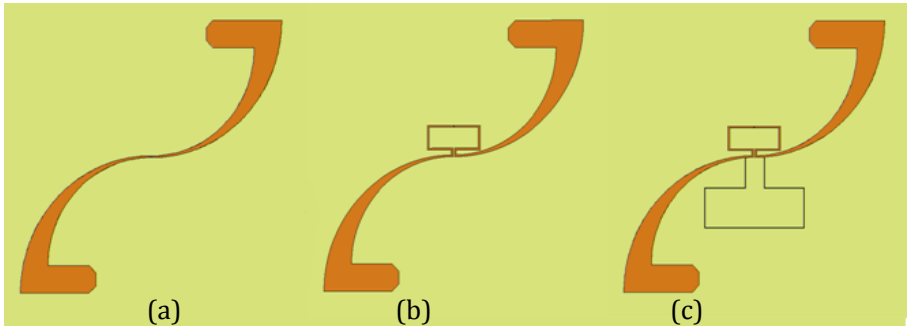

Figure 15. Step by step antenna design showing (a) Radiating body (b) Radiating body plus double inductive stub and (c) final antenna structure with the resistive stub.

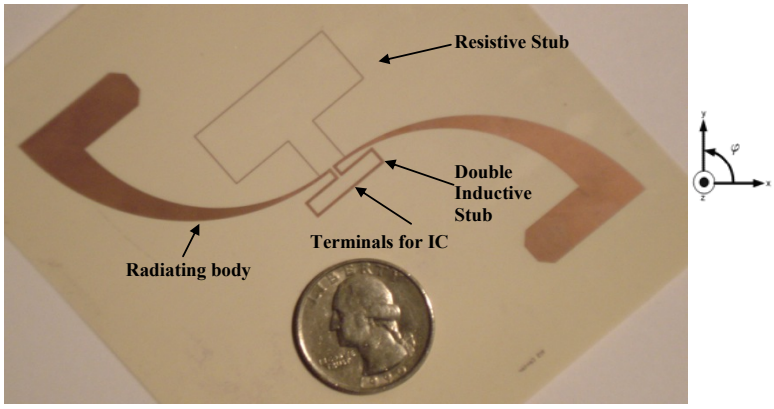

Figure 16. Photo of fabricated RFID Antenna Structure showing stubs.

The input impedance of the simulated antenna design is shown in Figure 17. The RFID UHF band (860→930 MHz) is outside the antenna self-resonance peak, resulting in a more flat response against frequency. This yields to a bandwidth of ~8% which is predominantly realized by the finite slope of the reactance of the antenna in the frequency of interest.

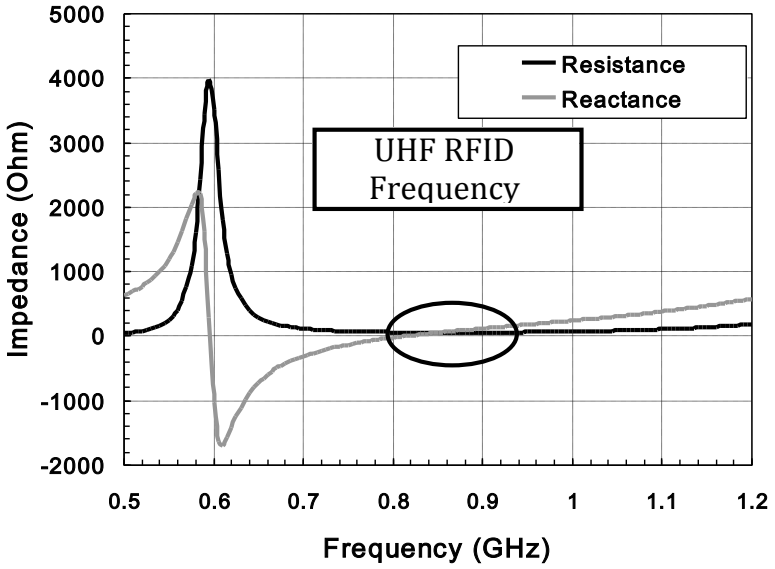

Figure 17. Simulated Input Impedance of the S-shaped Antenna.

The simulated impedance at the center frequency f_0= 895 MHz is 57.46+j112.1 Ω which results in an S_{11} <-18dB. This antenna has a bandwidth of 70 MHz where the bandwidth is defined by a Voltage Standing Wave Ratio (VSWR) of 2 or alternatively by an S_{11} of -9.6 dB. The reflection coefficient or S_{11} of this antenna was calculated based on the power S_{11} which takes into account the capacitance of the IC [28]:

$$\left|S^2\right| = \left|\frac{Z_{IC} - Z_{ANT}^*}{Z_{IC} - Z_{ANT}}\right|^2 \qquad \textbf{Equation 5}$$

Z_{IC} represents the impedance of the IC and Z_{ANT} represents the impedance of the antenna with Z_{ANT}* being its conjugate. In Figure 18 the 2-D radiation plot is shown for Φ=0° and Φ=90°. The radiation pattern throughout the bandwidth of the antenna has also shown to have an omnidirectional pattern similar to that of a classic (λ/2) dipole antenna.

A directivity of 2.1 dBi is achieved with a radiation efficiency of 97%. The omnidirectional radiation is a fundamental requirement for RFID allowing reading/writing operations independent of the orientation of the antenna with respect to the reader.

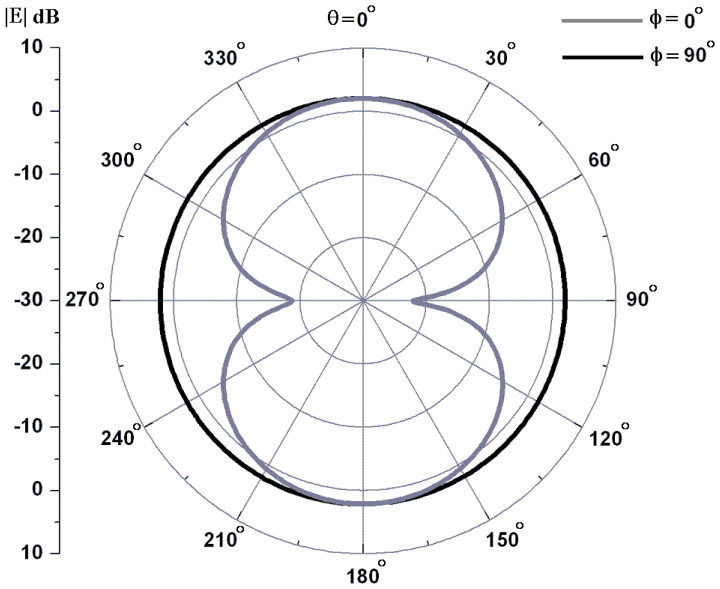

Figure 18. 2D far-field radiation plot for the Φ=0° and Φ=90° as defined in Figure 16.

3.1.1. UHF RFID S-shaped Antenna Modeling

In order to obtain a thorough understanding of the power reflection caused by any mismatch at the terminals of the feed structure of the antenna, a wideband equivalent circuit model has been developed. This model serves as a benchmark for the design of an

RFID antenna to theoretically match any Z_{IC} for maximum power flow resulting in optimum antenna efficiency and an excellent read range. Based on a physical approach, an equivalent lumped element circuit model was derived. The system level design and simulation tool Advanced Design System (ADS) was used to simulate the behavior of the circuit model and resulted in a negligible error function ($<10^{-5}$). Figure 19 shows the agreement between the lumped element model S_{11} and the simulated results.

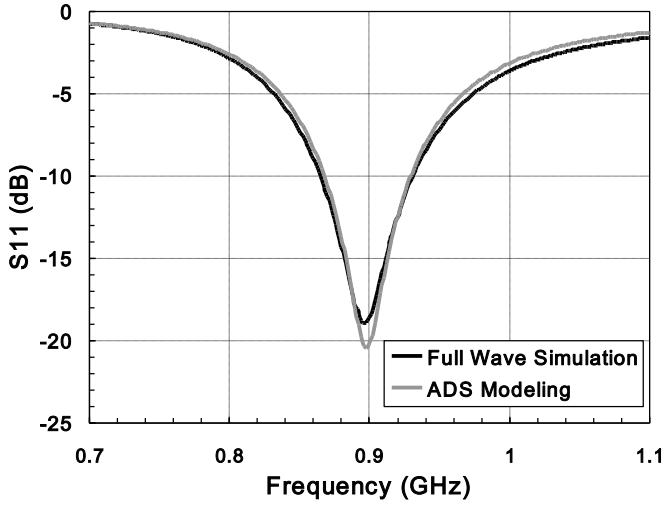

Figure 19. S_{11} for the exact structure and for the equivalent circuit model.

Figure 20 shows the detailed equivalent circuit of the radiating body only (with its simplified version also shown). Each arm of the radiating body consists of a resistor in series with an inductor, the combination of which models the metal effects. A capacitor in series with a resistor, which are located in parallel with the previous combination of L_s and R_s, model the substrate effects. Finally, the capacitive coupling or E-Field coupling between the two arms of the S-shaped antenna is modeled by the top and bottom capacitors (for air and dielectric capacitive coupling respectively).

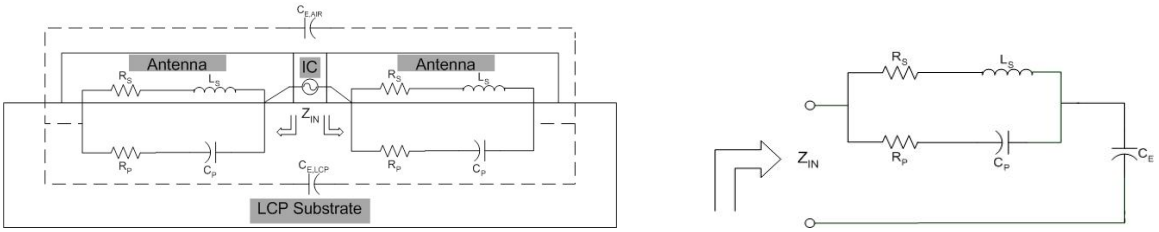

Figure 20. Cross-sectional detail (left) showing equivalent lumped model of RFID antenna shown in Figure 15 a and in Figure 15 b and its simplified version (right).

Since the double inductive stub is connected in series with the radiating body (the antenna is now fed in the center of the double inductive stub), the equivalent circuit model of the second stage design (radiating body plus inductive stub) as shown in Figure 15 b has the same circuit elements configuration as the one in Figure 20, with changes in values only. The final stage of the design has the circuit model configuration shown in Figure 21. Due to the configuration of the resistive shorting stub (connected in parallel with the radiating body plus inductive stub), the components: R_{s2}, L_{s2}, R_{p2}, C_{p2} are introduced as shown in Figure 21 below and model the same effects as those discussed previously for the radiating body circuit model (Figure 20).

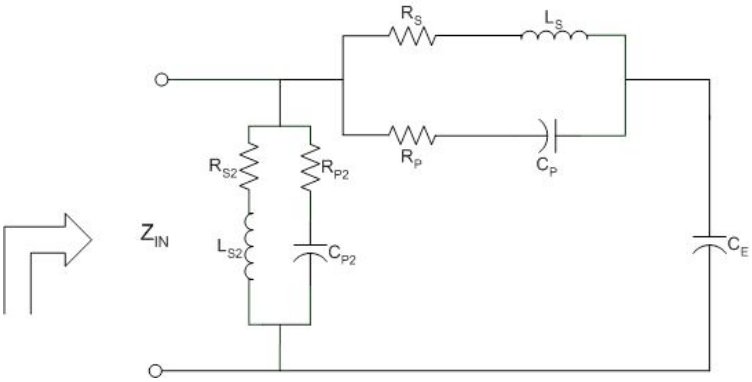

Figure 21. Equivalent circuit for antenna structure shown in Figure 15 c.

The equivalent circuit shows how stubs can be used to tune impedance for matching to an IC. Parametric sweeps can be used along different stub structures (for example

loops can be used for adding series inductance). The resistance of the antenna is mainly determined by the radiating body and can be tuned by the two stubs as shown above. This model also helps determine the amount of loss (as parallel resistance and capacitance) due to substrate loss, which helps in understanding radiation efficiency as a function of the substrate.

3.1.2. UHF RFID S-shaped Antenna Measurements

In order to accurately measure the input impedance of the RFID antenna, certain precautions should be taken into consideration. First of all, a traditional probe station was not suitable for such tests due to the undesired shorting effect of the metallic chuck, which behaves as a spurious ground plane for the dipole antennas. To tackle the problem, a custom-made probe station using wood and high-density polystyrene foam was built. This type of foam was selected due to its low dielectric constant (1.06) [29] resembling that of the free space. A photograph of the probe measurement setup is shown in Figure 22. A $5 \cdot \lambda/2$-thick foam station was designed in order to ensure minimum backside reflections of the antenna.

It was also taken into account that the antennas were balanced structures and a typical GS probe connected to a regular coaxial cable would provide an unbalanced signal. To prevent a current difference between the dipole arms, a $\lambda/4$ balun with an operational bandwidth of 840→930 MHz (which covers the band of interest for this design) was used. After all the mentioned precautions were taken and minding about the calibration process (TRL), S parameters were measured with an Agilent 8510C S parameter receiver and transformed to Z_{IN} or Z_{ANT}.

Figure 23 and Figure 24 show a very good agreement between the simulated results and the measurements for the antenna input impedance and S_{11} parameter respectively. The demonstrated antenna bandwidth allows for a universal operation of the proposed UHF RFID (Worldwide frequency coverage except Japan and some Asian countries that operate at a frequency of 950 MHz and higher).

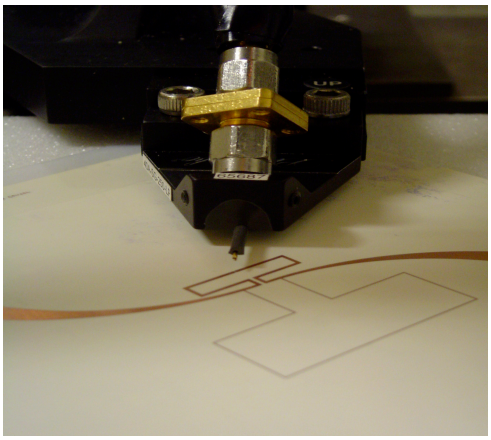

Figure 22. Photograph of the probe plus S-Shaped antenna.

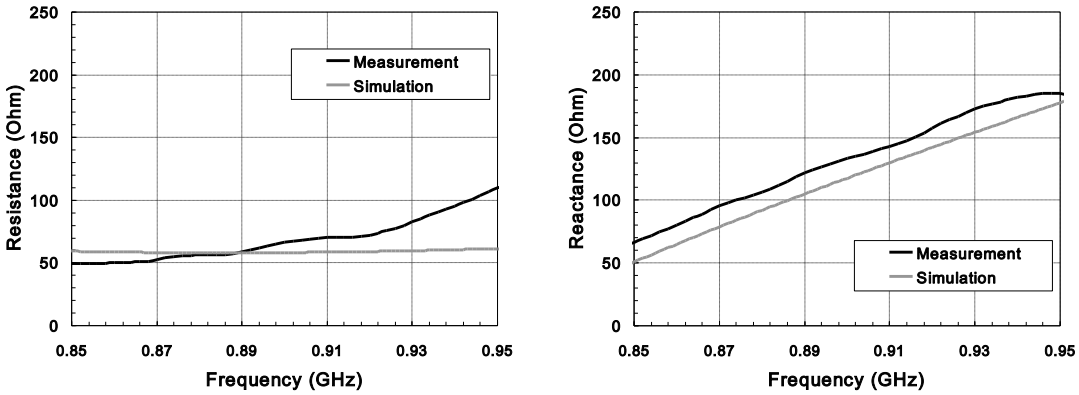

Figure 23. Measured and simulated data of input impedance: Resistance (left) and Reactance (right).

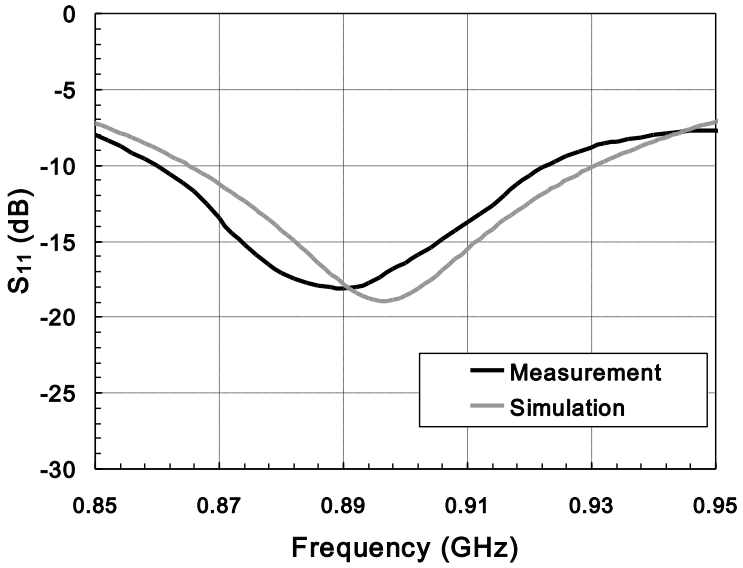

Figure 24. S_{11} of measured and simulated data.

3.1.3. Effect on Antenna Performance when placed on Common Packaging Materials: Papers and Plastics

In order to fully investigate the effect of the surroundings on the antenna parameters, such as the resonance, bandwidth, and radiation; the S-shaped antenna was simulated for 3 practical configurations: on a 4mm thick common plastic material [PET-Polyethylene terephthalate (ε_r=2.25 and tanδ=0.001)], on 4mm thick paper substrate as well in an embedded structure with 0.5mm thick paper (superstrate) on a 4mm paper substrate. Figure 25 shows S_{11} results for the PET and paper substrates. As seen in the figure, a shift in resonance frequency occurs (95 MHz for paper and 60 MHz for PET from the original antenna with center frequency 895MHz on LCP substrate). This observation can be easily corrected by scaling down the x-y dimensions of the antenna. In the paper case the antenna was scaled down by 87% while the antenna on PET by a factor

of 92% and the new S_{11} results as shown in Figure 26 were obtained. As seen in the figure, the detuning of the resonance can be easily performed by scaling the whole structure. For example, when placed on paper substrate, detuning becomes necessary if the thickness exceeds 1.5mm.

As for the most common case where these RFID tags are placed on cardboard boxes; the dielectric properties of cardboard do not impede antenna characteristics due to its low dielectric constant close to 1 and low loss properties. However, the effect of the enclosed materials and the distance of the RFID tag from the arbitrarily placed enclosed contents play a more important role than the size and thickness of the cardboard. An alternative way to increase the bandwidth of the antenna in order to compensate for the material/fabrication variations is the use of a more broadband matching section, potentially introducing an additional stub-line.

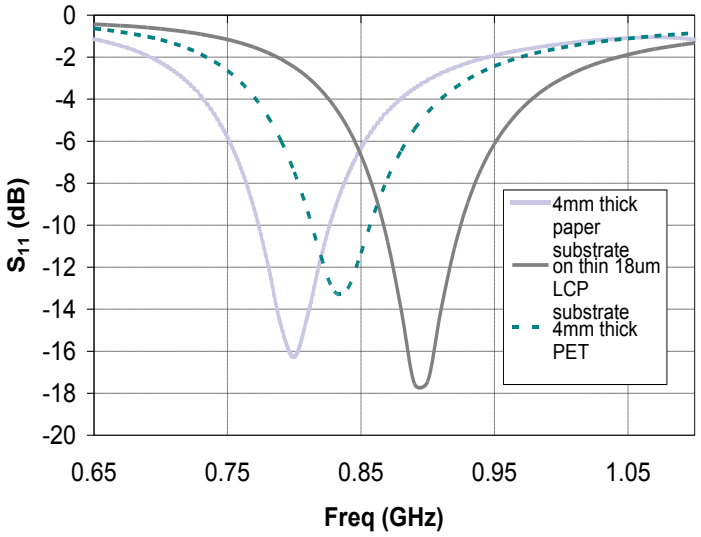

Figure 25. S_{11} for 4mm thick paper and PET substrates.

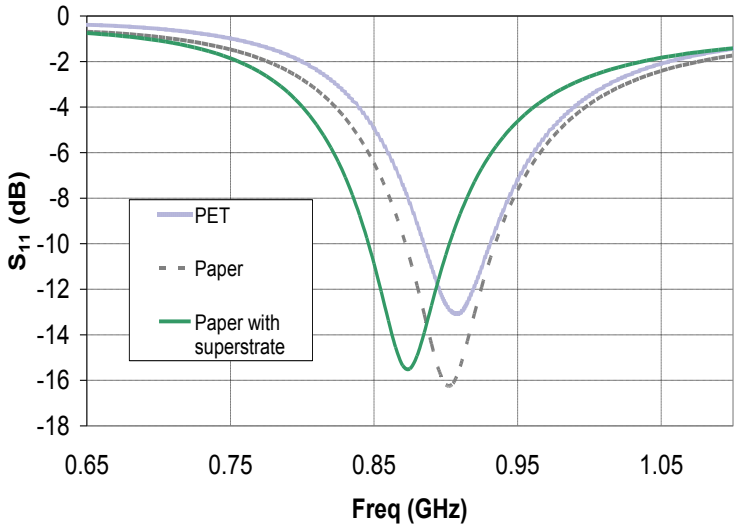

Figure 26. S_{11} for 4mm thick paper and PET substrates with modified antenna dimensions.

In order to analyze the effect of the radiation pattern of these materials, the gain for the S-shaped antenna has been plotted in Figure 27 for the LCP and paper substrates. The worst-case scenario observed for gain loss was 1.049 dB (on 4mm paper) for the E-plane or φ=0 degrees plane in comparison with 2.095 dB (on 18 um LCP).

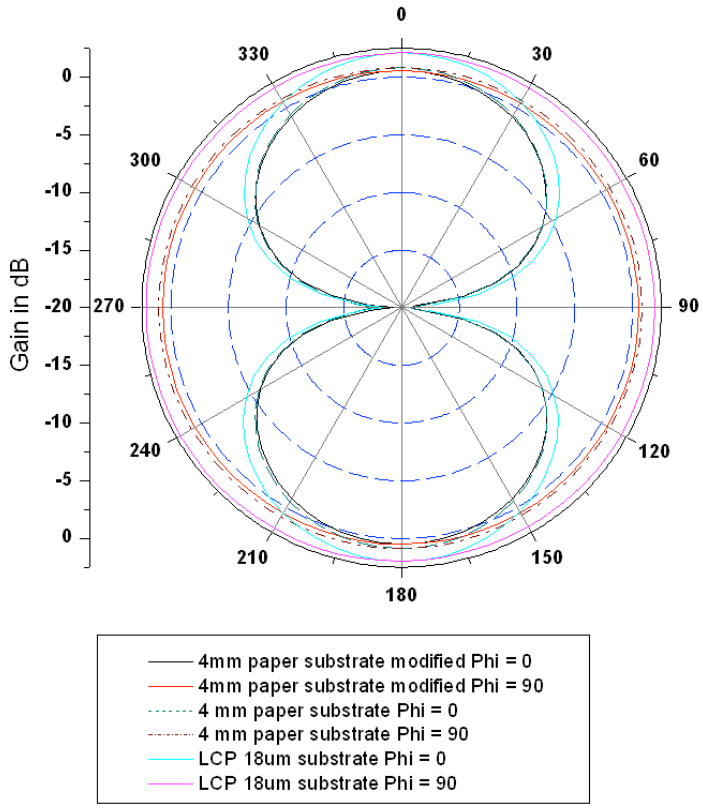

Figure 27. Radiation Pattern of the Gain of the S-shaped antenna on paper and LCP substrates.

3.2. Design and Development of X-Band Passive Filters on LCP with Ultra High Selectivity

This section bridges into higher frequencies (5GHz-15GHz) with emphasis on X-band. The aim is to develop higher frequency modules, specifically highly selective filter design on LCP for X-band radar and communication applications to be used as a benchmark for an easy adjustment for higher frequencies entering mm-Waves.

3.2.1. The Need for High Selectivity Filters and Previous Work

Interference (EMI) is a growing, pervasive threat to defense and mobile communication industry, which could lead to possible jamming in radars and to poor Quality-of-Service in communication applications and needs to be seriously addressed [30]. Usually, high selectivity can be attained through the use of dielectric resonator loaded cavity filters [31], which besides fabrication complexity are large in size. Waveguide–based structures are commonly used in high-power microwave applications due to their power handling capability; however, they are often bulky as well [32]. However, there are several other equally important characteristics that need to be fulfilled by practical filters including: small size, lightweight, and low-cost solutions, not to mention good electrical performance and reliability [31,33]. The use of planar printed microstrip line RF filters has gained much interest in the past decades [30,33] for its ease of fabrication, miniaturized size and integrability with 3D modules, especially recently with the development of multilayer RF modules using ceramic and organic low-loss flexible microwave substrates.

Several X-Band BPF designs have been developed recently. Those are either printed or

utilize other techniques such as [34] where the HTS superconducting method is used to achieve a high selectivity narrowband filter. Other designs such as [35], which uses a printed triangular loop resonator on Duroid substrate, [36], which entails a fifth order BPF on LCP, and [33] with printed dual-mode resonators on LCP; do not achieve an out-of-band rejection level better than 40 dB. In [37] defective- ground structures are reported for providing attenuation poles for wide stop-band characteristics or out-of-band rejection but this design still suffers from poor out-of-band rejection on the lower side of the frequency pass band. In [38] a cascade of lowpass to highpass filter is utilized for realizing wideband bandpass behavior; however, with poor out-of-band characteristics. A simple planar implementation that is most closely representative of this work is shown in [39] with a diplexer comprising of lowpass and bandpass filter topology, but with an IL significantly inferior to the ones reported in this work. In this paper, a novel topology of an ultra-selective hybrid microstrip filter with a maximally flat response in the pass band is presented. A third-order stepped impedance LPF is cascaded along with a fifth-order coupled line BPF. This filter topology can be easily extended to multi-channel applications with bandwidths ranging from 10% up to 30 %. The next section details the design process.

3.2.2. Filter Design and Characterization

In order to achieve a high selectivity, it is typical to choose a higher order band-pass-filter. For this reason and in order to achieve a steep skirt a 5th order parallel-coupled half-wavelength resonator filter was designed. Figure 28 shows the general structure of parallel (edge)-coupled microstrip band-pass filter. They are positioned so that adjacent resonators are parallel to each other along half of their length. This choice was based on

the fact that such filters could support wider bandwidths due to their relatively large coupling for a given spacing between the resonators. The general guidelines for this design start by finding a low pass filter prototype [30]. Next is identifying the normalized bandwidth, which is the normalized distance between the upper and lower frequency:

$$\mathbf{BW} = \frac{\omega_U - \omega_L}{\omega_o} \qquad \textbf{Equation 6}$$

The equations used for the parallel-coupled, half-wavelength resonator filter are (including the determination of the odd and even characteristic line impedances):

$$J_{01} = \frac{1}{Z_o}\sqrt{\frac{\pi}{2}\frac{BW}{g_o g_1}} \qquad \textbf{Equation 7}$$

$$J_{i,i+1} = \frac{1}{Z_o}\frac{\pi\, BW}{2\sqrt{g_i\, g_{i+1}}} \qquad \textbf{Equation 8}$$

$$J_{N,N+1} = \frac{1}{Z_o}\sqrt{\frac{\pi\, BW}{2\, g_N\, g_{N+1}}} \qquad \textbf{Equation 9}$$

$$Z_{o_o}|_{i,i+1} = Z_o\left[1 - Z_o\, J_{i,i+1} + (Z_o\, J_{i,i+1})^2\right] \qquad \textbf{Equation 10}$$

$$Z_{o_e}|_{i,i+1} = Z_o\left[1 + Z_o\, J_{i,i+1} + (Z_o\, J_{i,i+1})^2\right] \qquad \textbf{Equation 11}$$

Following this, the line widths and separations are determined according to Equations 5 through 9. The lengths of the lines are λ/4 at the center frequency, and the input and output lines have characteristic impedance Z_o of 50 Ohms. The exact dimensions are shown in Table 2.

However, to achieve very steep out of band rejection close in to the carrier is not possible with the BPF, and for this reason a cascade with more filters/elements needs to take place. This is illustrated in Figure 30. In order to keep minimum dimensions, a third-

order (three-pole) maximally flat Butterworth low-pass filter response was cascaded with the BPF. The order of the LPF was chosen to keep overall dimensions to the minimum possible while achieving an exceptional out-of-band rejection. The design procedure for the LPF is that of a typical stepped impedance filter and can be found in [30] and [40] and primarily selects a high and a low line impedance and solves for the line lengths. The two filters were then cascaded and optimized in Advanced Design System (ADS) for the filter response requirements with a 50 Ohm input and output feeding lines. Figure 29 illustrates the hybrid filter topology. In Figure 30 the response of the fifth-order coupled line BPF vs. the final filter topology are compared. The most critical design parameters are the impedance or width of the LPF lines, the lengths of the LPF lines, the order of the BPF and coupling distances or gaps. Finally it is necessary to use an EM optimization package to integrate the two filters together for fine tuning.

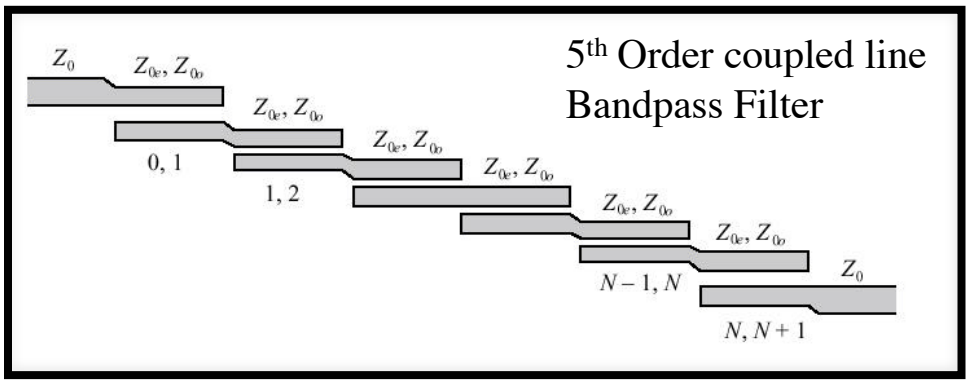

Figure 28. General Structure of parallel (edge)-coupled microstrip BPF.

Table 2. Microstrip Design Parameters of the Five-Pole, Parallel-Coupled Half-Wavelength Resonator Filter, dimensions in mm. S is the separation between parallel lines, i,i+1 refer to the overlapping elements and W refers to the width of the lines (resonators).

$S_{0,1}$	$S_{1,2}$	$S_{2,3}$	$S_{3,4}$	$S_{4,5}$	$S_{5,6}$	W
3.2	4.8	4.7	4.7	4.8	3.2	2.2

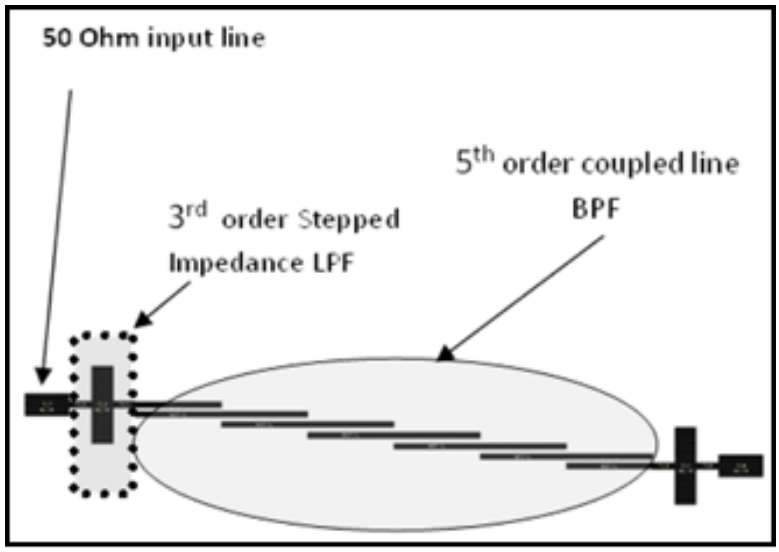

Figure 29. Illustration of hybrid microstrip filter concept.

The overall dimensions of the filter are: 4.3 cm x 0.75 cm including the two 50-Ohm input and output microstrip lines as shown in the illustration in Figure 29. A photograph of the fabricated board is shown in Figure 31, which shows several of the samples fabricated on the LCP board. In order to perform accurate measurements, the input and output feed ports need to be transitioned to Coplanar Waveguide (CPW) lines for probing. This was done by creating trenches at the edge of the 50 Ohm input and output lines, then by accurately inserting a JMT 1503 GSG to microstrip transition [41], which in turn was ribbon-bonded to the 50 Ohm microstrip line as shown in the photograph in

Figure 31.

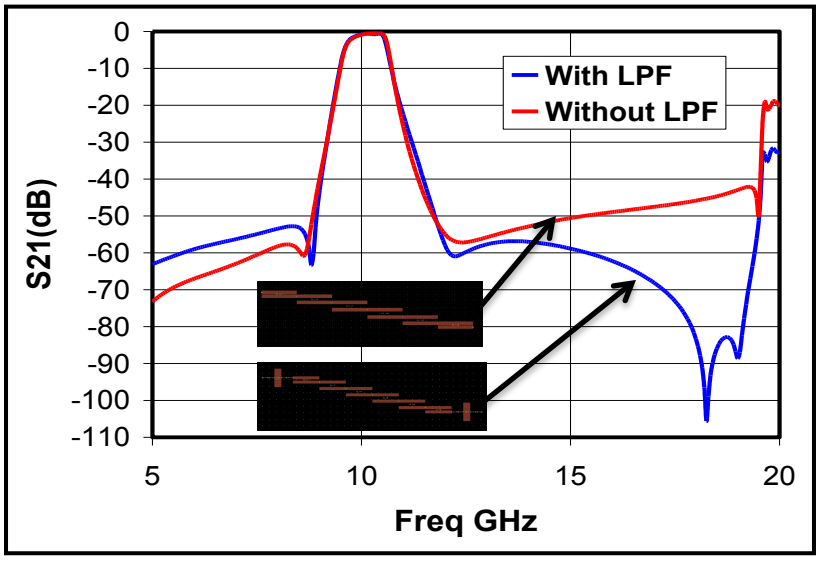

Figure 30. Filter Responses and schematics for BPF and the Hybrid Filter.

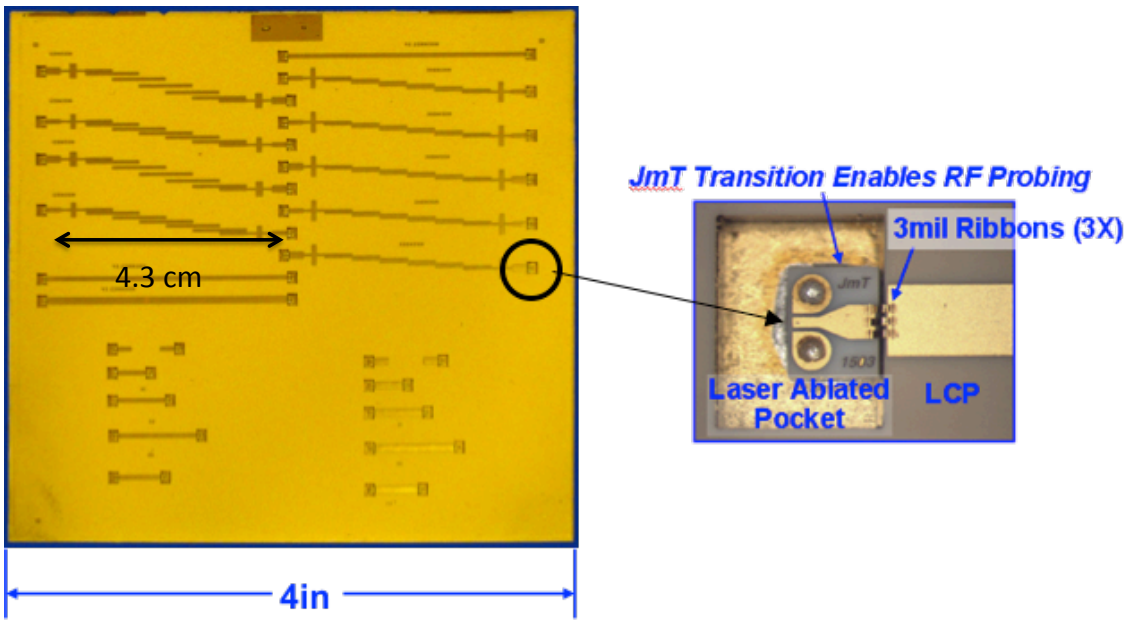

Figure 31. Photos of fabricated board on LCP (left) and ribbon-bonded JMT CPW-to-microstrip transition (right).

As a proof-of-concept of the proposed filter design, 10%, 25% and 35% BW filters are presented. Figure 32 shows the simulated and measured filter response for the 10% BW

Filter design showing good agreement, over a broad frequency spectrum. This filter is characterized by a maximum pass-band IL of 5 dB (3dB down from the best IL value within the pass-band). In a similar fashion Figure 33 and Figure 34 show the BPF response of the 25% BW (with maximum IL of 4.3dB) and the 35 % BW (with maximum IL of 4.1 dB) designs respectively. IL is expected to improve with a higher bandwidth or lower Q-factor.

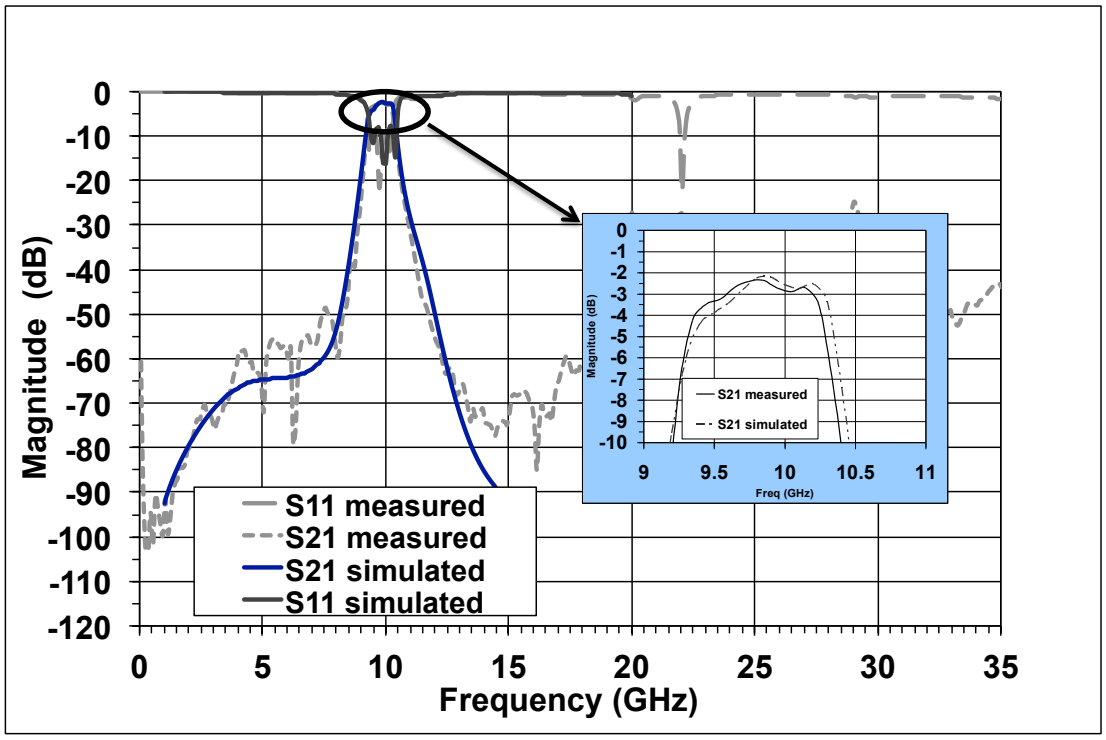

Figure 32. S-parameters (simulations and measurements) for the 10% BW Filter Design.

This work has shown a novel passive microstrip planar filter on organic LCP substrate, which exhibits ultra-high selectivity (out-of-band rejection levels). The use of parallel-coupled half-wavelength resonators and the cascading with one stepped impedance LPF leads to ultra high selectivity, and wide pass-band performance: min IL of 2.2dB for 10% BW centered at 10GHz and very favorable close-in and far-out rejection. Such planar passive microstrip filter is ideal for use in high QoS communication and defense

electronics such as protection from any RF Jammers (such as vehicular RF Jammers used in electronic warfare and/or portable bomb jammers).

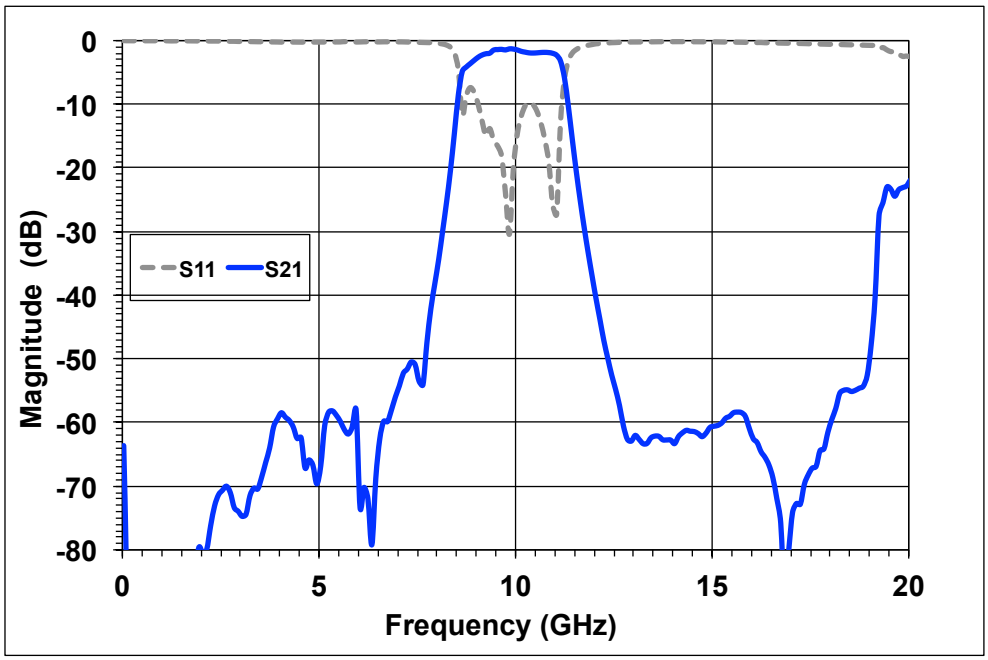

Figure 33. Measured S-parameters for the 25% BW Filter.

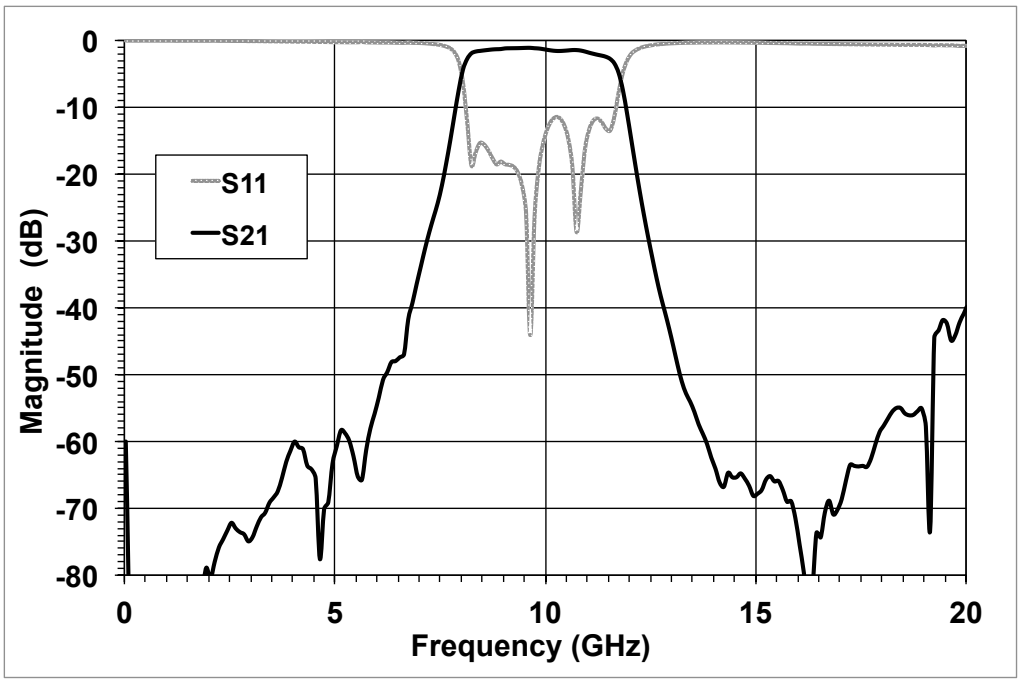

Figure 34. Measured S-parameters for the 35% BW Filter Design.

Chapter 4.

Conductive Inkjet Printing on Low Cost Paper and LCP Substrates

Modern inkjet printers operate by propelling tiny droplets of liquid down to several pL [42,43]. This new technology of inkjet printing [44,45] utilizing conductive paste or ink may rapidly fabricate prototype circuits without iterations in photolithographic mask design or traditional etching techniques that have been widely used in industry. Printing is completely controlled from the designer's computer and does not require a clean room environment. A droplet's volume is one of the parameters that determine the resolution of the printer, for an example a droplet of 10 pL gives ~ 25μm minimum thickness or gap size of printed traces/lines. In addition to that, the ink material, the substrate, the curing processes as well as the voltage waveform used on the jetting nozzles all play a role in the resolution, accuracy, and success of the inkjet printing.

The cartridge consists of a Piezo-driven jetting device with an integrated reservoir and heater [42]. A detailed description of the Inkjet printer used in this work is shown in Figure 35. The inkjet-printing is done in a horizontal bar-by-bar printing using a print-head or cartridge "DMC-11610" which has a nominal drop volume of 10 pL.

Inkjet Printing, unlike etching which is a subtractive method by removing unwanted metal from the substrate surface, jets the single ink droplet from the nozzle to the desired position, and therefore, not creating waste and result in an economical fabrication solution. A microscopic picture is shown in Figure 36 emphasizing a featured size of 50 μm. Silver nano-particle inks are usually selected in the inkjet-printing process

to ensure a good metal conductivity. After the silver nano-particle droplet is driven through the nozzle, a sintering process is found to be necessary to remove excess solvent and to remove material impurities from the depositions. The sintering process also provides the secondary benefit of increasing the bond of the deposition with the paper substrate [46]. The savings in fabrication/prototyping time that inkjet printing brings to RF/wireless circuits will be critical to the ever changing electronics market of today, verifying its feasibility as an excellent prototyping and mass-production technology for next generation electronics especially in RFID, wireless sensors, handheld wireless devices (e.g.4G/4.5G cell phones), flex circuits, and even in thin-film batteries [7]. After the printing process takes place, it is essential to cure the prototype in order to increase the conductivity of the silver ink. Curing is simply done by heating the fabricated antenna, so that the printed silver ink nano-particles melt and a good percolation channel is created for electrons to flow. The curing is performed in a high precision industrial oven, at a constant temperature of 100°C for 10 hours. The curing must be performed immediately after the printing, because the silver ink begins to oxidize which may result into permanent poor conductivity and efficiency of the antenna trace. It has to be noted that the maximum temperature that paper substrate can endure is 150°C. The conductivity of the printed ink was studied through the use of the Signatone Four Point Probe (www.signatone.com). To ensure good conductivity, three layers of ink were printed, and then treated in a thermal oven as described earlier. The resulting ink thickness was measured using the Wyko profilometer (www.veeco.com). The resulting thickness was around 3 μm with a consistent measured conductivity in the range $9x10^6$ [S/m] – $1.1x10^7$ [S/m]. In addition, DC characterization was performed in order to test the silver epoxy

and the integration of SMD devices. Figure 37 shows a photograph of the test setup highlighting a 1.6Ω DC Resistance measurement by the multimeter for the trace with a 1Ω SMD Resistor assembled in the center of the trace using silver epoxy. This proves that such connections using epoxy can be made with losses that are tolerable. It is recommended to use inkjet printing at lower frequencies for such reasons.

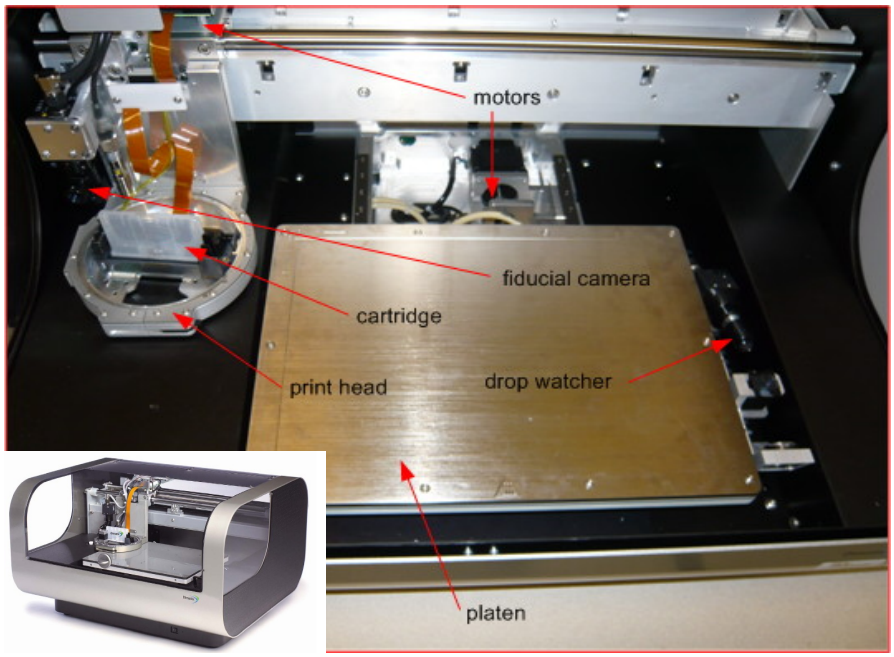

Figure 35. Details of Dimatix Material Printer DMP 2800

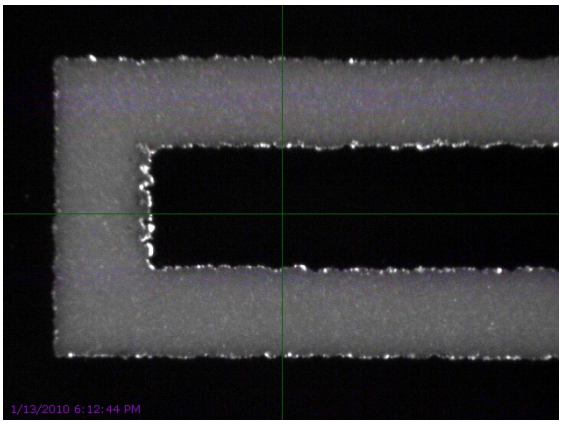

Figure 36. Realized feature size of 50 µm.

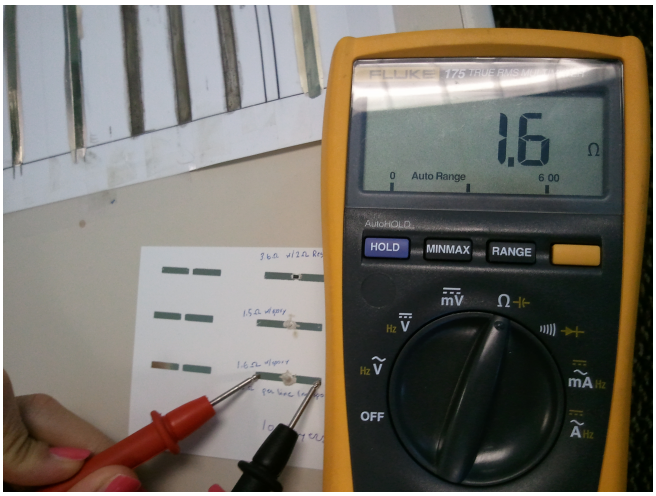

Figure 37. DC characterization for inkjet printed traces with epoxy and SMD 1Ω Resistor.

4.1. Inkjet-Printed Bowtie T-match RFID Antenna at UHF Frequencies

In this section a T-match folded bow-tie half-wavelength dipole antenna was designed to match the TI RI-UHF-Strap-08 IC with resistance R_{IC} = 380 Ohms and reactance modeled by a capacitor with value C_{IC}=2.8 pF [47]. The antenna was then fabricated on a commercial photo paper by the inkjet-printer method as well as by conventional metal etching for comparison purposes. The RFID prototype structure is shown in Figure 38 along with dimensions, with the IC placed in the center of the T-match arms. Figure 38 also shows the current distribution at 900MHz. The T-match arms are responsible for the impedance match through the fine tuning of the length L_3, height h, and width W_3.

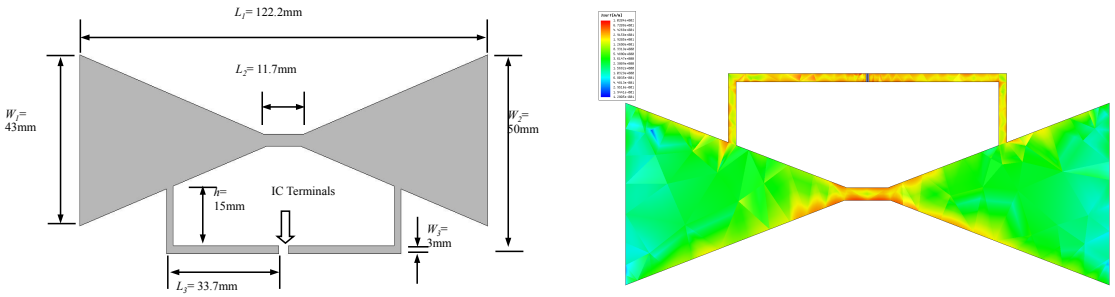

Figure 38. T-match folded bowtie RFID tag module configuration (left) and current distribution at 900MHz (right).

The return loss of this antenna was calculated based on the power reflection coefficient in Equation 1. The S_{11} plot is shown in Figure 39 demonstrating a good agreement for both paper metallization approaches. The nature of the bow-tie shape of the half-wavelength dipole antenna body allows for a broadband operation, with a designed bandwidth of 190MHz corresponding to 22% around the center frequency 854 MHz. This covers the universal UHF RFID bands. It has to be noted that the impedance value of the IC stated above was provided only for the UHF RFID frequency which extends from 850MHz to 960MHz; thus, S_{11} outside this frequency region, may vary due to potential IC impedance variations with frequency. If necessary, a thorough study may be performed by measuring the S-parameters of the IC.

The radiation pattern was verified using antenna chamber measurement as well as by using RFID reader measurements. The radiation pattern as shown in Figure 40 is almost omnidirectional at 915 MHz with directivity around 2.1dBi. The IC strap was attached to the IC terminal with H2OE Epo-Tek silver conductive epoxy cured at 80°C. A UHF RFID reader was used to detect the reading distance at different directions to the tag. These measured distances are theoretically proportional to the actual radiation pattern. The normalized radiation patterns of simulation, microwave chamber

measurement and reader measurement are plotted in Figure 40, showing a very good agreement between simulations and measurements, which can be also verified for other frequencies within the antenna bandwidth.

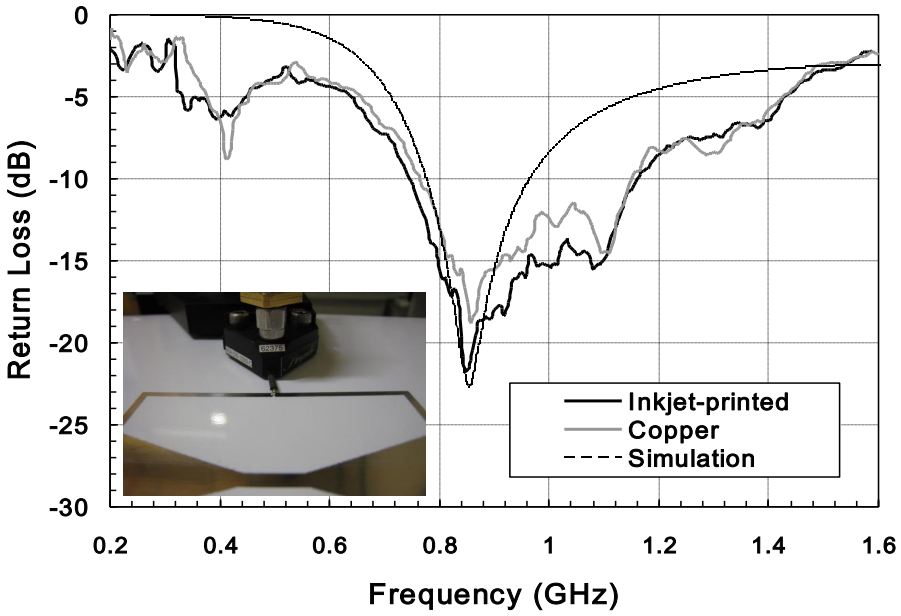

Figure 39. Measured and simulated Return Loss of the inkjet-printed RFID tag. Also showing a photograph of measurement setup using GS pitch probe.

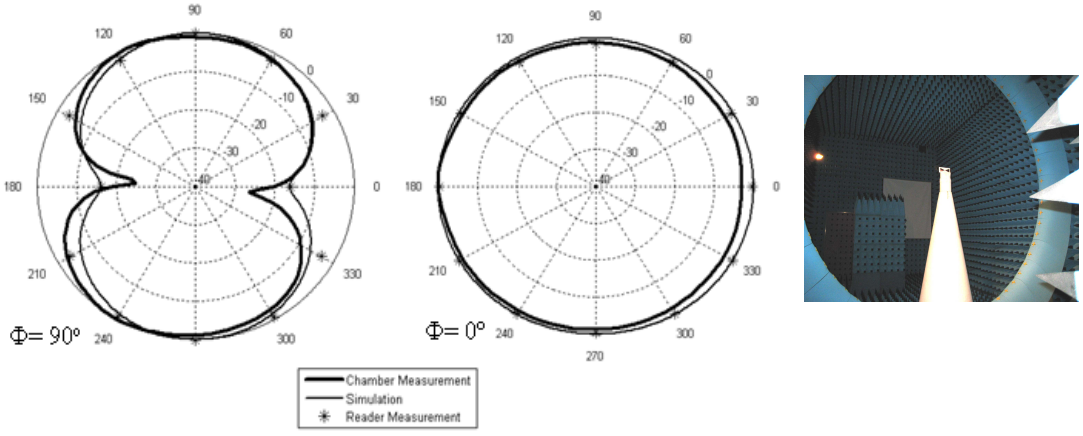

Figure 40. Normalized 2D far-field radiation plots of simulation, chamber measurement and tag reading distance measurement. Also showing a photo of radiation pattern measurement setup.

4.2. Inkjet-Printed Dual Band Conformal Antenna for Use in Wifi Frequency Bands

The proposed dual-band antenna is designed on a 20mm x 32.5mm, 156 μm thick Paper substrate. The antenna is microstrip-fed with feed line width w=3.72 mm that results in a 50Ω characteristic impedance. The length of the feed line is 8 mm and is terminated with narrow metal segments of width 2mm. The shorter stub length is 12 mm (the one that extends directly from the feed line) and the longer length results in 28mm if the two perpendicular segments are added. This is shown in Figure 41. The ground patch has dimensions 8 mm by 20 mm.

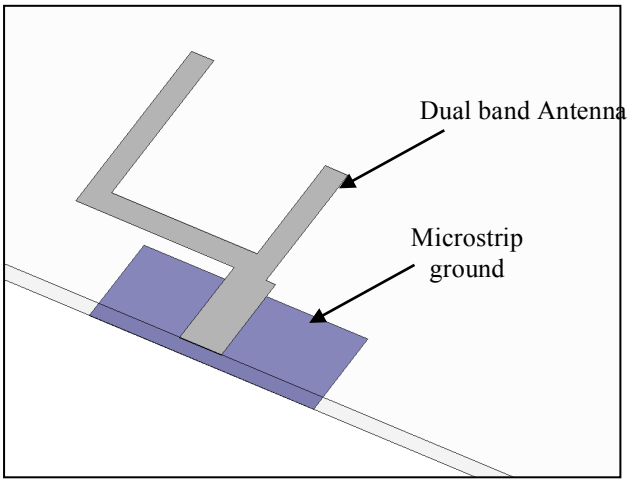

Figure 41. Dual Band Antenna Structure.

The entire circuit was printed using 7 layers of silver ink resulting in an optimum conductor thickness. The substrate was sintered continuously during the fabrication process at 60 °C using the hot base plate in the printing chamber of the printer. The printed structures were then cured in an industrial oven at 120 °C for 10 hours. This was done with the intent to increase the conductivity of the printed structures toward the higher end of the conductivity range achievable with this process, which is around

$2.5x10^7$ S/m. The antenna structures as well as the grounds were printed on the same paper substrate first and then assembled into the final configuration with an SMA connector for measurements. Figure 42 shows the simulation and measurement results, which exhibit good agreement till 7 GHz.

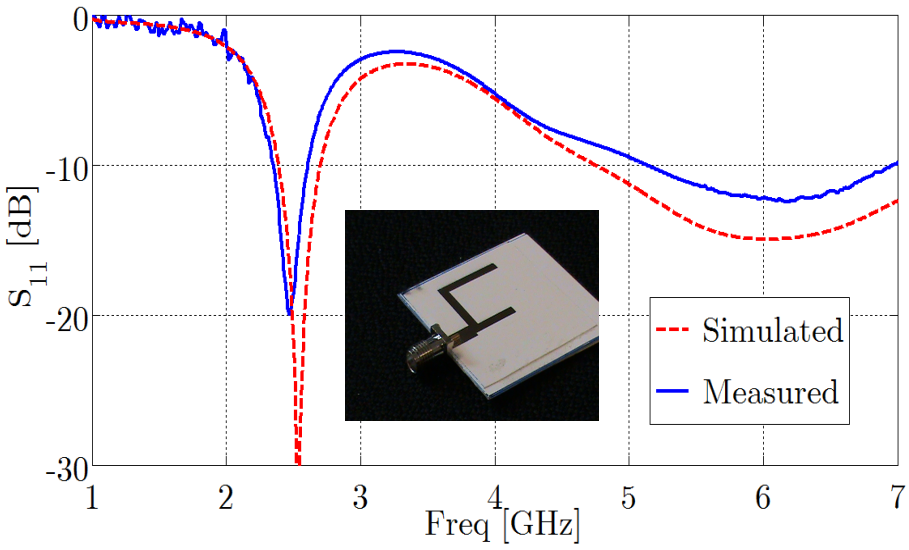

Figure 42. S_{11} results for the proposed antenna on paper.

4.3. Inkjet-Printed UWB Conformal Antenna

To investigate the applicability of inkjet-printed paper-based technology for the realization of UWB structures, a planar UWB monopole was adopted in this work for its simplicity [48] as a proof-of-concept geometry. The design was optimized through full-wave FDTD simulations -including the ink thickness effect along with the frequency-dependent permittivity of the paper substrate- using a commercially available solver from SPEAG (www.semcad.com). The antenna was printed on a paper sheet following the outlined guidelines. The paper sample was cut to a square slice of 58mmX58mm to form the overall antenna. Figure 43 shows the CAD model used in simulations. A model for a

long piece of coaxial cable was used in simulations to mimic the actual piece used in measurements. This usually helps in modeling the common-mode currents flowing on the feeding cable, and typically results in better correlation between the measured and simulated pattern/gain values.

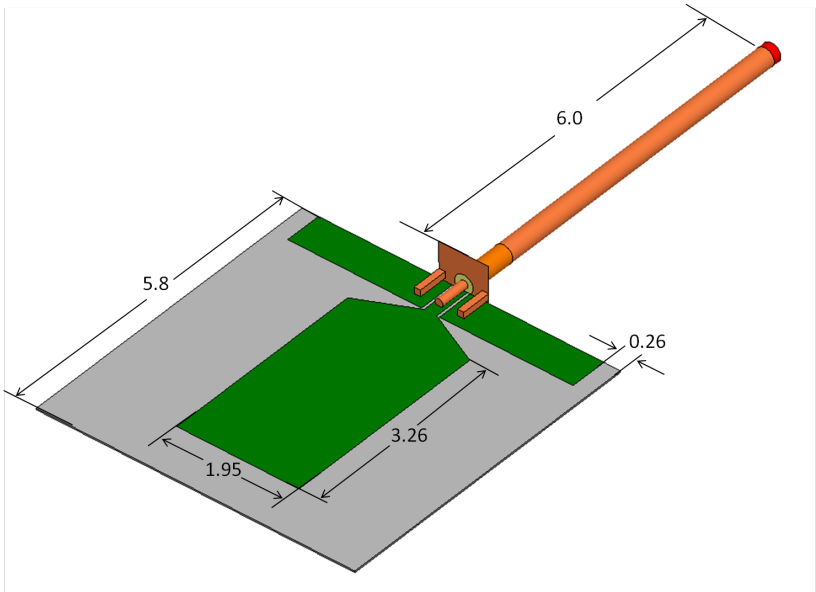

Figure 43. EM Model for the printed UWB antenna.

The Agilent PNA-X network analyzer (N5245A) was used for the scattering parameter measurements. Figure 44 shows good agreement between the simulated versus the measured responses at the input port of the antenna up to 16 GHz.

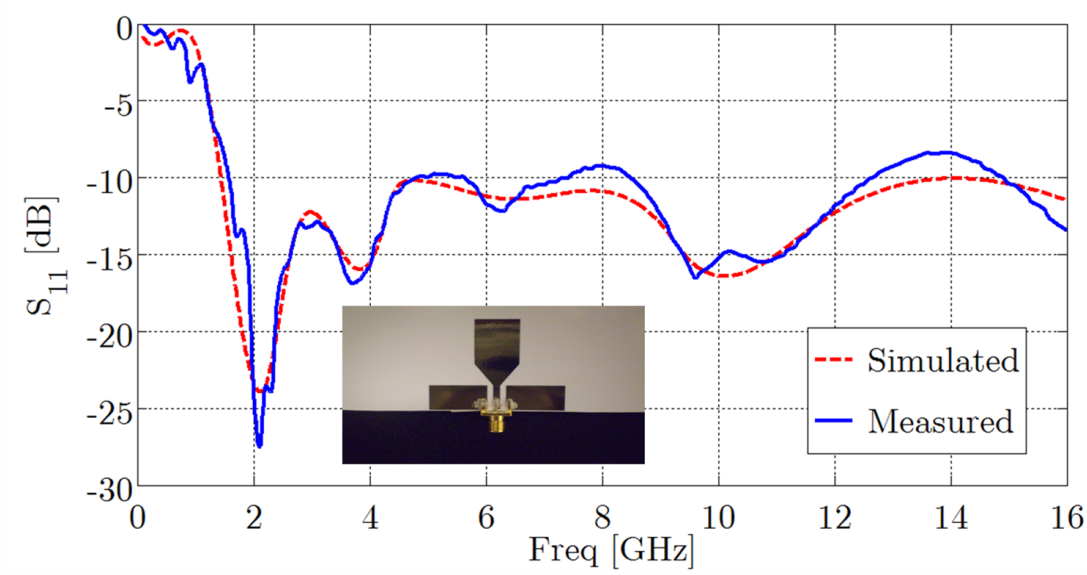

Figure 44. Simulated and Measured S_{11} performance of the UWB Antenna.

The radiation pattern was measured using Satimo's Stargate 64 Antenna Chamber measurement system. The NIST Calibrated SH8000 Horn Antenna was used for the calibration of the measured radiation pattern at the selected in-band frequencies (3, 4.5, 6, 7.5, 9, and 10.5 GHz). The prototype antenna was placed in the yz-plane as outlined in Figure 45 with the x-axis normal to the plane of the antenna. The measured radiation pattern at different elevation angles is shown in Table 3. The resulting pattern is almost uniform (omni-directional) for the selected in-band frequencies, which is ideal for many UWB applications. The antenna efficiency was better than 80% throughout the whole band. Fig. 6 shows good correlation between the measured and simulated directivity values. Better correlation can be achieved through accurate modeling of the feeding cable length, and its actual mounting configuration, in addition to proper choking of the common mode currents flowing on the cable.

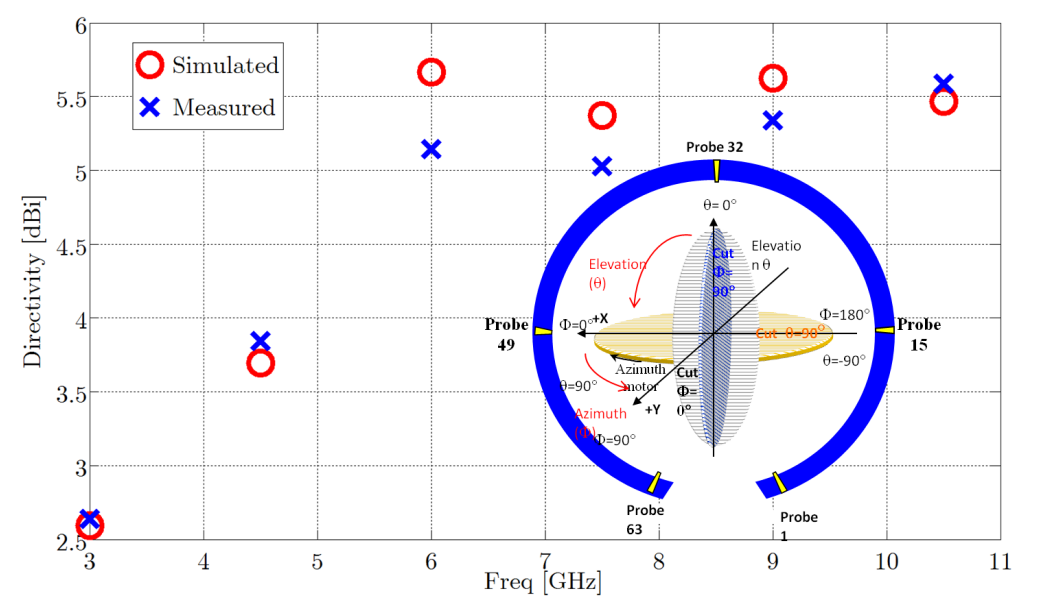

Figure 45. Measured and Simulated Directivity of the UWB Antenna.

Table 3. Measured Radiation Patterns at select in-band frequencies (— for xz-plane and -- for yz-plane)

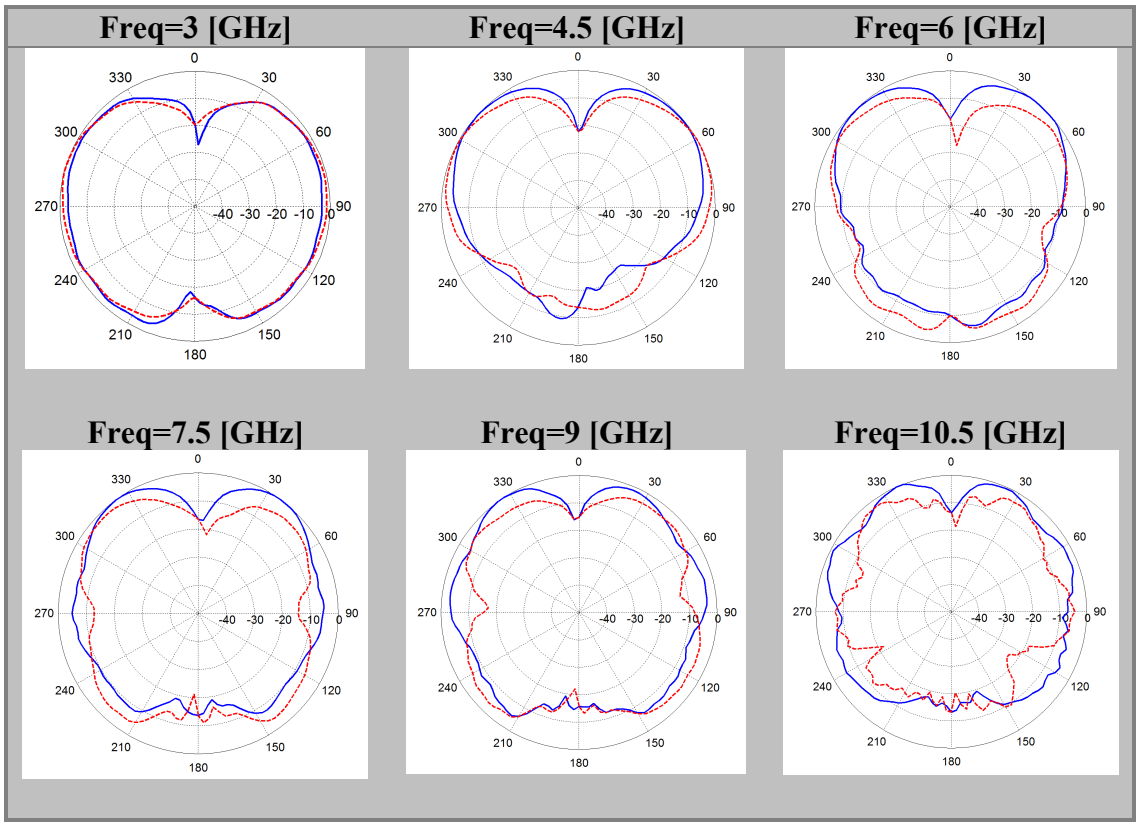

4.4. Inkjet-Printed UHF Antenna on Flexible and Organic LCP Substrate

A CPW-fed rectangular monopole antenna was designed and is shown in Figure 46, with the dimensions of the coplanar waveguide given by a signal width of w=3.8mm, a gap spacing of g=0.5mm, and a length Lg=30mm. Hence, the ground length is also Lg=30mm. The width of the ground planes is chosen to be Wg=35mm and a typical value for the height of the radiating element from the ground is chosen h=11mm. In addition, Lr=40mm and Wr=50 mm. This module was then inkjet printed using the procedure described in section 4.2.2 on a 50 micron thick LCP substrate. Figure 46 also shows the fabricated antenna connected to a typical SMA connector for S-parameter measurements using silver epoxy. The S_{11} results are shown in Figure 47 for measurements and simulations showing an overall good agreement, while the shift in frequency might have occurred due to the connectivity and silver epoxy used in the measurement setup and/or surrounding objects in the lab where the Vector Network Analyser (VNA) is placed. The radiation produces an omnidirectional pattern and a simulated gain of 0.7dB at 1 GHz.

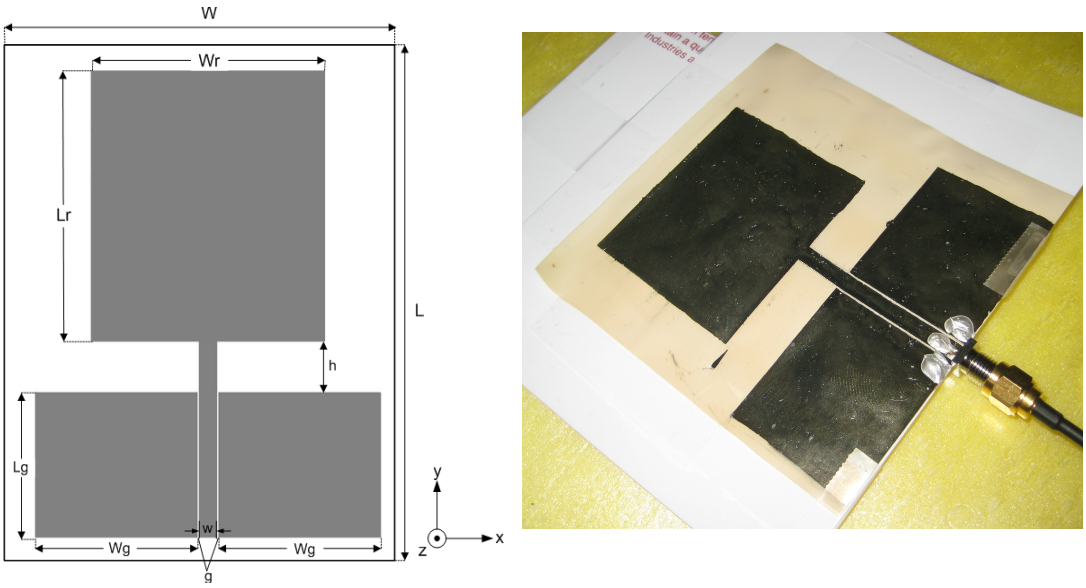

Figure 46. Planar rectangular UHF monopole antenna configuration (left) and a photograph of the fabricated antenna (right).

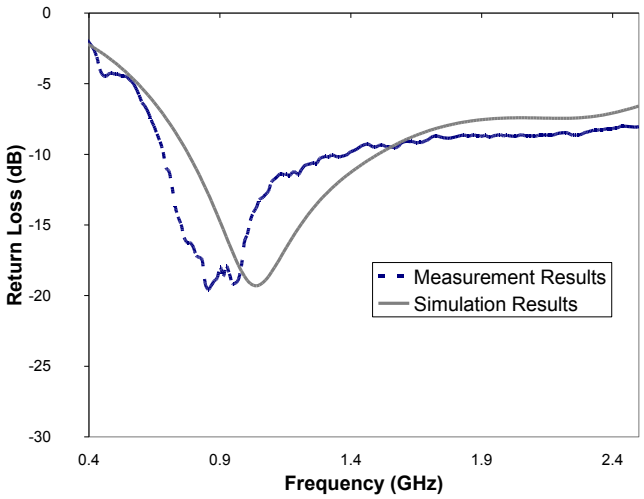

Figure 47. Measurement and Simulation Results for the S_{11} of the CPW-Monopole Antenna.

4.5. Inkjet-Printed mm-Wave Antennas on Flexible and Organic LCP Substrate

Here we demonstrate for the first time an inkjet printed antenna on LCP for mm-Wave applications. It is noteworthy to mention that several inkjet-printed antennas were demonstrated at low frequencies [4]. However, the fabrication of such antennas was not quite challenging, due to their relaxed tolerances.

With the rapid demand on more bandwidth and more functionality, mm-Wave antennas have become a crucial element in realizing efficient sensor systems. To this end, we present a proof-of- concept simple dual band antenna design that could serve as a sensor in the 24/60/70GHz bands. The antenna is a variation of the planar monopole antenna. By controlling the size of the side ground plane as well as the length of the center conductor along with the width to gap ratio, one can optimize the antenna to cover the aforementioned bands. Here, optimization was conducted using a commercially available FEM solver (Ansoft HFSS). The antenna was modeled as a thin conductor 5 um thick, with 1um surface roughness and conductivity of 3×106 [S/m]. The antenna model was fed in a GSG probe-mimicking scheme. Figure 48 shows the simulated gain. Simulated efficiency is above 80% even for the low conductivity value. Probe-based measurements of such antenna were quite challenging. Several ripples were present in the measurements due to measurement uncertainties. Figure 49 summarizes the result for the simulated and measured S_{11}.

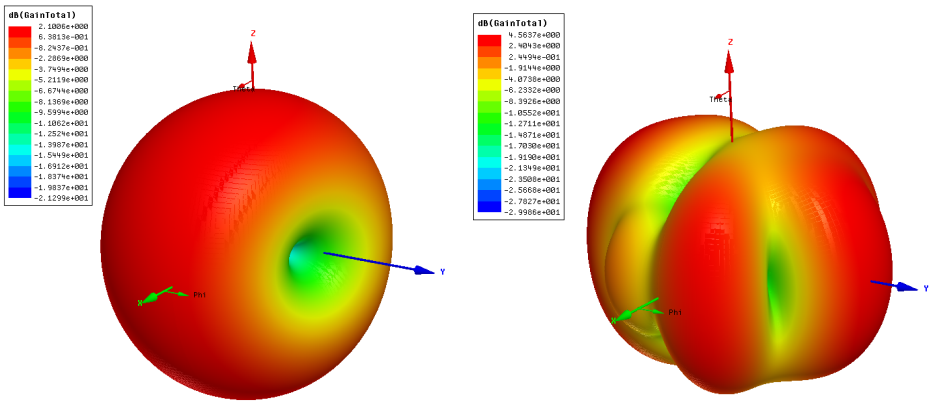

Figure 48. Simulated gain at 24GHz (left) and 70GHz (right).

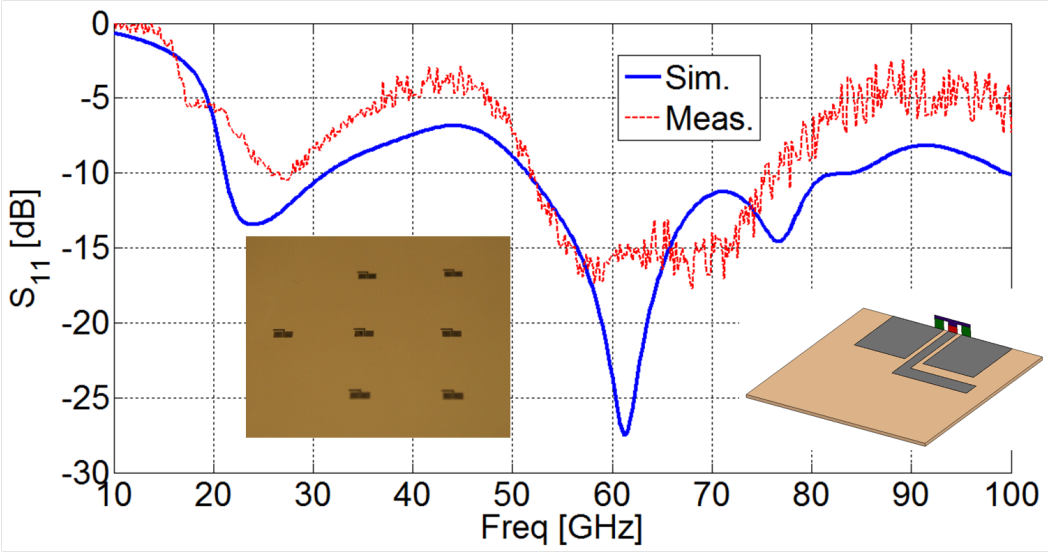

Figure 49. Simulated and measured S_{11} of an inkjet printed antenna on LCP up to 100GHz. Also in this figure are photographs of the inkjet printed antennas on LCP and the model in HFSS.

PART II. 3D INTEGRATED MM-WAVE RADAR FRONT-END

Chapter 5.

Integrated RF Architecture for mm-Wave Systems

In the past few years, the interest in the mm-wave spectrum at 30 to 300 GHz has drastically increased. To reiterate few points from the introduction as well as adding a few concerning mm-Waves:

- Wireless has become a critical, well accepted, and necessary part of everyday life
- There is an increasing need for Autonomous ID, Sensing, higher data rates (Gbps) and resolution
- Suitability of Si technology to enable radio design, integration, and operation at mm-Wave frequencies [10,11]
- The mm-Wave spectrum is an unlicensed operation
- Mm-Wave offer secure operation resulting from short transmission distances due to oxygen absorption (60GHz), narrow antenna beamwidth and no wall penetration
- High speed data transition in Gbps range
- Advantage of antenna diversity
- Good co-existence between mm-Wave systems and 802.11a/b/g and Bluetooth due to large frequency difference

A listing of applications include: high-definition video, automotive radar, high-resolution imaging. Figure 50 shows the average atmospheric gaseous attenuation of mm-Waves propagation at sea level indicating the applicability from short to long ranges depending on the frequency of operation (example 60GHz vs. 77 GHz).

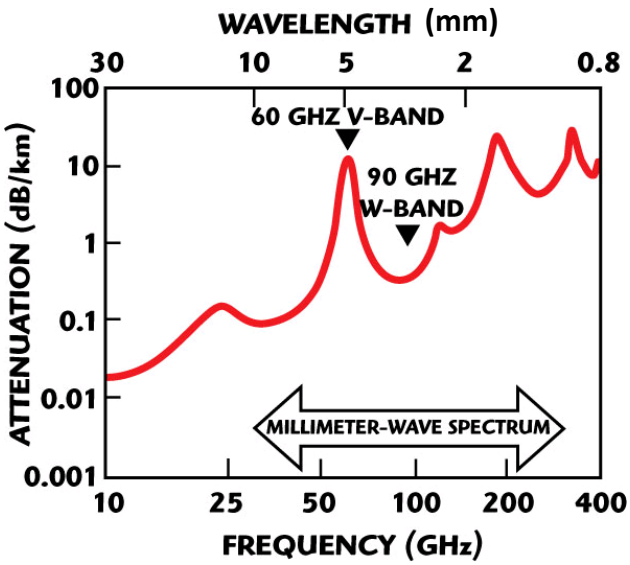

Figure 50. Average atmospheric gaseous attenuation of mm-Wave propagation at sea level [49].

There is a growing need to solve the huge technical hurdles to achieve cost efficiency. For example, the current automotive radars are expensive and bulky. Most of the existing automotive radars use metallic frames to provide both packaging and support, but also interconnection between the planar array and the RF front-end (by using metalized waveguides). This increases the overall profile of the radar. The thorough investigations on these radars have been performed [50, 51,52,53,54,55] and are summarized in Table 4. Table 4 highlights the different existing automotive radars and their specifications. Two main categories, mainly array-based systems and lens/reflector-based systems currently are in use. For a low cost and lightweight overall system the array-based methodology should be applied and is investigated in this work. Some of the issues that exist in current systems and that influence the cost of the overall radar are:

- The entire radar is packaged using a polished metallic frame. This metallic frame provides three main functionalities: 1) It provides the metalized waveguide

sections that are needed for transitioning the system from the MMIC to the antennas, 2) it packages the components and reduces crosstalk and interference within the system (especially from noisy components such as VCO), and 3) it provides mechanical support and cooling for the system. However; this metallic frame increases the overall cost of the system, especially due to the fact that the waveguide sections need to be polished in order to reduce the losses that they exhibit at mm-Wave frequencies.

- Different interconnection schemes are necessary for different parts of the radars. As was previously mentioned the antenna is a planar microstrip array printed on a thin membrane for increased efficiency (the thin membrane is approximating free-space conditions). However, since no MMIC can be mounted on this membrane, the signal needs to be transitioned to a metalized waveguide (Transition 1: microstrip to waveguide). The waveguide, on its other end, is terminated by a second transition (Transition 2: waveguide-to-microstrip), which converts the waveguide mode back to a microstrip one. The microstrip in now printed on a substrate such as alumina (a fairly expensive microwave substrate). The received signal is then transitioned to a mm-Wave PCB substrate (Transition 3: microstrip-to-CPW, wirebond, CPW-to-microstrip). Finally the signal is fed into the LNA by a wirebond connection (Transition 4). The interconnection scheme includes four different transitions from one type of transmission line to another. Such an interconnection scheme suffers from increased loss, which severely affects the noise figure of the system and deteriorates the radar sensitivity and range. Moreover, it is limited in bandwidth because the waveguide-to-microstrip

transitions have at most 5-6% bandwidth due to the use of resonance stubs (this corresponds to about 4 GHz of bandwidth). These facts make the radar very sensitive to manufacturing tolerances and extreme care needs to be taken in order to ensure good operation. This translates to multiple tests during fabrication and assembly processes which increase the production time, testing, and costs fore each unit.

Table 4. Survey of existing (state of the art) automotive radars and the main parameters related to the field of study.

	Array-Based Systems					**Lens / Reflector-Based Systems**			
Supplier	**Denso**	**Fujitsu Ten**			**Delphi**		**Robert Bosch GmbH**	**M/A-Com**	**Groeneveld**
Product Name/Number	DNMWR002	Old System	Next Gen Sys	Short Range	Multi-Mode ESR	AC3B (under dev)	LRR3	ARS 300	Roadeye PSR2
Appearance									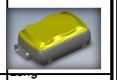
Long Range or Short Range	Long Range	Long Range	Long Range	Short Range	Long Range/Short Range switchable	Long Range	Long Range	Long Range	Range/Short Range switchable
External Dimensions (mm)	**77 x 107 x 53**	**89 x 107 x 86**	**89 x 107 x 70**	**87 x 67 x 46**	**120x100x60?**	**98 x 98 x 39**	**77 x 74 x 58**	**70 x 103 x 50**	**130x90x53**
Mass (kg)	0.495	< ~0.650	< 0.650	Not Available	0.225	0.5	< ?0.3?	< 1	0.6
Angle Detection Method	Digital Beam Forming	Mechanical Scan	Mechanical Scan	Monopulse	Digital Beam Forming	Not Available	Beam Conversion	Beam conversion	Beam Switching
Operative Temperature Range	-30° C to 70° C	Not Available	-40° C to 100° C	Not Available	Not Available	-40° C to 105° C	-40° C to 90° C	-40° C to 85° C	Not Available
EHF Device	MMIC	MMIC	Not Available	MMIC	Not Available	Not Available	SiGe MMIC	GUNN	Not Available
Center Frequency	**77 GHz**	**76-77 GHz**	**76.5 GHz**	**76 GHz**	**76.5GHz/76.5GHz**	**76-77 GHz**	**76.6 GHz (in testing)**	**77 GHz**	**Not Available**
Bandwidth	Not Available	Not Available	Not Available	Not Available	Not Available	Not Available	**~300 MHz**	**Not Available**	Not Available
Antenna Type	**Patch antenna phased array**	**Patch antenna phased array**	**Patch antenna phased array**	**Patch antenna**	**Patch antenna phased array**	**Cassegrain with lens**	**4 patch elements behind a dielectric lens**	**Folded reflector**	**Not Available**
Antenna Gain	**~20dBi (testing)**	Not Available	Not Available	Not Available	Not Available	Not Available	Not Available	Not Available	Not Available
Side Lobe Level	-15 dBi (testing)	Not Available	Not Available	Not Available	Not Available	Not Available	Not Available	Not Available	Not Available
Polarization	E-Plane (45)	Not Available	Not Available	Not Available	Not Available	Not Available	Not Available	Not Available	Not Available
Number of Channels	9 Receive	Not Available	Not Available	Not Available	Not Available	Not Available	Not Available	Not Available	Not Available
Beam Width	**15° (testing)**	Not Available	**2.8° horizontal, 3.9° horizontal**	Not Available	**3.5/10**	Not Available	**5 deg**	**2°**	Not Available
Detection Range (m)	~2 to over 150	4 to over 120	2 to 150	45	200/60	0 to 200m	2 to 250	0.25 to 170	up to 200m
Range Detection Accuracy	+/- 0.5%(1%)	< 1m(0.83%)	+/-5%(10%),+/-1.0m	Not Available	0.35m?	3% 0.75m	0.1m	+/- 0.25m(0.29%)	0.15m
Modulation Method	FMCW (triangular frequency modulation)	FMCW	Not Available	FMCW	Simultaneous Transmit and Receive Pulsed Doppler (STAR PD)	LFMSK (Linear Modulation Freq Shift Keying), Doppler for speed detection	FMCW with triangular shape	Pulsed Doppler (Pulsed FM)	Not Available
Horizontal Detection Angle (Field of View) (degrees)	20	16	15	30	20/90	16	30	18	24 normal/30 reduced range
Horizontal Angle Resolution (degrees)	0.5	0.8	0.6	Not Available	1/0.5	0.3	0.25	1	0.3
Relative Speed Detection Range	-199.8 kph to 100.08 kph	Not Available	Not Available	0 to 100 kph	Not Available	+/-220 kph	-288kph +108kph	-89 kph to 265 kph	Not Available
Relative Speed Resolution	2.268 kph	Not Available	+/- 2.7 kph	Not Available	Not Available	0.22 kph	0.36 kph	2.76 kph	Not Available

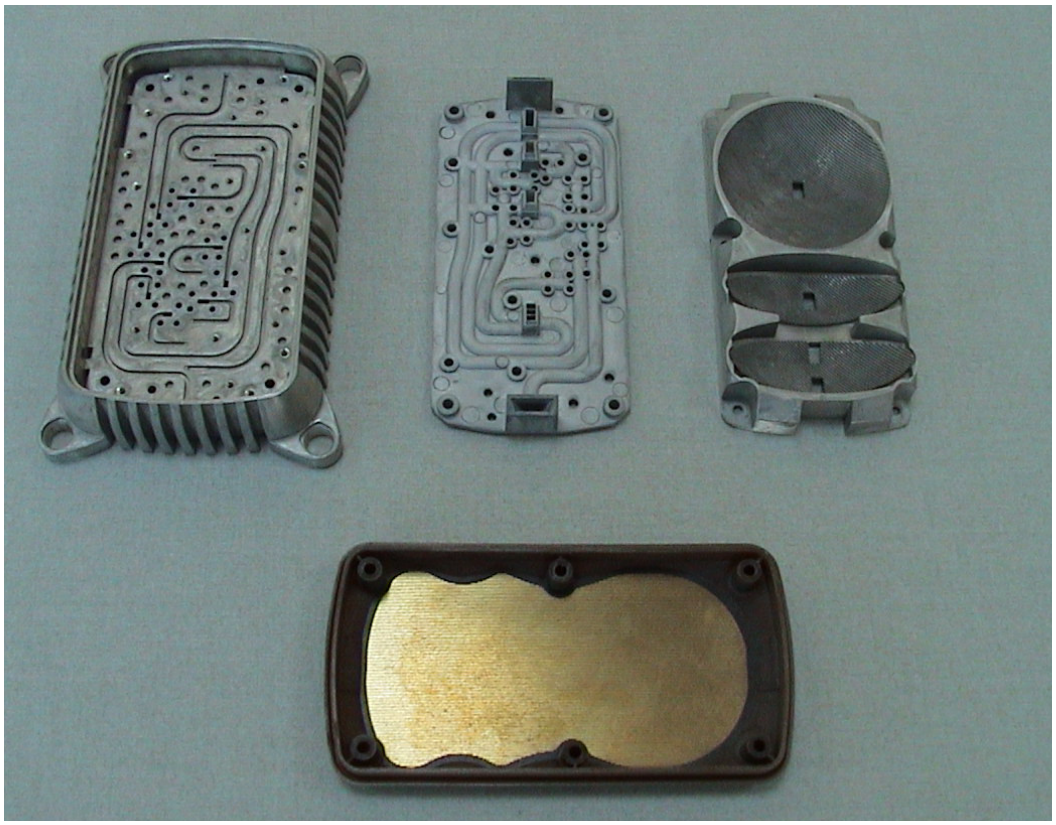

Figure 51. Photograph of an existing automotive radar showing all the metallization and WG transitions [56].

The objective of this work is to produce solutions replacing waveguide transitions with wideband 3D RF transitions while considering low-cost materials and packaging, integration as well as a good antenna design. This pyramid of RF Performance dependencies is shown in Figure 52 highlighting the importance of the key aspects towards the final RF system performance. Figure 53 shows the evolution of the proposed Radar Front-End from current radar systems through a list of improvements or better yet requirements for low cost mm-Wave radar. These are: miniaturizing the overall dimensions, replacing WG transitions by 2D/3D transitions on low cost LCP substrate and using a phased-array antenna for beam steering. Figure 54 shows the front and back views of the proposed architecture in better detail while honing in on the necessities of

creating a 3D transition in order to propagate the signal from/to a T/R module (on the back) to the antenna array on the front. Also shown in Figure 54 is the necessity of having the TL bends for miniaturization reasons and in order to interface with the IC. This is because the channels of the IC have different physical restraints (center to center distance among its channels) than the RF part or antenna array where the center-to-center distance is close to λ/2. Also shown is the necessity of minimizing cross-coupling among adjacent TLs. Figure 55 shows the cross section of the proposed module showing the location and details of proposed heat rejection (through thermal vias), DSP and digital blocks mounted on a mm-Wave PCB.

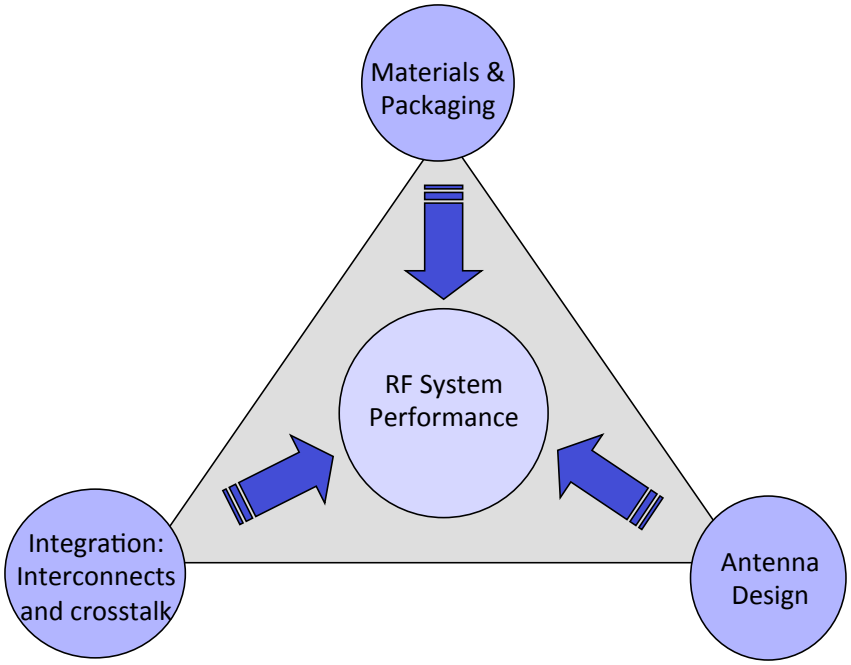

Figure 52. Key Aspects of mm-Wave Design.

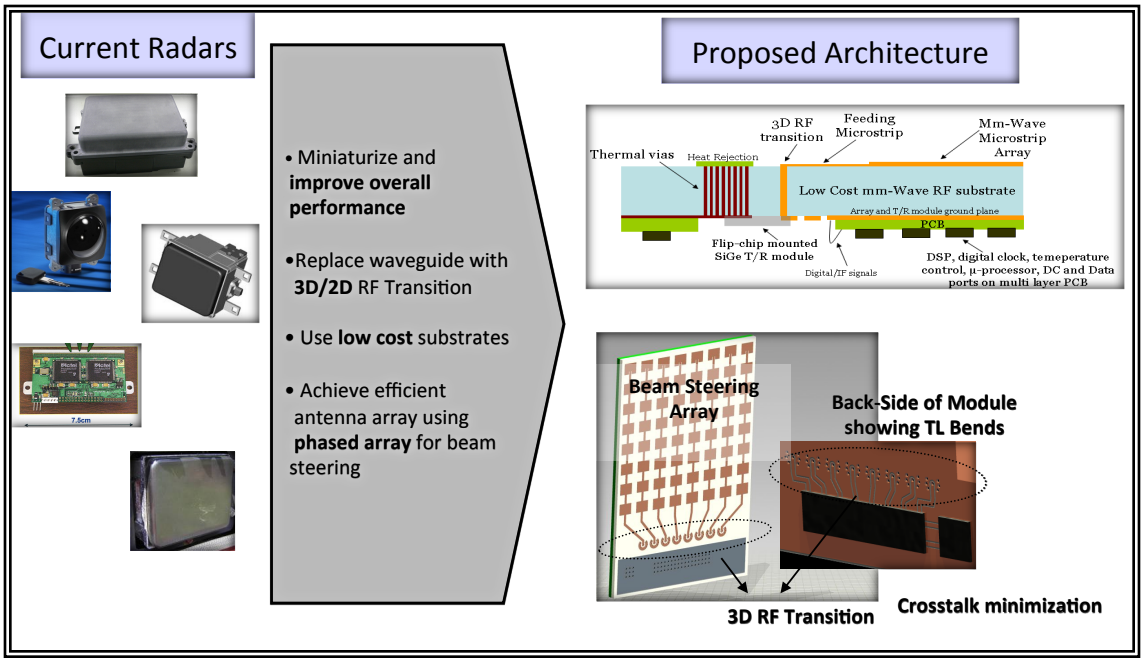

Figure 53. Current Radars and evolution towards proposed Radar Architecture.

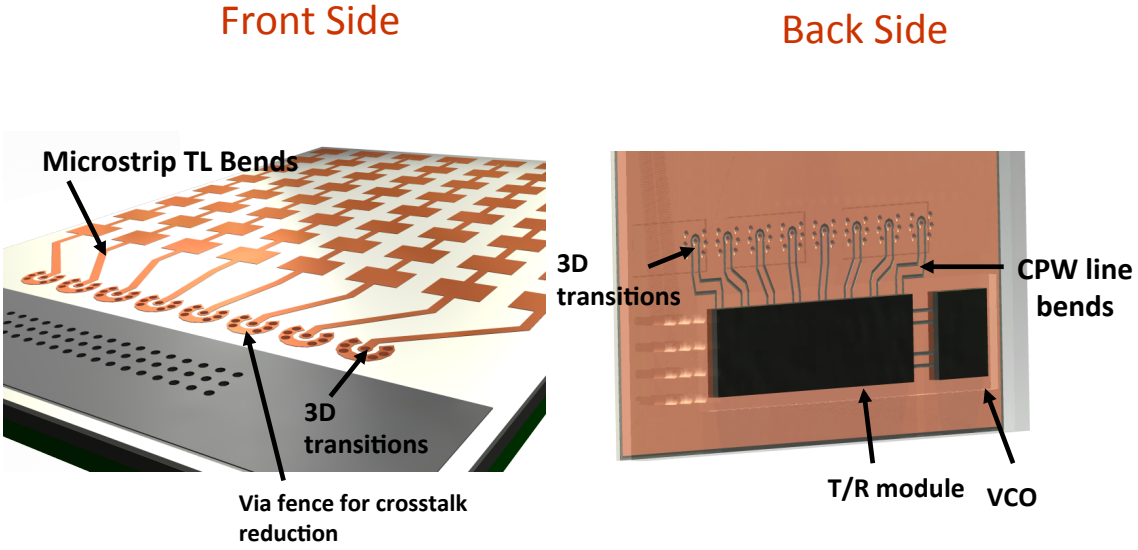

Figure 54. Front and Back side views for the proposed architecture for the 3D integrated mm-Wave Radar Front-End showing the necessity for Microstrip TL bends, CPW TL bends, 3D RF Transitions as well as Cross-talk reduction.

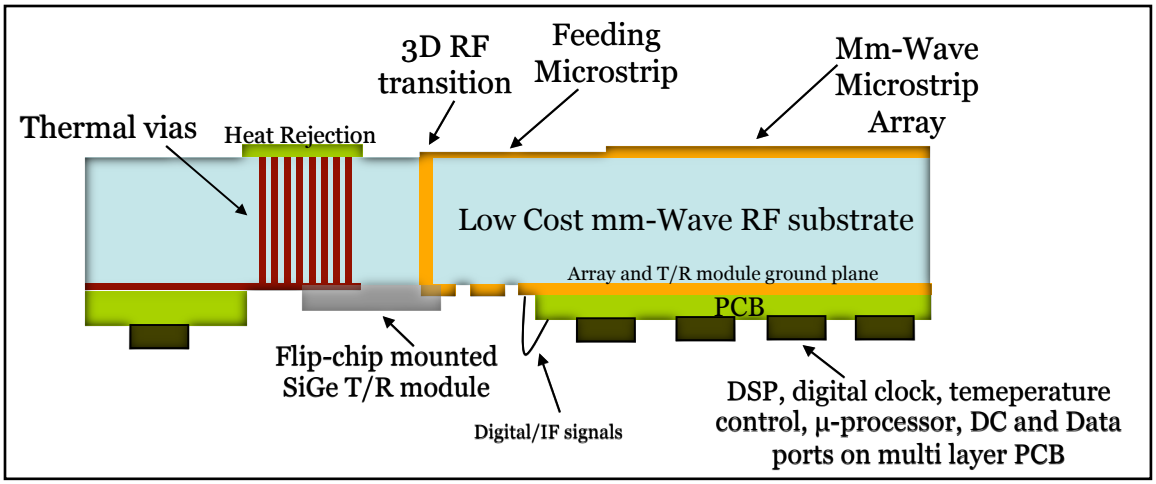

Figure 55. Schematic of multilayer low cost mm-Wave RF substrate based radar including vertical transitions and microstrip planar arrays**.**

Finally, Figure 56 shows the proposed radar front-end assembly, showing front and back views of printed circuit board and the LCP antenna substrate with a detailed view of part of the front-end assembly focusing on the 3D RF transition. This therefore leads to the main objectives of this section of this work, which are:

1. Substrate selection (covered in Chapter 2)
2. Architecture Design (this chapter)
3. 3D RF transitions from T/R module to array (Chapter 6)
4. 2D transmission line transitions for optimizing sharp bends or corners (Chapter 6)
5. Integration of antenna elements with 3D transition (Chapter 7)
6. Methods to minimize crosstalk among transmission lines to/from T/R module (Chapter 8)
7. An optimized antenna array for phased-array operation made up of several channels that feed individually to a T/R phased array module. This array must also satisfy bandwidth, gain, efficiency, beam steering and size requirements. (Chapter 9)

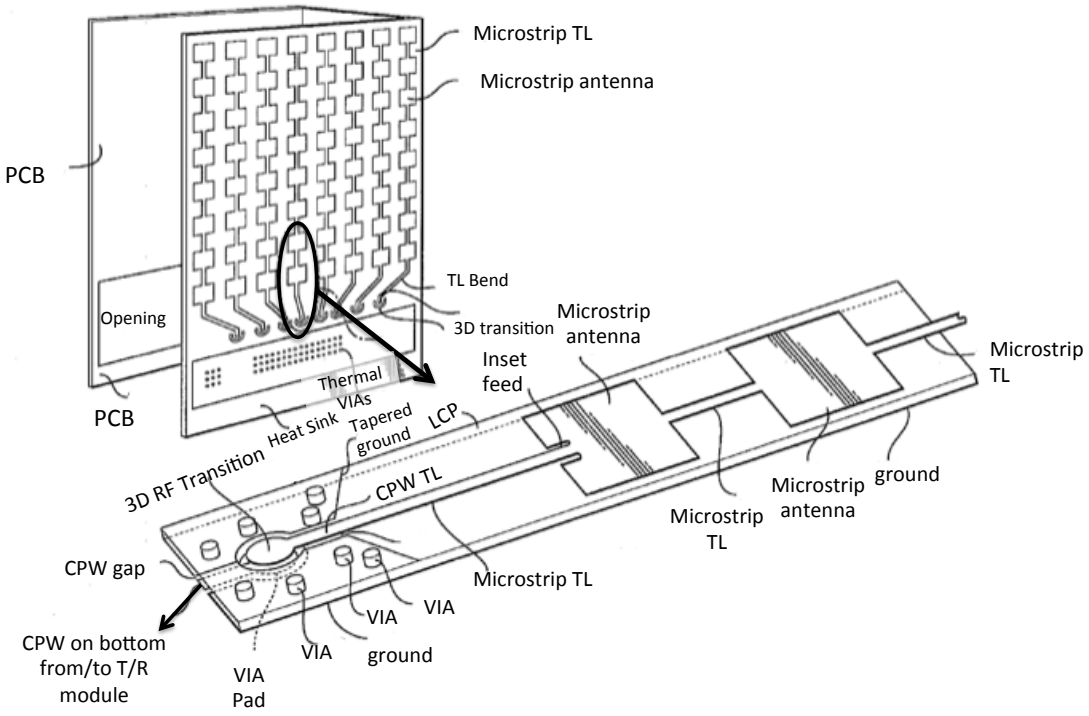

Figure 56. Proposed Radar Front-End Assembly, showing front and back views of Printed Circuit Board and LCP Antenna Substrate with a detailed view of part of the Front-End assembly focusing on the 3D RF transition.

Chapter 6.

Wideband RF Interconnections up to 100GHz

The purpose of this chapter is to describe a method for the development of easy-to-fabricate low-cost 3D and 2D transitions on the flexible organic Liquid Crystal Polymer (LCP) for use in mm-wave (up to 100GHz) front-end applications such as broadband high-speed wireless LAN [9], automotive radar and imaging systems. LCP has recently gained much consideration as a potential high-performance microwave medium with excellent "dual" (substrate and packaging) functionality due to its very good electrical, mechanical and hermeticity properties. Moreover LCO has attractive high frequency properties for developing mm-wave circuitry [26]. LCP can be easily laminated and micro-machined to form 3D multi-layer modules. Due to its near-hermetic characteristic, LCP is used for the integration of embedded bare IC's without the use of additional packaging material - something that allows for the module miniaturization, but also necessitates the development of broadband low-loss 3D CPW-to-CPW and CPW-to-Microstrip (MSTRIP) interconnects. For the purpose of this work, the dielectric characterization of the utilized LCP material was performed using a free space method and, as stated in Chapter 3, the dielectric constant (ε_r) was measured to be around 3.0 for the frequencies of interest.

A recently reported 3D micromachined transition on Si features good performance up to 50GHz [57], but it is very costly due to the tedious formation of cavities. In [58] another broadband vertical transition has been realized; however with supported measurement results up to 60 GHz and with a 4-layer cross section. In [59] an ultra-

wideband microstrip to CPW transition has been reported with a 0.7dB/transition up to 40GHz. Other reported efforts, such as [60], utilize waveguide-to-microstrip line transitions from one layer to another, however they are bulky and limited in bandwidth and they require the use of waveguide-based topologies.

In this work, two simple wideband 3D transitions, one for Coplanar Waveguide (CPW)-CPW-MSTRIP Line and another for CPW-CPW-CPW Line will be presented on LCP and up to 100 GHz utilizing two layers of metallization only. Both of these consist of a vertical and a horizontal transition. In addition, 2D or horizontal transitions will be demonstrated for microstrip and CPW lines. All dimensions on the designed structures are based on existing commercially available design rules and the use of mechanical drilling for via formation.

6.1. Wideband 3D Transitions

This section details the design of the 3D transitions, namely CPW-CPW-MSTRIP and CPW-CPW transitions. Design methodology, simulation results demonstrating in many cases the field confinement of these mm-Wave transitions, experimental setups, measurement considerations, as well as any fabrication observations are presented in this section.

6.1.1. Wideband 3D Transitions: CPW-CPW-MSTRIP

6.1.1.1. CPW-CPW-MSTRIP: Design

The proposed design achieves a very good wideband RF performance by utilizing a tapered ground plane and by placing grounding vias in appropriate locations in order to suppress parasitic modes and eliminate radiation losses due to open-end effects. The via pads and gaps are optimized so as to match the series inductance of the via transition and maintain a 50 Ohm characteristic impedance throughout the transition, allowing for a very broadband response up to 100GHz. Furthermore, the design consists of one via-based vertical transition used to connect the CPW signal (center) transmission lines printed on both sides of a single LCP layer (~100 μm thick), as well as grounding vias connecting the top and bottom ground layers. Figure 57 shows the cross sectional view of the layout explaining in details the design. Figure 58 shows the top and bottom views of the design schematic with the specific via placements. The effect of the strategically chosen placement of the vias is demonstrated in the field plot shown in Figure 59, which signifies the importance of having the ground tapered with a specific angle in order to suppress all E-field edge radiation effects. Figure 59 also shows the step-by-step process used in order to achieve the optimal results for the transition. After designing the shape and dimensions of the via, via pad, and slot width to achieve minimum return loss for a wideband operation, a minimum amount of vias had to be chosen for the low cost requirement while in accordance to the fabrication design rules. This is illustrated in Figure 59 where the addition of the two vias around the center of the transition via had to be added, followed by the addition of the vias close to the edge of the CPW grounds, and

furthermore the tapering of the CPW grounds as well as the addition of two extra vias to suppress any radiation at the edges (open end effects). Having an extra set of vias completely suppresses any radiation due to sharp ends and ensures a better performance and field suppression of T.L. end effects at mm-Wave frequencies especially after fabrication and during measurements. Finally Figure 60 demonstrated the E-Fields at 76.5 GHz for the back-to-back structure and that will be fabricated for measurement and demonstration.

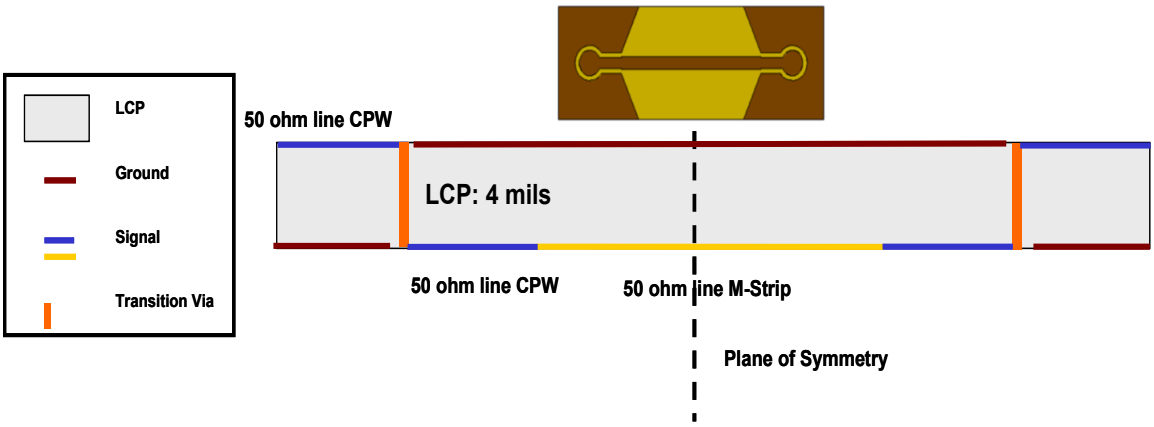

Figure 57. Cross Sectional View of the 3D CPW-CPW-MSTRIP Transition.

The top layer of the transition (Figure 58 b) starts as a CPW launch with characteristic impedance Z_0 of 50 Ohms, realized by appropriately choosing the signal line width and the gap between the signal line and the ground. The CPW slot width (~85 um) is responsible for maintaining a desired CPW mode for the wide frequency band up to 100 GHz throughout the CPW section of the transmission line (top and bottom), so it is kept at a constant value around the via pad, resulting in minimum field reflections and very

good impedance matching.

The transition via lies within a wide circular disk shape to accommodate the via pad, that has an extra 300 μm larger radius compared to the via (75 μm), as is specified by the fabrication requirements for metallization purposes. A 75 μm via diameter was chosen. This dimension is the smallest diameter that could be mechanically drilled and metalized, thus determining the smallest via size with a satisfactory RF performance. The CPW ground planes on the top layer have been tapered at an angle α of ~27°. The tapering of the CPW ground has been utilized in previous work such as [59] for an optimized transition between the CPW and the microstrip and the value α was chosen based on simulation optimizations.

The characteristic impedance of the microstrip line can be calculated according to [40]:

$$Z_o = \begin{cases} \frac{60}{\sqrt{\in_e}} ln\left(\frac{8d}{W} + \frac{W}{4d}\right) & for\ {}^{W}/_{d} \leq 1 \\ \frac{120\pi}{\sqrt{\in_e}\left[{}^{W}/_{d} + 1.393 + 0.667 \ln\left({}^{W}/_{d} + 1.444\right)\right]} & for\ {}^{W}/_{d} \geq 1 \end{cases} \quad \textbf{Equation 12}$$

$$\in_e = \frac{\in_r + 1}{2} + \frac{\in_r - 1}{2} \frac{1}{\sqrt{1 + 12d/W}} \quad \textbf{Equation 13}$$

where W is the width of the microstrip line, d is the height of the substrate, which is 4 mils in this case (or equivalently 100 μm) and $\in_e$ is the effective permittivity. This results in a W = 236 μm for a 50 Ohms characteristic impedance. The CPW TL's characteristic impedance is more complicated and contains more parameters such as the gap between the signal and the ground and references such as [61] are recommended for analytic equations. TL calculators as the ones provided by Agilent [62] can always be used to facilitate design steps.

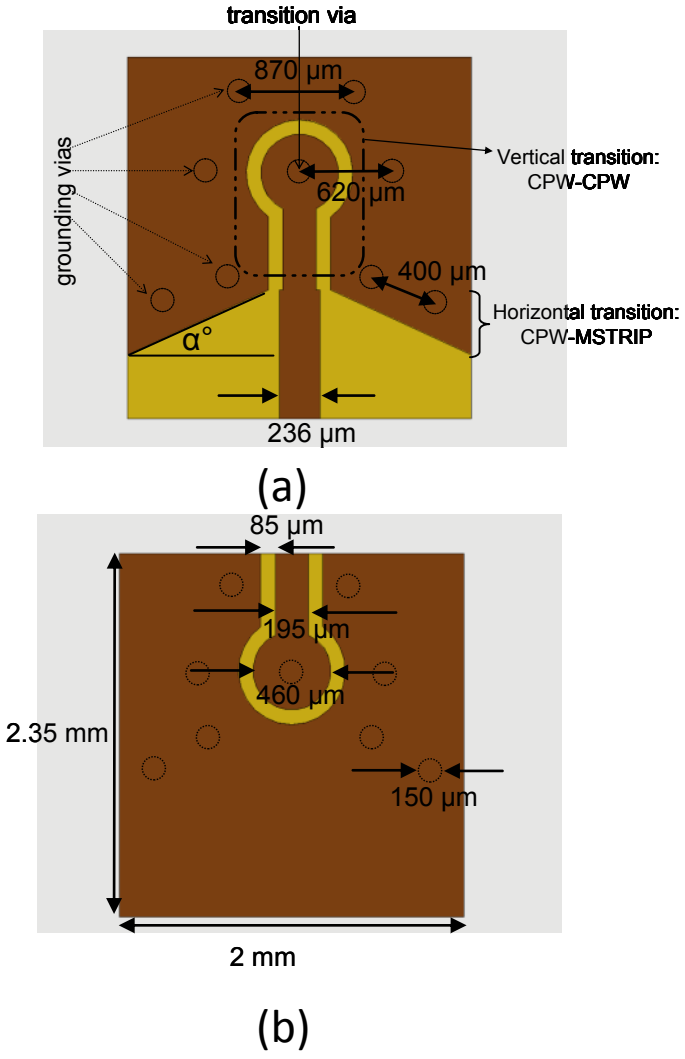

Figure 58. Schematic for Wideband Vertical CPW-CPW-MSTRIP Transition (a) Bottom view (b) Top view.

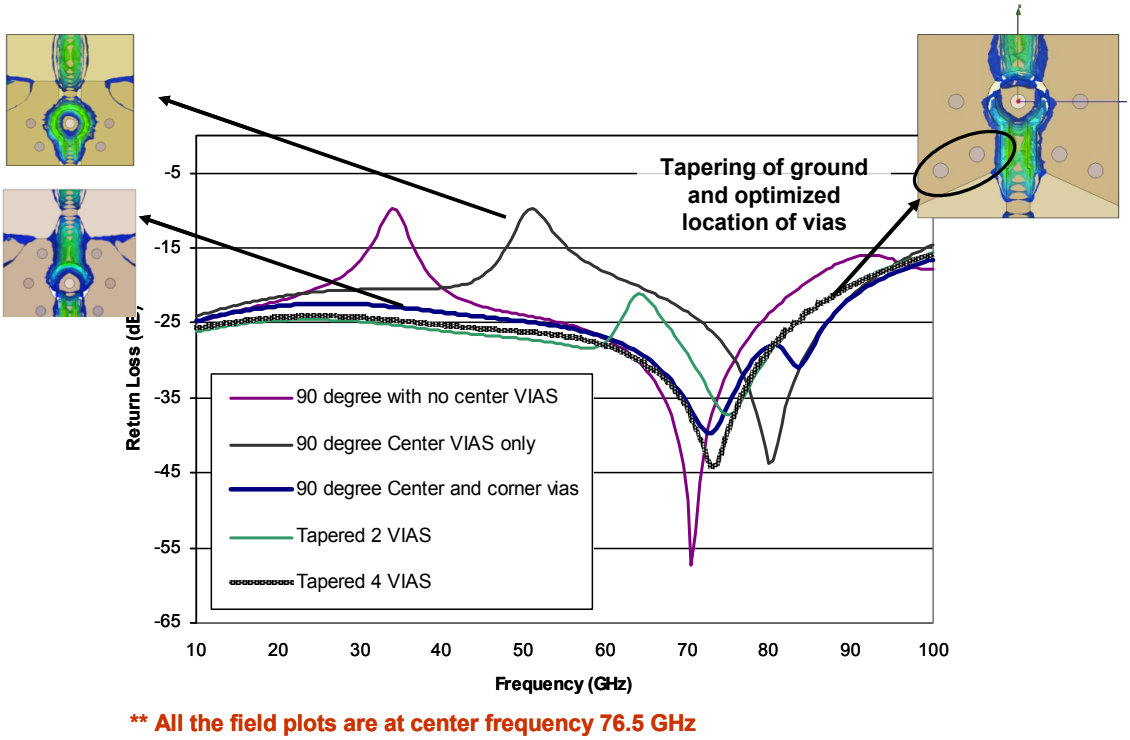

Figure 59. S_{11} and E-field distribution at 76.5 GHz for the design stages in the CPW-CPW-MSTRIP Transition.

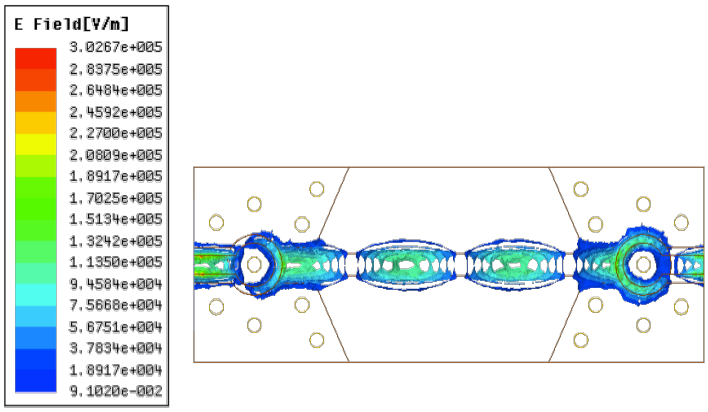

Figure 60. E-field distribution at 76.5 GHz for the final design back-to-back structure.

6.1.1.2. CPW-CPW-MSTRIP: Sensitivity Analysis

In order to examine the viability of the presented design in a large-scale production environment, a sensitivity analysis based on the tolerances and design rules provided by the manufacturer was performed. Figure 61 and Figure 62 summarizes the results for return and insertion loss respectively. It can be seen that even in the worst via-to-pad misalignment case of ±3 mils the CPW-CPW-MSTRIP transition maintains an acceptable performance at 76.5 GHz (simulated Return loss below -15 dB and insertion loss of -0.35 dB), despite the fact it could cause a shift in the central design frequency.

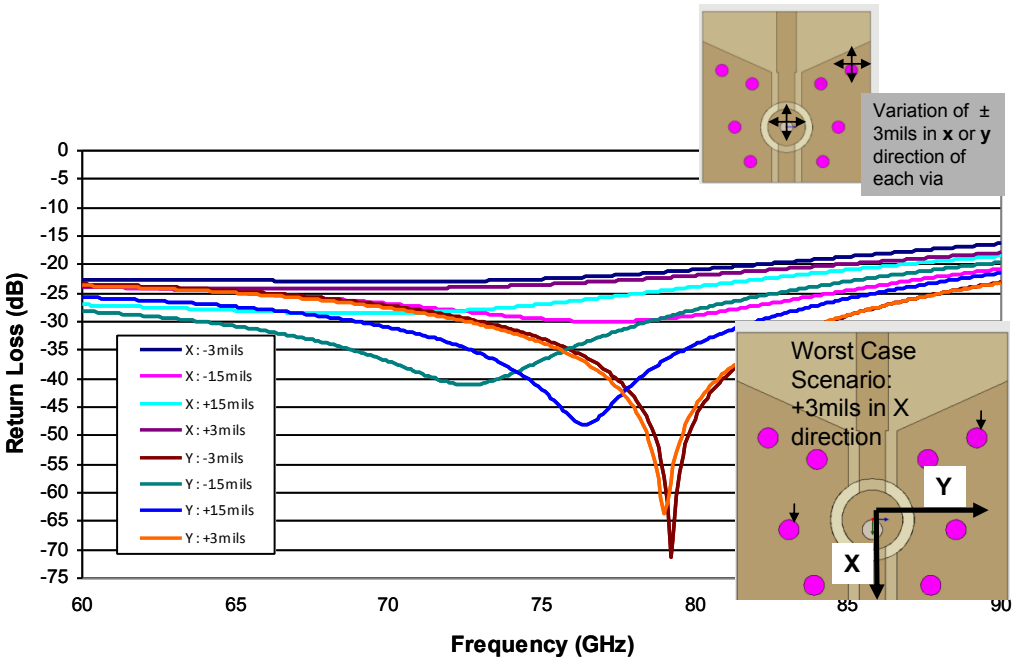

Figure 61. Return Loss of 3D Transition for off-center vias.

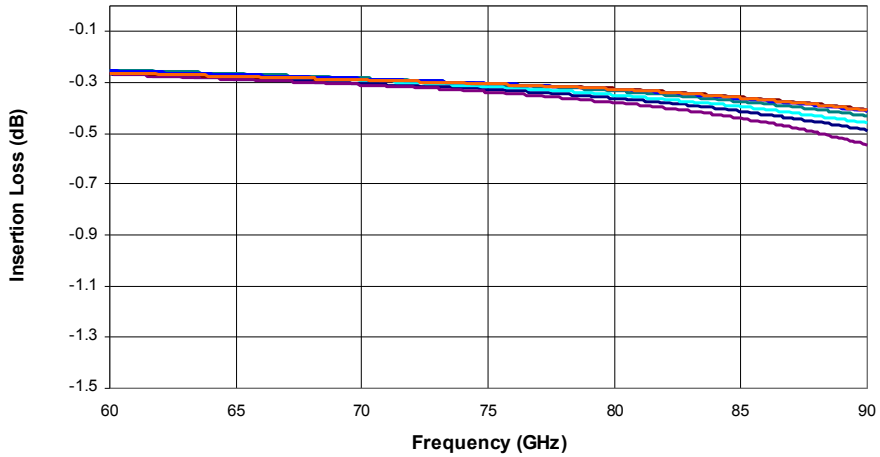

Figure 62. Insertion Loss of 3D Transition for off-center vias.

6.1.1.3. CPW-CPW-MSTRIP: Measurement Considerations

Figure 63 and Figure 64 show the photographs of the fabricated structures (top and bottom) that were used for measurements. Attention had to be taken in these measurements since given the nature of the structure; there is no common ground plane. Of specific notice is the thick FR4 material that was laminated around the structures as seen in Figure 64 in order to create a cavity so that the structures do not directly sit on the metallic chuck on the probe station. In addition to this, the probes used for measurements up in the GHz frequencies typically have very narrow footprints such as 100 to 150 μm [63]. Figure 65 shows a photograph of an individual sample CPW-CPW-MSTRIP 3D transition emphasizing an additional transition that is intended only from measurement purposes. The additional CPW-CPW horizontal transition here was simulated for an optimum Return Loss and minimum Insertion Loss and is a necessary part of the structures for compatibility with GSG probes with a footprint of 150 μm. Figure 66

shows the dimensions of the structure at the transition reflecting less than 10% deviation from the ideal (design) values.

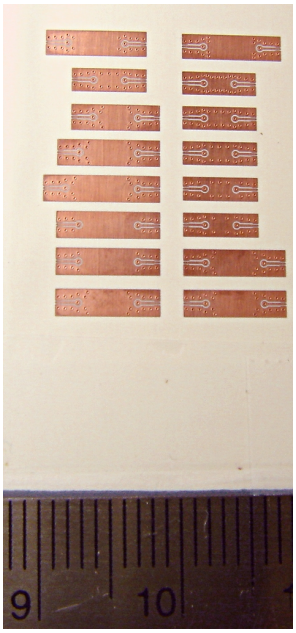

Figure 63. Photograph of the fabricated 3D transitions on LCP (Top View).

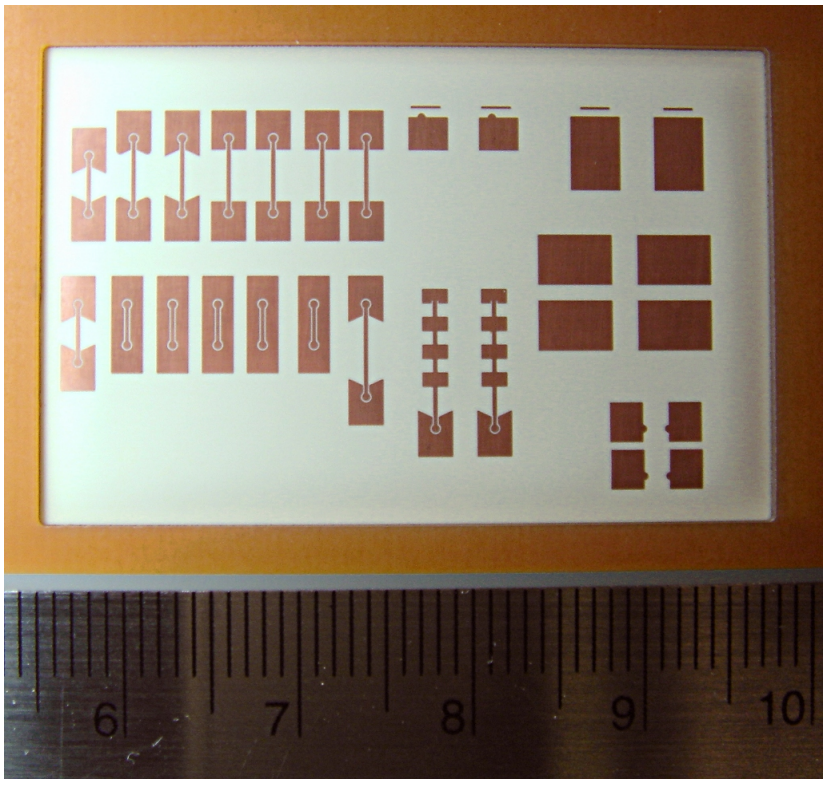

Figure 64. Photograph of the fabricated 3D transitions on LCP (bottom view) with FR4 support on the boundaries for mechanical support during measurements.

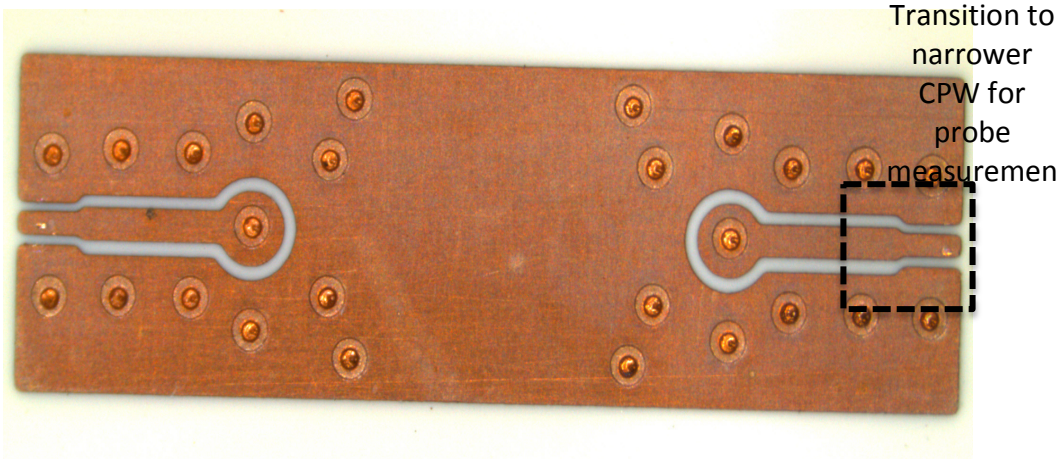

Figure 65. Photograph of an individual fabricated back-to-back CPW-CPW-MSTRIP 3D Transition showing transition to narrower CPW input for probe measurements.

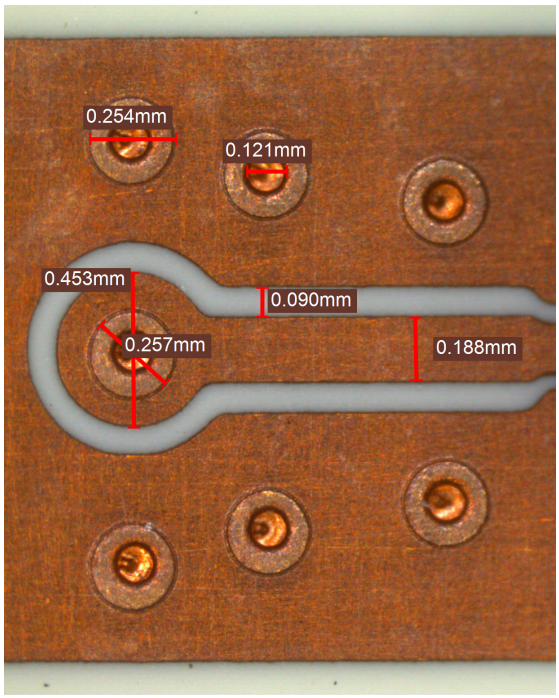

Figure 66. Photograph of the fabricated CPW-CPW-MSTRIP transition with dimensions.

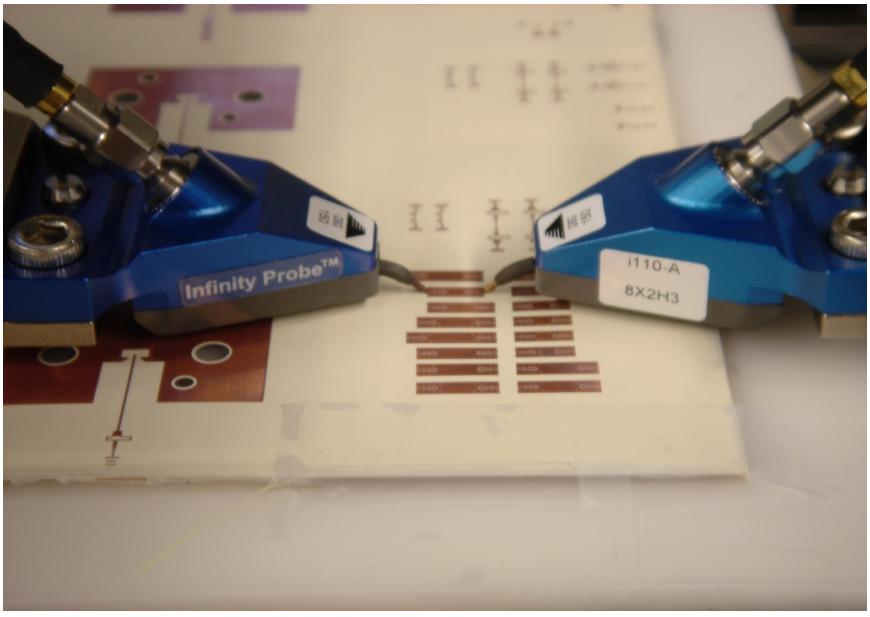

Figure 67. Photograph of the probe measurement setup.

6.1.1.4. CPW-CPW-MSTRIP: Discussion of Results

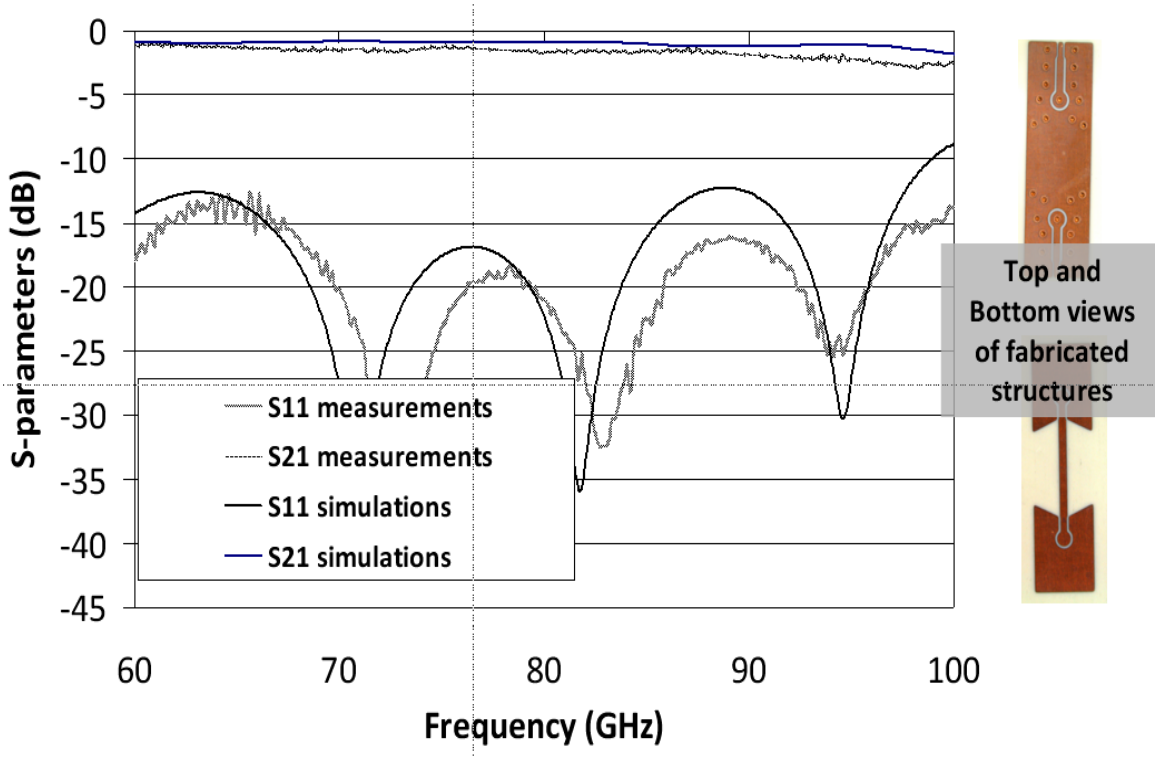

Figure 68. S-parameters and photos of the fabricated structure for CPW-CPW-MSTRIP Transition.

Figure 68 shows the results for the simulated and measured S-parameters exhibiting good agreement over a very broadband response. The simulations were performed using Ansys HFSS [64]. The calibration technique for the measurement setup utilized is TRL. The Insertion Loss of the whole structure with back- to-back transition as shown in Figure 68 and for a total length of 6.6mm (length of the back-to-back module starting with CPW line on one side of the substrate, transitioning to CPW line on the other side of the substrate then in turn transitioning to microstrip line) is 0.9 dB after de-embedding the input launch lines. This corresponds to an IL of 0.45 dB per transition (of length 3.3mm) at 77 GHz and 1.175 dB at 100 GHz.

6.1.2. Wideband 3D Transitions: CPW-CPW

The same design approach was followed for designing a wideband 3D CPW-CPW. This design features only CPW transmission lines (Figure 69), therefore it contains one less transition in comparison to 4.1.1. However, it was chosen as the showcasing structure for the critical importance of the optimal via spacing for a broadband satisfactory ground equalization between the top and bottom ground layers for the CPW lines.

6.1.2.1. CPW-CPW: Design & Discussion of Results

In an effort to obtain optimum performance while minimizing the cost, a minimum number of vias is essential. Here samples were fabricated with via spacings of 250 μm, 500 μm, and 1000 μm and are shown in Figure 70. Is was found that maintaining a via spacing of 500 μm yielded the optimum results satisfying both performance and optimum number of vias. In this case the results obtained by the 1000 μm via spacing are very similar to those of the 500 μm spacing and hence are not recommended for cost purposes. The S-parameters results are presented in Figure 71 exhibiting a return loss below 20 dB for the 50-90 GHz frequency range. The insertion loss is 0.5dB at 77GHz for the back-to-back transition of total length 5.6mm, or equivalent to 0.25dB IL for a single transition of total length 2.8mm. For this design the major focus was the selection of the optimum number of vias and spacing between the vias in the CPW section.

Maintaining a 500 μm spacing ($\sim\lambda_g/4$) via-via spacing was necessary in order to suppress the parasitic radiation due to the parallel-plate CPW mode and achieve good

performance while keeping the transition and the resulting front-end real-estate at a minimum.

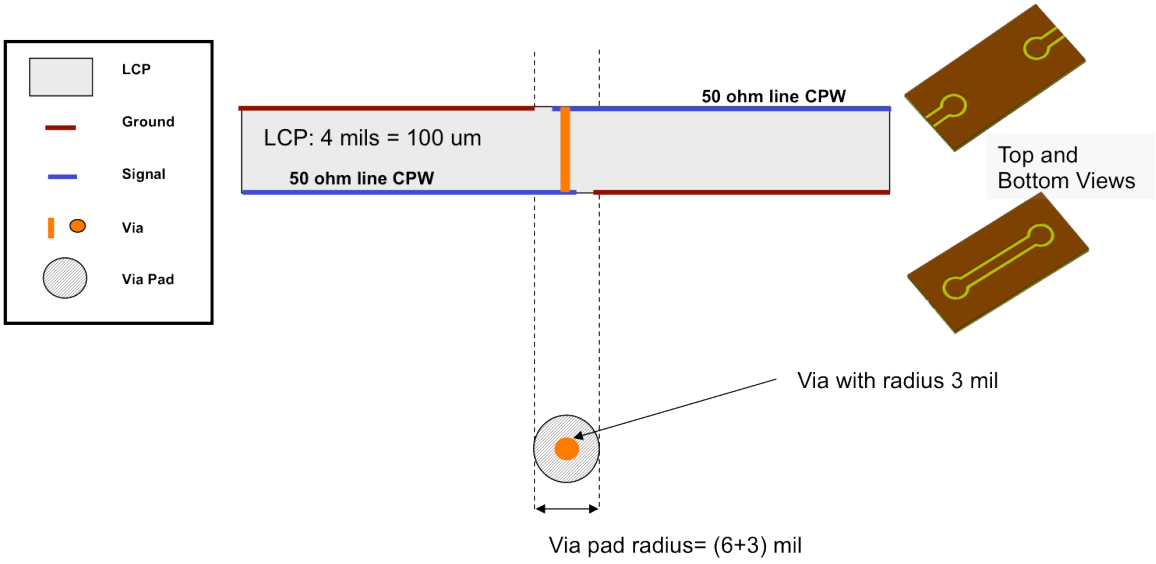

Figure 69. Cross Sectional View of the 3D CPW-CPW-MSTRIP Transition.

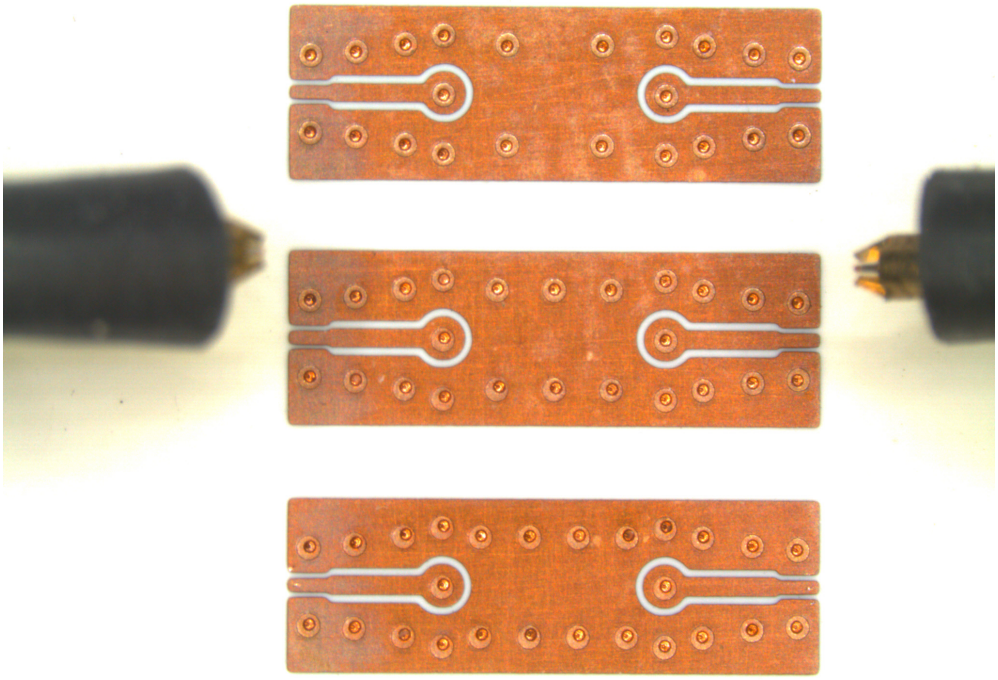

Figure 70. Photograph of the fabricated structures with different via spacings.

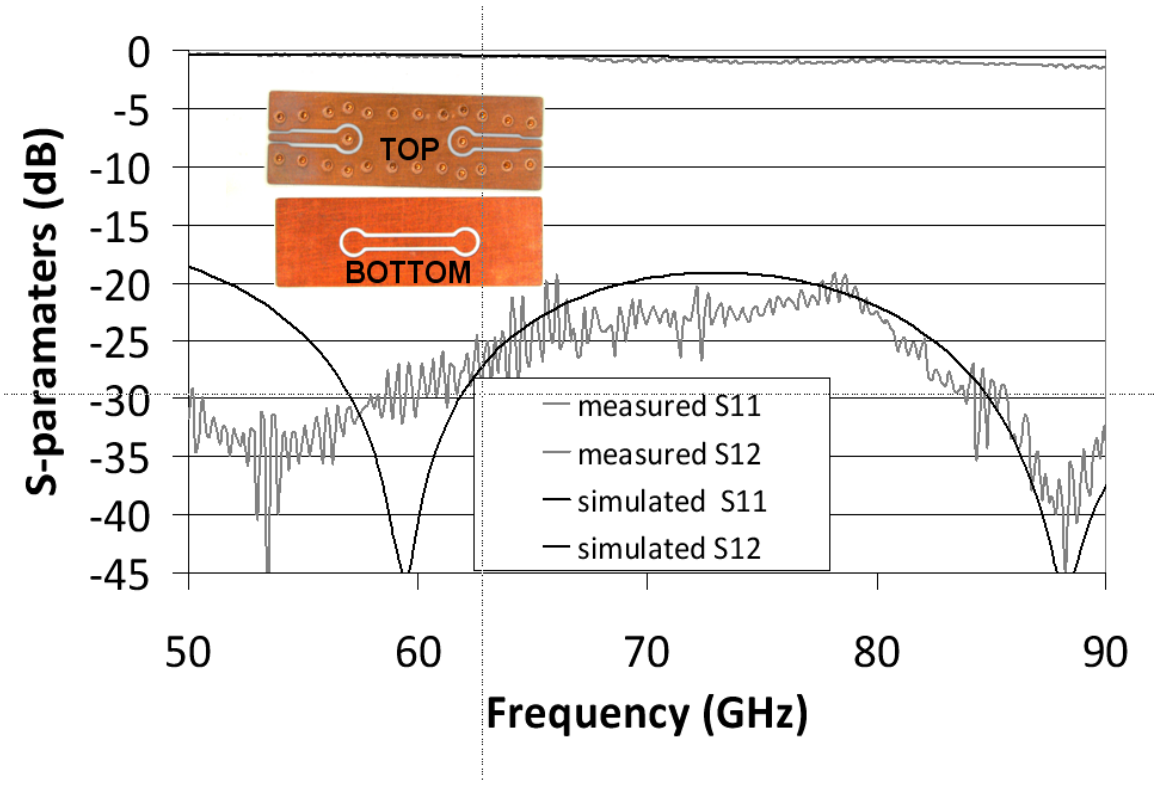

Figure 71. S-parameters and photos of the fabricated structure for CPW-CPW Transition.

6.2. Wideband 2D Transitions up to 110GHz

This section is divided into 2D Microstrip TL (horizontal) bends and CPW TL bends; both of which are necessary in order to realize the proposed design objective. As depicted in 1.2, the planar or 2D transitions of microstrip and CPW lines become a critical part of RF modules with large antenna arrays. This is due to the far more stringent spatial requirements on the spacing and separation distances among the sub-array antenna elements (typically $\lambda/2$) in comparison to the interconnection spacing among the feeding lines to a multi-channel T/R modules or IC's ($< \lambda/2$).

6.2.1. Wideband 2D Transitions: MICROSTRIP LINE Transitions

A design approach which allows wideband, high-performance 90° bends on microstrip is presented in this section. The structure schematic is shown in Figure 72. The Return Loss is shown in Figure 73 where the comparison between a sharp corner and a mitered corned is presented. In our the presented approach, the bend was mitered until the optimum response (lowest S_{11}) was achieved. While the sharp corner works well with an S_{11} below -40 dB at 10GHz and lower frequencies in general, it proves to be very problematic as frequency goes up and especially above 70GHz where the S_{11} exceeds -15dB. It is clear from the simulated response that there is a 20 dB improvement at 77 GHz (frequency allocation used for automotive radar application) and 25 dB improvement at 94 GHz (imaging application). Figure 73 shows the variation of return loss (S_{11}) with respect to the chamfer depth W'. The optimum response occurs at 1.86W.

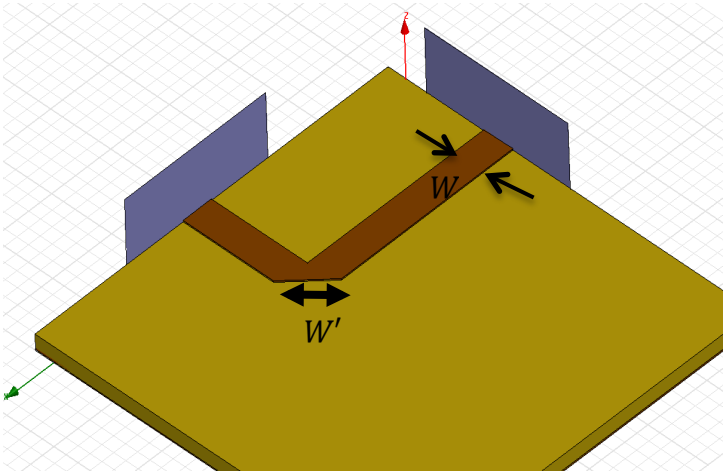

Figure 72. Schematic of optimum 90° microstrip bend.

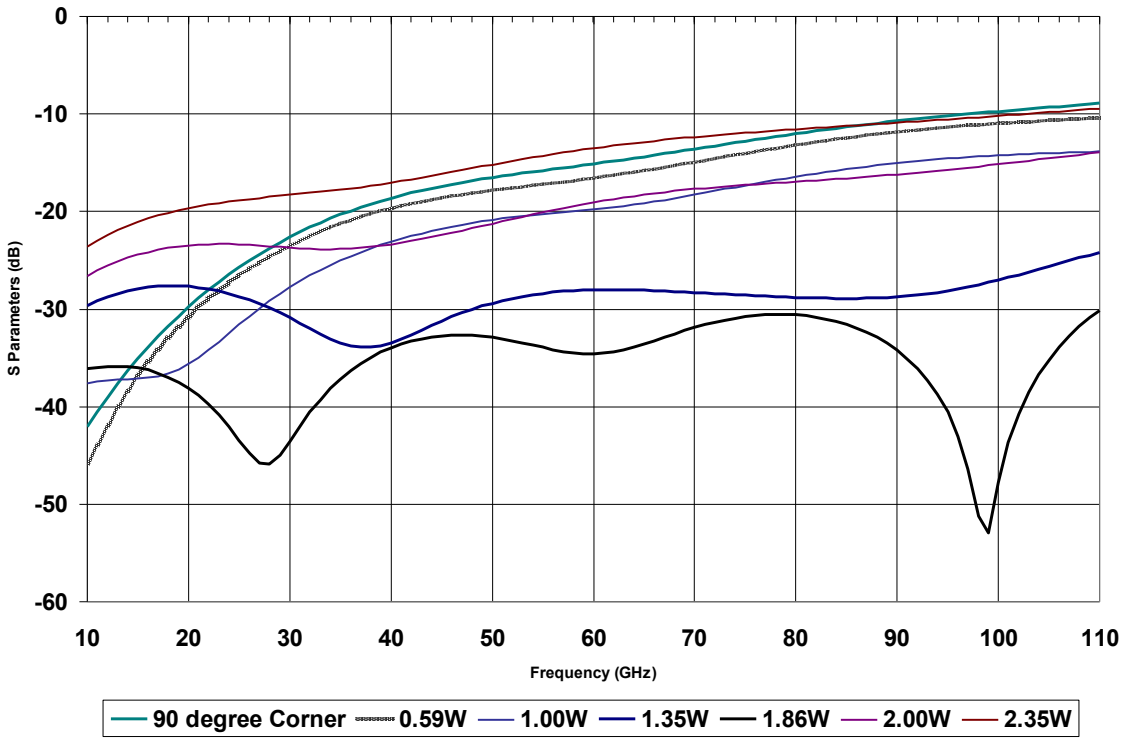

Figure 73. Simulated S_{11} vs. Frequency Response of several cases of bending microstrip line.

To demonstrate experimentally, **Figure 74** shows the S-parameters measurements results for the microstrip TL bends for a sharp cornered structure and for the optimum structure (with $W' = 1.86W$). From such results, one can clearly understand the importance of such considerations for passive mm-Wave RF designs. A note worth mentioning here is that the results in **Figure 74** are those for the entire structure as shown also in **Figure 74** and which includes the CPW-Microstrip transition for probe measurement purposes. Table 5 lists some values of the S-parameters from **Figure 74**.

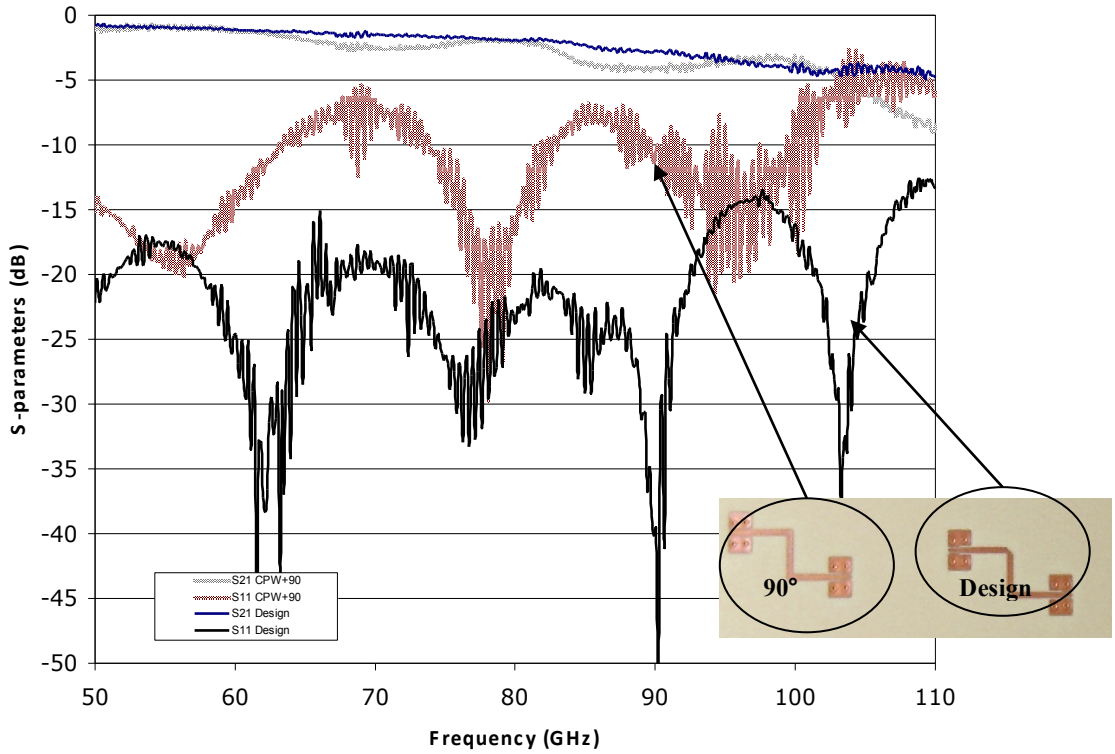

Figure 74. S-parameters measurements for Microstrip transmission line bends.

Table 5. S-parameters Comparison between Microstrip TL (Sharp Corners and the Chamfered Design)

Frequency (GHz)	S_{21}-Design (dB)	S_{11}-Design (dB)	S_{21}-Sharp Corners (dB)	S_{11}-Sharp Corners (dB)
65	-1.3	-22	-1.9	-7.9
70	-1.4	-19	-2.5	-8.7
90	-2.6	-39	-4.0	-10.4
110	-4.8	-13.4	-8.5	-5.9

6.2.2. Wideband 2D Transitions: CPW-G Transitions

Previous work in CPW and CPW-G bends have considered the use of air bridges [65], which add cost and mechanical limitations to the circuit fabrication. In [66] slow wave compensation, requiring very stringent fabrication tolerances, was used to optimize the CPW bend up to 50GHz.

In this work, a design approach which allows wideband, high-performance 90° bends on Grounded-Coplanar-Waveguide (CPWG) is presented for operability up to 110 GHz. The goals of the design are the following:

- Minimize return and insertion losses for Microstrip and CPWG 90° bends.
- Reduce cost through the use of smallest possible board real estate (minimum number of vias, short traces) and the use of mechanical instead of laser drilled vias.
- Utilize commercially available design rules.
- Achieve ultra wideband operation in order to reduce the sensitivity of the design to fabrication and assembly tolerances.

The structure schematic is shown in Figure 75. In this design approach, both the signal and the ground planes are chamfered. The CPWG line uses periodic vias placed at 750 μm separation with a radius of 3 mils (~ 75 μm) in order to deliver exceptional transmission performance at such high frequencies. This separation distance was chosen as the optimum for: 1) best RF performance (minimum reflections and losses) and 2) minimum number of vias used. Furthermore, vias are used to suppress the parasitic parallel plate and slot-line modes. The location of the additional vias at the bend (as pointed out in Figure 75) is very critical for achieving the good performance of the bend

and significant effort was invested in optimizing this. To the authors' knowledge, this is the first time that such an approach for optimizing CPWG bends has been proposed. The via diameter and inter-via spacing are based on low-cost, commercially available fabrication processes compatible with LCP substrates, and therefore the vias can be easily manufactured. The same figure also includes a field plot of the electric field as it propagates on the CPWG line.

The simulated response of the structures is presented in Figure 76, which summarizes the return loss of the structure, while Figure 77 shows the insertion loss. It is clear that the sharp corner bend cannot be used for frequencies higher than 60 GHz due to its Return Loss performance. Upon chamfering the bend, one can observe the improvement in the performance up to 75 GHz but not beyond 75 GHz. The final design that includes both the chamfered bend and the vias is shown to have good performance at frequencies up to 90 GHz. Figure 78 demonstrates measurement results of the step-by-step optimization procedure starting with a 90° CPWG bend, then chamfering or tapering the signal line only, followed by the tapering of both signal and ground lines, and eventually the final design which includes the placement of additional strategically positioned vias around the bend. The final design features a very good performance at frequencies up to 110 GHz with a return loss lower than 15dB. The insertion loss of the structure of total length 12.7mm consisting of two CPW (back-to-back) bends is 1.5dB at 77GHz, equivalent to 0.12dB/mm of the CPW bend structure. These results are reported for the first time for frequencies up to 110GHz and for simple-to-fabricate 2D transition topologies.

It is to be noted that although these structures were characterized on LCP, they could be as well utilized for other mm-Wave substrates with minor changes (modification of dimensions for optimization of performance).

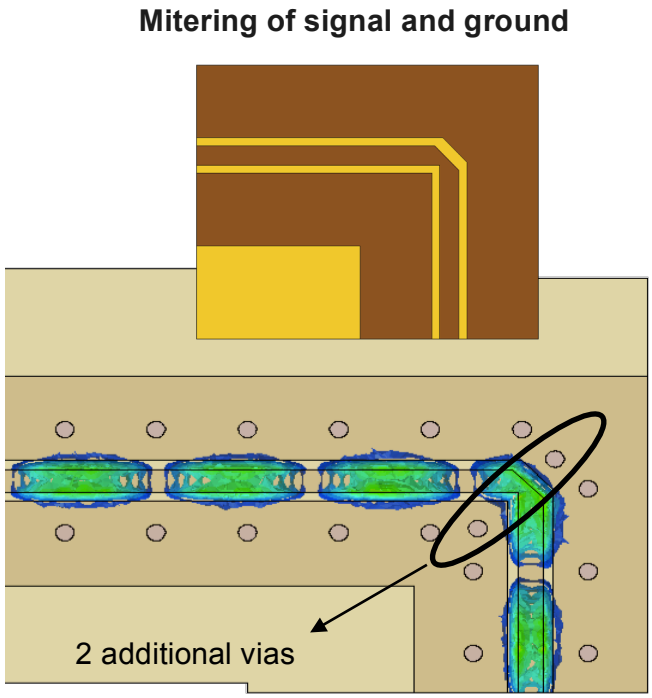

Figure 75. Schematic of CPWG TL Bend and E-field at 76.5 GHz.

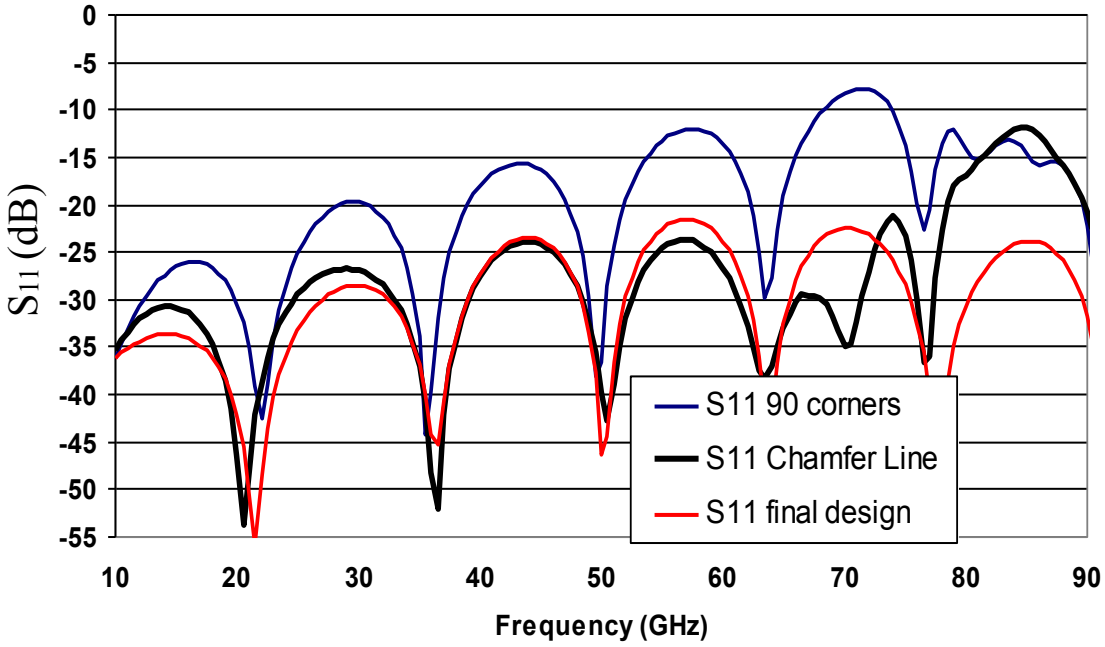

Figure 76. S_{11} vs. Frequency of the CPWG TL Bend at the different design stages.

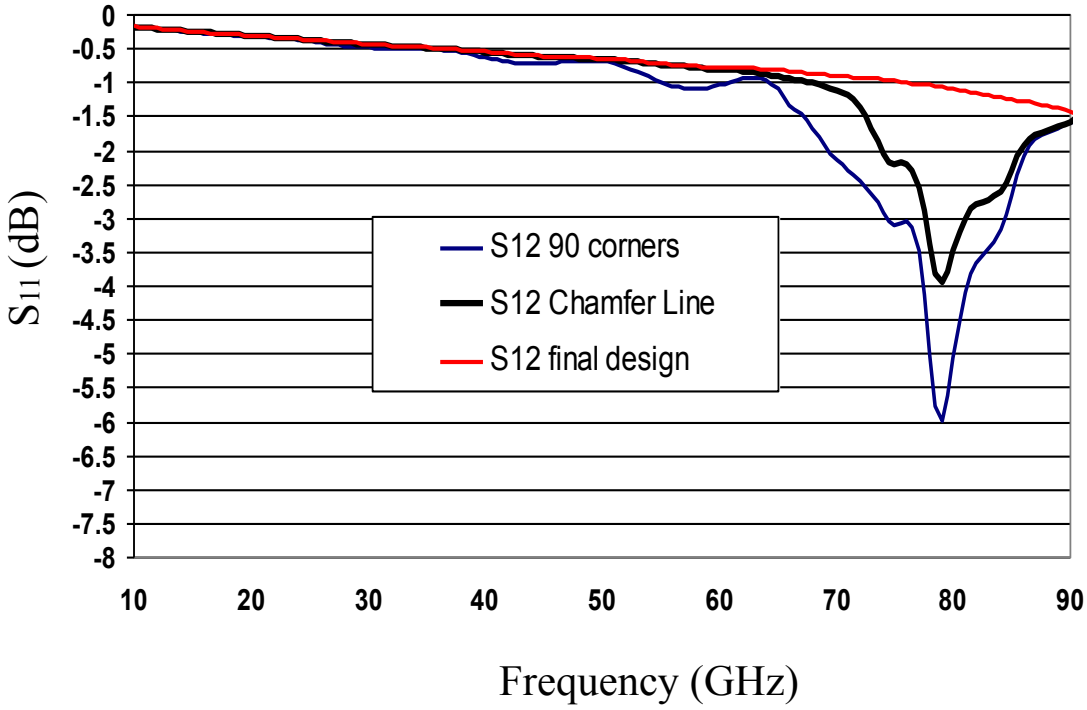

Figure 77. S-parameters measurements for Microstrip transmission line bends.

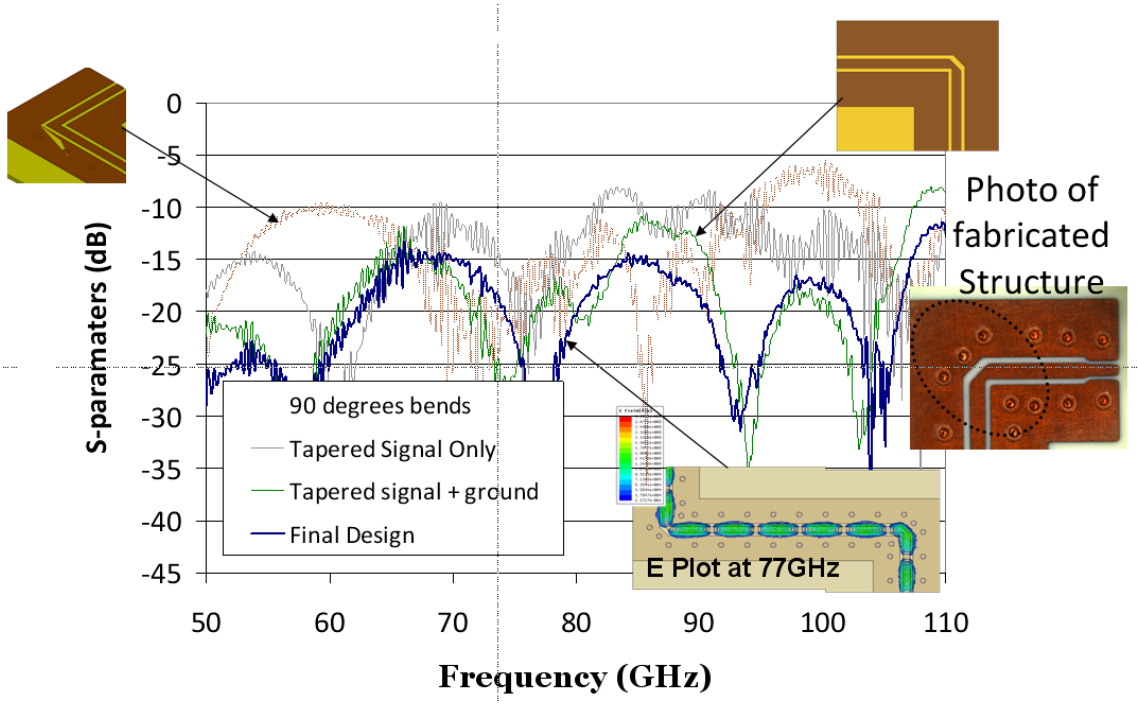

Figure 78. S_{11} for the step-by-step design process for the CPW-Bends.

Chapter 7.

Integration of 3D Transitions With Antenna Array

This integrated 3D transition with an antenna makes a very attractive configuration. This is especially useful as a radiation reduction mechanism between the feed network and the mounted IC packages with the antenna array. The radiation reduction is achieved by suppressing any undesired radiation that could be due to sharp edges and/or significant electrical length of the feeding lines as well as mismatches between the feeding lines and the IC. All of which could be detrimental for the radiation performance of the antenna array.

7.1. 4x1 Array for S-parameter measurements

The easy integration of the proposed 3D interconnects can be demonstrated in Figure 79 showing the integrated topology of the CPW-CPW-MSTRIP 3D transition with a 4-element microstrip antenna array, designed to resonate at the automotive mm-Wave radar frequency of 77 GHz. The S_{11} parameters are shown to exhibit good response with a minor shift in resonance frequency due to etching effects and/or the process tolerances in dielectric properties, especially that of ε_r. The simulated radiation efficiency (at 77 GHz) was found to be 75% and a total gain of 10 dBi. With an overall good agreement, this verifies the proof of concept of the easy and effective integration of the proposed 3D transitions with practical antenna arrays to be used in large array systems for mm-Wave applications such as automotive radars.

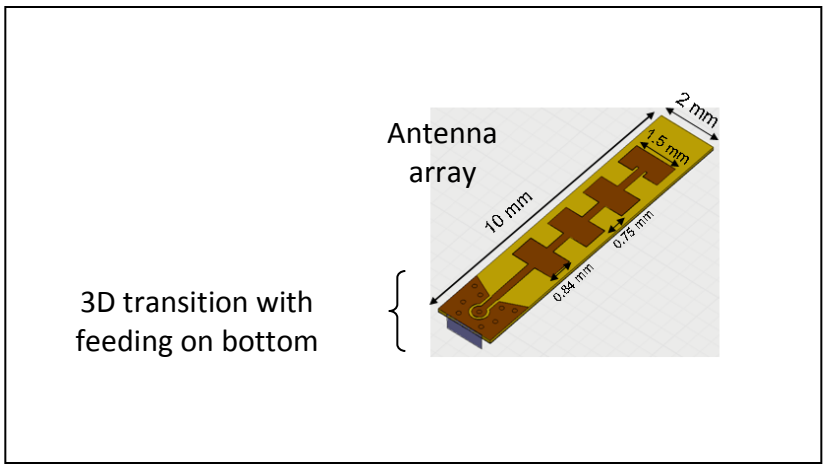

Figure 79. Schematic of the integration of 3D CPW-MSTRIP Transition with 4-Element Patch Antenna Array.

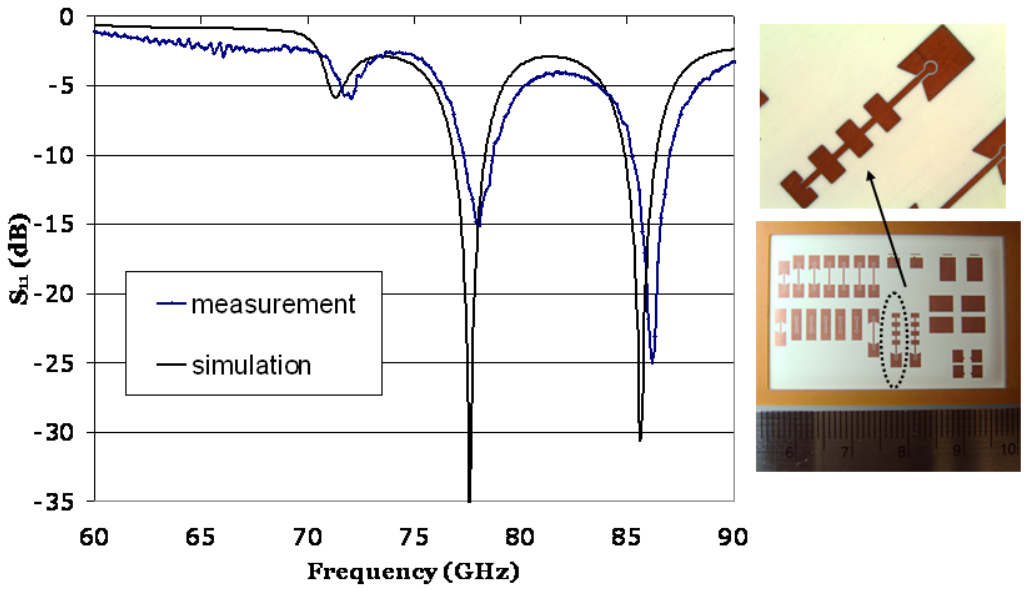

Figure 80. S_{11} results for the integrated 3D CPW-MSTRIP Transition with the 4-Element Patch Antenna Array.

7.2. 8x2 Antenna Array for S-parameter and Radiation Measurements

The structure in 7.1 successfully demonstrated the applicability of the integration of the 4x1 antenna with the 3D transition through S-parameter measurements. This section will investigate the radiation performance of the antenna in addition to S-parameter measurements. An 8x2 microstrip antenna array has been designed in the 3D Electromagnetics simulator HFSS for the frequency 79 GHz, another mm-Wave frequency that is predicted for the UWB mm-Wave frequencies and to be used in applications such as RSS. The schematic of the antenna is shown in Figure 81 and Figure 82. Figure 81 shows the top view of the structure, showing the 3D transition vias as the feeding point of the sub-arrays. Figure 82 shows the bottom view of the structure, zooming in on the T-match or power splitter/combiner that was designed for the array. This power combiner was optimized to have equal and maximum power delivery to each one of the sub-arrays of the 8x2 array. Chamfering or mitering of the Microstrip TL, and as discussed in 6.2.1, have been utilized here. In addition, the curving of the CPW ground at the Microstrip to CPW transition has been used, in a similar fashion to tapering the ground of the CPW as in 6.1.1. As a result, the performance at the design frequency is optimum with minimum reflections on the bottom or at the T-match and a dominant mode for the antenna array. This is shown in Figure 83.

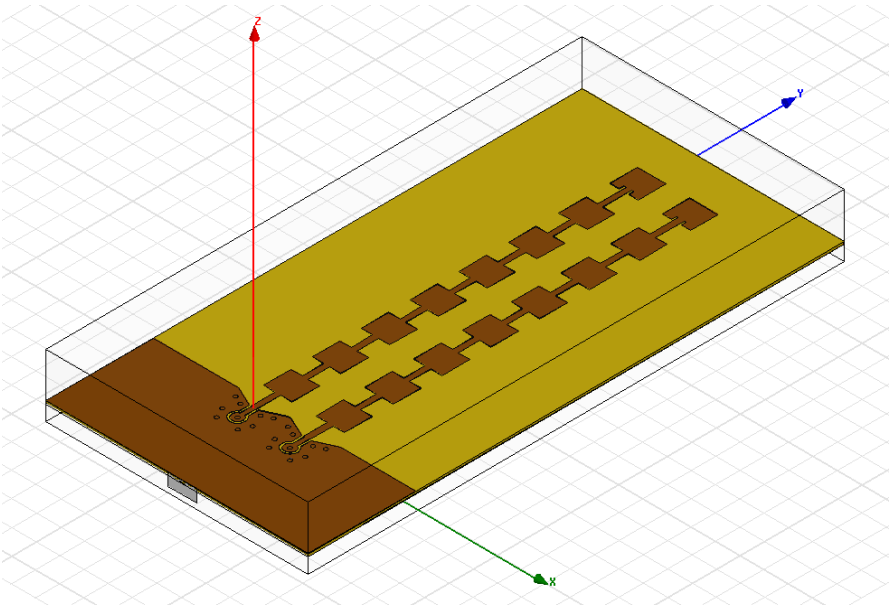

Figure 81. Schematic of the 8x2 prototype array with 3D Transition (Top View).

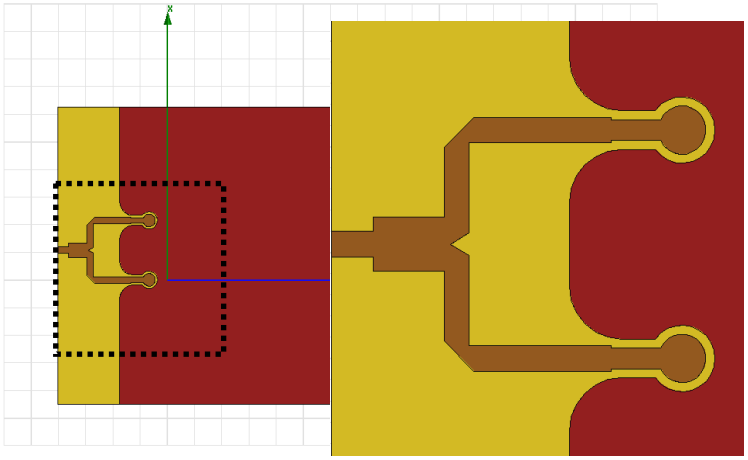

Figure 82. Schematic of the 8x2 prototype array with 3D Transition (Bottom View).

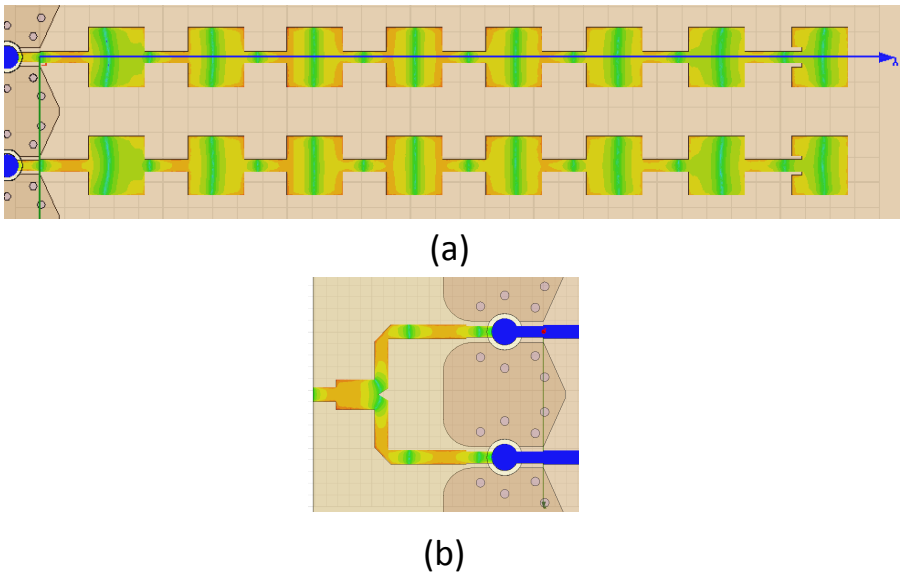

Figure 83. E-field distribution at 79 GHz for the integrated 8x2 antenna array with the 3D transition (a) top view and (b) bottom view.

However an additional step had to be taken in order to measure the radiation performance. The reason for this is that the receiver inside the mm-Wave antenna chamber is not capable of hosting a probe station and alternatively has standard waveguide connectors. For this purpose a microstrip to waveguide transition was built.

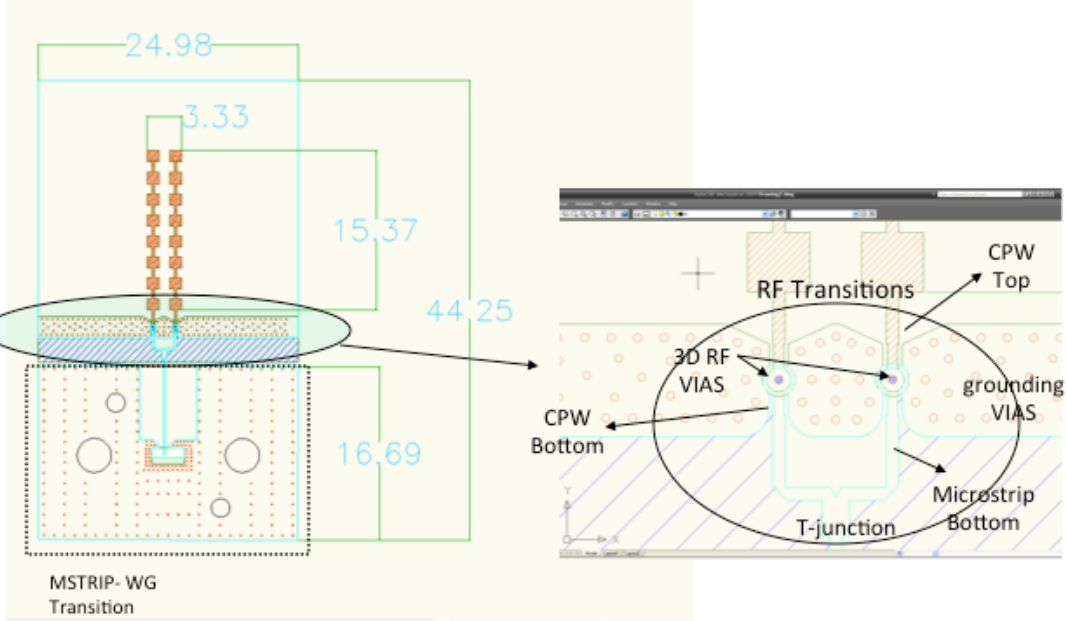

Figure 84. Artwork of the integrated 8x2 antenna array with 3D transitions or antenna under test (AUT).

Figure 84 shows the artwork for the 8x2 integrated antenna array with the 3D transition or simply the antenna under test (AUT) highlighting the microstrip to waveguide transition and detailing the rest of the structure. Figure 85 shows the WG-Microstrip transition part of the circuitry that was used to connect mechanically to the WG connector. A WR-10 WG connector is shown connected to the AUT in Figure 86, and which is in turn connected to the receiver of the mm-Wave antenna chamber through other WG adapters.

The fabricated AUT is seen in better detail in Figure 87. While the quality of the fabrication was generally good, some over-etching occurred on the bottom part of the AUT and can even be seen with the naked eye around one of the 3D RF transitions. Although the over etching took place in a strategic place in the design, both the S-parameters and gain results were within the 5% error margin from the ideal (simulations). That can be seen in Figure 88 and Figure 89 for the S_{11} and gain results respectively. It

can be noted that the S_{11} covers very well the design frequency of 79GHz (~-15dB). The gain (H-plane) was measured for the calibrated frequency of 80GHz. It is to be noted here that some loss compensation had been taken into account in the measurement plot of the gain in Figure 89. This was due to the added loss that is presented by several WG connections as well as the WG-Microstrip transition seen in Figure 86.

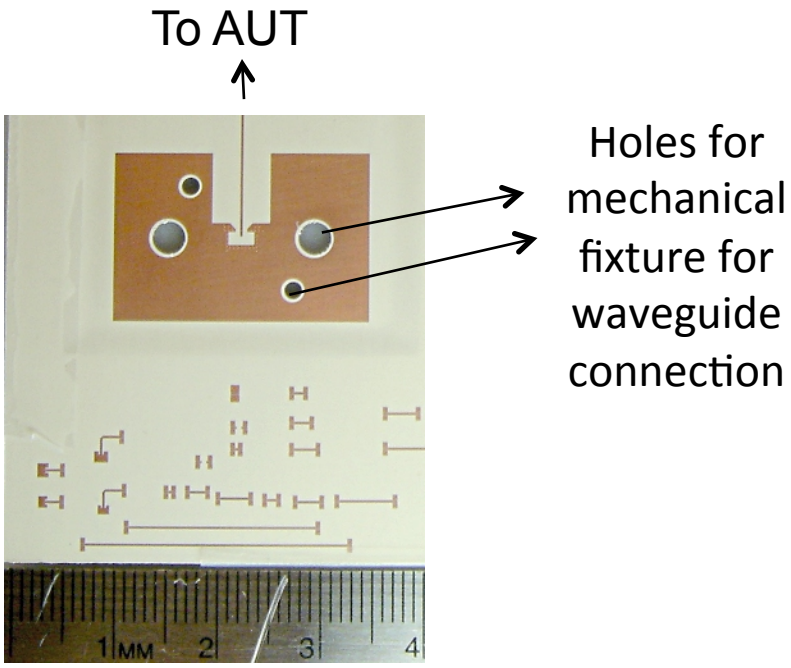

Figure 85. Microstrip-Waveguide Transition for radiation measurements in the mm-Wave Antenna Chamber.

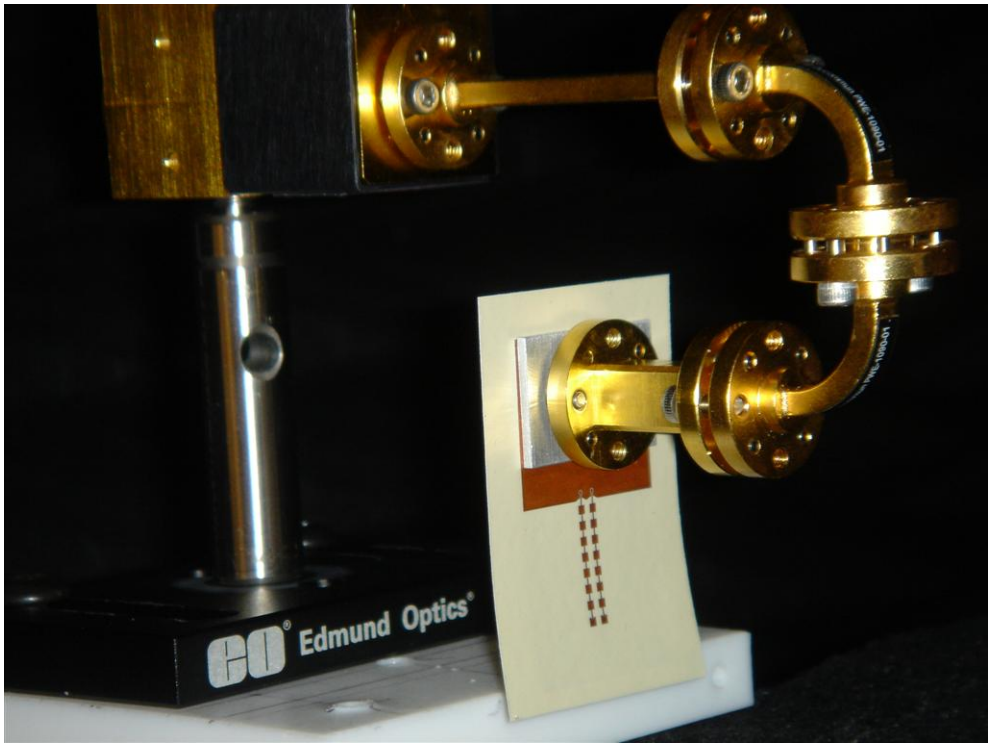

Figure 86. Photograph of the AUT with the Waveguide connected in the mm-Wave Antenna Chamber.

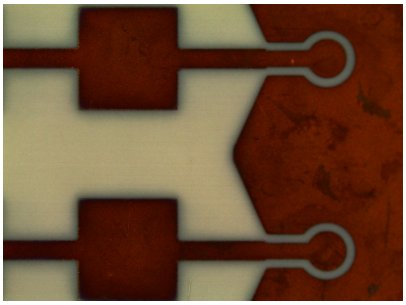

(a)

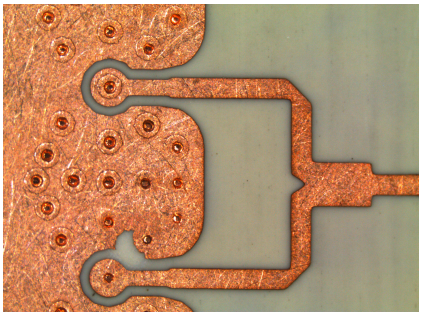

(b)

Figure 87. Photographs of the fabricated AUT (a) Top View and (b) bottom view.

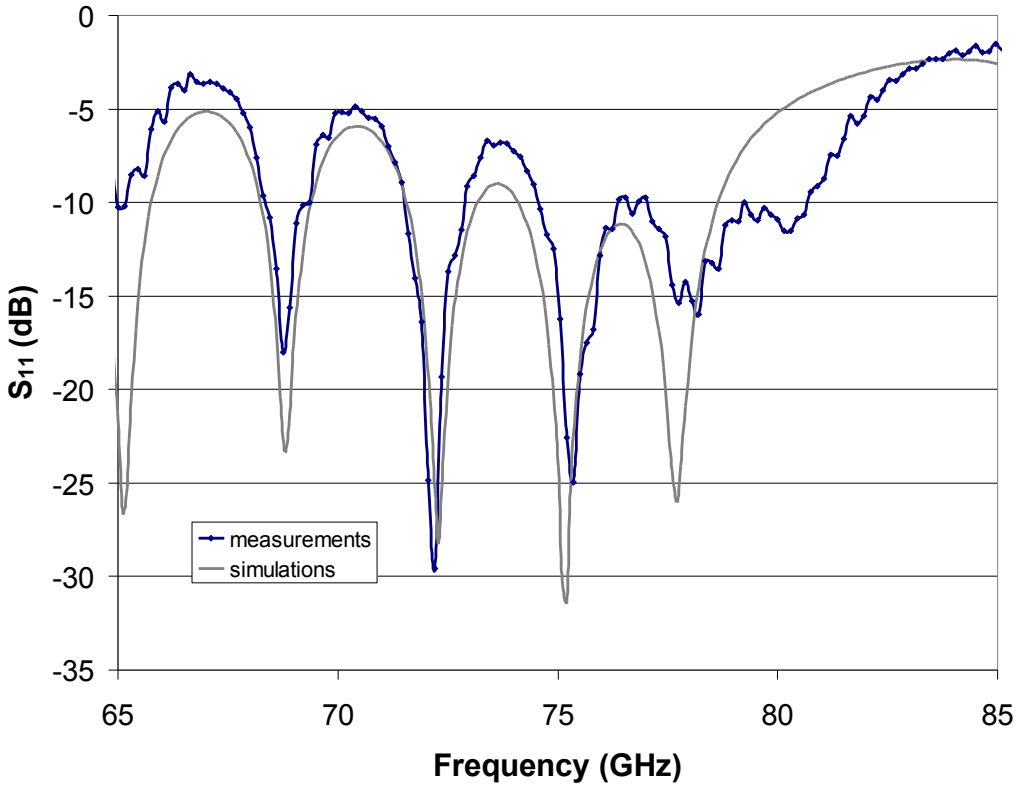

Figure 88. S_{11} results for the 8x2 AUT.

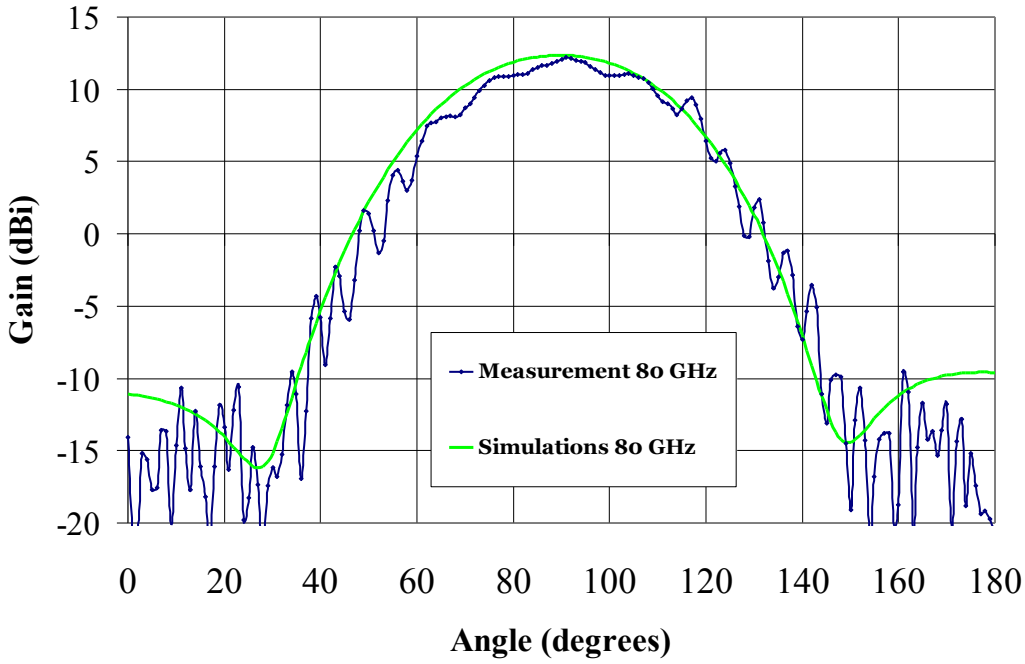

Figure 89. Antenna Gain results for the 8x2 AUT.

This section supports the ideas and concepts of surrounding the 3D transitions with antenna arrays. This integration is especially useful at mm-Waves since the generation of power is extremely challenging and hence preserving the available signal strength should be achieved by optimum designs. This configuration has the potential to block radiation due to: mismatch between the feed lines, PA (non-50 Ω) or other active circuitry, and any segment ~ λ/2. In addition, the ground also acts as a shield that improves isolation and may also be utilized as a thermal dissipater for the T/R module mounted on the backside. This general idea can be expanded to large arrays such as an eight-channeled array shown in Figure 90 and Figure 91. In these layouts the phased arrays can be placed at the 3D transition interface on the bottom layer where they can be programed in a certain way to create automatic beam steering.

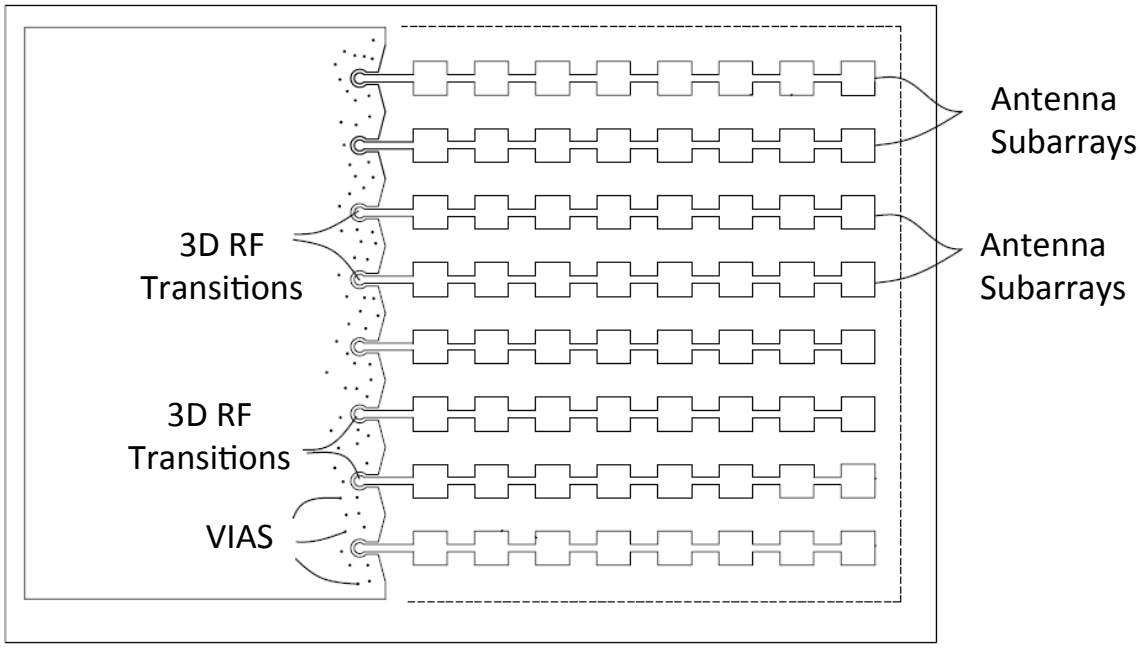

Figure 90. Top view of the schematic of an eight-channeled phased array concept.

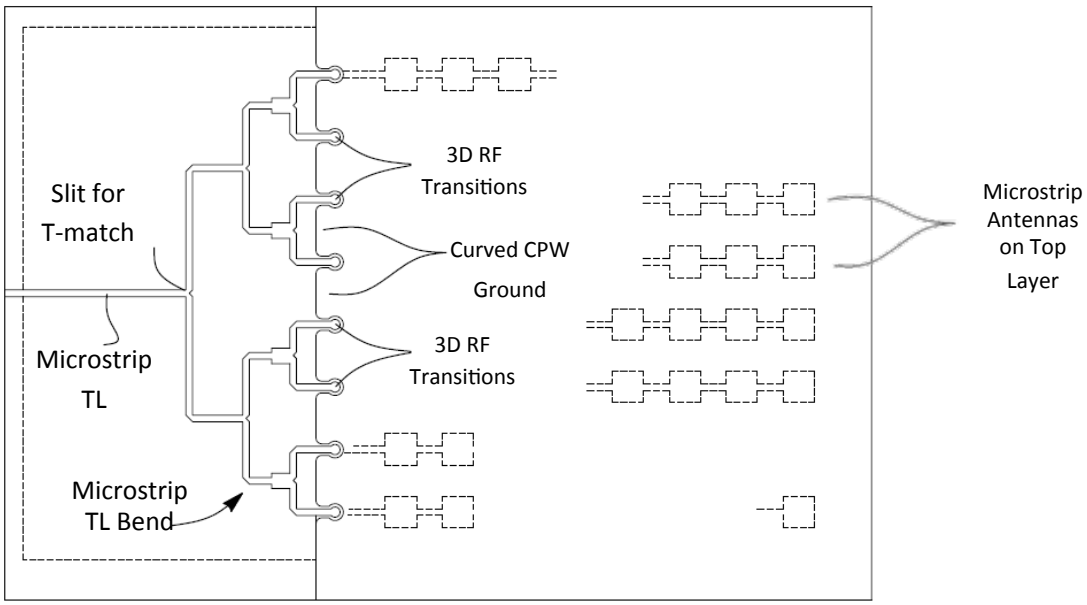

Figure 91. Bottom view of the schematic of an eight-channeled phased array concept.

Chapter 8.

Isolation/Crosstalk Reduction Mechanisms for mm-Wave Interconnections and Transmission Lines

Crosstalk is a serious issue in EMI/EMC and becomes a threat to signal integrity at higher frequencies. Crosstalk may deteriorate signals severely at mm-Waves since RF power is limited. This chapter discusses crosstalk issues where high frequency interconnections may suffer. This happens when the transmission lines are closely spaced; a condition that is more likely to happen in mm-Wave frequency regions due to the size of the wavelength. Several recommendations are given in each section for reducing crosstalk or improving isolation.

8.1. Microstrip TL Crosstalk analysis and Reduction

This section focuses on the crosstalk caused by microstrip TLs. To illustrate, Figure 92 shows the E-Field distribution of two neighboring microstrip TLs. It is evident that crosstalk becomes significant in cases where the spacing C (center-to-center) is small. Figure 93 gives a definition of backward and forward couplings to be used in this chapter.

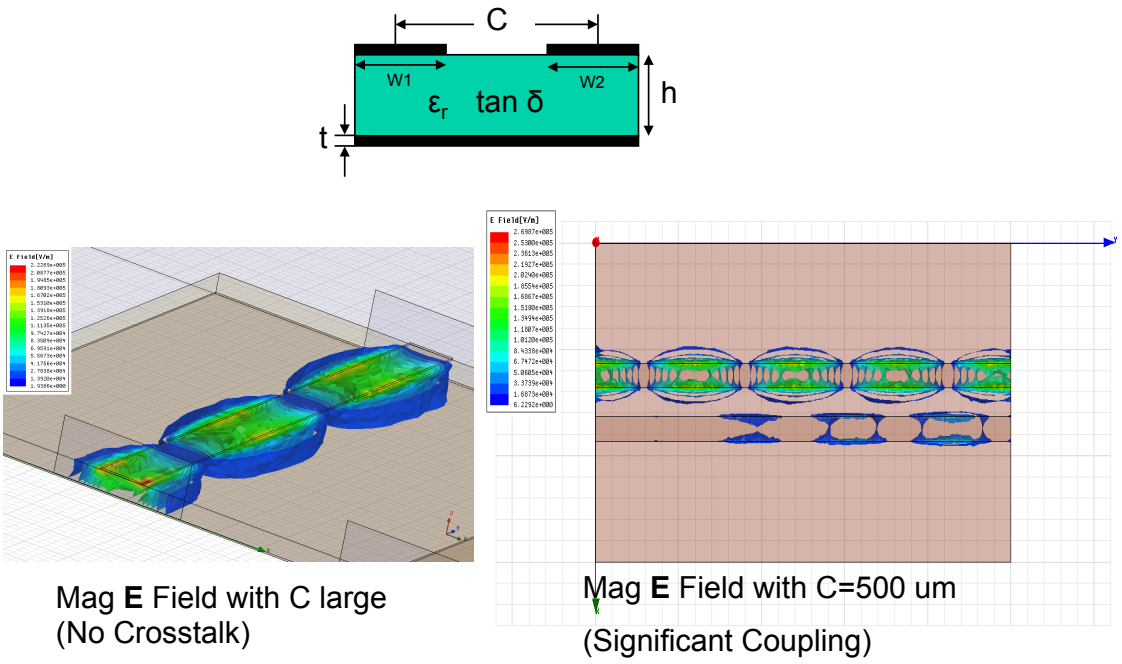

Figure 92. Demonstration of Microstrip TLs and E-Field distribution for different separations at 76.5 GHz.

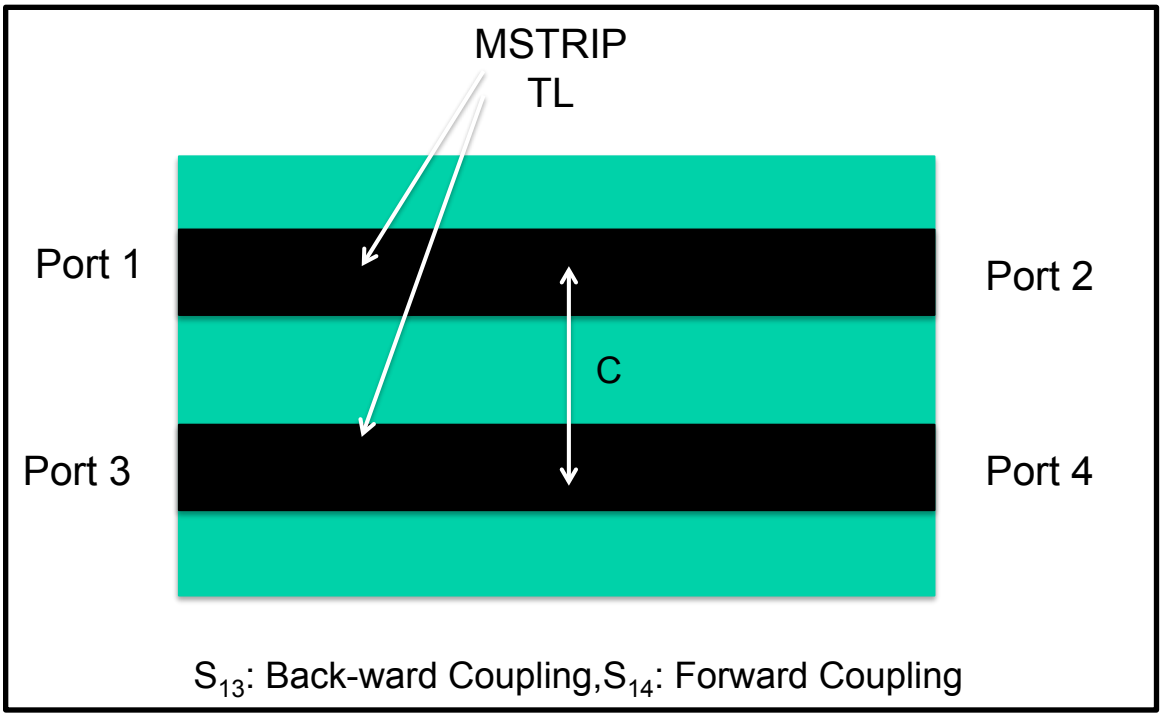

Figure 93. Illustration of Forward and Backward Coupling.

A simple yet effective method is the addition of a wall of vias in between the two neighboring TLs. A schematic of this suggestion and a schematic of the EM model are shown in Figure 94. The vias were modeled as solid copper cylinders and are connected on the topside of the substrate; which has been removed in the illustration of Figure 94 in order to show the details of the vias. The crosstalk value continues to increase with frequency at a constant spacing C as depicted in Figure 95, and is more critical for forward coupling than backward coupling. Also shown in Figure 95 is that a significant crosstalk reduction can be achieved through the addition of a via wall in between the two adjacent microstrip TLs. A 7dB and 5 dB reduction in the forward and backward coupling respectively was achieved at 80 GHz for C=650μm, a length of MSTRIP TL of 600μm, via radius of 100um and a via spacing (center-to-center) of 750μm.

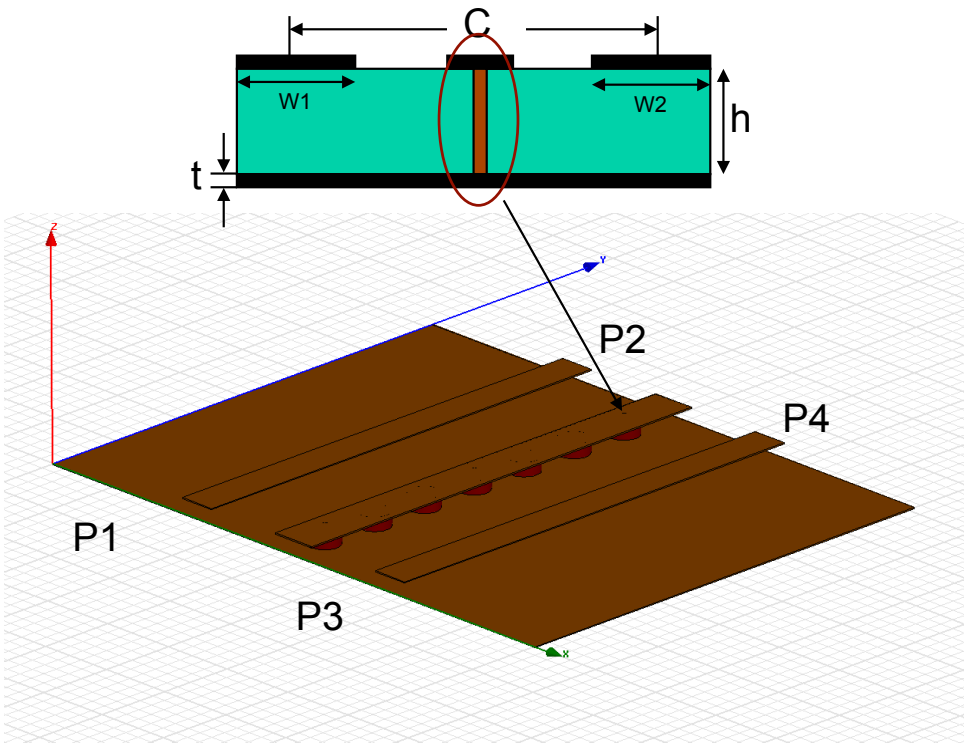

Figure 94. Crosstalk reduction by adding a wall of vias in between the Microstrip TLs.

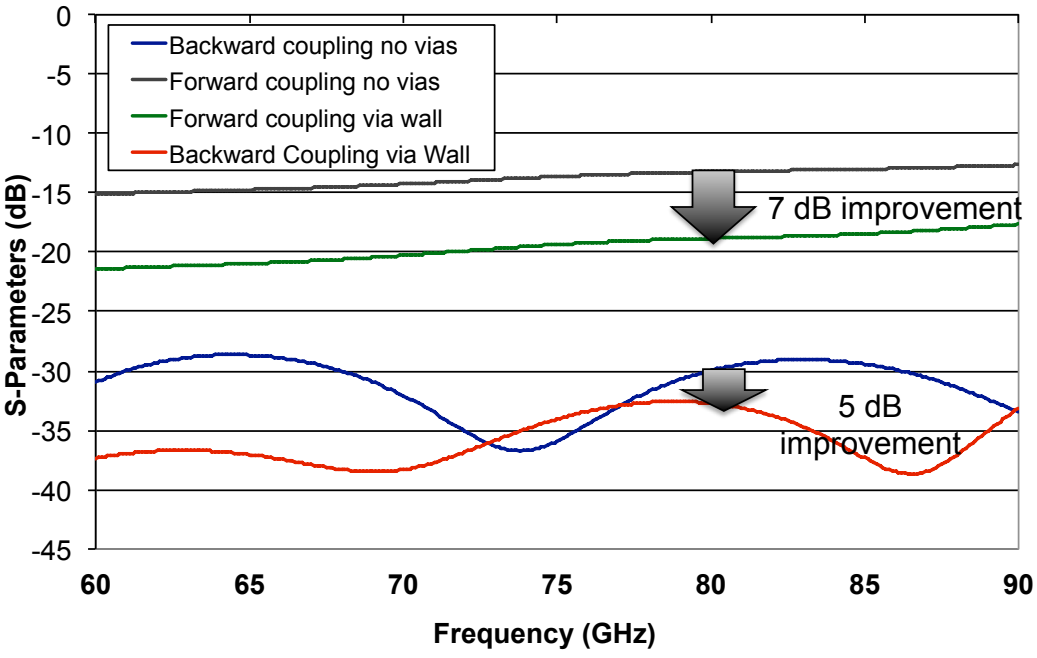

Figure 95. Forward and Backward coupling improvement through the placement of a via wall.

Detailed analysis was performed on the center-to-center via separation distance in order to find the optimum performance or lowest crosstalk for two neighboring microstrip TLs. The results are presented in Figure 96 for the backward coupling or S_{14} and while keeping C constant at 600µm. It is observed that a via separation of 750µm need to be maintained as a minimum center-to-center via separation. In order to find the optimum number of vias while keeping minimum number of vias for low cost purposes, a similar analysis is required for every line-spacing (C). The forward coupling or S_{14} is presented in Figure 97 and a similar observation concerning the via separation as in the optimum backward coupling case was made. A 32dB improvement in both backward and forward coupling levels is noticed when comparing a via separation of 1.25mm with the optimum one recommended (0.75mm) around 80GHz.

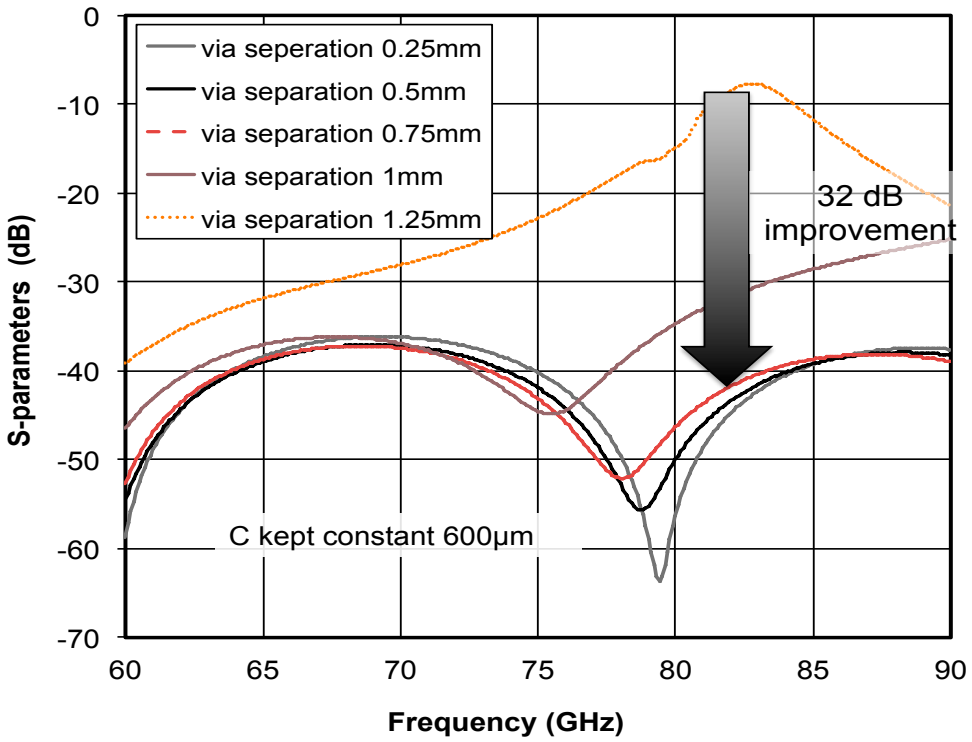

Figure 96. Backward coupling or S_{13} vs. frequency with different VIA separations for C=600 µm.

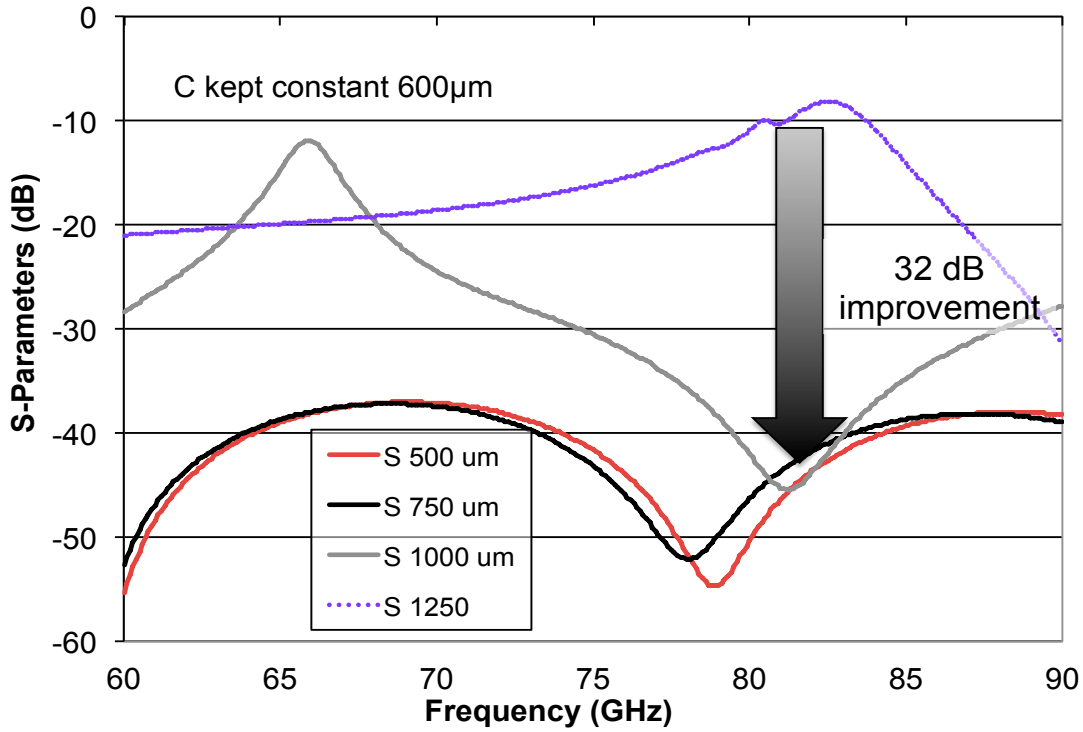

Figure 97. Forward coupling or S_{14} vs. frequency with different VIA separations (S) for C=600 µm.

In addition to the analysis performed on the via separation, a double row of vias was taken into consideration in the crosstalk analysis. This is illustrated in Figure 98 with S being the center-to-center vias spacing (this also applies for the single row of vias), xr the space between the two adjacent vias and which was kept 50µm. Figure 99 shows the backward coupling vs. frequency for difference via separations (S) for both cases single and double via rows. From Figure 99, it is not necessary to include a double row of vias since the coupling levels are comparable with those of the single wall of vias. However, as seen in Figure 100 which shows the forward coupling levels for three cases: no vias, single via wall, and a double via wall with c, a double via wall can further reduce the crosstalk by 7dB when compared with a single via wall and may be necessary depending on the level of crosstalk required. Finally, Figure 101 presents the forward and backward

coupling vs. C (center-to-center distance of the microstrip TLs) for a single wall of vias with optimum S=750µm at 76.5GHz. This figure was included in order to give a detailed analysis for the Long Range Automotive Radar frequency application.

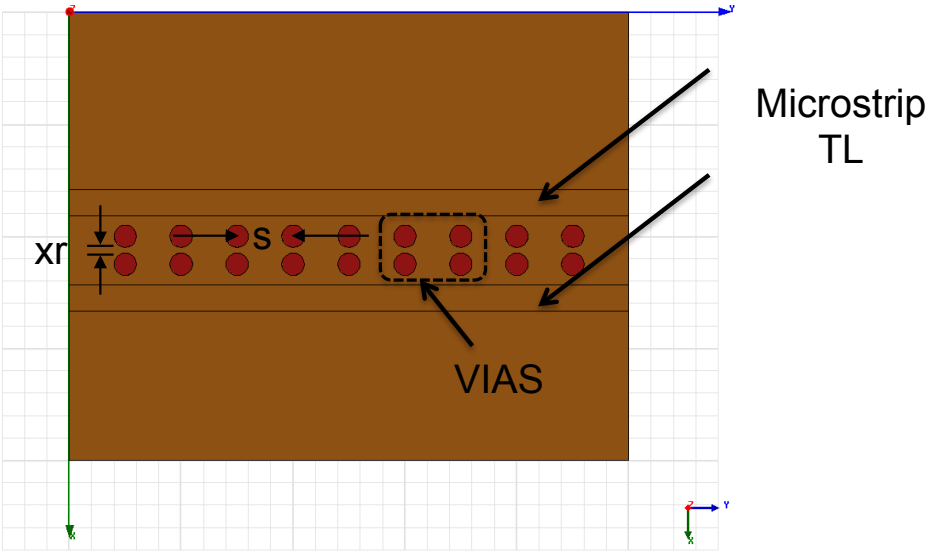

Figure 98. Schematic of the double VIA Columns for crosstalk reduction, xr was kept 50 µm.

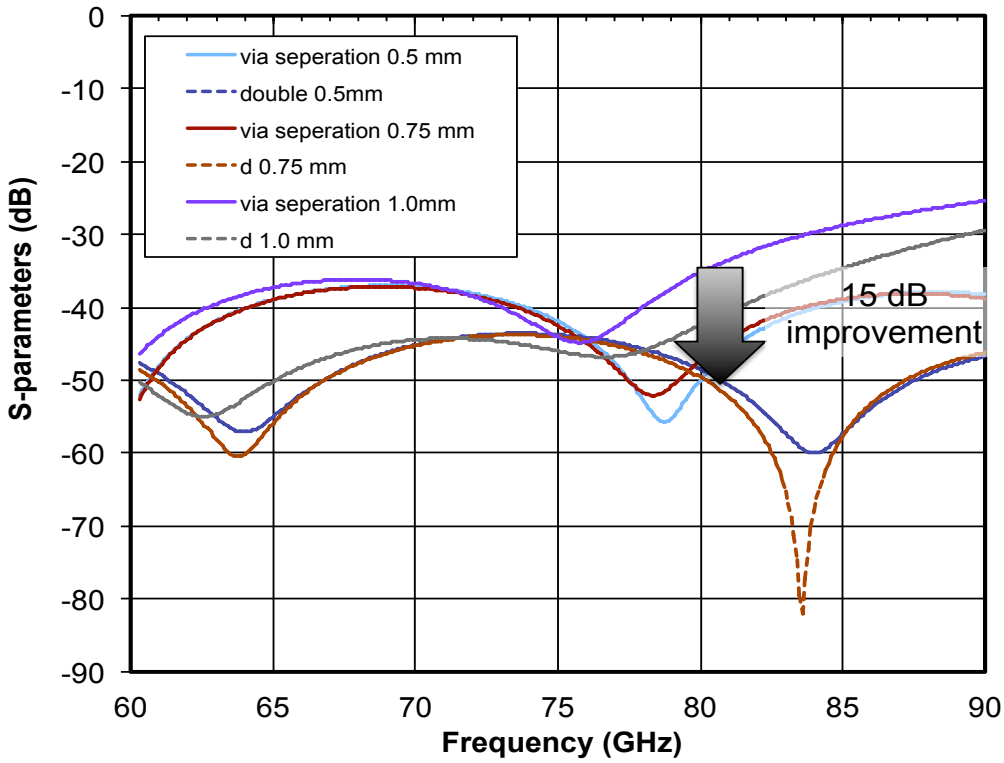

Figure 99. Backward coupling or S_{13} vs. frequency with different VIA separations for single and double via columns.

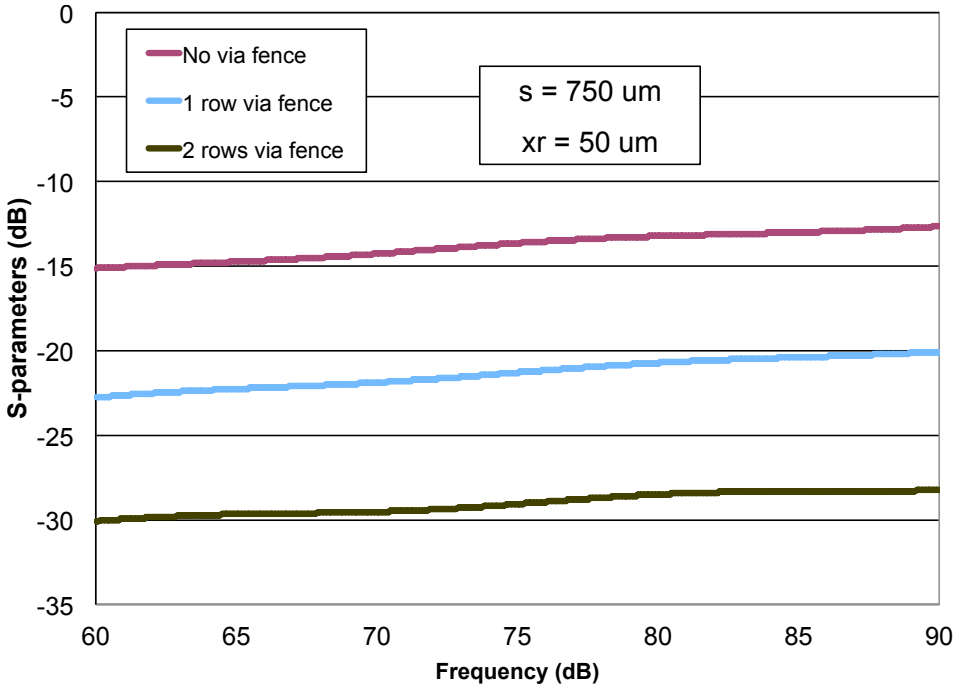

Figure 100. Forward coupling or S_{14} vs. frequency for no via fence, single and double row of vias, with s=750 µm and xr=50µm.

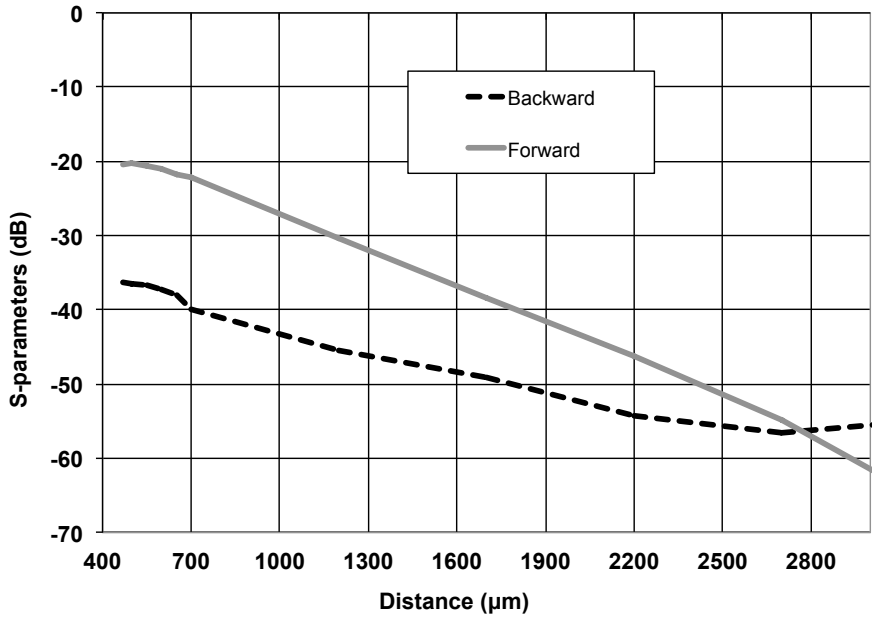

Figure 101. Forward (S_{14}) and Backward (S_{13}) Coupling analysis vs. C (center-to-center distance of the Microstrip TLs) for single via wall with S=0.75 mm.

8.2. CPW TL Crosstalk analysis and Reduction

As discussed in 1.2, CPW lines are most appropriate for flip chip assembly with T/R Modules at mm-Waves. This is illustrated again in Figure 102. An important phenomenon that the designer needs to be fully aware of is the reduction of the crosstalk among the CPW TLs. This is extremely important for the optimum operation of integrated antenna arrays with 3D transitions in order to maintain signal integrity. Figure 103 shows the schematic of CPW TLs used as a model for the EM analysis of the crosstalk. Dimensions such as via separation, ground dimensions, and common vs. broken CPW ground plane are extremely important for the crosstalk reduction mechanisms and are highlighted in this section.

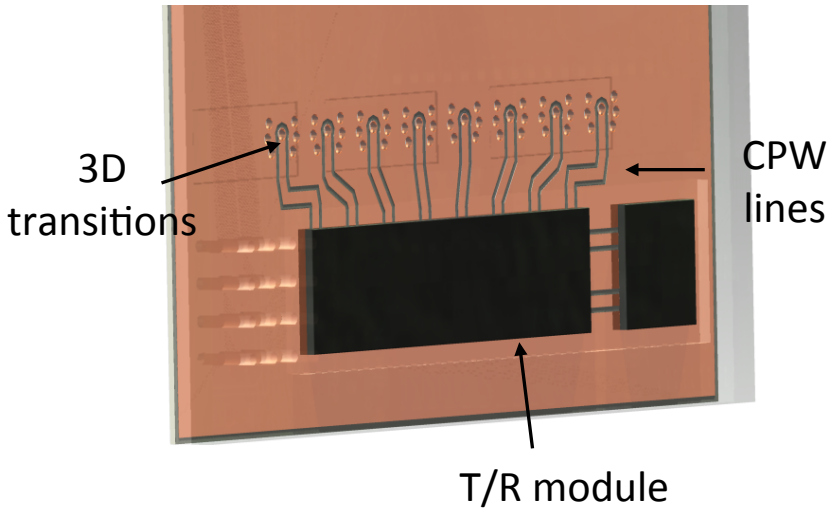

Figure 102. Schematic (back-side) of the 3D Integrated mm-Wave Radar showing the CPW interconnections.

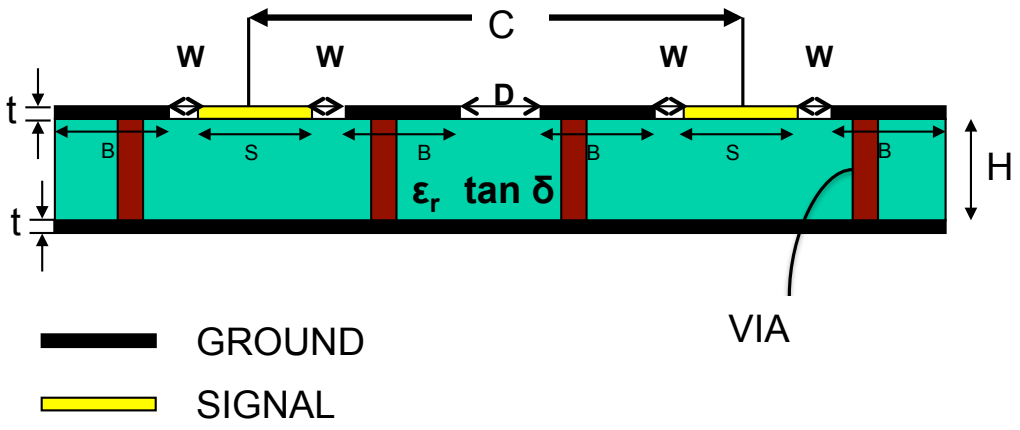

Figure 103. Schematic of CPW lines used for modeling crosstalk reduction.

The first step in the crosstalk analysis for the CPW lines was to determine whether to use a common or broken ground for the top layer. It was found that an optimum performance is achieved with a broken ground with gap between the two CPW grounds ≥ 50μm. This is shown in Figure 104 where the backward coupling was simulated for different values of the parameter D or the gap between the two CPW grounds, which was varied from 0 (common ground) to 200μm. This broken ground configuration has also been favored by other designers [67]. Although creating a gap in between the two CPW ground plates introduces a slot line mode, it remains much smaller than the parallel plate mode induced by having a common ground.

The next step was to determine the optimum size of the top CPW ground plane. Again the backward coupling was simulated with different ground sizes this time. This is shown in Figure 105 where the parameter b (ground width) was varied from 2s to 4s; where s is the width of the CPW signal line and as indicated in Figure 103. It is recommended here that a b=3.5s to be used for optimum performance results while keeping minimum dimensions.

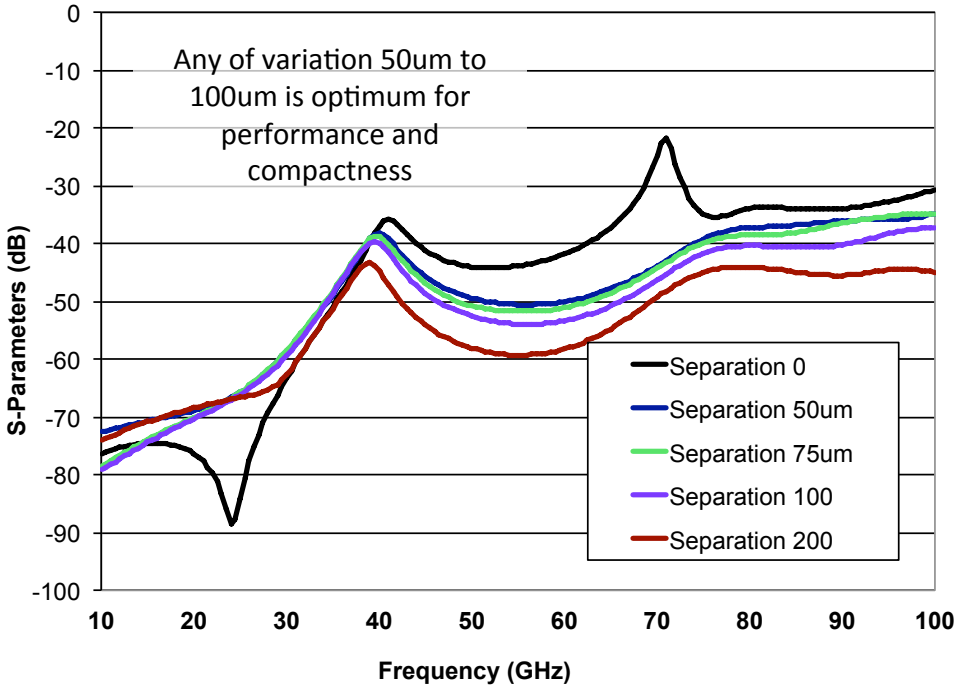

Figure 104. Backward coupling S_{13} crosstalk analysis: Ground Separation.

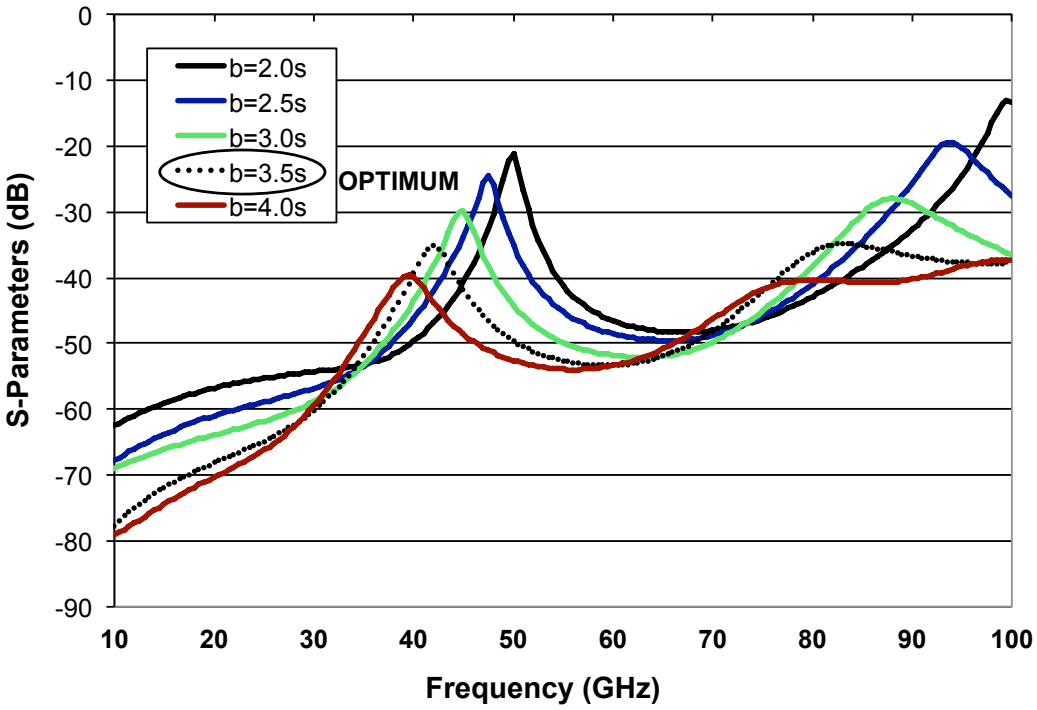

Figure 105. Backward coupling S_{13} crosstalk analysis: Ground Width.

The third and last step that was taken for the CPW TL crosstalk reduction was the analysis of vias. Single and double columns of vias were simulated and the backward and forward couplings were calculated. This is shown in Figure 106. A via separation of 425µm was chosen after rigorous simulations and was determined to be an optimum value. A 20dB improvement is observed around 80GHz for both backward and forward couplings if either a single or double row of vias is used.

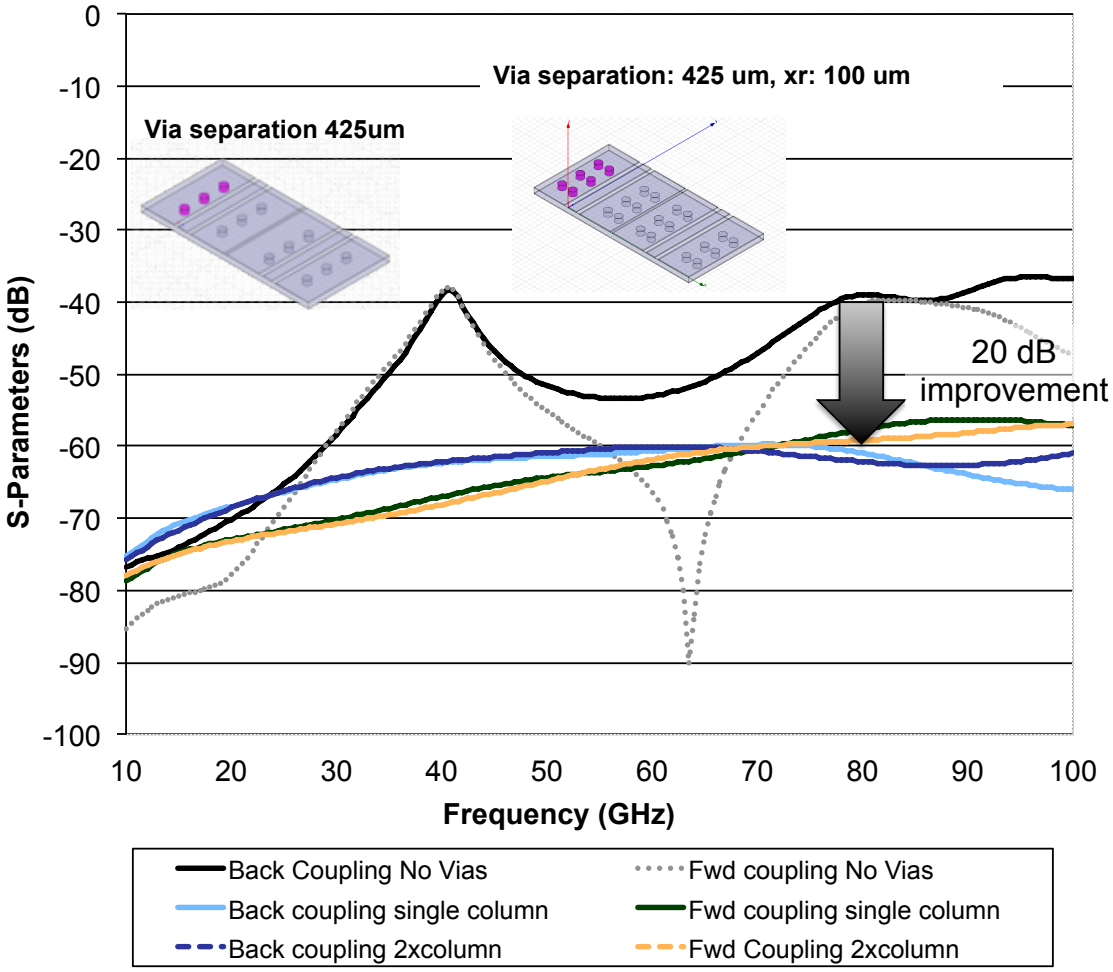

Figure 106. S-parameter summary for: no vias, single and double via rows.

Figure 107 shows a conceptual schematic of a mm-Wave RF interconnection to be used in the integrated mm-Wave architecture consisting of the interface of the CPW

interconnections with a T/R module or RFIC chip and utilizing: 3D transitions, broken CPW ground plane, single and double via fence, and varying CPW ground width for optimum RF performance.

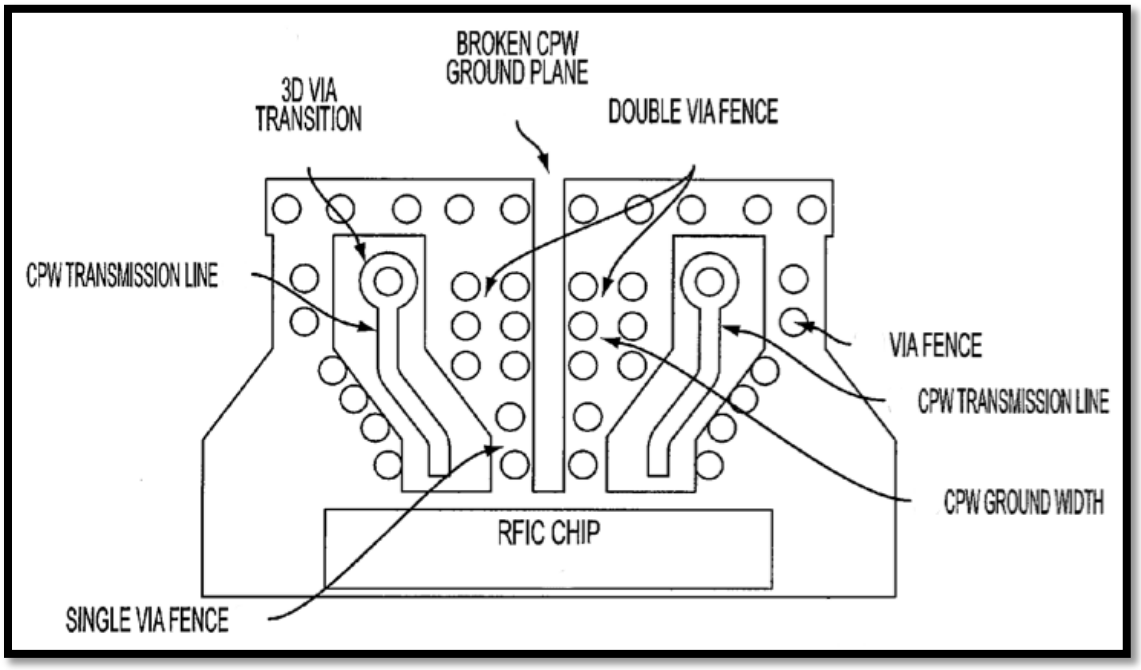

Figure 107. Schematic of interface of RF interconnections w/3D transitions at the T/R Module or RFIC showing crosstalk reduction implementation.

Chapter 9.

Novel Antenna Array Designs for mm-Wave Phased Array Applications

This chapter focuses on the antenna section of the proposed mm-Wave 3D integrated radar. It has three sections: antenna considerations at mm-Waves, edge fed microstrip antennas, and proximity coupled fed microstrip antennas with the final antenna array(s) discussing its design and realization.

9.1. Antenna Considerations at Millimeter Waves

The antenna performance is of exceptional importance at mm-Waves and large arrays become necessary. To understand why large antenna areas may be required, attention should first be given to the free space attenuation of microwaves vs. frequency. Atmospheric absorption increases by several orders of magnitude across the mm-wave band, and as a result, many mm-wave applications may require moderate to large (in comparison to multiples of the wavelength) substrates with many antenna elements to increase the radiation directivity. Figure 108 shows the drastic increase in atmospheric absorption of electromagnetic energy in the mm-wave range and illustrates the importance of efficient directive antennas.

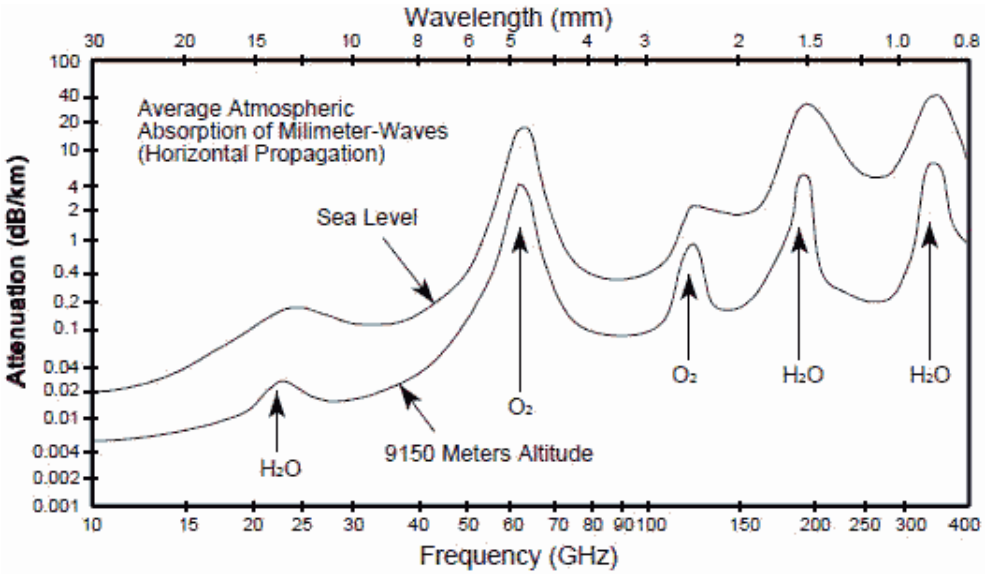

Figure 108. Atmospheric attenuation of electromagnetic energy by water vapor and oxygen as function of frequency at sea level and at an altitude of 9150 meters from 10GHz till 400GHz.

The following is a tangible example of what this atmospheric absorption means for the antenna requirements. Consider a 77 GHz collision avoidance radar, which requires antenna beamwidth of 2-3° and gain > 30 dB [26]. To obtain this gain, a theoretical minimum of 512 antenna elements is needed. This assumption is based on a single patch providing the maximum theoretically possible gain of 7 dB and each doubling of the elements providing an additional 3 dB. Using this methodology, 512 elements give an idealized maximum theoretical gain of 31 dB. However, due to several practical implementation factors such as feeding network effects, a more realistic array might require 1024 or even 2048 elements.

One advantage here that relates the size of the required board including edge clearance (required) and LCP is that LCP is not constrained by fabrication size limitations (in comparison with LTCC for example). Additional LCP benefits include the

significantly higher efficiency, the ability to be mechanically conformed, and increased mechanical durability compared to a large antenna on LTCC.

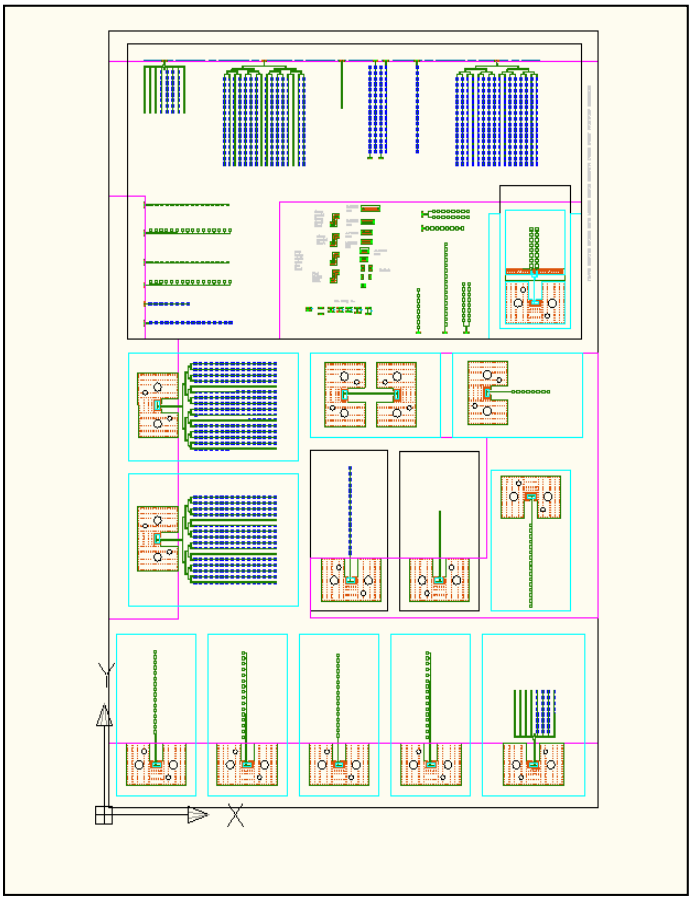

Figure 109. An 8' x 12' artwork layout for several Antenna Arrays and other RF structures on LCP. This provides a good example of how LCP can benefit from fabricating large areas which is a characteristic of a low cost fabrication technology.

Thus, for applications like short-range ultra-high bandwidth wireless communications at 60 GHz, for the previously mentioned automotive collision avoidance radar at 77 GHz, or for any application that would benefit from highly directive antenna arrays, a larger substrate area with a low dielectric constant would be beneficial. Some additional applications are for space or air-based imaging arrays and radars. For satellites, antennas on LCP could be deployable in flat panels or rolled out due the mechanical

flexibility. Aircraft could also utilize the flexible nature by conforming antenna arrays on LCP to the fuselage or other external surfaces.

The reasons for suggesting LCP as a mm-wave substrate and packaging material is related to the topics of this research. LCP is certainly not the only capable low dielectric constant substrate that can be used for antenna arrays or other microwave applications. However, in evaluating available microwave materials, LCP could be unique in its ability to create near-hermetic homogeneous multilayer dielectric laminations at a temperature (~285 ◦C) low enough to potentially package both active and passive devices in compact, vertically integrated RF modules. The environmentally invariant LCP antenna arrays previously discussed could thus have the additional benefit of enclosing all additional RF components in laminated layers below the antenna to create near-hermetic packaged mm-wave systems out of a low-cost polymer material. Antennas at mm-wave frequencies of operation must therefore be efficient radiators and the designer must take into account several critical factors [9]:

- At mm-Wave frequencies power generation is extremely challenging and DC power is costly making the antenna efficiency paramount
- Since the antenna is integrated with the chip or chip package, interconnection losses must be taken into account
- Distance to RF electronics and proximity effects to nearby materials. T-junctions may influence (undesired) radiation patterns and must be taken into account
- Matching to the T/R module
- The ability to do beam scanning
- Receiver NF and transmit power

This work aims to design, develop, and make recommendations for the automotive radar frequencies at 77GHz. In addition to that frequency, speculations about utilizing the 78-81 GHz spectrum for UWB Short Range Radar (SRR) as seen in Figure 110 have been made at the time of this research.

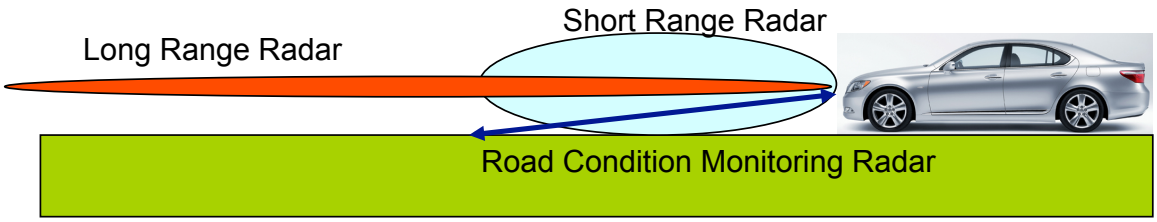

Figure 110. Multifunctional Automotive Radar showing Long Range Radar (LRR) for collision avoidance and automatic cruise control (ACC) as well as Short Range Radar (SRR) for road condition monitoring.

Among the listing of proposed improvements to the current automotive radar systems in Chapter 5 was the use of phased arrays. Owing to technologies such as SiGe [10], the integration of phase shifters and antenna arrays is close to reality. This is illustrated in Figure 111.

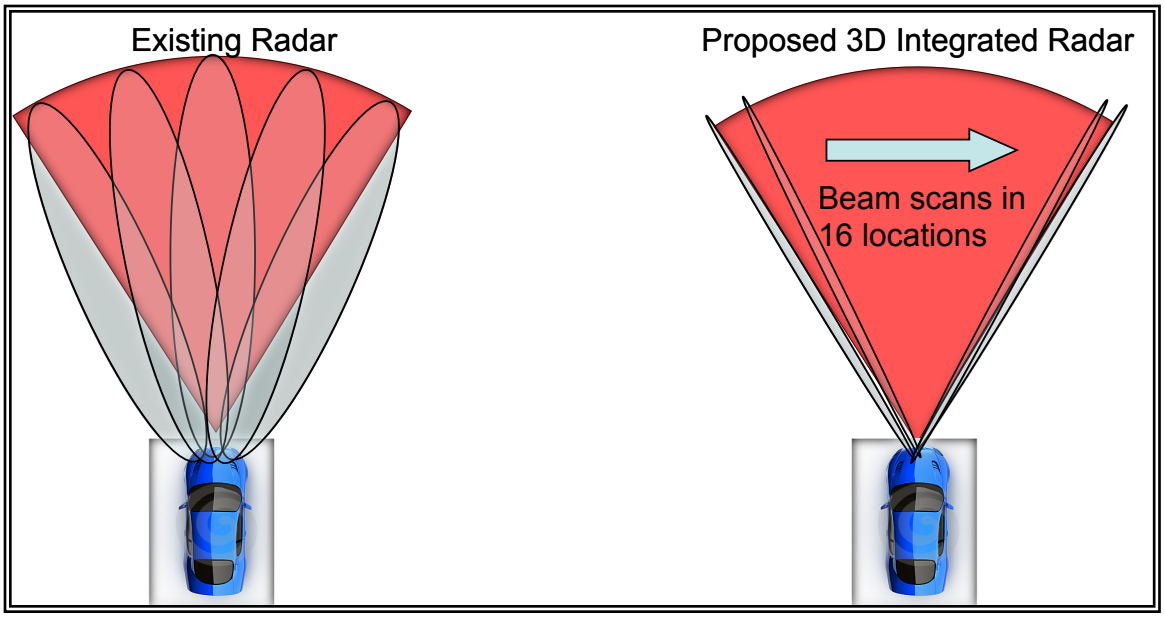

Figure 111. Comparison between the existing Radar (switched beam) and the Proposed Automotive Radar using phase array antenna.

9.2. Edge Fed Microstrip Antennas

There are many configurations that can be used to feed microstrip antennas. The four most popular are: microstrip line, coaxial probe, aperture coupling, and proximity coupling. All of these have been considered with the exception of coaxial feeding since it is not appropriate for the array to be developed as depicted in the proposed architecture in Figure 56. The simplest type is the edge fed microstrip antenna and is shown in Figure 112. With h=4mils, $h << \lambda_o$ which is one of the main requirements for microstrip antennas. It is to be noted that Equation 11 and Equation 12 apply here as well.

Equation 13 describes the additional effective length (which sums up to be greater than physical dimensions) as a function of effective dielectric constant $\in_e$. Equation 14 is the design equation to find the parameter L. After taking ΔL into account in the element design for the effective length, an appropriate matching method; recessed

feeding as shown in Figure 113, was used. Figure 114 shows the S_{11} results for a recessed feed microstrip antenna with the parameters: L=1.05, W=1.96, W_o=0.24, xa=0.35, ya=0.2, and h=0.1016, all in mm on an LCP substrate. The BW of this antenna is 2.5%, which is typical of such microstrip feeding configurations. Figure 115 shows the gain patterns for both the E- and H- planes and also resembles a typical pattern of a microstrip patch antenna. This configuration is one of great interest especially as it is very attractive from a manufacturing point of view requiring only one substrate layer and would be an optimum configuration for a low cost solution as proposed in Chapter 5. Figure 116 demonstrates the S_{11} for two edge fed microstrip antennas with recessed feeding on 4mil thick LCP substrate designed for 77GHz and 96GHz.

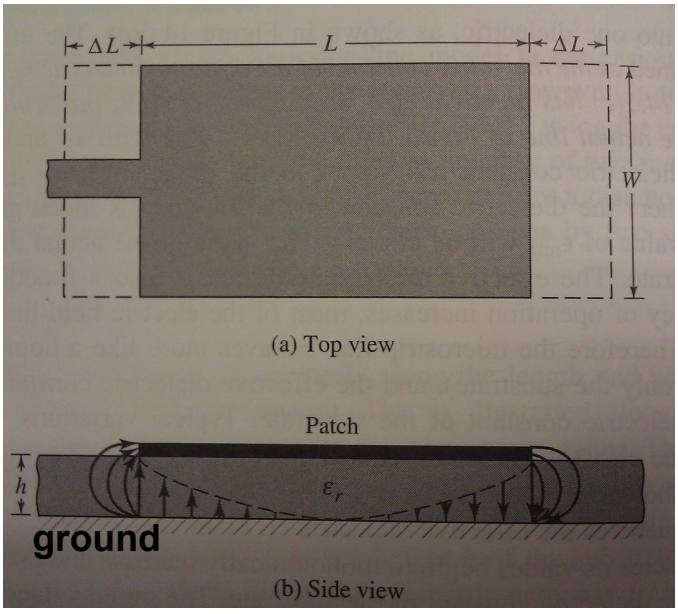

Figure 112. Physical and effective lengths of rectangular microstrip patch [68].

$$\frac{\Delta L}{h} = 0.412 \frac{(\epsilon_e + 0.3)}{(\epsilon_e - 0.258)} \frac{(\frac{W}{h} + 0.264)}{(\frac{W}{h} + 0.8)} \qquad \textbf{Equation 14}$$

$$(f_r)_{dominant\ mode} = \frac{1}{2(L + 2\Delta L)\sqrt{\epsilon_e}\sqrt{\mu_o \epsilon_o}} \qquad \textbf{Equation 15}$$

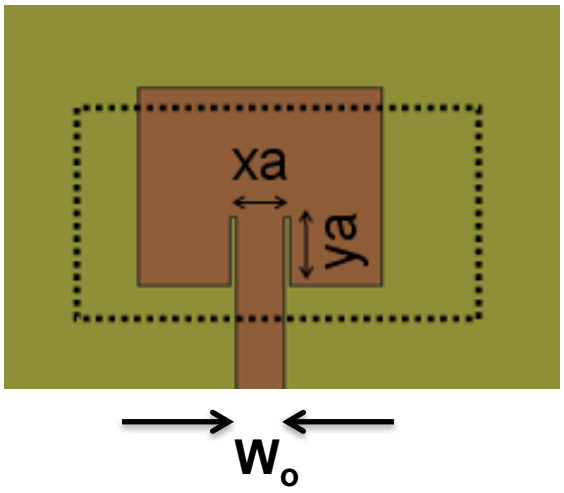

Figure 113. Illustration of recessed Feeding.

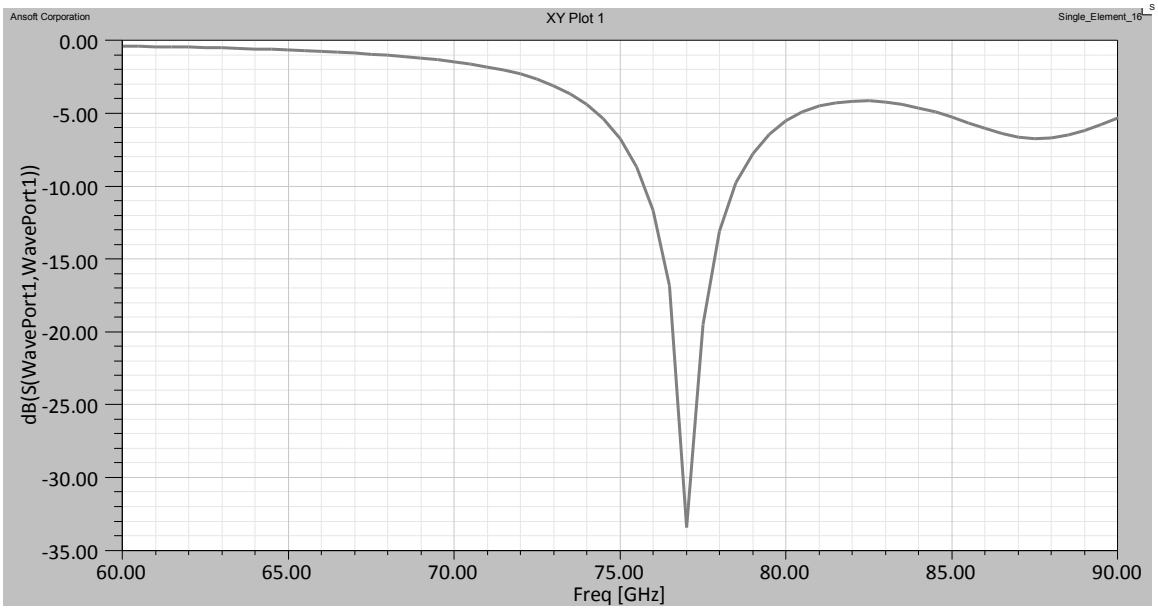

Figure 114. S_{11} vs. Frequency of the rectangular recessed feed microstrip patch (L=1.05 W=1.96 W_o=0.24 xa=0.35 ya=0.2 h=0.1016, all in mm with center frequency at 77GHz).

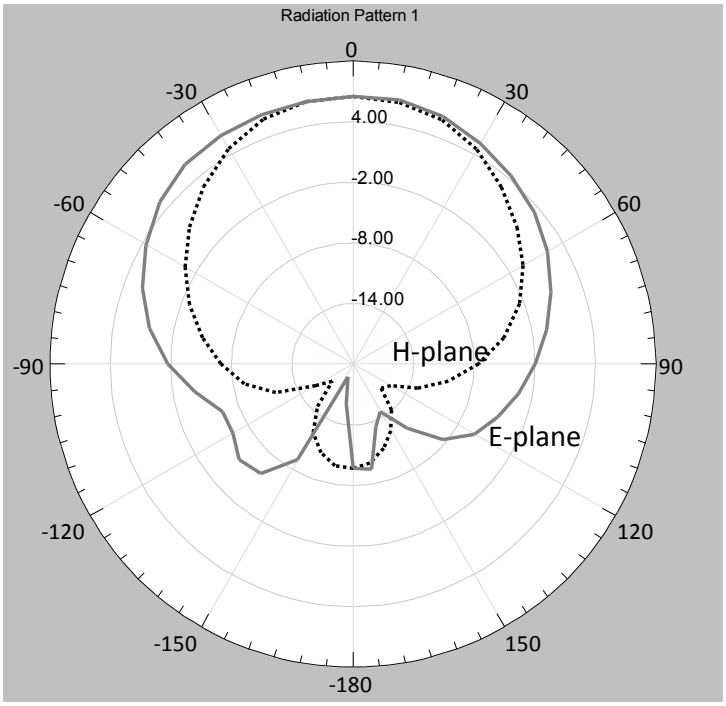

Figure 115. Simulated E- and H- plane gain patterns of the rectangular recessed feed microstrip patch (L=1.05 W=1.96 W_o=0.24 xa=0.35 ya=0.2 h=0.1016, all in mm). Maximum gain is 6.6dBi.

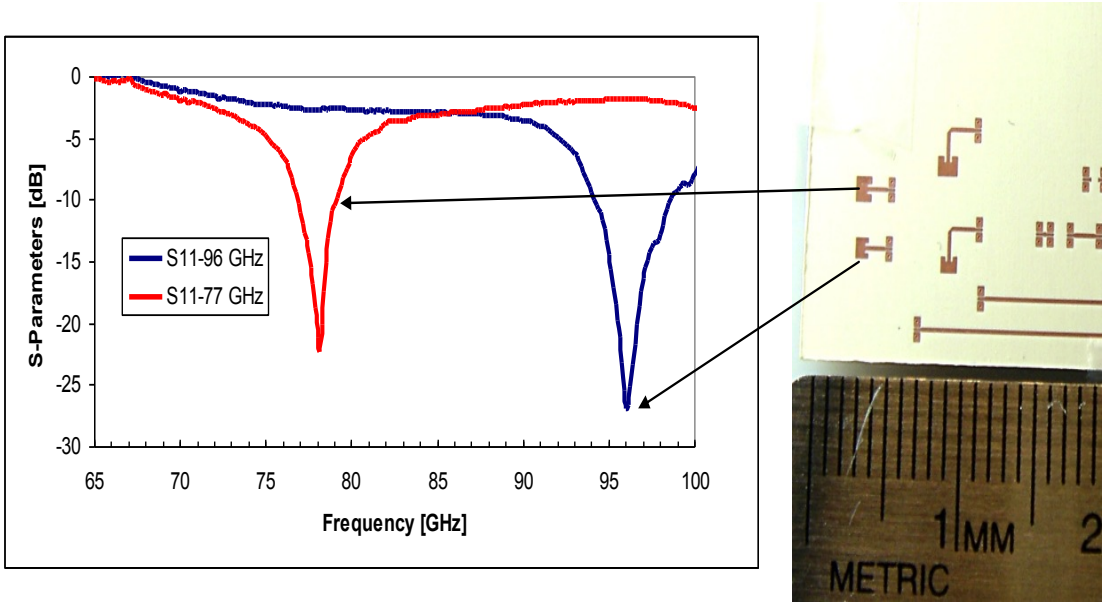

Figure 116. S_{11} Measurements for two edge fed microstrip antennas with recessed feeding on 4mils LCP substrate designed for 77GHz and 96GHz. The antennas were measured using GSG probes and the structures had a microstrip to CPW transition for probing purposes.

In addition, this recessed feed can be utilized on the last element of a sub-array of several elements that are connected in a series feed configuration such as the designs featured in Figure 79 and Figure 81. A note worth making here is that a quarter wavelength transformer could as well be used for matching the microstrip TL to the antenna element and result in better pattern characteristics; however that would not be an appropriate configuration for the proposed architecture solution with a series feed array (Figure 56).

A 16x1 sub-array of individual patch antennas of size 1.2 mm x 1 mm is designed in this section. The size of the individual element was chosen for the successful operation of the sub-array at the frequencies of 79GHz and 80GHz. The element spacing was chose to have a spacing that is close to $\lambda_g/2$ and more importantly to create an in phase excitation among all of the elements at the given design frequencies. The layout of the design and its dimensions are shown in Figure 117. This sub-array is designed on a 5 mil thick (0.127 mm) LCP with dielectric properties as discussed in Chapter 2. This is another advantage of LCP; which comes in 1mil, 2 mil, and 4mil thicknesses and with the available lamination capabilities (of any of those thicknesses) almost any practical thickness can be achieved. It is also to be noted that the metallization was modeled as non-ideal copper with a thickness of 9 μm, a common metallization thickness for mm-Wave circuitry. Although 5 μm is available as of the time of writing this thesis (a 5 μm would be more favorable for better accuracies in fabrication [69]), the fabrication houses have not yet declared it as available and mature process. The S-parameter results for the 16x1 sub-array are shown in Figure 118. These results demonstrate very good performance for the design frequencies.

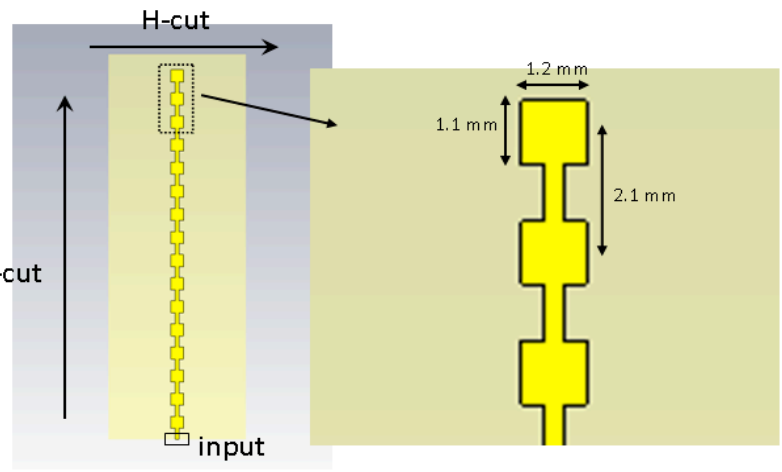

Figure 117. Layout of the 16x1 Subarray.

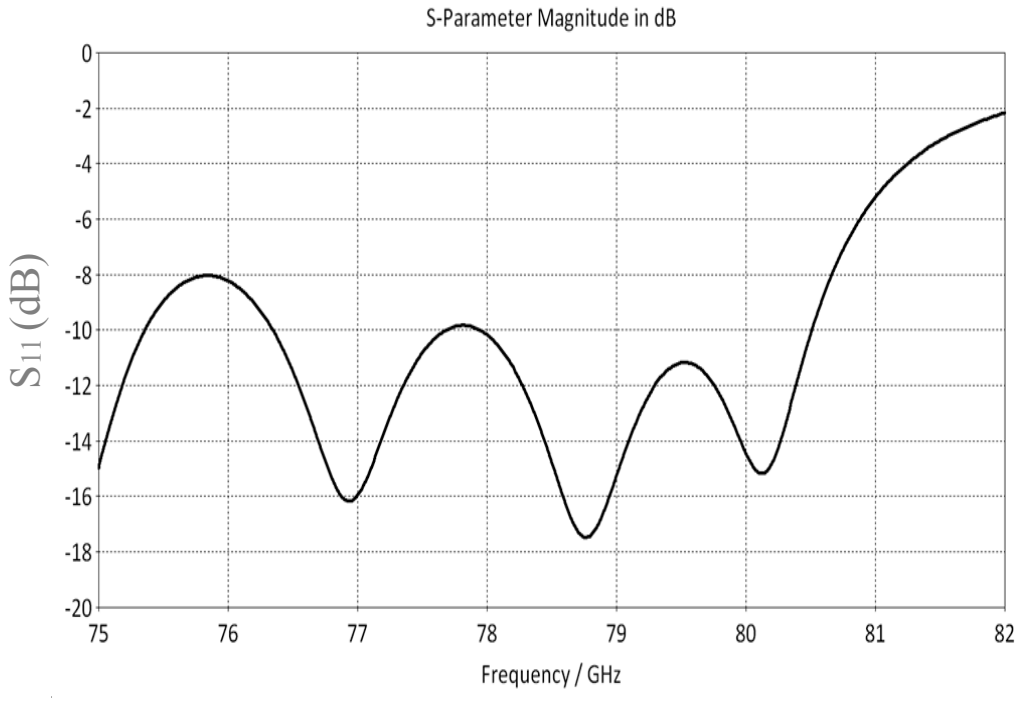

Figure 118. S_{11} for the 16x1 Sub-array shown in Figure 117.

Figure 119 shows the gain pattern for the E-cut (as defined in Figure 117). In the following figures theta denotes the elevation plane and phi the azimuth plane. The pattern shows a maximum gain of 17.8 dBi, 3dB angular width of 5.6°, and a side-lobe level

(SLL) -10.7dB. The following will focus on the 80GHz frequency but it is to be noted that the 79GHz has an equivalent good performance.

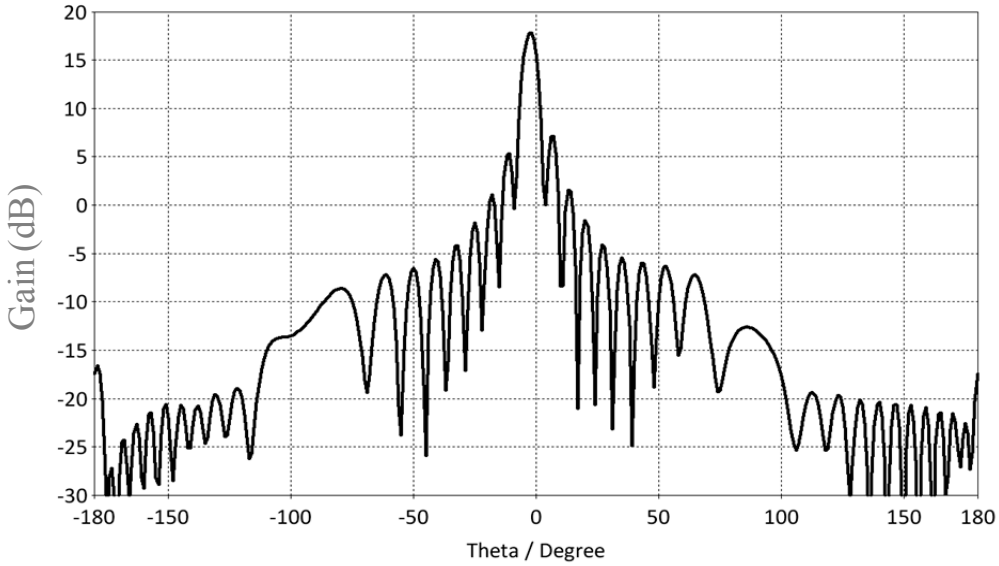

Figure 119. Gain (E-cut, Phi=90) for the 16x1 Sub-array at 79GHz.

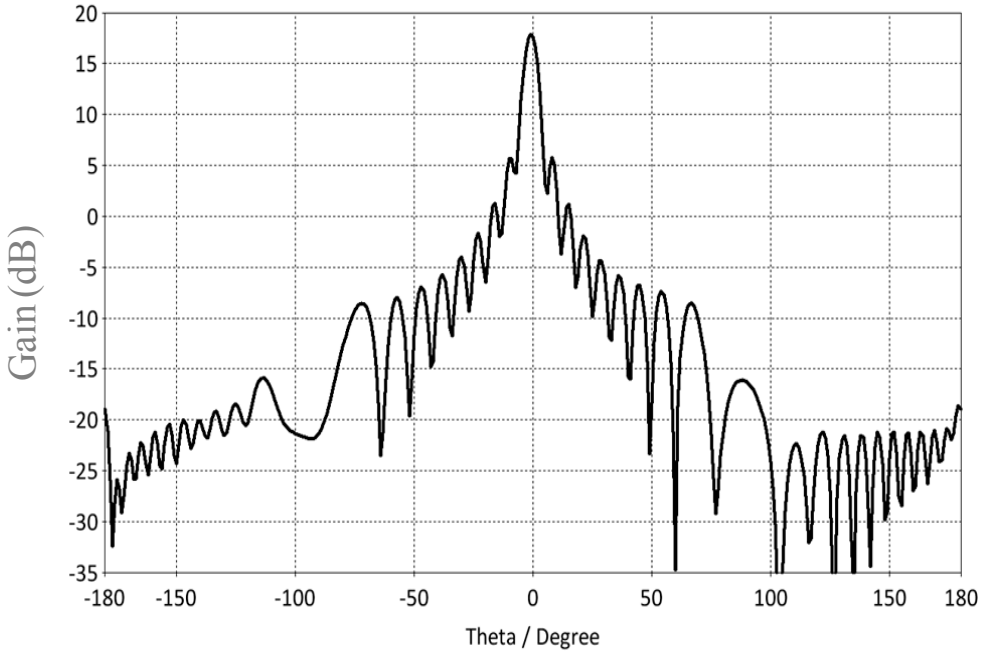

Figure 120. Gain (E-cut, Phi=90) for the 16x1 Sub-array at 80GHz.

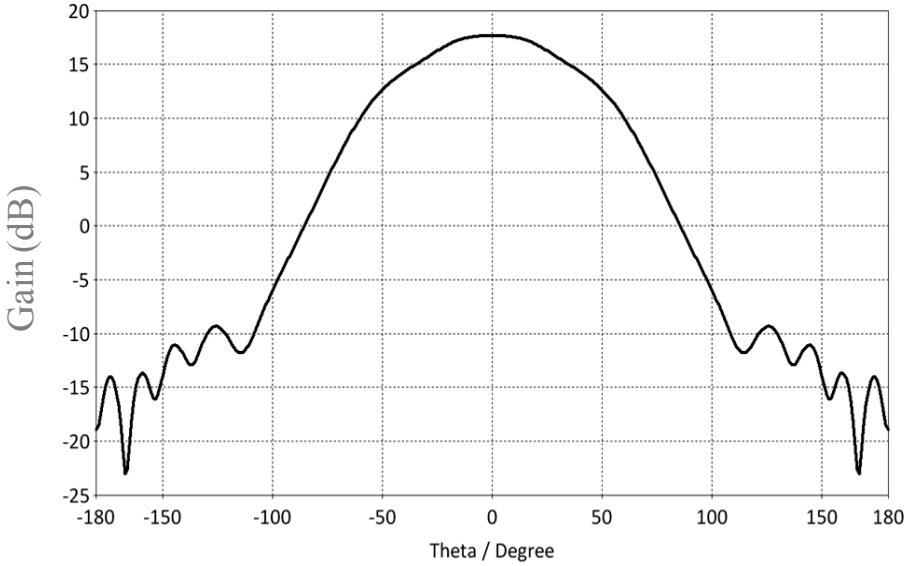

Figure 121. Gain (H-cut, Phi=0) for the 16x1 Sub-array at 80GHz.

Figure 120 shows the gain pattern for the E-cut at 80 GHz with a maximum gain of 17.9dBi, 3dB angular width of 5.8°, and a side-lobe level (SLL) -12.1dB. Figure 121 shows the H-cut (Phi=0) of the 16x1 sub-array at 80GHz with a 3dB angular width of 75°.

So far we have considered 1D arrays. At this point it is appropriate to define the Array Factor and few points about large arrays (our 2D arrays). The total field of the array is equal to the field of a single element (in this case a sub-array, for example Figure 119) multiplied by a the Array Factor AF:

$$\boldsymbol{AF = \frac{1}{N}\frac{\sin(\frac{N}{2}\psi)}{\sin\frac{\psi}{2}}} \qquad \textbf{Equation 16}$$

where:

$$\boldsymbol{\psi = kd\cos\theta + \beta} \qquad \textbf{Equation 17}$$

where N is the number or elements (in this case the number of sub-assays), k is the wavenumber $2\pi/\lambda$, and d is the center-to-center spacing between adjacent sub-arrays or channels. Θ here is the elevation angle and is depicted in Figure 122 where each of the grey rectangles represents a sub-array or an element of the larger array. β is the phase delay between the elements and is the element responsible of resulting in beam scanning. For instance, in order to obtain a beam tilt of Θ=10°, a progressive phase delay of β=0.6 rads or 34.5° needs to be applied at the input of each sub-array.

An example of a 16x16 array is presented in Figure 123 and Figure 124. This also represents the ideal case or the implementation of the 16x1 sub-array in a full array configuration and is the proposed solution to the radar architecture (Chapter 5). In this case N=16, d=0.5λ at 79GHz or 1.9mm, and β and Θ are zero since we don't require a beam tilt. Figure 123 shows the current distribution at 79GHz revealing good uniformity among the elements of a sub-array. Figure 124 shows the E-cut (which closely resembles the radiation pattern or E-field of the single element or sub-array) and the H-cut, which in this case closely resembles the array factor. One can also notice the higher side lobes by the E-cut due to the non-idealities of the fields resulting from the series connection of the sub-array when compared with that of the H-cut or the array factor. If the maximum radiation of the array is required to be oriented at an angle Θ_0 ($0° \leq \Theta \leq 180°$), the phase excitation β between the elements would have to be adjusted so that $\psi = kd\cos\theta + \beta|_{\theta=\theta_0} = kd\cos\theta_0 + \beta = 0 \Longrightarrow \beta = -kd\cos\theta_0$. For an orientation Θ =10°, β would have to be = 0.6 radians or 34.5°. Achieving this value of β would be the job of the phase shifter or the T/R module as suggested in Chapter 5.

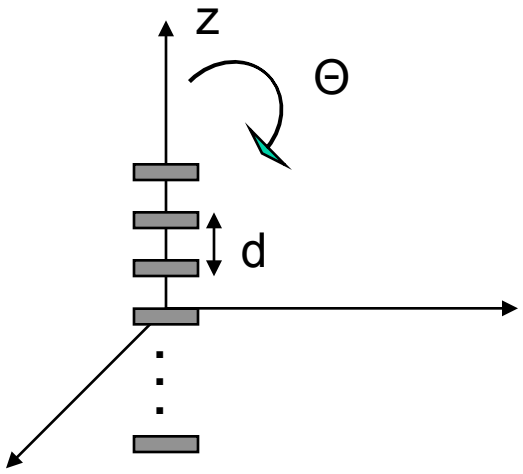

Figure 122. Illustration for the phase shift concept, Array Factor.

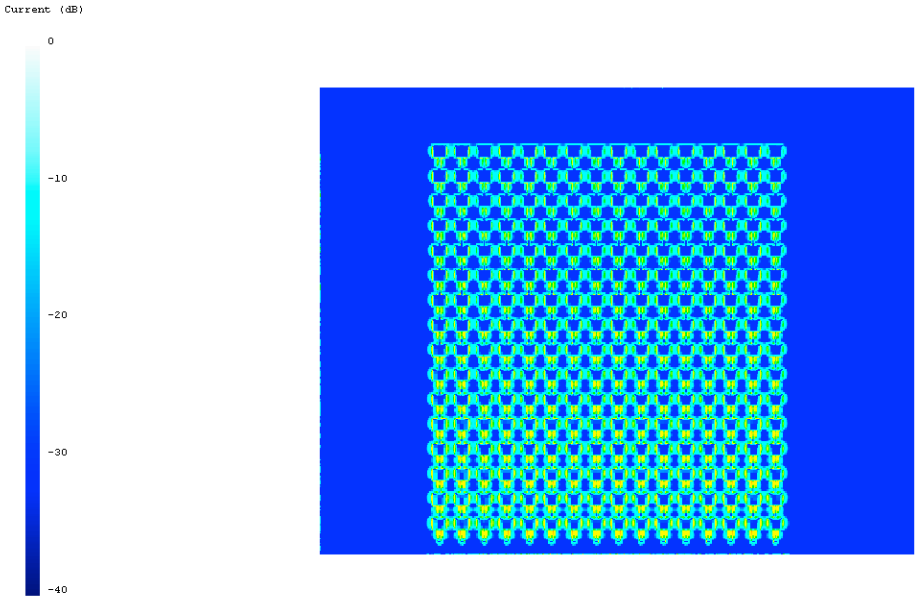

Figure 123. Surface Currents for 16x16 array showing uniformity in distribution among all elements.

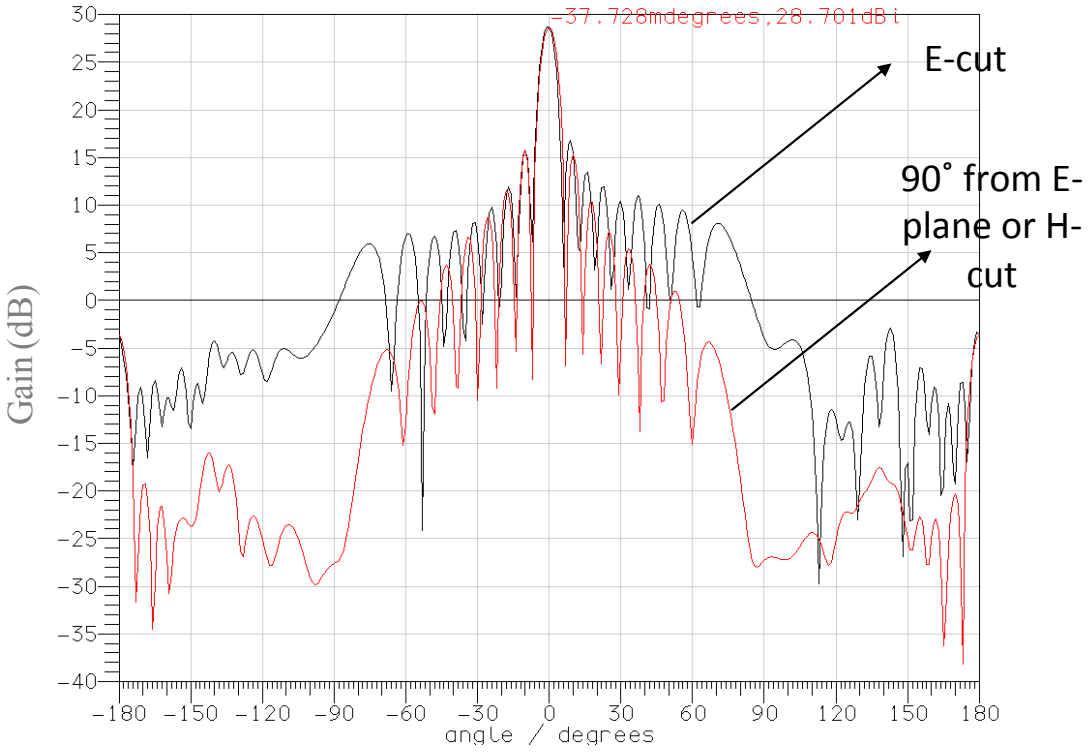

Figure 124. Gain (ideal) for the 16x16 array at 79GHz showing E-cut and H-cut.

Table 6 provides the simulated values for the gain for 16x1, 16x8, 16x16, as well as 16x32 elements. In ideal cases (lossless) a 3dB increase would occur when doubling the amount of elements. Here it is shown with some non-idealities due to the modeling of lossy substrate (tan δ) and non-ideal metal (copper with σ=5.8E7 Siemens). An ideal phased array antenna may utilize phase shifters at the input of each channel or sub-array, which is also ideal for lower loss performance since the signal gets amplified right before/after it, gets transmitted/received and without being severely degraded by the rest of the RF Front-End. An ideal 16x32 array with center-to-center spacing of 1.9mm of adjacent sub-arrays was simulated for a total gain of 31.5 dBi at 80 GHz and a SLL of -12dB.

Table 6. Gain (dB) for ideal array configuration at 80GHz.

Structure	Gain (dB)
16x1	17.8
16x8	25.9
16x16	28.7
16x32	31.5

The large array uses a hybrid of series and corporate feeding networks where the sub-arrays' individual elements are connected in series while the sub-arrays are connected in a parallel configuration (corporate network). This can be seen in Figure 127. Each of the T-junctions of the feeding network has been designed for optimum power division/combination as shown in Figure 125. The S-parameters are shown in Figure 126 with S_{11} below -25dB and insertion loss S_{12}=S_{13}=-3.4 dB; which is close to ideal (-3dB or half power split at the frequencies of interest), and while taking into account material

(substrate and ohmic) losses. It can also be noticed that tapered corners as described in 6.2 have been utilized to eliminate additional undesired radiation due to sharp edges at such high frequencies.

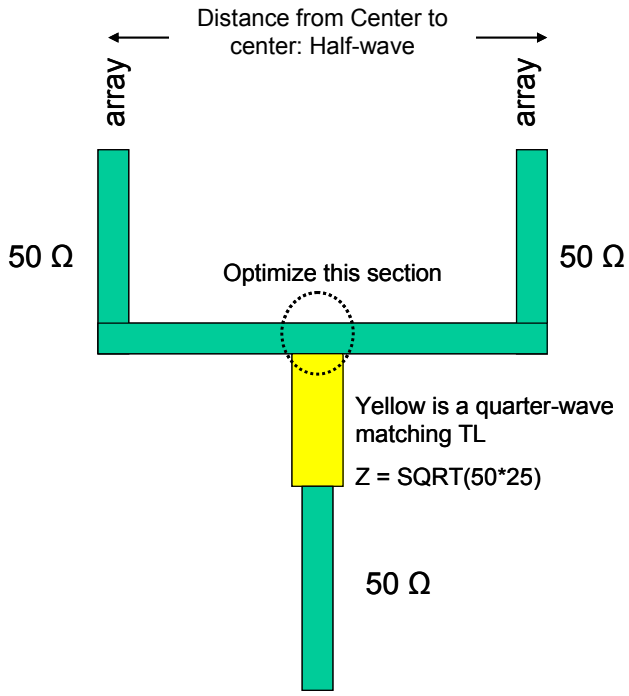

Figure 125. Illustration for T-match section for the array antenna.

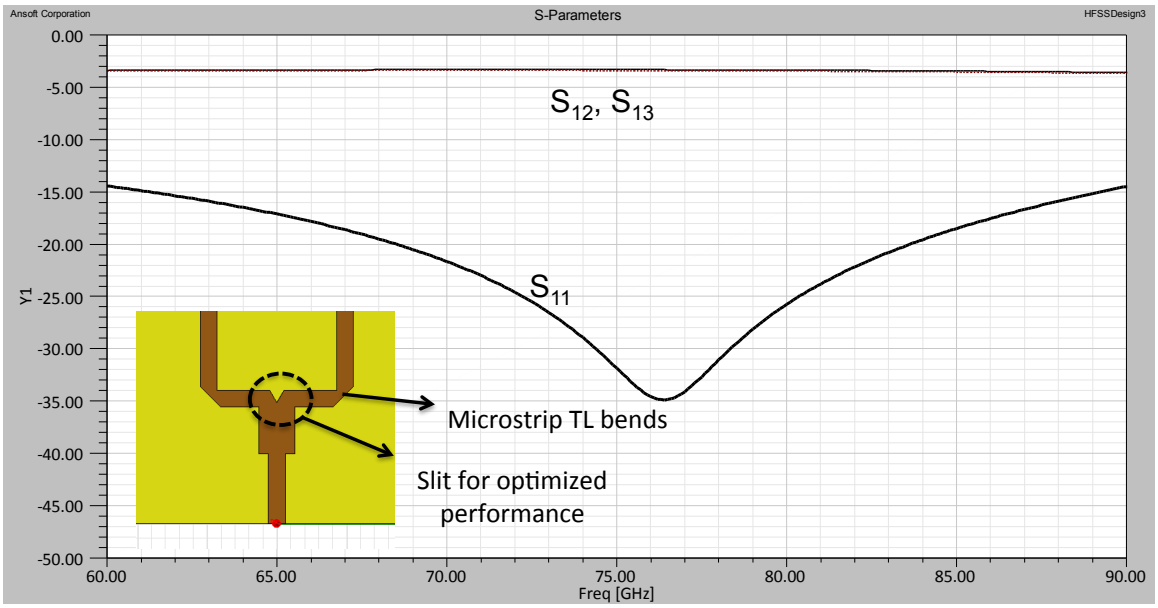

Figure 126. S-parameters (in dB units) for the T-match section shown in Figure 125 with S_{12}=S_{13}=-3.4dB which is close to ideal case (half energy or -3dB).

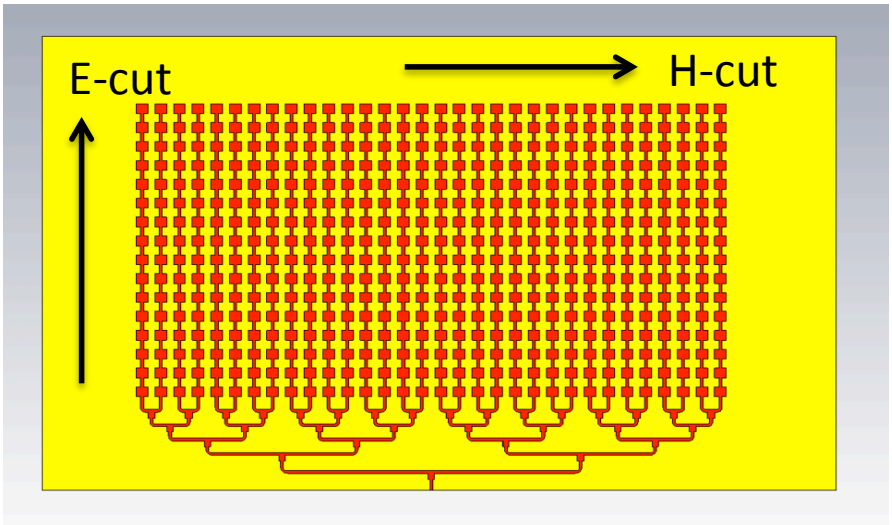

Figure 127. Layout for the 16x32 Array with Feeding Network.

The S-parameter results for the 16x32 array; including the corporate feeding network are shown in Figure 128, demonstrating a very good matching for the design frequencies. The S_{11} at 79GHz is -13dB and at 80 GHz is -12 dB. Figure 129 shows the gain pattern (E-cut) of the array of Figure 127 with a maximum gain of 26.2 dBi, a 3dB angular width of 6.1°, and a SLL of -11.1dB and a radiation efficiency of 78%. An

observation worth mentioning here is the increased level of the side lobes due to the feeding network as its dimensions starts to affect the radiation performance in the mm-Wave frequencies. The H-cut gain plot is also shown in Figure 130 resembling the array factor for 32 sub-arrays or elements with spacing (center to center) of 1.9mm having a 3dB angular width of 3° and a SLL of -14dB. Figure 131 shows the 3D gain pattern at 79GHz as well as the definitions of theta and phi angles.

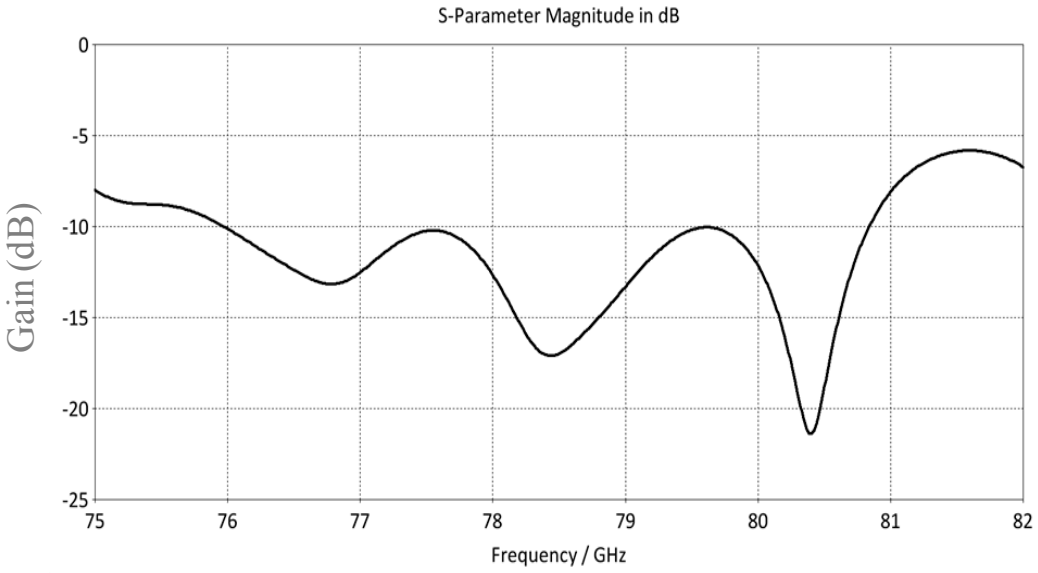

Figure 128. S_{11} for the 16x32 Sub-array shown in Figure 127.

Figure 129. Gain (E-cut, Phi=90) for the 16x32 Antenna Array at 80GHz.

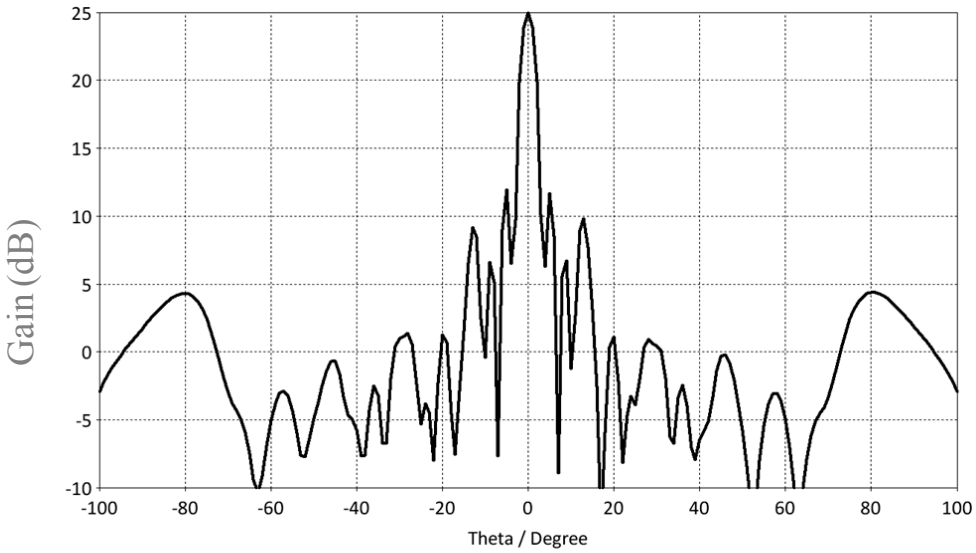

Figure 130. Gain (H-cut, Phi=0) for the 16x32 Antenna Array at 80GHz.

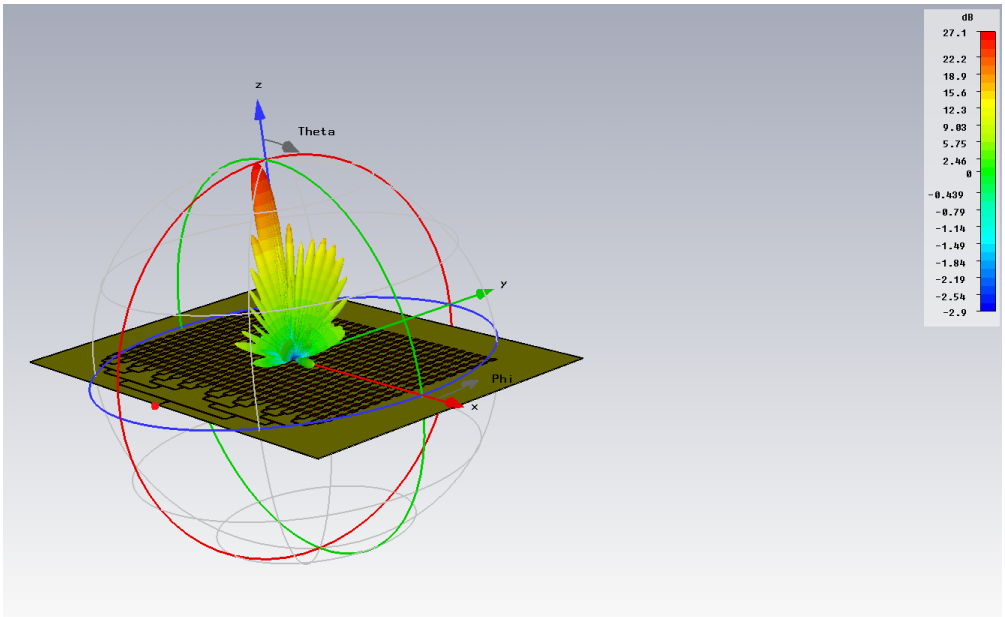

Figure 131. Gain in 3D at 80GHz also showing the definition of theta (elevation) and phi (azimuth) angles.

In order to reduce the effect of the feed network RF 3D interconnections may be utilized (Chapter 6) or simply a shielded corporate feeding such as the one shown in Figure 132 and Figure 133 which includes an unsymmetrical strip line configuration for the corporate feed (15 mil substrate above the microstrip line, 5 mil below it). The gain pattern in Figure 134 has a major shoulder radiation improvement when compared to that shown in Figure 129 and a slight increase in the maximum gain from 26.2dBi to 26.5dBi.

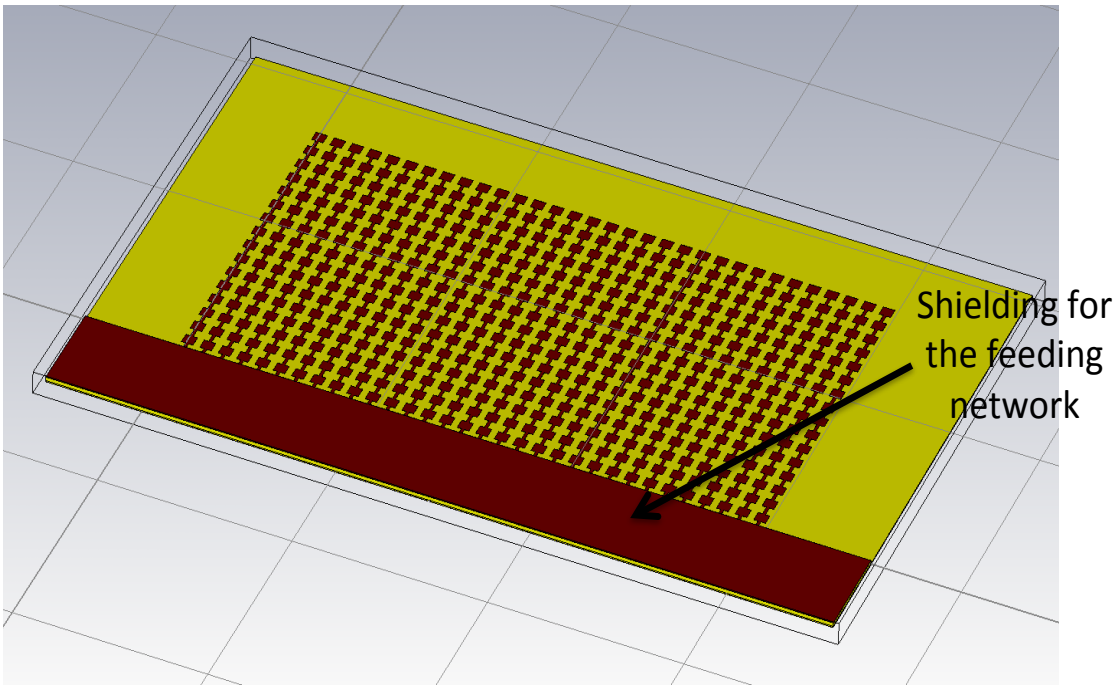

Figure 132. Layout for the shielded feeding 16x32 Antenna Array.

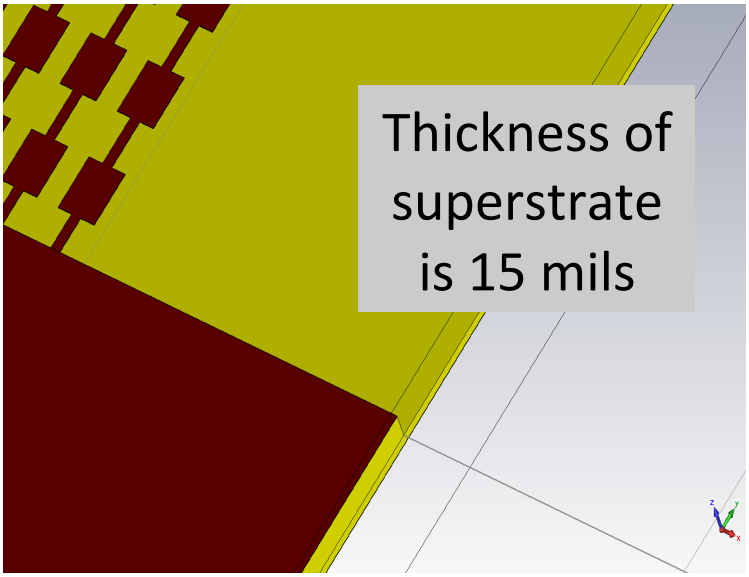

Figure 133. Zoomed in version of the layout for the shielded feed.

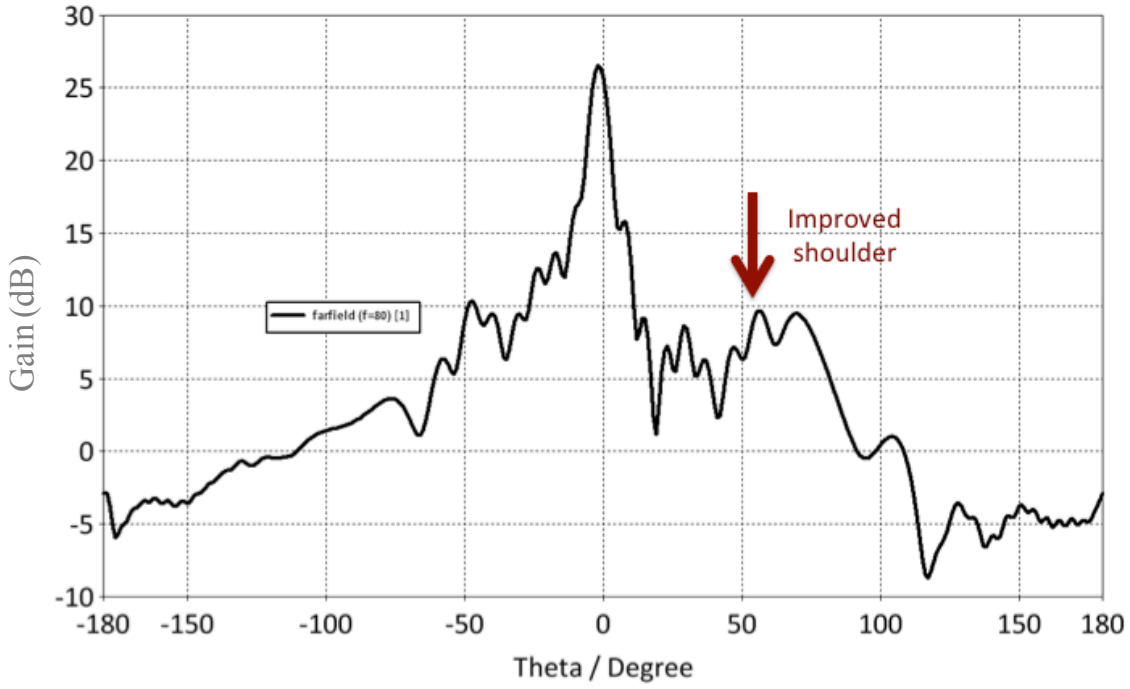

Figure 134. Gain (E-cut, Phi=90) for the 16x32 Antenna Array with shielded feeding

It is to be noted that the final configuration of the proposed architecture would resemble the one in Figure 123 (ideal configuration) with the antenna gain values listed in Table 6. The large antenna arrays shown in Figure 127 and Figure 132 are mainly designed in order to have a single port structure appropriate for measurements.

9.3. Proximity Coupled Microstrip Antenna

Of the four major feeding mechanisms for patch antennas (microstrip line, probe, aperture coupled, and proximity-coupled) the proximity-coupled feeding has the largest bandwidth [68]. This section will explore proximity-coupled feeding mechanism in an array configuration.

The schematic of the antenna is shown in Figure 135. A 50 Ohm embedded microstrip line feeds the resonant microstrip patch elements. There are two layers of LCP

in this configuration, each 4mil thick with the embedded microstrip TL in the center of the two layers. A schematic of a 16 element (sub-array) antenna using proximity coupled feeding is shown in Figure 136. Each individual element has length of 1.0mm and a width of 0.8mm. The center-to-center separation between the elements is 1.2mm. The embedded microstrip line is designed to have 50Ohm input impedance and then its width gets adjusted accordingly in order to have 50Ohms impedance looking into the sub-array (since coupling with the antenna elements affects the impedance). This is also shown in Figure 136. The S_{11} parameters for this design are presented in Figure 137. The -10dB BW covers the range 75.1GHz to 78.3GHz which is a 4%BW (and wide enough to cover the automotive radar frequencies 76GHz to 77GHz). Figure 138 and Figure 139 present the normalized gain plots (E- and H- cuts) at 76GHz and 77GHz respectively, resembling gain plots of practical 1D antenna arrays. The maximum gain is 16.8dBi at 76GHz and 16.6dBi at 77GHz, which includes the mismatch and material losses. This design could be easily scaled for mm-Wave UWB systems covering 79GHz to 81GHz.

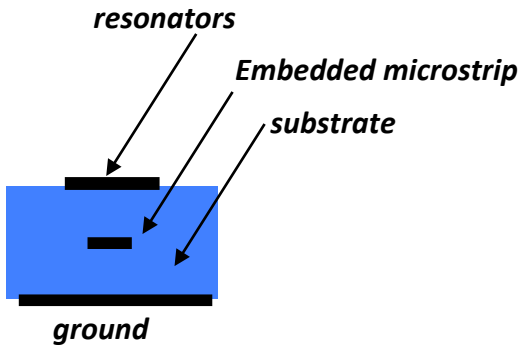

Figure 135. Cross section of the proximity coupled Microstrip Antenna with dual layer LCP (4mils thick each).

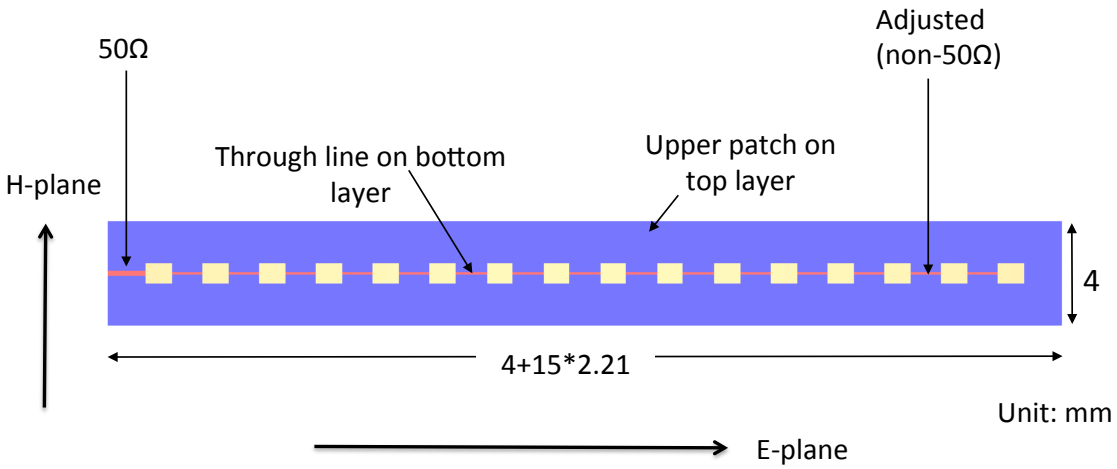

Figure 136. Schematic of the dual layer proximity coupled (Sub-Array) Antenna.

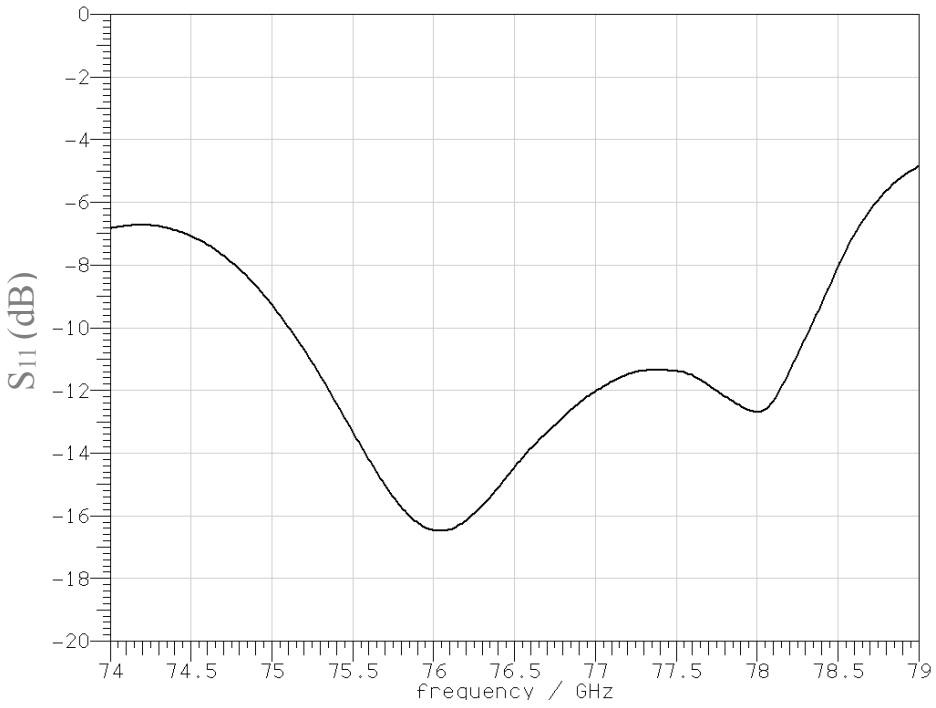

Figure 137. S_{11} for the sub-array antenna shown in Figure 136.

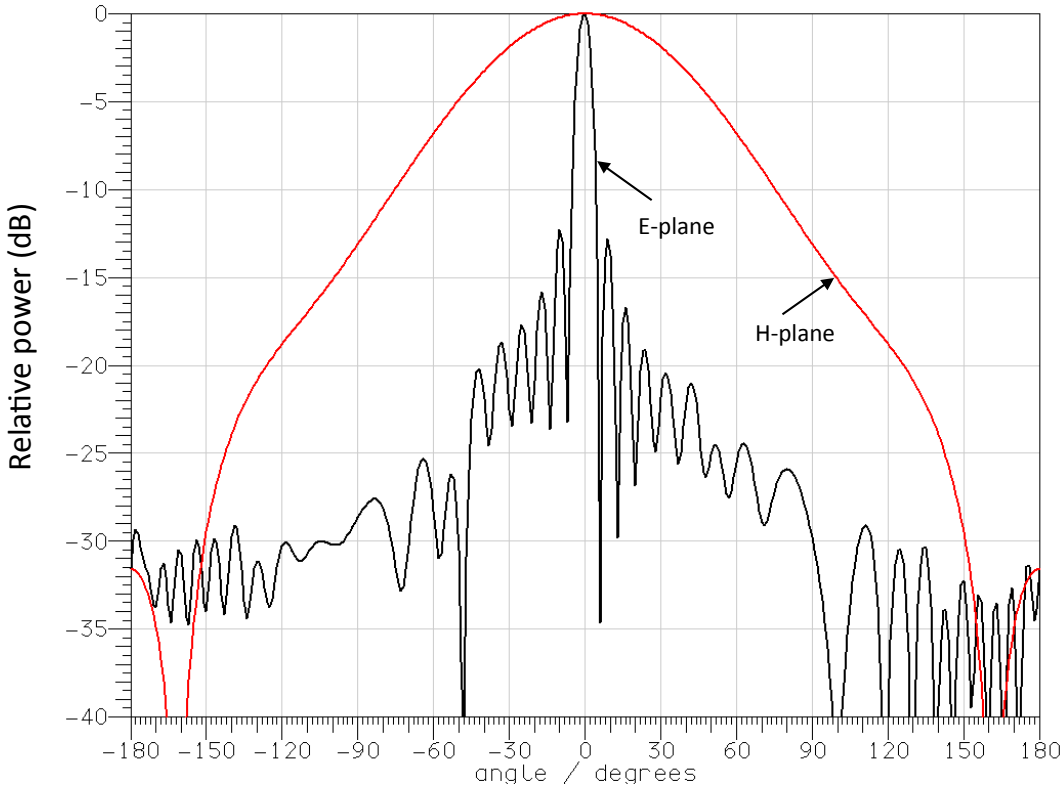

Figure 138. Normalized gain for the sub-array antenna at 76GHz.

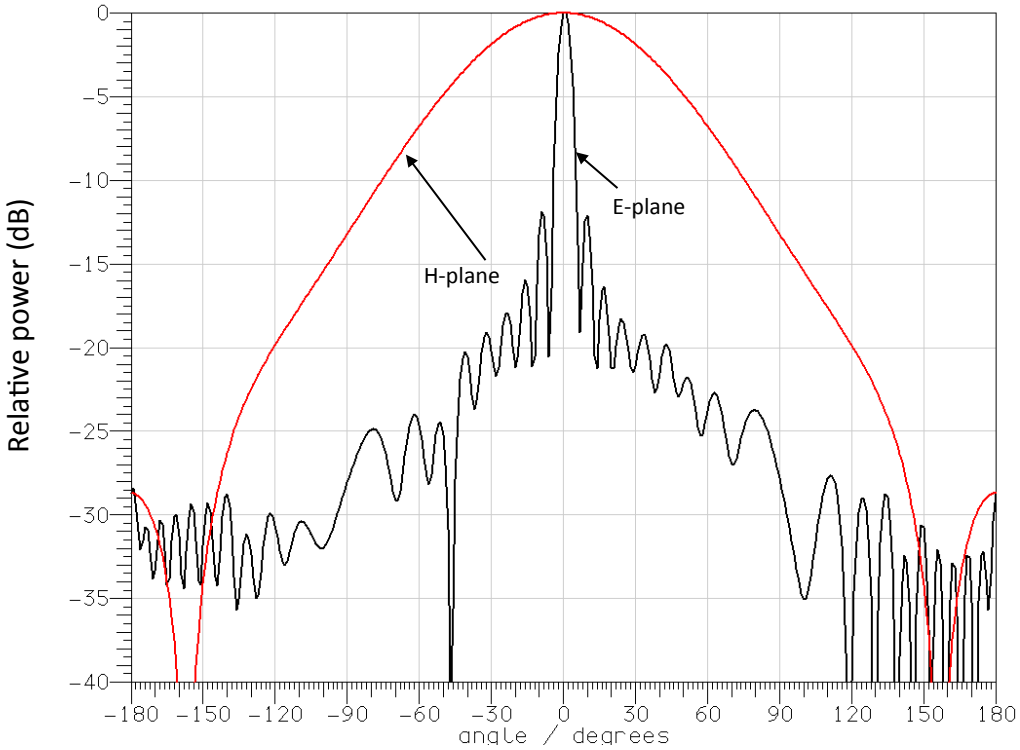

Figure 139. Normalized gain for the sub-array antenna at 77 GHz.

In order to develop this into a configuration compatible with phased arrays, a 16x16 array has been designed with center-to-center distance (between sub-arrays) of 1.4mm. The schematic of the structure is shown Figure 140. Also shown are Port1 and Port2 in this 16x16 configuration in order to preform return loss and coupling S-parameters analysis. This is presented in Figure 141 showing a coupling level below -20dB across the frequencies 74GHz to 79GHz. Figure 142 and Figure 143 present the normalized gain plots (E- and H- cuts) at 76GHz and 77GHz respectively, with maximum gain of 28dBi at 76GHz and 77GHz, which includes the mismatch and material losses. The aperture efficiency is 78%, which is a high value for frequencies at this range.

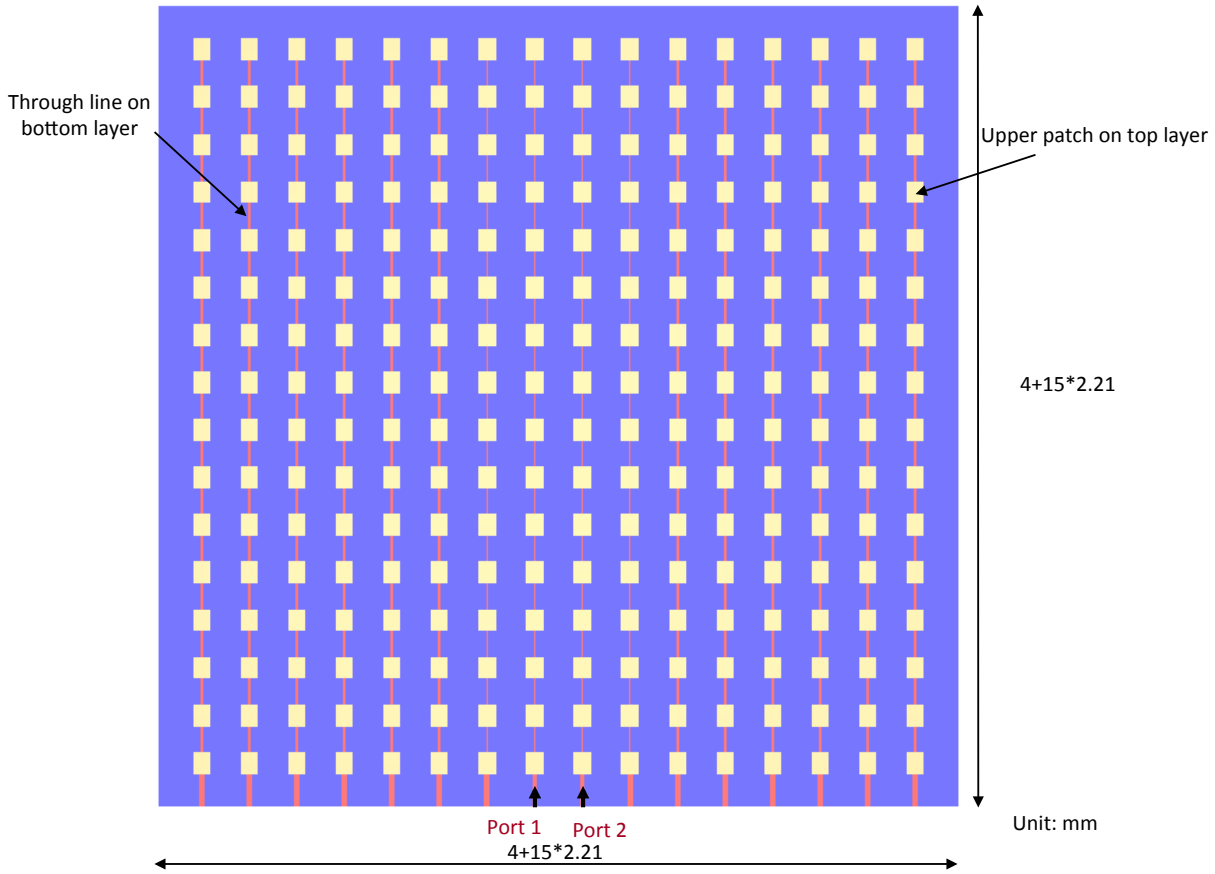

Figure 140. Schematic of the 16x16 antenna array, showing Port1 and Port2 for coupling analysis.

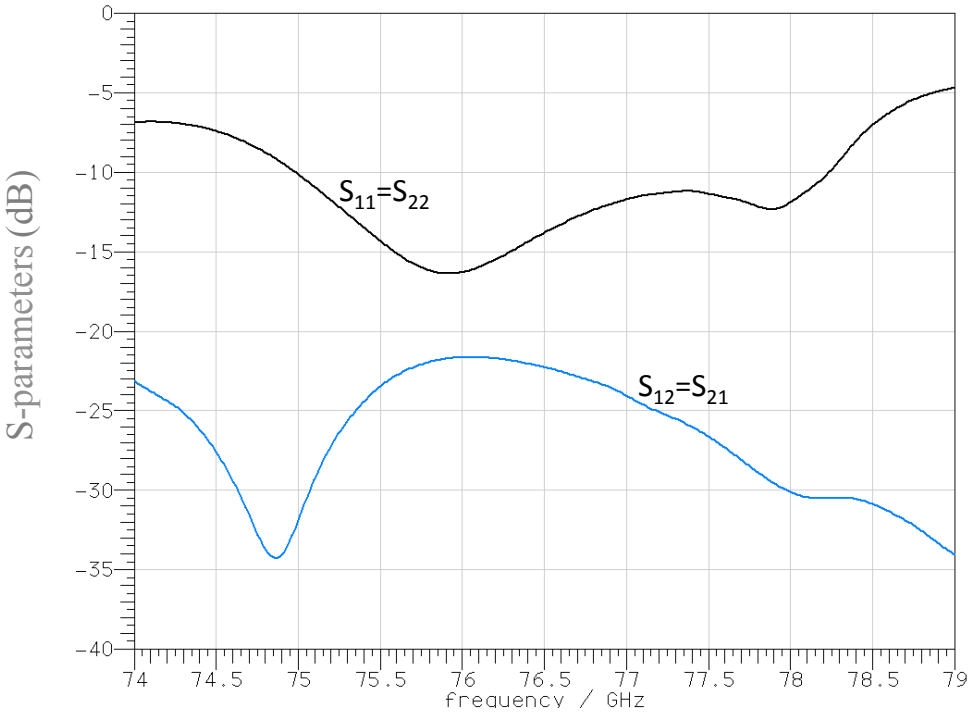

Figure 141. S_{11} and S_{12} (coupling of Port1 and Port2).

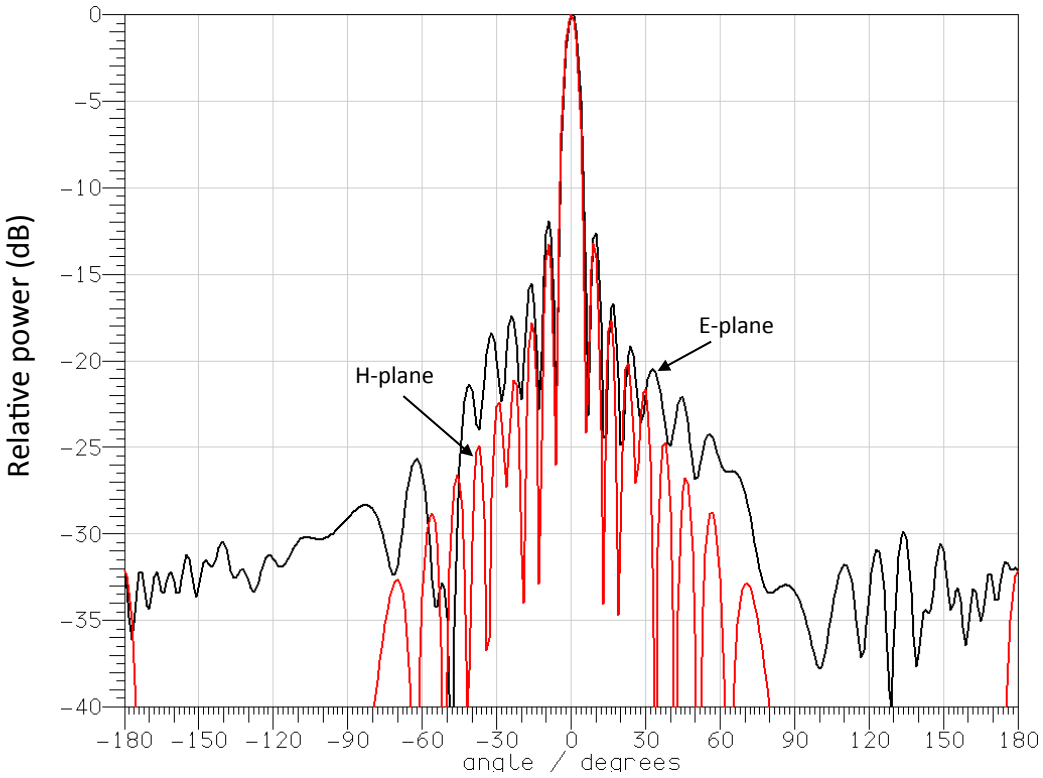

Figure 142. Normalized gain for the 16x16 array antenna at 76 GHz.

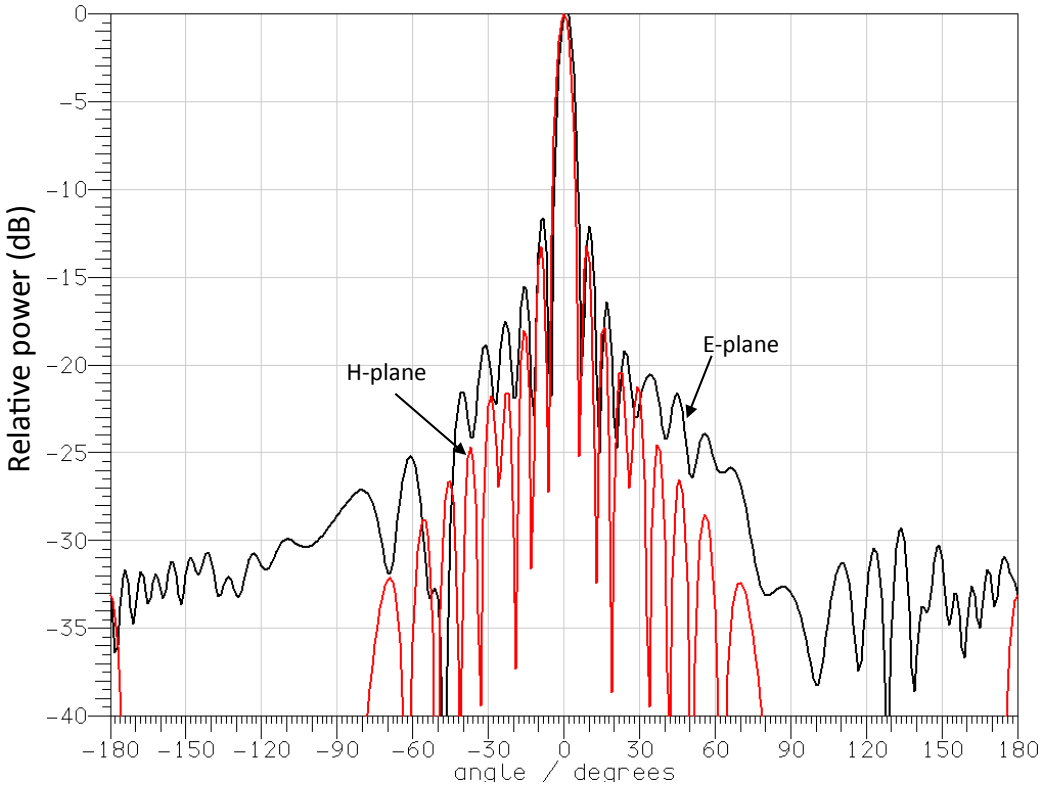

Figure 143. Normalized gain for the 16x16 array antenna at 77 GHz.

The large array designed for characterization purposes uses a hybrid of series and corporate feeding network where the sub-arrays' individual elements are connected in series while the sub-arrays are connected in a parallel configuration (corporate network). This is also similar to the edge fed large array antenna. This can be seen in Figure 144. The S_{11} results are shown in Figure 145 covering a -10dB BW from 74.3GHz to 78.7GHz. The normalized gain plots are shown in Figure 146 with an expected E-plane side-lobe increase due to the feeding network, a problem that can be mitigated through the use of a shielded feed similar to the one in Figure 132. The maximum gain at 77GHz is 24.7dBi with an aperture efficiency of 43%. This is a significant decrease when compared with the ideal case (Figure 140). Figure 147 shows the normalized gain for the shielded feeding network design exhibiting better sidelobes and an increased maximum

gain of 25.8dBi and an aperture efficiency of 70%. Table 7 compares the three designs (or design stages): ideal 16x16, corporate feed 16x16, as well as the shielded feed 16x16 antenna arrays in terms of gain and aperture efficiency at 77GHz.

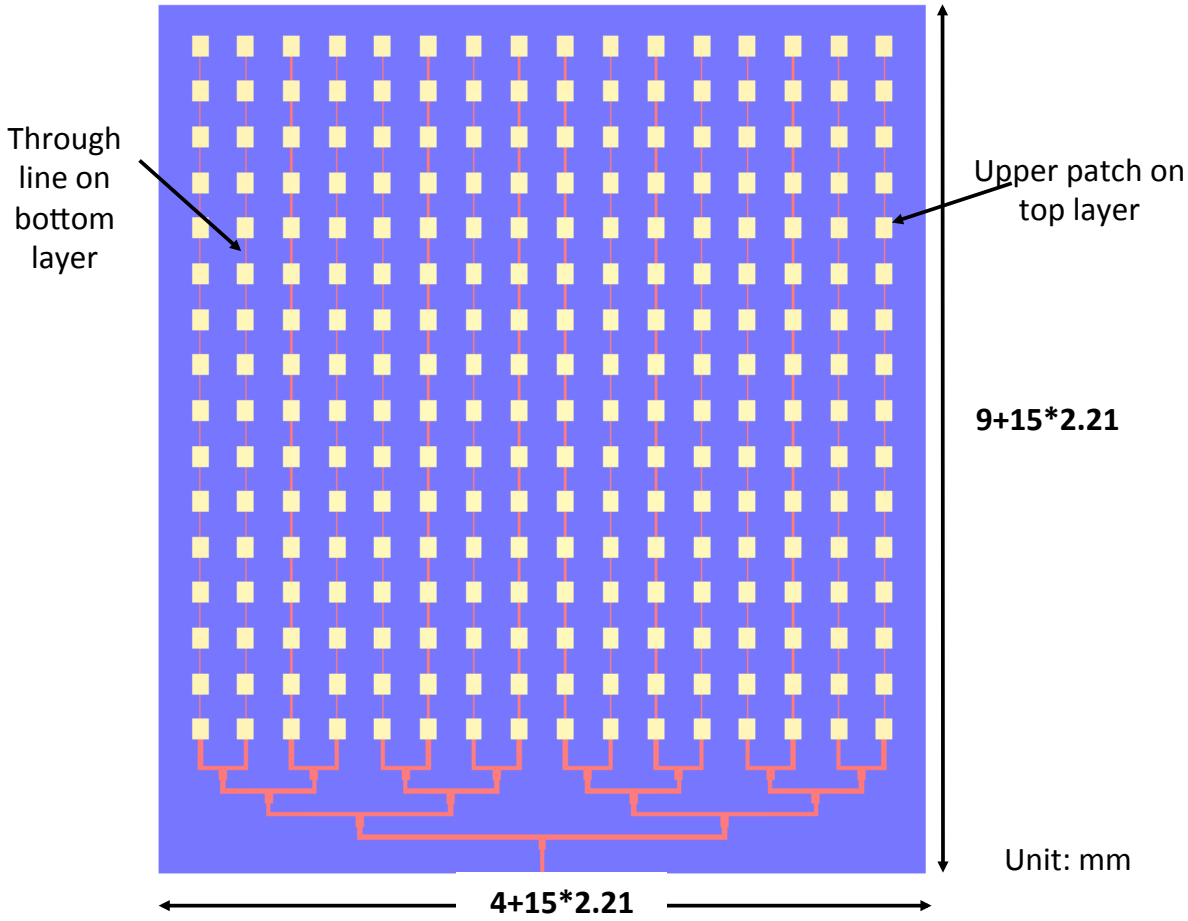

Figure 144. Schematic of the 16x16 antenna array with corporate feeding.

Table 7. Gain and Aperture Efficiency Comparison Among ideal, corporate feed, and shielded feed at 77GHZ for the 16x16 antenna array.

	Gain (dBi)	Aperture Efficiency (%)
Ideal 16x16	28	78
With feeding network unshielded (Figure 144)	24.7	43
With shielded feed (Figure 147)	25.8	70

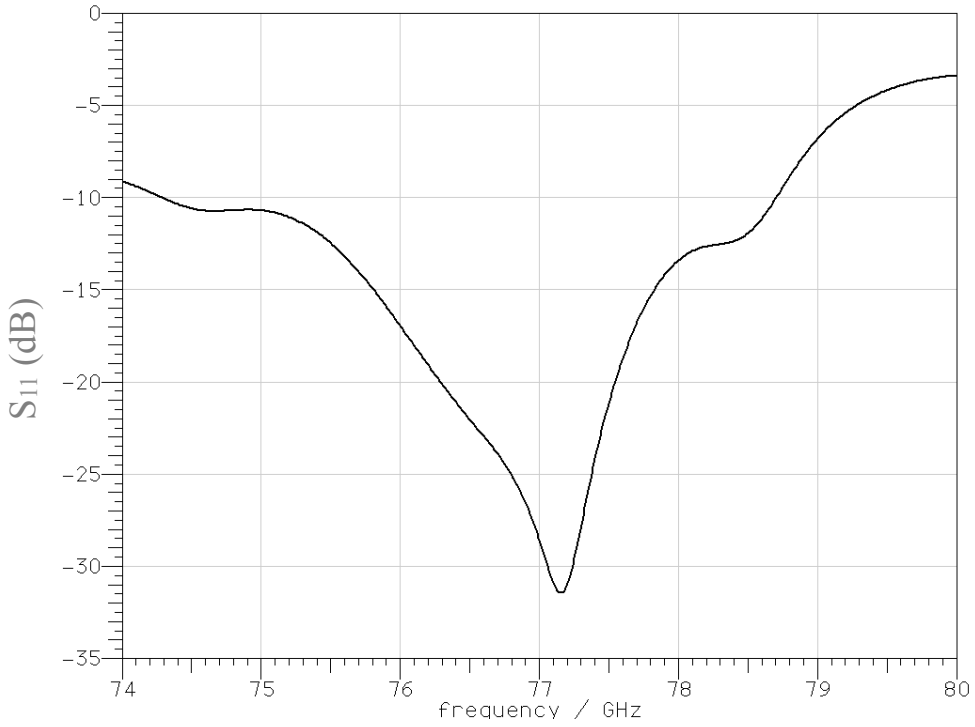

Figure 145. S_{11} vs. frequency for the corporate fed antenna array.

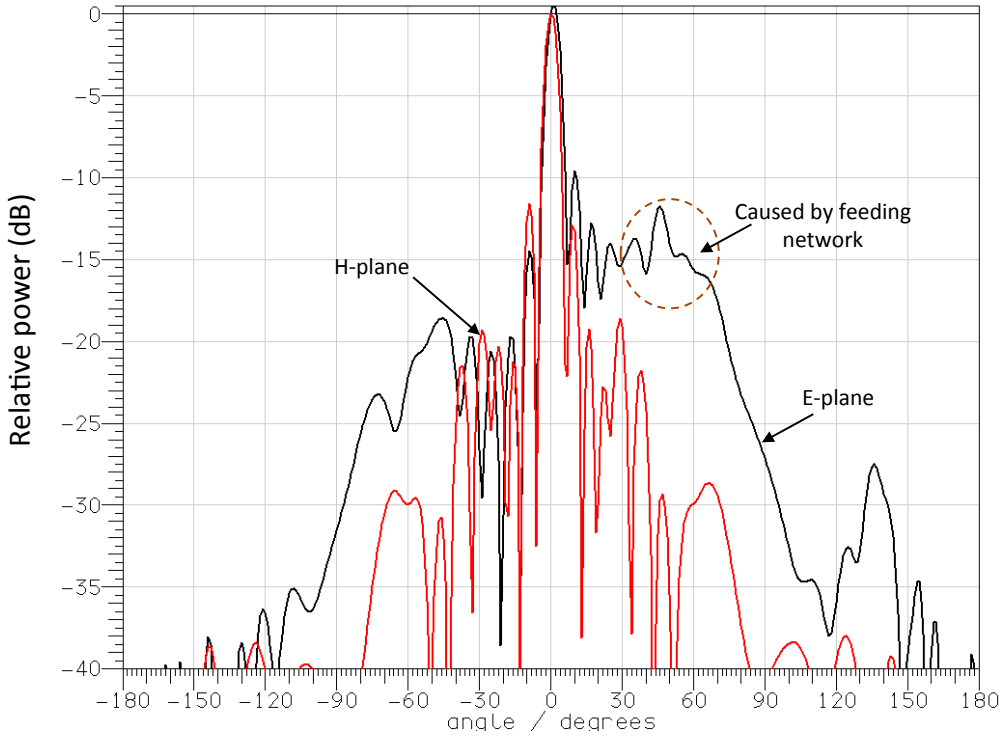

Figure 146. Normalized gain for the corporate fed antenna array at 77GHz.

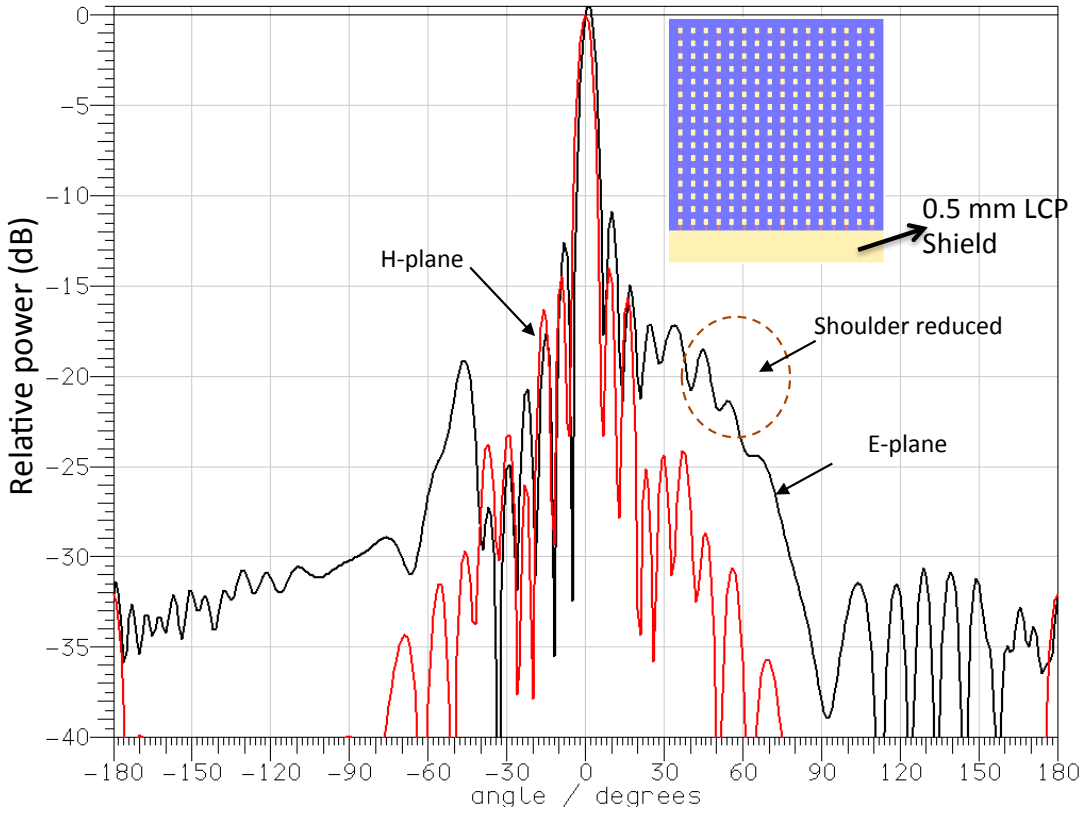

Figure 147. Normalized gain for the shielded feeding 16x16 antenna array at 77GHz.

A 16x1 structure as well as a 16x16 corporate feed antenna array has been developed on LCP for characterization purposes. Figure 148 and Figure 149 present the S_{11} measurement results for the 16x1 sub-array. It can be observed that around the frequency of interest (76-77 GHz for mm-Wave automotive application) the simulations cover a -10 dB bandwidth of 75.1 GHz to 78.3 GHz while the measurements covers 74 GHz to 77.5 GHz. The discrepancy between the simulation and measurement results could be explained by any fabrication errors or tolerances as well as by the feeding CPW line that was used for probing the Antenna Under Test (AUT), which is shown in Figure 150. The CPW line may have introduced some reflections due to misalignments with the

top layer on which the resonant elements sit. In addition, some oxidation was observed at the CPW pads.

The S_{11} for the 16x16 antenna array with the corporate feed (Figure 144) is shown in Figure 151. With an overall agreement, and especially since the measurements cover a wider BW around the design frequencies, the discrepancy here can be explained by fabrication misalignments, where it is to be noted that a slight misalignment at these frequencies in a dual layer resonance structure could lead to severe changes. In addition to that, the S_{11} in Figure 151 was measured with a waveguide connection and not probes. An additional microstrip to WG transition was required here and is depicted in Figure 152. This was necessary for antenna gain measurements (described in Chapter 7). Figure 152 and Figure 153 describe the W-band antenna measurement setup that was utilized to produce the results in Figure 154 for the total gain of the AUT or the 16x16 antenna array as shown in Figure 152. The measurements were performed at 78GHz, since it was the calibrated frequency for the chamber, and produced a good overall agreement between the simulated and measurement results. The peak simulated gain is 23.6dBi and the measured gain is 21.16 dBi for the H-plane. It is to be noted that 2.26 dB account for the microstrip and transition loss used for the connection to the oscillator as shown in Figure 152.

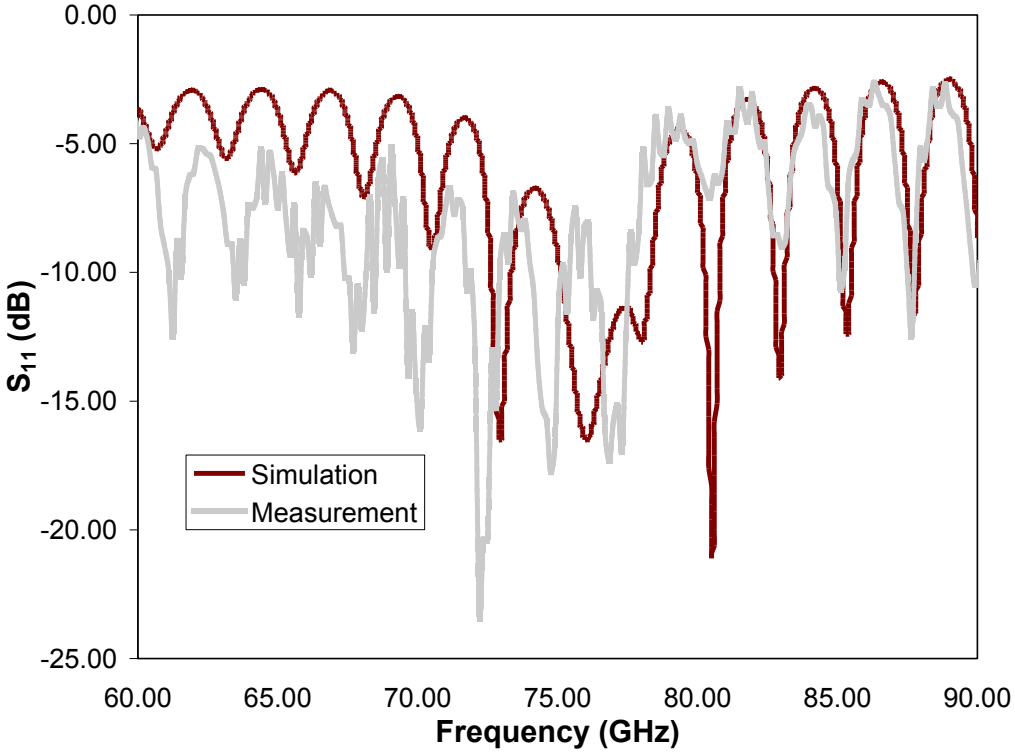

Figure 148. S_{11} results for the 16x1 sub-array antenna.

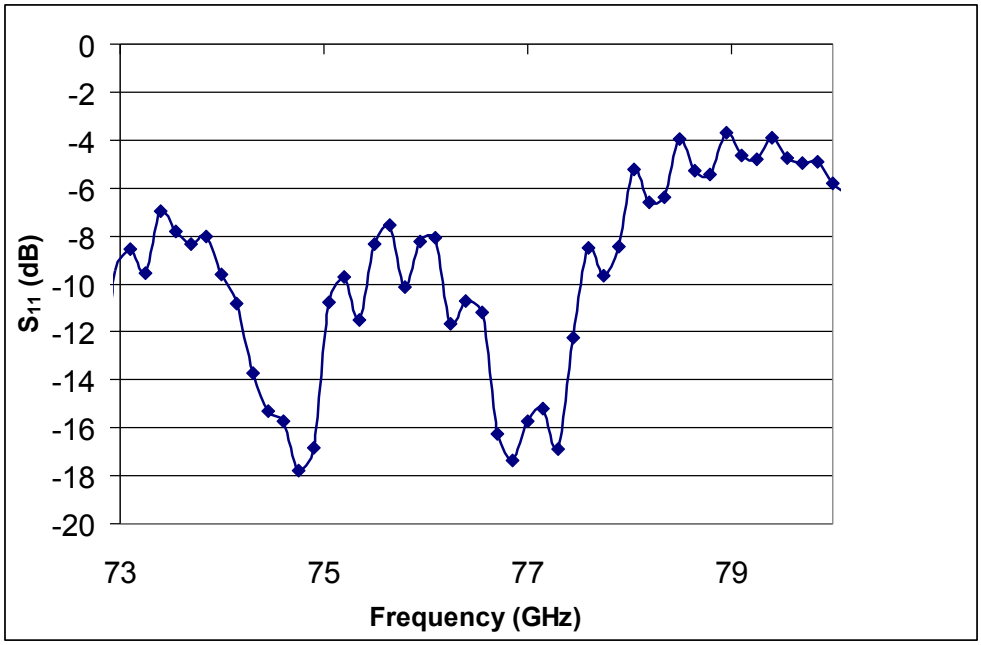

Figure 149. Measured S_{11} for the 16x1 sub-array (73GHz → 80GHz).

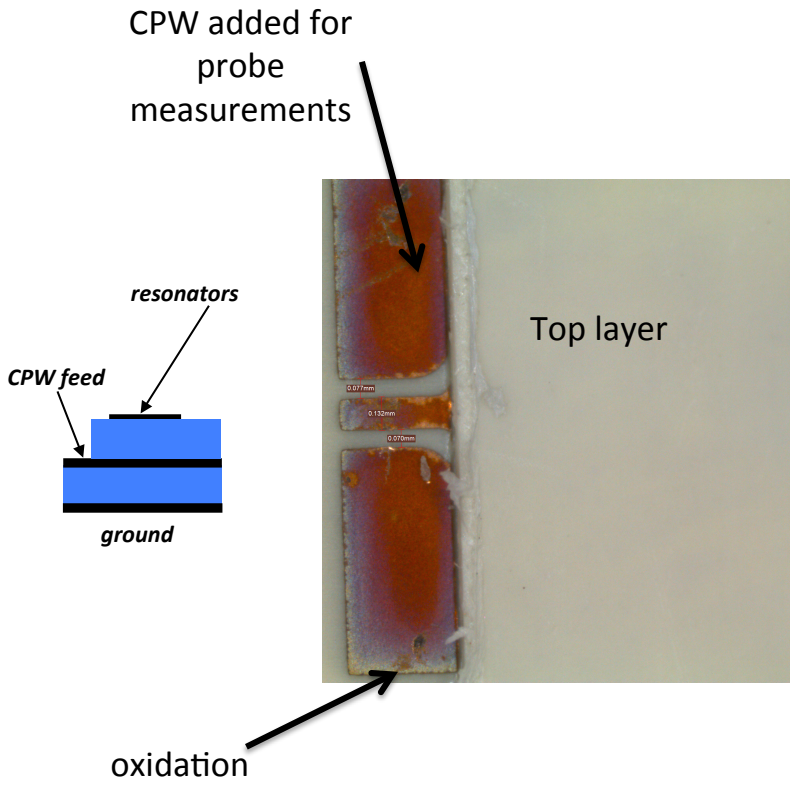

Figure 150. Cross-sectional illustration of the AUT and a microscopic photo of the feeding (CPW) to the Antenna.

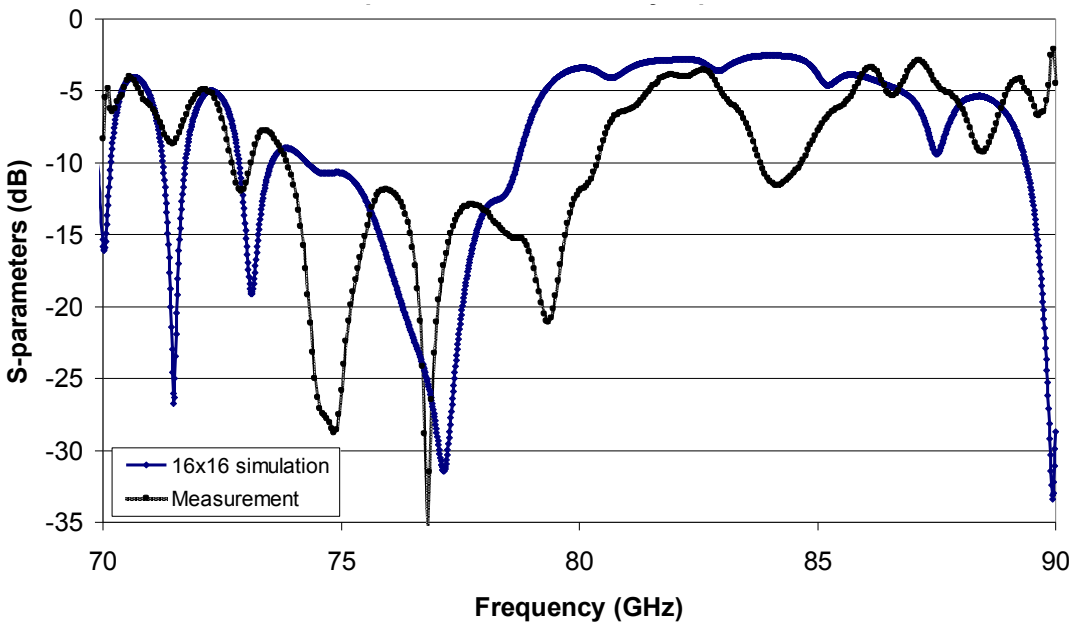

Figure 151. Measured and simulated S_{11} for the corporate feed 16x16 AUT.

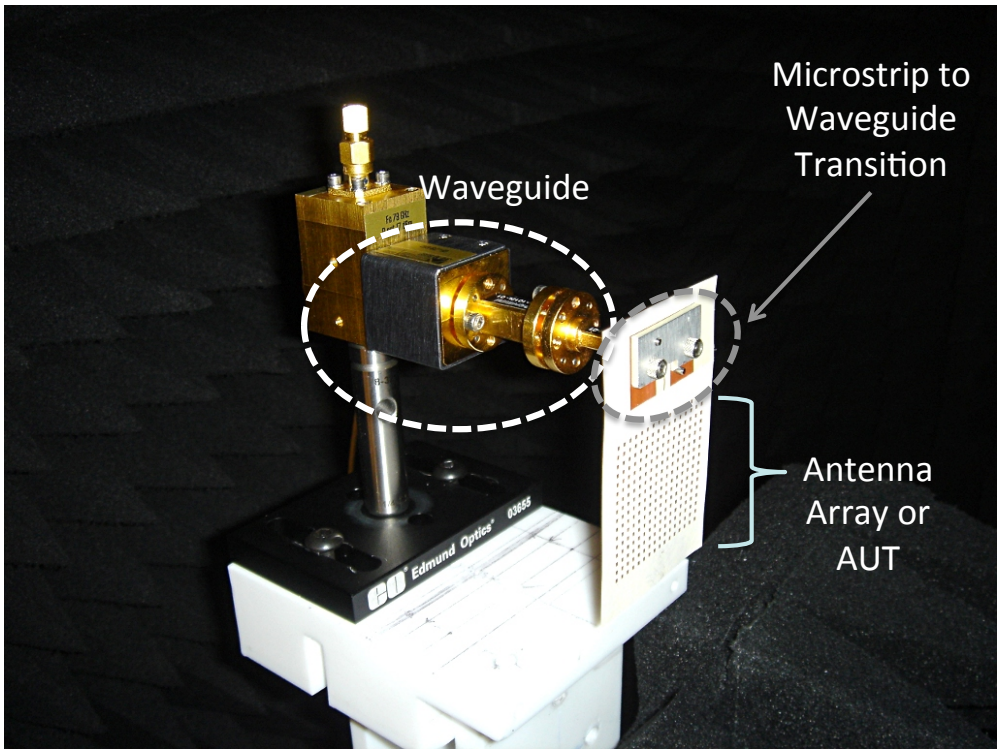

Figure 152. Photo of this antenna with a transition to Waveguide input to oscillator for radiation pattern measurement.

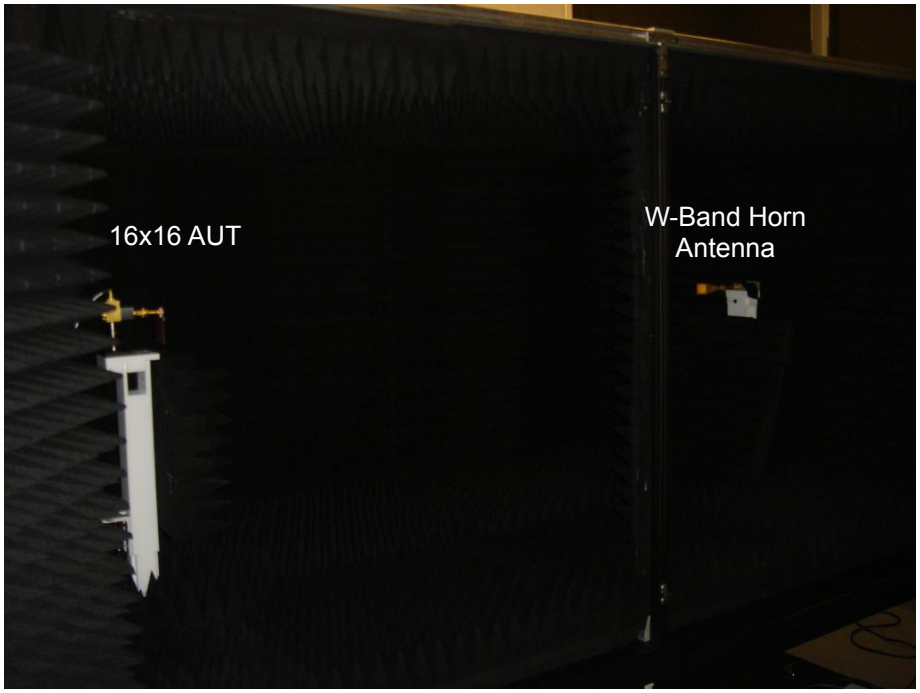

Figure 153. W-band Antenna chamber setup.

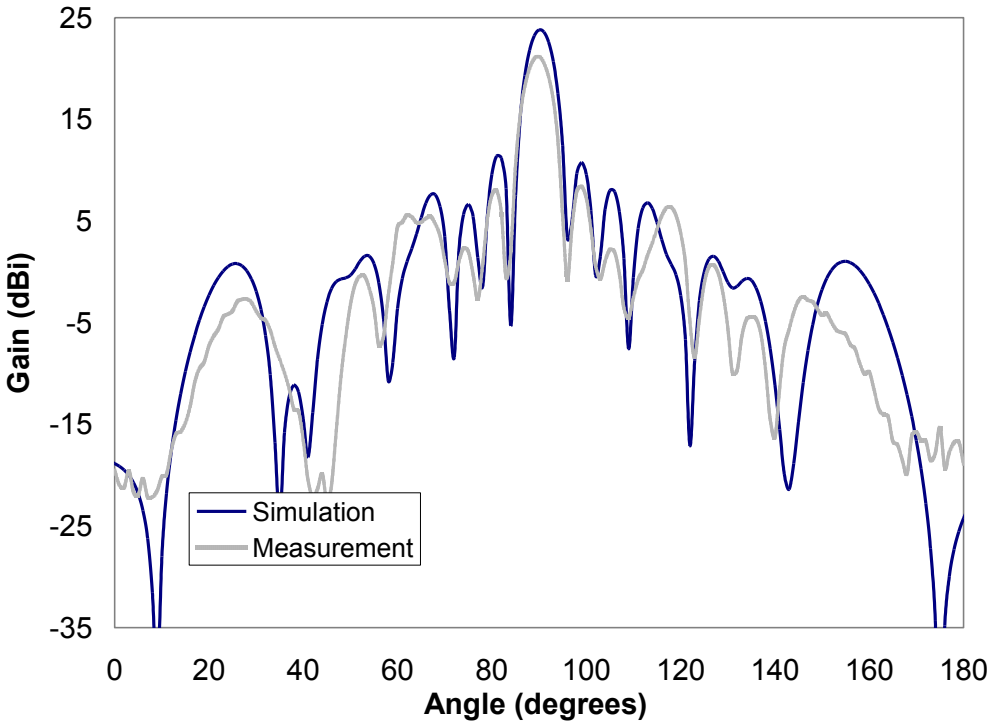

Figure 154. Antenna Total Gain for the structure shown in Figure 152.

Chapter 10.

Contributions, Patents, and Publications to Date

Contributions

This work has established the foundation of low-cost, practical, and high performance RF design methodologies for identification & sensing, communication, and radar applications on LCP and paper substrates. It can also be extended to the sub-terahertz frequencies (120/230 GHz) for imaging applications. This work has systematically explored the design and development of a series of RF structures for developing solutions for high-performance low-cost passives for radar, identification, and communication applications up to mm-Wave frequencies while proposing potential solutions that will meet three main requirements: small size (or low weight), high performance, and low cost.

There have been many contributions both to the academic and industry communities - mostly in helping better understand advantages and challenges brought by these technologies. Perhaps the most substantial of these contributions are the following:

PART I:

- Characterization of paper substrate up to UWB frequencies
- Utilizing paper as an environmentally friendly substrate with inkjet (ubiquitous and digital) fabrication for identification and communication applications

- Successfully utilizing conductive inks on paper and LCP substrates with feature sizes (~50 μm)
- Successful inkjet-printed antenna modules at: UHF, microwave, UWB, and mm-Wave frequencies
- Design and developments of a highly selective filter design on LCP for X-band radar applications and that could be easily scaled up/down for use in radar filter banks and other communication or defense applications

PART II:

- Substrate selection for mm-Wave (up to 100GHz)
- Architecture design for integrated mm-Wave radar front-end
- 3D RF transitions from T/R module to antenna array
- 2D transmission line transitions for optimizing sharp bends or corners
- Integration of antenna elements with 3D transition
- Methods to minimize crosstalk among transmission lines to/from T/R module
- An optimized antenna array for phased-array operation made up of several channels that feed individually to a T/R phased array module. This array must also satisfy bandwidth, gain, efficiency, beam steering and size requirements

In addition, this work has resulted in patents (with industry), books, book chapters, peer-reviewed technical journals and conference papers/presentations (listed in chronological order):

Patents

- ***SYSTEM AND METHOD FOR IMPROVING PERFORMANCE OF COPLANAR WAVEGUIDE BENDS AT MM-WAVE FREQUENCIES***, US20100182107A1
- ***WIDEBAND RF 3D TRANSITIONS ON LIQUID CRYSTAL POLYMER***, US20100134376A1
- ***INTERCONNECTION APPARATUS AND METHOD FOR LOW CROSS-TALK CHIP MOUNTING FOR AUTOMOTIVE RADARS***, US20100182103A1
- ***ANTENNA WITH TAPERED ARRAY***, Toyota Technical Center, Docket No. TTC-88502/08 (pending).
- ***THREE-DIMENSIONAL ARRAY ANTENNA ON A SUBSTRATE WITH ENHANCED BACKLOBE SUPPRESSION FOR MM-WAVE AUTOMOTIVE APPLICATIONS,*** Toyota Technical Center, Docket No. 90181-3400 (pending)
- ***MICROWAVE ANTENNA***, Docket No. 88602/08 (pending).
- ***IMPLEMENTATION OF WIRELESS SENSOR NETWORK USING LOW COST RFID TAGS AS SENSOR NODES***, Georgia Tech Invention Provisional, GTRC ID 4077, Jan. 2007.

Publications

Books

1. **Amin Rida, Li Yang, Manos Tentzeris**, *RFID Enabled Sensor Design and Applications, Norwood, MA, Artech House* **ISBN: 978-1-670783-981-1**
2. **Li Yang, Amin Rida, Manos Tenzeris**, *Design and Development of Radio Frequency Identification (RFID) and RFID-Enabled Sensors on Flexible Low Cost Substrates,* A Publication in Morgan and Claypool Publishers Series, Synthesis Lectures on RF/Microwaves , 2009. **ISBN 9781598298604 (Paperback) 9781598298611 (E-book).**

Book Chapters

1. **A. Rida,** L. Yang, S. Basat, M. M. Tentzeris, "RFID: Beyond the Basics", chapter in *RFID Applied*, edited by J.Banks, D.Hanny, M.Pachano, L.Thompson, pp.95-123, **John Wiley and Sons, 2007, ISBN 978-0-471-79365-6**
2. **A. Rida,** L. Yang, S. Basat, M. M. Tentzeris, "RFID: Issues of Security and Privacy", chapter in *RFID Applied*, edited by J.Banks, D.Hanny, M.Pachano, L.Thompson, pp.95-123, **John Wiley and Sons, 2007, ISBN 978-0-471-79365-6**
3. L. Yang, **A. Rida**, A. Traille, M. M. Tentzeris, "RFID Design", chapter in *Time Domain Methods in Electrodynamics*, A tribute to W. Hoefer, by Russer, Peter, Siart, Uwe (Eds), In series Springer Proceedings in Physics, Vol 121, 2008 **ISBN: 978-3-540-68766-5**

Journal papers/Articles

[1] **A. Rida**, F. Colomb, and M.M. Tentzeris, "Design and Development of X-Band Passive Filters on LCP with Ultra High Selectivity" submitted to IEEE Microwave Wireless Components Letters.

[2] **A. Rida**, A. Margomenos, J. Lee, P, Schmalenberg, S. Nikolaou, and M.M. Tentzeris, "Integrated Wideband 2D & 3D Transitions for Millimeter-Wave RF Front-Ends" IEEE Antennas and Wireless Propagation Letters, Vol. 9, pp. 1080-1083, 2010.

[3] V. Lakafosis, **A. Rida**, R. Vyas, L. Yang, S. Nikolaou, and M.M. Tentzeris, "Progress Towards the First Wireless Sensor Networks Consisting of Inkjet-Printed, Paper-Based RFID-Enabled Sensor Tags" Proceedings of the IEEE, pp(s). 1601-1609, vol. 98, Issue 9, 2010.

[4] G. Orecchini, L. Yang, **A. Rida**, F. Alimenti, M.M. Tentzeris, and L. Roselli, "Green Technologies and RFID: Present and Future" Applied Computational Electromagnetics Society Journal, Special Issue on Computational and Experimental Techniques for RFID Systems and Applications, pp. 230-238, vol. 25, no. 3, March 2010.

[5] **A. Rida,** L. Yang, S.S. Basat, A.F. Vidal, S. Nikolaou, and M.M. Tentzeris, "Design, Development, and Integration of Novel Antennas for Miniaturized UHF RFID Tags" IEEE Transactions on Antennas and Propagation, pp. 3450-3457, Vol 57, November 2009.

[6] **A.Rida,** L.Yang, R. Vyas, and M.M. Tentzeris, "Conductive Inkjet-Printed Antennas on Flexible Low-Cost Paper-Based Substrates for RFID and WSN

Applications" IEEE Antennas and Propagation Magazine, pp.13-23 Vol. 51, No. 3, June 2009.

[7] R. Vyas, V. Lakafosis, **A. Rida**, N. Chaisilwattene, S. Travis, J. Pan, and M.M. Tentzeris, "Paper-Based RFID-Enabled Wireless Platforms for Sensing Applications" IEEE Trans on Microwave Theory and Techniques, pp. 1370-1382, Vol. 57, No. 5, May 2009.

[8] L. Yang, **A. Rida**, R. Vyas, M. M. Tentzeris, "High-Frequency Characterization of Paper Substrate and Development of Paper-based Inkjet-Printed RFID and Microwave Structures", *IEEE Transactions on Microwave Theory and Techniques*, pp. 2894-2901,Vol. 55, Issue 12, Part 2, Dec. 2007.

[9] **A. Rida**, L. Yang, R. Vyas, D. Staiculescu and M. M. Tentzeris, "Novel Miniaturized Inkjet-printed Paper-Based UHF Components for RFID and Sensing Applications," *Proceedings of the European Microwave Association*, Special Issue on RFID, pp. 67-76, vol 3, Issue 4, Dec. 2007.

Conference Papers

[1] G. Shaker, **A. Rida**, S. Nikolaou, S. Naeini, and M.M. Tentzeris "Inkjet Printing of UWB Antennas on Paper Based Substrates" accepted for presentation/publication in EuCAP 2011 in Rome, Italy.

[2] **A. Rida**, S. Nikolaou, and M.M. Tentzeris, "Design of Low Cost Microstrip Antenna Arrays for mm-Wave Applications" to be presented at the APS 2011, Spokane, Washington, USA.

[3] C. Occhiuzzi, **A. Rida**, G. Marrocco, and M. Tentzeris, "CNT-based RFID Passive Gas Sensor" to be presented at the 2011 IMS, Baltimore, Maryland, USA.

[4] **A. Rida**, R. Li, P. Schmalenberg, J.S. Lee, and M.M. Tentzeris, "Proximity Coupled Fed Antenna Arrays on LCP for mm-Wave Applications" pp. 1-4, IEEE Antennas and Propagation Society International Symposium, Toronto, ON, Canada, July 2010.

[5] M.Tentzeris, R. Vyas, V. Lakafosis, A. Traille, **A. Rida**, and G. Shaker, "Inkjet-printed System-on-paper/polymer "Green" RFID and Wireless Sensors"60th Proc. of Electronic Component and Technology Conf, pp. 1552-1555, 2010. **BEST OF SESSION AWARD**

[6] **A. Rida,** G. Shaker, E. Tan, S. Nikolaou, and M.M. Tentzeris, "Design, Integration, and Packaging of a Wireless Module for Location Finding and Healthcare Applications" Accepted for Publication in EuCAP**,** Barcelona Spain, 2010.

[7] **A. Rida**, G. Shaker, S. Nikolaou, and M.M.Tentzeris, "Inkjet Printing of Dual Band Conformal Antenna for use in Wifi Frequency Bands", *IEEE Radio and Wireless Symposium,* New Orleans, LA USA, 2010.

[8] **A. Rida**, A. Margomenos, T. Wu, and M. M. Tentzeris, "Novel Wide-band 3D Transitions on Liquid Crystal Polymer for Millimeter-Wave Applications up to 100 GHz", pp. 953-956, *IEEE International Microwave* Symposium Boston, MA, USA, June 2009.

[9] **A.Rida,** A. Margomenos, and M.M. Tentzeris, "Wideband mm-wave Compensated 90° Bends for Grounded Coplanar Waveguide and Microstrip

Transmission Lines on Flexible LCP Substrate" pp. 2000-2003, 59th *Electronic Components and Technology Conference,* San Diego, CA USA, May 2009.

[10] **A. Rida,** F. Nasri, A. Margomenos, and M.M. Tentzeris, "Integration of Novel mm-Wave Components on Flexible Organic Substrates for Automotive Radar Applications" pp. 1327-1330, *European Microwave Conference,* Rome, Italy, 2009.

[11] **A. Rida,** S. Nikolaou, and, M.M. Tentzeris, "Broadband UHF RFID/Sensor Modules for Pervasive Cognition Applications" pp. 2344-2347, *3rd European Conference on Antennas and Propagation*, Berlin, Germany, 2009.

[12] A. Konstas, **A. Rida,** R. Vyas, K. Katsibas, N. Uzunoglu, and, M.M. Tentzeris, "A Novel "Green" Inkjet-Printed Z-Shaped Monopole Antenna for RFID Applications" pp. 2340-2343, *3rd European Conference on Antennas and Propagation*, Berlin, Germany, 2009.

[13] **A. Rida**, L. Yang, T. Reynolds, E. Tan, S. Nikolaou, and M.M. Tentzeris, "Inkjet-Printing UHF Antenna for RFID and Sensing Applications on Liquid Crystal Polymer" pp. 1-4, *IEEE International Symposium on Antennas and Propagation,* Charleston, SC, USA, 2009.

[14] M.M.Tentzeris, A. Traille, L. Yang, V. Lakafossis, R. Vyas, **A. Rida**, A. Haque, and D. Staiculescu, "RFID-Enabled Biosensing Wireless Modules" pp. 131-134, *IEEE Radio and Wireless Symposium,* San Diego, CA, USA, 2009.

[15] A. Traille, L. Yang, A. Rida, V. Lakafossis, and M.M. Tentzeris, "Novel Miniaturized Antennas for RFID-Enabled Sensors" pp. 912-915, *IEEE Sensors Conference*, New Zealand 2009.

[16] **A. Rida,** L. Yang, N. Chaisilwattana, S. Travis, S. Bhattacharya, and M.M. Tentzeris, "3D Packaging Architecture Using Paper as a Dielectric Medium" pp. 371-373*, 58th Electronic Components and Technology Conference*, Lake Buena Vista, FL USA 2008.

[17] R. Vyas, **A. Rida,** L. Yang, and M.M. Tentzeris, "Design and Development of the First Entirely Paper-Based Wireless Sensor Module" pp. 1-4, *IEEE Antennas and Propagation Symposium*, San Diego, CA USA 2008.

[18] **A. Rida**, L. Yang, R. Vyas, S. Bhattacharya, and M. M. Tentzeris, "Low Cost Inkjet-printing Paper-Based Modules for RFID Sensing and Wireless Applications", pp. 294-297, *Proc of 2008 IEEE European Microwave Conference, RAI, Amsterdam,* Oct 2008. **TOP FIVE PAPERS MICROWAVE PRIZE**

[19] L.Yang, R. Vyas, **A.Rida,** J.Pan, and M.M. Tentzeris, "Wearable RFID-Enabled Sensor Nodes for Biomedical Applications" pp. 2156-2159, *58th Electronic Components and Technology Conference*, Lake Buena Vista, FL USA 2008.

[20] A. Traille, L. Yang, **A. Rida**, and M.M. Tentzeris, "A Novel Liquid Antenna for Wearable Bio-monitoring Applications" pp. 923-926, *IEEE MTT-S International Microwave Symposium*, Atlanta, GA USA, 2008.

[21] R. Vyas, A. Rida, A. Yang, and M.M. Tentzeris, "Design, integration, and characterization of a novel paper-based wireless seosor module" pp. 1305-1308, *IEEE MTT-S International Microwave Symposium*, Atlanta, GA USA, 2008. **HONORARY MENTION**

[22] M.M.Tentzeris, L.Yang, **A. Rida**, A.Traille, R.Vyas, and T.Wu, "Inkjet-Printed RFID Tags on Paper-Based Substrates for UHF Congnitive Intelligence Applications" pp. 1-4, *IEEE 18th International Symposium on Personal, Indoor and Mobile Radio Communications*, 2007.

[23] M.M.Tentzeris, L.Yang, **A. Rida**, A.Traille, R.Vyas, and T.Wu, "RFID's on Paper using Inkjet-Printing Technology: Is it the first step for UHF Ubiquitous Cognitive Intelligence and Global Tracking?" pp. 1-4, *1st Annual RFID Eurasia*, Turkey, 2007.

[24] A. Traille, L. Yang, A. Rida, T. Wu, and M.M. Tentzeris, "Design and Modeling of Novel Multiband/Wideband Antennas for RFID Tags and Readers Using Time-/Frequency- Domian Simulators" pp. 1-3, *Workshop on Computational Electromagnetics in Time-Domain, CEM-TD*, Perugia, Italy, 2007.

[25] R. Vyas, **A. Rida**, L. Yang, and M.M. Tentzeris, "Design and Development of a Novel Paper-Based Inkjet-Printed RFID-Enabled UHF (433.9 MHz) Sensor Node" pp. 1-4, *Asia-Pacific Microwave Conference*, Thailand, 2007.

[26] **A. Rida**, L. Yang, R. Vyas, S. Bhattacharya, and M. M. Tentzeris, "Design and Integration of Inkjet- printed Paper-Based UHF Components for RFID and Ubiquitous Sensing Applications", pp. 724-727, *Proc of 2007 IEEE European Microwave Conference, Munich, Germany,* Oct 2007.

[27] L. Yang**, A. Rida,** J. Li, and M.M. Tentzeris, "Antenna Advancement Techniques and Integration of RFID Electronics on Organic Substrates for UHF RFID Applications in Automotive Sensing and Vehicle Security" pp. 2040-2041, *IEEE 66th Vehicular Technology Conference*, Baltimore, MD 2007.

[28] **A. Rida**, R. Vyas, T. Wu, R. Li, and M. M. Tentzeris, "Development and Implementation of Novel UHF Paper-Based RFID Designs for Anti-counterfeiting and Security Applications", pp. 52-56, *Proc of 2007 IEEE International Workshop on Anti-counterfeiting, Security, Identification,* Xiamen, China, April 2007.

[29] **A. Rida,** L. Yang**,** and M.M. Tentzeris, "Design and Characterization of Novel Paper-based Inkjet-Printed UHF Antennas for RFID and Sensing Applications" pp. 2749-2752, *IEEE Antennas and Propagation Symposium*, Honolulu, HI 2007 **BEST STUDENT PAPER AWARD**

[30] R. Vyas, **A. Rida,** S. Bhattacharya**,** and M.M. Tentzeris, "Liquid Crystal Polymer (LCP): The Ultimate Solution for Low-Cost RF Flrxible Electronics and Antennas" pp. 1729-1732, *IEEE Antennas and Propagation Symposium*, Honolulu, HI 2007.

[31] L. Yang, **A. Rida,** T. Wu, S. Basat, and M.M. Tentzeris, "Integration of Sensors and Inkjet-Printed Tags on Paper-based Substrates for UHF Cognitive Intelligence Applications" pp. 1193-1196, *IEEE Antennas and Propagation Symposium*, Honolulu, HI 2007.

[32] **A.Rida,** L.Yang, R. Vyas, S. Basat, S. Bhattacharya, and M.M. Tentzeris, "Novel Manufacturing Processes for Ultra-Low-Cost Paper-Based RFID Tags with Enhanced Wireless Intelligence" pp. 773-776, *57th Electronic Components and Technology Conference*, Reno, NV USA 2007.

[33] **A.Rida,** R. Vyas, S. Basat, A. Ferrer-Vidal, L. Yang, S. Bhattacharya**,** and M.M. Tentzeris, "Paper-Based Ultra-Low-Cost Integrated RFID Tags for Sensing

and Tracking Applications" pp. 1977-1980, *57th Electronic Components and Technology Conference*, Reno, NV USA 2007.

[34] S. Bhattacharya, M.M. Tentzeris, L. Yang, S. Basat, **A. Rida**, "Flexible LCP and Paper-based Substrates with Embedded Actives, Passives, and RFIDs" pp. 159-166, IEEE Polyteronic Conference, Japan, 2007.

[35] S. Basat, S. Bhattacharya, **A. Rida**, S. Johmston, L. Yang, M.M. Tentzeris, and J. Laskar, "Fabrication and Assembly of a Novel High-Efficiency UHF RFID Tag on Flexible LCP Substrate" pp. 1352-1355*, 56th Electronic Components and Technology Conference*, 2006.

[36] A. Ferrer-Vidal, **A. Rida**, S. Basat, L. Yang, and M.M. Tentzeris, "Integration of Sensors and RFID's on Ultra-low-cost Paper-based Substrates for Wireless Sensor Networks Applications" pp. 126-128, *2nd IEEE workshop on Wireless Mesh Networks*, Reston VA 2006.

[37] L. Yang, S. Basat, **A. Rida**, and M.M. Tentzeris, "Design and Development of Novel Miniaturized UHF RFID Tags on Ultra-low-cost Paper-based Substrates" pp. 1493-1496, Proceedings of Asia-Pacific Microwave Conference, Yokohama, Japan, 2006. **BEST CONFERENCE PAPER AWARD**

[38] S. Basat, S. Bhattacharya, L. Yang, **A. Rida**, and M.M. Tentzeris, "Design of a Novel High-efficiency UHF RFID Antenna on Flexible LCP Substrate with High Read Range Capability" pp. 1031-1034, *IEEE Antennas and Propagation International Symposium*, 2006.

REFERENCES

[1]World Health Statistics WHO 2007, Ten Statistical Highlights in Global Public Health, Internet,http://www.who.int/healthinfo/global_burden_disease/GBD_report_2004update_part2.pdf, date accessed: April 2010

[2]ABIresearch, "RFID Market to Reach $5.35 Billion This Year." Internet, http://www.abiresearch.com/press/1618-RFID+Market+to+Reach+$5.35+Billion+This+Year, date accessed: April 2010

[3]Research And Markets, "Consumer Electronics: Global Industry Guide" Internet, http://www.researchandmarkets.com/research/ea88c7/consumer_electroni, date accessed: April 2010

[4]RIDA, A., *RFID-Enabled Sensor Design and Applications*. Boston, MA: Artech House, 2010.

[5]FINKENZELLER, K., *RFID Handbook, Second Edition*. New York, NY, Wiley, 2004.

[6]K. KUROKAWA, "Power Waves and the Scattering Matrix," *Microwave Theory and Techniques, IEEE Transactions on.,* vol. MTT-13, no. 3, pp. 194-202, Mar. 1965.

[7]A. FERRER-VIDAL, A. RIDA, S. BASAT, L. YANG, AND M.M. TENTZERIS, "Integration of sensors and RFIDs on ultra-low-cost paper-based substrates for wireless sensor networks applications" *IEEE Workshop on Wireless Mesh Networks*, 2006 Page(s):126 – 128

[8] S. Nickolaou, "Design and implementation of compact reconfigurable antennas for UWB and WLAN applications" Ph.D. ddissertation, Georgia Institute of Technology, 2007.

[9] HUANG, K.C., *Millimeter Wave Antennas for Gigabit Wireless Communications*. New York, NY: Wiley, 2008

[10]KASPER, E., et al., "High Speeds in a Single Chip" IEEE Microwave Magazine, Vol. 10, No. 7, Dec 2009, pp. 28-33.

[11]XIAO, S.Q., *Millimeter Wave Technology in Wireless PAN, LAN, and MAN*, Boca Raton: FL: CRC Press, 2008

[12]High Frequency Materials Product Selector Guide, Rogers Corp, Internet: http://www.rogerscorp.com/documents/776/acm/High-Frequency-Laminates---Product-Selector-Guide.aspx

[13]Kyocera website. Internet: http://americas.kyocera.com/kai/semiparts/pdfs/DesignGuide.pdf, Date accessed: Feb. 2011.

[14]D. THOMPSON, O. TANTOT, H. JALLAGEAS, G. PONCHAK, M. M. TENTZERIS, J. PAPAPOLYMEROU, "Characterization of LCP material and transmission lines on LCP substrates from 30 to 110GHz," IEEE Trans. Microwave Theory and Tech., vol. 52, no. 4, pp. 1343-1352, April 2004.

[15] H.INOUE, S.FUKUTAKE, AND H.OHATA,"Liquid crystal polymer film heat resistance and high dimensional stability," in Proc. Pan Pacific Microelect. Symp., Feb. 2001, pp. 273–278

[16] X. WANG, J. ENGEL, AND C. LIU, “Liquid crystal polymer (LCP) for MEMS: processes and applications,” J. Micromech. Microeng., vol. 13, 2003.
[17]L. M. HIGGINS III, “Hermetic and optoelectronic packaging concepts using multi-player and active polymer systems,” Advancing Microelectronics, vol. 30, no. 4, pp. 6–13, July 2003.
[18] G. ZOU, H. GRONQVIST, P. STARSKI, AND J. LIU, “High frequency characteristics of liq- uid crystal polymer for system in a package application,” in IEEE 8th Int. Advanced Packaging Materials Symp., Mar. 2002, pp. 337–341.
[19] G.ZOU, H.GRONQVIST, J.P.STARSKI, ANDJ.LIU,“Characterizationofliquidcrystalpolymer for high frequency system-in-a-package applications,” IEEE Trans. Adv. Packag., vol. 25, 2002.
[20] LIU, D., Advanced Millimeter-wave Technologies, New York, NY: Wiley, 2009
[21]S. Simula, S. Ikalainen, and K. Niskanen, “Measurement of the dielectric properties of paper,” J. Imag. Sci. Technol., vol. 43, no. 5, Sep.1999
[22] RIDA, A, “Conductive Inkjet Printed Antennas on Flexible Low-cost Paper-Based Substrates for RFID and WSN Applications” MS. Thesis, Georgia Institute of Technology, 2009.
[23]L. YANG, A. RIDA, R. VYAS, M. M. TENTZERIS, "RFID Tag and RF Structures on a Paper Substrate Using Inkjet-Printing Technology," Microwave Theory and Techniques, IEEE Transactions on Volume 55, Issue 12, Part 2, Dec. 2007 Page(s):2894 – 2901
[24] J.M. HEINOLA, “Dielectric characterization of printed wiring board materials using ring resonator techniques: a comparison of calculation models” Dielectrics and Electrical Insulation, IEEE Transactions on Volume 13, Issue 4, Part 2, Aug. 2006 Page(s):717 – 726
[25]Krupka, J., Derzakowski, K., Abramowicz, A., Riddle, B., Baker-Jarvis, J., Clarke, R.N., Rochard, O.C., "Bounds on permittivity calculations using the TE01δ dielectric resonator," 14th International Conference on Microwaves, Radar and Wireless Communications, 2002. MIKON 2002.
[26]THOMPSON, D. “Characterization and Design of Liquid Crystal Polymer (LCP) Based Multilayer RF Components and Packages” Ph.D. dissertation, Georgia Institute of Technology, 2006.
[27] "UHF Gen-2 System Overview," Texas Instruments, Internet: http://rfidusa.com/superstore/pdf/UHF_System_Overview.pdf, September,2005
[28]P. V. NIKITIN , S. RAO, S. F. LAM, V. PILLAI, AND H. HEINRICH, "Power Reflection Coefficient Analysis for Complex Impedances in RPID Tag Design," IEEE Transactions on Microwave Theory and Techniques, 53, 9, September 2005, pp. 2721-2725
[29]J. D. GRIFFIN, G. D. DURGIN, A. HALDI, AND B. KIPPELEN, “RF tag antenna performance on various materials using radio link budget,” IEEE Antennas Wireless Propag. Lett., Dec. 2006.
[30]J. HONG AND M.J. LANCASTER, Microstrip Filters for RF/Microwave Applications, Wiley, 2001.

[31]L. ACCATINO, G. BERTIN, M. MONGIARDO, G. RESNATI, "A New Dielectric-Loaded Dual-Mode Cavity for Mobile Communications Filters" 31st European Microwave Conference, pp. 1-4, London, England 2001
[32]J.H. LEE, AND M.M. TENTZERIS, Three-Dimensional Integration and Modeling A Revolution in RF and Wireless Packaging, Morgan and Claypool, 2008
[33]R. BAIRAVASUBRAMANIAN, AND J. PAPAPOLYMEROU, "Multilayer Quasi-elliptic filters using dual mode resonators on Liquid Crystal Polymer Technology" IEEE International Microwave Symposium, pp. 549-552, June 2007
[34]D. NIU, T. HUANG, H. LEE, AND C. CHANG, "An X-Band Front-End Module Using HTS Technique for a Commercial Dual Mode Radar, IEEE Transactions on Applied Superconductivity, VOL. 15, NO. 2, June 2005
[35]C. LUGO, AND J. PAPAPOLYMEROU, "Bandpass Filter Design Using a Microstrip Triangular Loop Resonator With Dual-Mode Operation" IEEE Microwave and Wireless Components Letters, VOL. 15, NO. 7, July 2005
[36]C. QUENDO, E. RIUS, C. PERSON, J. FAVENNEC, Y. CLAVET, A. MANCHEC, R. BAIRAVASUBRAMANIAN, S. PINEL, J. PAPAPOLYMEROU, AND J. LASKAR, "Wide Band, High Rejection and Miniaturized Fifth Order Bandpass Filter on LCP Low Cost Organic Substrate" IEEE MTT-S International Microwave Digest, pp. 2203-2205, vol. 4, 2005
[37]J. PARK, AND J. YUN, "A Design of the Novel Coupled-Line Bandpass Filter Using Defected Ground Structure With Wide Stopband Performance" IEEE Transactions on Microwave Theory and Techniques, pp. 2037-2043, Vol. 50, No. 9, Sept 2002
[38] K.C. LEE, H.T. SU, AND W.S.H. WONG, "Realization of a Wideband Bandpass Filter Using Cascaded Lowpass to Highpass Filter", pp. 14-17, International Conference on Microwave and Millimeter Wave Technology, ICMMT 2008
[39] M.H. CAPSTICK, "Microstrip lowpass-bandpass diplexer topology" Electronics Letters, pp. 1958-1960, vol. 35, issue 22, 1999
[40]D. POZAR, Microwave Engineering, Wiley, 2005
[41]JMT Transitions, spec sheet, available: http://www.jmicrotechnology.com/PP15.pdf
[42]Dimatix datasheet http://www.dimatix.com/files/DMP-2831-Datasheet.pdf, date visited: Sep 2008
[43]O. AZUCENA, J. KUBBY, D. SCARBROUGH, AND C. GOLDSMITH, "Inkjet printing of passive microwave circuitry" IEEE MTT-S International Microwave Symposium Digest, pp: 1075-1078, June 15-20
[44]M. CARTER, J. COLVIN, AND J. SEARS, "Characterization of conductive inks deposited with maskless mesoscale material deposition", TMS2006, Mar. 12-16, San. Antonio, Texas, USA
[45]J. SIDEN, M.K. FEIN, A. KOPTYUG, AND H,-E, NILSON, "Printed antennas with variable conductive ink layers" IET Microwaves, Antennas and Propagation, Volume 1, Issue 2, pp: 401-407, April 2007
[46]A. PIQUE, AND D. B. CHRISEY, "Direct-write Technologies for Rapid Prototyping Applications", Academic Press, 2002. International Standard Book Number: 0-12-174231-8.

[47]Texas Instrument, "UHF Gen2 Strap RI-UHF-STRAP-08," Data Sheet, October 2006.
[48]G. SHAKER, A. RIDA, S. SAFAVI-NAEINI, M.M. TENTZERIS, AND S. NIKOLAOU, "Inkjet Printing of UWB Antennas on Paper Based Substrates" accepted for publication/presentation in European Conference on Antennas and Propagation, Rome, Italy 2011
[49] J. LASKAR, S. PINEL, D. DAWN, S. SARKAR, B. PERUMANA AND P. SEN, "The Next Wireless Wave is Millimeter Wave" Vol. 50 l No. 8 | August 2007 | Pg. 22 in Microwave Journal
[50] Denso, information was provided by vendor upon request
[51] Fujitsu Ten, information was provided by vendor upon request
[52] Delphi, information was provided by vendor upon request
[53] Bosch Automotive, information was provided by vendor upon request
[54] Groneveld Roadeye, information was provided by vendor upon request
[55] M/A Com, information was provided by vendor upon request
[56] RoadEye, 2nd generation Radar Sensor for Adaptive Cruise Control, Groeneveld Active Safety Systems, a presentation given by Peter Hendrickx
[57]A. MARGOMENOS, Y. LEE, AND L. P. B. KATEHI, "Wideband Si micromachined transitions for RF wafer-scale packages," in Proc. IEEE SiRF, Long Beach, CA, Jan. 2007, pp. 183–186.
[58]A. STARK AND A. F. JACOB, "A broadband vertical transition for millimeter-wave applications," in Eur. Microw. Conf. 2008 Dig., Amsterdam, The Netherlands, Oct. 2008, pp. 476–479.
[59]Y. G. KIM, K. W. KIM, AND Y. K. CHO, "An ultra-wideband microstrip-to-CPW transition," in Proc. IEEE MTT-S Int. Microw. Symp. 2008, pp. 1079–1082.
[60]W. MAYER, M. MEILCHEN, W. GRABHERR, P. NUCHTER, AND R. GUHL, "Eightchannel 77-GHz front-end module with high performance synthesized signal generator for FMCW sensor applications," IEEE Trans. Microw.Theory Tech., vol. 52, no. 3, pp. 993–1000, Mar. 2004
[61]K. C. Gupta, R. Garg, I. Bahl, and P. Bhartia, Microstrip Lines and Slotlines 2nd ed. Norwood, MA: Artech House, 1996.
[62]Advanced Design Systems, Agilent, Internet: http://www.home.agilent.com/agilent/product.jspx?cc=US&lc=eng&ckey=1297113&nid=-34346.0.00&id=1297113
[63]Picoprobe by GGB Industries, Internet: http://www.ggb.com/40a.html
[64]HFSS Ansys,Internet: http://www.ansoft.com/products/hf/hfss/
[65] N. H. L. KOSTER, S. KOBLOWSKI, R. BERTENBURG, S. S. H. S. HEINEN, AND I. A. W. I. WOLFF, "Investigations on air bridges used for MMICs in CPW technique," in Proc. 19th Eur. Microw. Conf., Sep. 1989, pp. 666–671.
[66] H. KIM AND R. F. DRAYTON, "Wire-bond free technique for right-angle coplanar waveguide bend structures," IEEE Trans. Microw. Theory Tech., vol. 57, no. 2, pp. 442–448, Jan. 2009
[67]PAPAPOLYMEROU, J. ; PONCHAK, G.E. ; DALTON, E. ; BACON, A. ; TENTZERIS, M.M., "Crosstalk between finite ground coplanar waveguides over polyimide layers for 3-D

MMICs on Si substrates" IEEE Trans. Microw. Theory Tech., vol. 52, no. 4, pp. 1292–1301, Jan. 2004
[68]C. BALANIS, Antenna Theory: Analysis and Design, Wiley, 2005
[69]B. Kappar, Metro Circuits, private communication. Sept. 2009.